Experimental investigation of heat transport in nanomaterials using electro-thermal methods

Jessy Paterson

THÈSE

Pour obtenir le grade de

DOCTEUR DE L'UNIVERSITÉ GRENOBLE ALPES

Spécialité : Physique de la Matière Condensée et du Rayonnement

Arrêté ministériel : 25 mai 2016

Présentée par

Jessy PATERSON

Thèse dirigée par **Olivier BOURGEOIS**, Directeur de Recherches, Université Grenoble Alpes
et codirigée par **Dimitri TAINOFF**, Université Grenoble Alpes

préparée au sein du **Laboratoire Institut Néel**
dans **l'École Doctorale Physique**

Etude expérimentale du transport de chaleur dans les nanomatériaux par méthodes électrothermiques

Experimental investigation of heat transport in nanomaterials using electro-thermal methods.

Thèse soutenue publiquement le **18 novembre 2020**,
devant le jury composé de :

Monsieur JEAN-YVES DUQUESNE
CHARGE DE RECHERCHE, CNRS DELEGATION PARIS-CENTRE, Rapporteur
Monsieur AITOR LOPEANDIA FERNANDEZ
PROFESSEUR ASSOCIE, UNIV. AUTONOME DE BARCELONE - ESPAGNE, Rapporteur
Madame SEVERINE GOMES
DIRECTRICE DE RECHERCHE, CNRS DELEGATION RHONE AUVERGNE, Examinatrice
Monsieur JULIEN PERNOT
PROFESSEUR DES UNIVERSITES, UNIVERSITE GRENOBLE ALPES, Président
Monsieur GILLES PERNOT
MAITRE DE CONFERENCES, UNIVERSITE DE LORRAINE, Examinateur
Monsieur DAVID LACROIX
PROFESSEUR DES UNIVERSITES, UNIVERSITE DE LORRAINE, Examinateur

Remerciements

J'aimerais remercier premièrement mes deux encadrants, Olivier Bourgeois et Dimitri Taïnoff, qui m'ont introduit à la physique du transport thermique lors de mon arrivée à l'Institut Néel en stage de Master 2. Je souligne vos qualités scientifiques et humaines qui permettent à tout étudiant de se sentir en pleine confiance dans le laboratoire. Vous m'avez accordé une très grande liberté pendant ces quatre années de doctorat, et a posteriori je pense que c'est ce qui m'a permis de m'investir pleinement et de m'épanouir dans ce projet qui m'a réellement passionné.

Je remercie ensuite les membres de mon jury, Jean-Yves Duquesne, Aitor Lopeandia Fernandez, Severine Gomes, Julien Pernot, Gilles Pernot et David Lacroix, d'avoir accepté d'apporter leur expertise sur mon travail, et de m'avoir fourni des critiques constructives.

Les résultats obtenus pendant cette thèse n'auraient pu voir le jour sans l'implication de nombreuses personnes qui m'ont apporté leur aide. Je remercie l'équipe Nanofab (Gwenaëlle, Bruno, Latifa, Thierry, Seb, Jean-François) pour les nombreuses lithographies laser ! Un grand merci à Gaël et Manu et plus généralement le Pole Capteur dirigé par Jean Luc Garden pour les dépôts de platine avec des coefficient de température défiant toute concurrence ! Merci également à Eric Mossang et Olivier Leynaud du pôle X'press pour leur aide concernant les mesures de XRD et XRR. Un très grand merci également aux membres du Pole Electronique, en particulier Jean-Luc Mocellin et Olivier Exshaw pour leur aide vis-à-vis du pont différentiel et du boitier MMR3. Je remercie également Valentina Giordano et Pierre Noé avec qui j'ai pu collaborer durant cette thèse. Je remercie le soutien financier de l'Agence Nationale de la Recherche, par le biais du projet Mesophon qui a financé l'intégralité de cette thèse. C'était quand même agréable d'avoir un salaire.

Un soutien encore plus important que le soutien financier est évidemment le soutien émotionnel. Sans nul doute le déroulement de cette thèse aurait été différent sans le soutien à toute épreuve de Julie, qui, peut-être, au bout de quatre ans, aura appris ce qu'était un phonon. Une très grande fierté ! Merci pour ta patience, ton soutien et ta confiance, sans parler de tes talents culinaires hors du commun. Il en va de même pour ma famille, qui depuis mon enfance me pousse vers le haut. J'ai toujours été baigné dans un climat de confiance et d'amour et je vous en remercie. Merci à maman, Olivier, Kelly, Gary, Lily, Chipie, Papy, Mamy, les tontons, les tatas, les cousins et les cousines. Je place une huge dédicace pour mes amis d'Orléans (et Tours), Alex, Steve, Alice, Jordan, Roathar, et les jumeaux. Ça fait presque 15 ans qu'on se connaît ! Incroyable mais vrai, comme l'émission sur TF1. On se voit moins souvent mais à chaque fois c'est appréciable, surtout les minasses à la chouffe.

Je retiens que cette thèse s'est déroulée dans une ambiance incroyablement chaleureuse, que ce soit au laboratoire ou dans les bars grenoblois. L'équipe TPS, maintenant dirigée par Hervé Guillou, est une formidable équipe que je ne pourrais que recommander à n'importe quel étudiant, tant son dynamisme, sa bienveillance et sa bonne humeur contribuent grandement à rendre l'expérience qu'est la thèse extrêmement agréable. Je remercie une fois de plus Olivier et Dimitri, Hervé, Jean-Luc, Gaël, Manu, Jacques, Cécile. Une attention particulière va vers les plus jeunes de l'équipe ! Adib (et ses rasaka), Clothilde, Céline (reviens à Grenoble

stp), Rahul (my man), Dhruv (my man as well), Etienne (nion nion nion), Judith (nnnnice), Anthony (futur collègue !) et j'en oublie sûrement. Merci à Christophe et Jeremie pour leurs remarques sur le manuscrit ! Notre QG « Le Hasard » évidemment, et son merveilleux choix de pintes. La folie grenobloise aurait eu une autre saveur sans la présence de Myriam, Mathilde, Julien, Élie, Kiki, Hugo, Antho, Flo et encore d'autres !

Je pense également au « MP des cons », on se connaît depuis plus de dix ans et on a toujours quelque chose à se raconter. Des aléas sentimentaux jusqu'aux Bitcoins, en passant par un découpage propre de stickers et des release de Bicep. Je suis certain qu'on sera en contact dans encore 10 ans quand on sera tous millionnaires grâce à un fine gestion de nos portefeuilles d'actions. Merci mes bons kheys.

Merci également à tous les développeurs bénévoles derrière les superbes logiciels tel qu'Inkscape ou bien LaTeX. Un merci également à de nombreuses communautés sur internet qui permettent de ne pas passer plusieurs jours à débuguer un programme, en particulier le site stackoverflow. Sans ce genre de forum j'aurais probablement terminé ma thèse en une quinzaine d'années !

Abstract

This dissertation presents an experimental study of heat transport in various types of materials that greatly differ in their structure, size and thermal properties. The motivations behind this study are multiple. The technological stakes related to the increased mastery of thermal management of current and future technologies are considerable, given the important correlation between the overall performance of a device and the efficient management of thermal gradients that develop within it. In particular, the performance of applications such as thermoelectric generators or phase-change memories are greatly enhanced when their architecture is based on materials with low thermal conductivities. From a fundamental point of view, the study of low dimensional materials, structured at scales comparable to the characteristic lengths defining heat transport, such as the mean free path of phonons or their wavelength, is of crucial importance in order to understand the mechanisms responsible for atypical thermal properties that are reported for low-dimensional and/or nanostructred materials. The experimental investigation of heat transport is carried out by means of electro-thermal methods, whose principles and foundations are particularly detailed. In particular, the 3ω method has been implemented to measure the thermal conductivity of bulk materials, thin films down to 17 nm thick, as well as thermal boundary resistances present in multilayer systems. We were able to demonstrate a reduction of more than a factor of 3 in the thermal conductivity of a crystalline germanium matrix with crystalline spherical nano-inclusions having an average diameter of 16 nm compared to its non-nanostructured counterpart. The reduction of the thermal conductivity of this nano-structured material is attributed to phonon scattering by the spherical nano-inclusions whose concentration plays an important role in reducing the mean free path of heat carriers in this heterogeneous material. A reduction in thermal conductivity by a factor of 5 is also observed in another germanium-based nanostructured material, GeTe, after the introduction of carbon – a reduction that can be explained by the presence of nano-sized grains surrounded by amorphous carbon. The versatility of the 3ω method has allowed us to quantify the contribution of thermal boundary resistances for systems such as Pt/Al_2O_3/germanium, Pt/Al_2O_3/sapphire or Pt/SiN/Si. Our findings indicate that the thermal boundary resistance at the Al_2O_3/germanium interface can contribute substantially to the overall thermal resistance of a multilayer system, which may be detrimental if applications based on structures with this type of interface are considered. Finally, anisotropic thermal properties of a sapphire substrate have been experimentally investigated using the 2ω method.

Version en langue française

Les travaux effectués lors de cette thèse portent sur l'étude expérimentale des propriétés de transport de chaleur dans divers types de matériaux, de l'échelle macroscopique jusqu'à l'échelle du nanomètre. Les motivations ayant donné naissance à cette étude sont multiples. Les enjeux technologiques liés à la maîtrise accrue de la gestion thermique des technologies actuelles et de demain prennent une ampleur considérable, étant donné la corrélation importante qui existe entre les performances globales d'un dispositif et la gestion efficace des gradients thermiques apparaissant en son sein. En particulier, les performances des applications telles que les générateurs thermoélectriques ou bien les mémoires à changement de phase sont grandement améliorées lorsque leur architecture est basée sur des matériaux possédant des faibles conductivité thermiques. D'un point de vue fondamental, l'étude de matériaux de basse dimension, structurés à des échelles comparables aux longueurs caractéristiques définissant le transport de chaleur, comme le libre parcours moyen des phonons ou leur longueur d'onde, est d'une importance cruciale afin de comprendre les mécanismes responsable des propriétés thermiques atypiques observées dans des matériaux de basse dimension et/ou structurés à l'échelle nanométrique. Cette étude est menée à l'aide de méthodes dites électro-thermiques qui sont décrites de manière approfondie, en particulier concernant la modélisation des données expérimentales. En particulier, la méthode 3ω a été implémentée afin de mesurer la conductivité thermique de matériaux massifs, de couches minces d'épaisseur descendant jusqu'à 17 nm, ainsi que des résistances thermiques d'interfaces présentes dans des systèmes multicouches. Nous avons pu mettre en évidence la réduction de plus d'un facteur 3 de la conductivité thermique d'une matrice cristalline de germanium possédant des nano-inclusions sphériques cristallines d'un diamètre moyen de 16 nm, comparée à son homologue non nanostructuré. La réduction de la conductivité thermique de ce matériau nano-structuré est attribuée à des processus de diffusion des phonons par les nano-inclusions sphériques dont la concentration joue un rôle important quant à la réduction du libre parcours moyen des porteurs de chaleur dans ce matériau hétérogène. Une réduction de la conductivité thermique d'un facteur 5 est également observé dans le chalcogène GeTe après introduction de carbone – réduction pouvant être expliquée par la présence de grains de tailles nanométriques entourés de carbone amorphe. Le caractère polyvalent de la méthode 3ω nous a permis de quantifier la contribution des résistances thermiques d'interfaces pour des systèmes de type Pt/Al_2O_3/germanium, Pt/Al_2O_3/sapphire ou bien Pt/SiN/Si. Nos conclusions indiquent que la résistance thermique à l'interface Al_2O_3/germanium peut contribuer de manière substantielle à la résistance thermique globale d'un système multicouche, pouvant être préjudiciable si des applications basées sur des structures comportant ce type d'interface sont envisagées. Enfin, les propriétés thermiques anisotropes d'un substrat de saphir ont été étudiées, en utilisant la méthode 2ω.

Contents

List of Symbols

x, y, z	Position	m
t	Time	s
T	Temperature	K
ϕ	Heat flux across a surface	$\mathrm{W\,m^{-2}}$
	Phase	deg
q_V	Volumetric power source	$\mathrm{W\,m^{-3}}$
k	Thermal conductivity	$\mathrm{W\,m^{-1}\,K^{-1}}$
	Wavevector	$\mathrm{m^{-1}}$
k_e	Electronic contribution to the thermal conductivity	$\mathrm{W\,m^{-1}\,K^{-1}}$
k_{latt}	Lattice contribution to the thermal conductivity	$\mathrm{W\,m^{-1}\,K^{-1}}$
k_{f}	Thermal conductivity of a film	$\mathrm{W\,m^{-1}\,K^{-1}}$
k_{s}	Thermal conductivity of a substrate	$\mathrm{W\,m^{-1}\,K^{-1}}$
k_{i_x}	Thermal conductivity of element i in x direction	$\mathrm{W\,m^{-1}\,K^{-1}}$
k_{eff}	Effective thermal conductivity	$\mathrm{W\,m^{-1}\,K^{-1}}$
k_{xy}	Thermal anisotropy ratio in the xy plane	-
k_{zy}	Thermal anisotropy ratio in the zy plane	-
E	Energy	J
$\dot{E}$	Rate of energy	$\mathrm{J\,s^{-1}}$
U	Internal energy	J
ρ	Density	$\mathrm{g\,m^{-3}}$
C_p	Specific heat	$\mathrm{J\,g^{-1}\,K^{-1}}$
M	Mass of an atom	g
K	Force constant between atoms	$\mathrm{g\,s^{-2}}$
u	Atomic displacement	m
ω	Phonon angular frequency	$\mathrm{rad\,s^{-1}}$
f	Electrical frequency	$\mathrm{s^{-1}}$
$\omega_e = 2\pi f$	Electrical angular frequency	$\mathrm{rad\,s^{-1}}$
$\omega = 2 \times \omega_e$	Thermal angular frequency	$\mathrm{rad\,s^{-1}}$
v	Phonon group velocity	$\mathrm{m\,s^{-1}}$
v_t	Transverse phonon group velocity	$\mathrm{m\,s^{-1}}$
v_l	Longitudinal phonon group velocity	$\mathrm{m\,s^{-1}}$
v_s	Speed of sound	$\mathrm{m\,s^{-1}}$
k_B	Boltzmann constant	$\mathrm{m^2\,kg\,s^{-2}\,K^{-1}}$
$\hbar$	Reduced Planck constant	J s
i	Imaginary number	-
s	Phonon polarization	-
F	Force	$\mathrm{g\,m\,s^{-2}}$
n	Distribution function	-
n_0	Distribution function at equilibrium	-
φ	Interface density	$\mathrm{m^{-1}}$
τ	Collision time	s

V	Volume	m^3
D	Density of states	-
θ_D	Debye temperature	K
ω_D	Debye frequency	$\mathrm{rad\,s}^{-1}$
Λ	Phonon mean free path	m
λ	Phonon wavelength	m
λ_dom	Dominant phonon wavelength	m
G	Reciprocal lattice wave-vector	m^{-1}
S	Seebeck coefficient	$\mathrm{V\,K}^{-1}$
σ	Electrical conductivity	$\mathrm{S\,m}^{-1}$
	Cross section	m^2
	Stefan-Boltzmann constant	$\mathrm{W\,m}^{-2}\,\mathrm{K}^{-4}$
η	Particle concentration	m^{-3}
r_ni	Radius of nano-inclusion	m
d_ni	Diameter of nano-inclusion	m
χ	Size parameter	-
R_int	Thermal boundary resistance	$\mathrm{m}^2\,\mathrm{K\,W}^{-1}$
$R_{i/j}$	Thermal boundary resistance between materials i and j	$\mathrm{m}^2\,\mathrm{K\,W}^{-1}$
R_th	Thermal resistance	$\mathrm{m}^2\,\mathrm{K\,W}^{-1}$
R_film	Thermal resistance of one particular film	$\mathrm{m}^2\,\mathrm{K\,W}^{-1}$
$\alpha_{1\to2}$	Transmission coefficient	-
d_f	Thickness of a film	m
d_s	Thickness of a substrate	m
d_tr	Thickness of the transducer	m
$V_{1\omega_e}$	First harmonic of the electrical voltage	V
$V_{2\omega_e}$	Second harmonic of the electrical voltage	V
$V_{3\omega_e}$	Third harmonic of the electrical voltage	V
V_DC	Direct electrical voltage	V
$I_{1\omega_e}$	AC current at electrical frequency $1\omega_e$	A
I_{DC}	DC current	A
I_1	Amplitude of the AC current at electrical ferquency $1\omega_e$	A
P	Electrical power	J
P_l	Electrical power per unit length	$\mathrm{J\,m}^{-1}$
Z_{th}	Thermal impedance (scaled with area)	$\mathrm{m}^2\,\mathrm{K\,W}^{-1}$
q	Thermal wavevector (in y direction if not specified)	m^{-1}
q_x	Thermal wavevector in x direction	m^{-1}
β	Temperature coefficient of resistance	K^{-1}
λ_tpd	Thermal penetration depth (in y direction if not specified)	m
$\lambda_{\mathrm{tpd},x}$	Thermal penetration depth, in x direction	m
Z_e	Electrical impedance	Ω
C	Electrical capacitance	F
L	Electrical inductance	H
b	Half-width of the heater/thermometer	m
l	Length of the heater/thermometer	m
l_th	Length between the inner leads of the thermometer	m

α	Thermal diffusivity	$\mathrm{m^2\,s^{-1}}$
ϵ	Emissivity	-
d_{ht}	Heater to thermometer distance	m
K_0	Zeroth-order modified Bessel function of the 2^d kind	-
K_1	First-order modified Bessel function of the 2^d kind	-
γ	Euler-Mascheroni constant	-
$S^y_{x_i}$	Sensitivity of model y to parameter x_i	-
δ	Dirac delta function	-
Φ	Volume fraction of nano-inclusions	%
$g(r, \alpha_g, \beta_g)$	Gamma distribution function	-
η	Number of particles per unit volume	$\mathrm{m^{-3}}$
L	Lorenz number	$\mathrm{W\ \Omega\ K^{-2}}$
ρ_e	Electrical resistivity	Ω m

List of Abbreviations

TBR	Thermal Boundary Resistance
TPD	Thermal Penetration Depth
TCR	Temperature Coefficient of Resistance
MFP	Mean Free Path
TDTR	Time-Domain thermoreflectance
RTA	Relaxation time approximation
XRR	X-Ray Reflectivity
NW	Nanowire
NI	Nano-inclusion
ND	Nanodot
NP	Nano-particle
AMM	Acoustic Mismatch Model
DMM	Diffuse Mismatch Model
PRL	Phonon Radiation Limit
MD	Molecular Dynamics
AFM	Atomic Force Microscopy
ADC	Analog to Digital Converter
DAC	Digital to Analog Converter
THD	Total Harmonic Distortion
PID	Proportional Integral Derivative
FT	Fourier Transform
FEM	Finite Element Modelling/Finite Element Method
DC	Direct Current, also used for voltage with constant polarity
ALD	Atomic Layer Deposition
UV	Ultraviolet
RBS	Rutherford Backscattering
PGEC	Phonon-Glass Electron-Crystal
MBE	Molecular Beam Epitaxy
TEM	Transmission Electron Microscopy
XRD	X-ray diffraction
mEMA	modified Effective Medium Approximation
PCM	Phase change material/phase change memory

Introduction

The ever-increasing power density required in today's microelectronic devices is one of the main catalyst behind the continued miniaturization of novel electronic equipments. The implementation of low-dimensional materials in next-generation devices is alas accompanied with great challenges to face – one of which is the efficient management of heat in size-constrained structures, an essential matter for achieving long-term reliability and preventing rapid failure of downscaled devices. From the efficient dissipation of heat away from hot spots for achieving increased working performances in computers, smartphones, or data centers, to the localization of heat within a small volume for controlling a material's phase in such application as non-volatile phase change memories, a large variety of applications rely upon the thermal properties of their constituting materials. This breadth of applications consequently entails the need for the discovery, growth and characterization of materials that span an extended range of thermal properties.

As a result, the critical, industry-driven need for an accurate knowledge of the thermal properties of low-dimensional materials has been paralleled by the development of increasingly sensitive thermal characterization techniques within the last three decades – in tandem with the ceaseless development of clean room fabrication methods and high-precision measurement apparatus. Tuning the thermal properties of a material is thus of consequent technological interest, and requires a crisp understanding of the mechanisms responsible for heat conduction in nanoscale materials. From a thermal characterisation standpoint, the size reduction of structures implemented in nowadays' devices poses additional challenges. Indeed, creating both a heat source and a thermometer in size-constrained structures is challenging from a technological point of view. Additionally, the interpretation of experimental data becomes more complex when the size of the probed material is commensurate to that of the heat source, thermometer, or to characteristic lengths defining heat transport. Besides, for multilayer systems, the contribution of interfacial thermal resistances often becomes commensurate to the thermal resistance of the layer that is studied, leading to little information about the source of the thermal resistance that is measured in such systems.

The present thesis is devoted to the experimental investigation of heat transport in nanomaterials, in particular, thin films that are structured at the nanometer scale such that their thermal properties are strongly modified. An important emphasis is put on the measurement technique that have been used – the 3ω method. The detailed analysis of the electro-thermal technique guided us for the design of sensitive experiments, conducted for determining the thermal conductivity of materials that diverge greatly in terms of size, structure, and thermal properties.

Chapter 1 is a general introduction to heat transport in solids, gradually decreasing from macroscopic heat transport in bulk materials to phonon transport across interfaces. This introductory chapter allows to define several fundamental quantities that we use throughout the thesis. We put emphasis on the microscopic description of thermal conductivity, and review several nanostructures where heat transport has been experimentally reported to be impacted by nanostructuration.

Chapter 2 introduces the 3ω method, a popular method for measuring the thermal conductivity of bulk materials and thin films, and its implementation in a laboratory environment, along with some of the constraints we have faced in doing so.

In **Chapter 3**, we provide a detailed derivation of the thermal model that is used in subsequent chapters to extract thermal parameters from experimental data. We review and detail some popular techniques that are used to infer thermal properties of substrates, thin films and thermal boundary resistances, along with the conditions to satisfy in order to use simple or not-so-simple thermal models.

Chapter 4 retraces several assumptions that are usually made in the literature, and that we have made in Chapter 3, concerning the thermal model that is used in order to infer thermal properties from 3ω experiments. In particular, using Finite Element Modelling, we quantify the effect of heat conduction within the heater according to its geometry and thermal properties. An analytical 3D model for 3ω experiments is proposed for multilayer structures, from which we derive an additional criteria for using the so-called "slope method" for determining the thermal conductivity of a substrate with minimal error.

Chapter 5 is dedicated to the so-called 2ω method, a more recent technique introduced by Ramu and Bowers[1] for measuring anisotropic thermal properties of bulk samples. We use the derivation of the thermal model for the 3ω geometry and adapt it to the 2ω geometry, and provide an analytical solution for the temperature oscillation sensed in a 2ω geometry, for multilayer systems. We show by analytical means that this method is insensitive to the thermal boundary resistance at the heater/substrate interface. Based on the multilayer solution derived in the 2ω geometry, we propose a frequency-dependent heat spreader method, adapted from Refs. 2,3, for measuring the thermal conductivity of thin films using the 2ω method.

Chapter 6 presents all the thermal conductivity measurements that have been performed during this thesis. The materials that have been studied vary in terms of their size, structure, and thermal properties. Among other materials, we have used the 3ω method to measure the thermal conductivity of amorphous aluminium-oxide thin films ranging from 17 nm to 120 nm in thickness, along with the thermal boundary resistances of the systems Pt/Al_2O_3/sapphire and Pt/Al_2O_3/germanium. Additionally, the thermal conductivity of two germanium-based nanostructured materials, a germanium matrix with Ge_3Mn_5 nano-inclusions, and a GeTe alloy doped with carbon, was investigated as the internal structure and innovative nanostructuration of both materials can be seen as models for studying phonon scattering in the presence of boundaries, doping, spherical inclusions and grains. Eventually, we show an example of thermal anisotropy measurement using the 2ω method, on a sapphire substrate.

Version en langue française

La densité de puissance toujours croissante requise dans les dispositifs microélectroniques actuels est l'un des principaux catalyseurs responsable de la miniaturisation continue des nouveaux équipements électroniques. L'implémentation de matériaux de faible dimension dans les dispositifs à l'état de l'art s'accompagne de grands défis technologiques à relever – la gestion efficace de la chaleur dans les nanostructures en étant un exemple considérable. En effet, une maîtrise rigoureuse de la dissipation de chaleur dans les nanostructures est un élément essentiel permettant d'atteindre une fiabilité à long terme et éviter une défaillance rapide des dispositifs. La conductivité thermique des matériaux de faible dimension, tels que les couches minces, lorsqu'elles sont implémentées dans un dispositif, est l'un des paramètres clés qui dictera à terme l'efficacité et les performances du dispositif.

De la dissipation efficace de la chaleur loin des points chauds pour obtenir des performances accrues dans les ordinateurs, les smartphones ou bien les centres de données, à la localisation de la chaleur dans un volume réduit de taille nanométrique pour contrôler la phase d'un matériau dans des applications telles que les mémoires à changement de phase, une grande variété d'applications repose sur les propriétés thermiques de leurs matériaux constitutifs. Cet éventail d'applications implique donc la nécessité de découvrir, de fabriquer et de caractériser des matériaux couvrant un large éventail de propriétés thermiques.

Par conséquent, le besoin critique, dicté par l'industrie, de posséder une connaissance précise des propriétés thermiques des matériaux de faible dimension a été concomitant avec le développement de techniques de caractérisation thermique de plus en plus sensibles au cours des trois dernières décennies – parallèlement au développement incessant des méthodes de fabrication de salle blanche, et d'appareils de mesure de haute précision. La possibilité d'ajuster les propriétés thermiques d'un matériau présente donc un intérêt technologique conséquent, et nécessite une compréhension fine des mécanismes responsables de la conduction de la chaleur dans les matériaux à l'échelle nanométrique. Du point de vue de la mesure thermique, la réduction de la taille des structures implémentées dans les dispositifs actuels donne naissance à des défis supplémentaires. En effet, imposer une source de chaleur et mesurer les gradients thermiques qui en découlent sur des matériaux de taille réduite est un défi d'un point de vue technologique. En outre, l'interprétation des données expérimentales devient plus complexe lorsque la taille du matériau sondé est commensurable à celle de la source de chaleur, du thermomètre ou aux longueurs caractéristiques des porteurs de chaleur. De plus, pour les systèmes multicouches, la contribution des résistances thermiques d'interface devient souvent du même ordre de grandeur que la résistance thermique de la couche étudiée, ce qui conduit à une certaine ambiguïté quant à l'origine des sources de résistance thermique dans ces systèmes hétérogènes.

La présente thèse est consacrée à l'étude expérimentale du transport de chaleur dans les nanomatériaux, avec un accent important sur la technique de mesure qui a été utilisée – la méthode 3ω. L'analyse détaillée de la technique électro-thermique nous a guidé pour la conception d'expériences sensibles, menées pour déterminer la conductivité thermique de matériaux qui divergent fortement en termes de taille, de structure et de propriétés thermiques.

Le **Chapitre 1** est une introduction générale au transport de chaleur dans les solides, en commençant par le transport de chaleur macroscopique dans les matériaux massifs pour aller graduellement vers le transport phononique à travers les interfaces. Ce chapitre d'introduction

permet de définir plusieurs grandeurs fondamentales que nous utilisons tout au long de la thèse. Nous mettons l'accent sur la description microscopique de la conductivité thermique, et passons en revue plusieurs types de structures qui présentent des réductions en terme de conductivité thermique de part leur structuration à l'échelle nanométrique.

Le **Chapitre 2** présente la méthode 3ω, une méthode très répandue permettant de mesurer la conductivité thermique de matériaux massifs et de couches minces, et sa mise en œuvre dans un environnement de laboratoire, ainsi que certaines des contraintes auxquelles nous avons dû faire face.

Dans le **Chapitre 3**, nous fournissons une dérivation détaillée du modèle thermique qui est utilisé dans les chapitres suivants pour extraire les paramètres thermiques à partir des données expérimentales. Nous passons en revue et expliquons certaines techniques populaires qui sont utilisées pour déduire les propriétés thermiques des substrats, des couches minces et des résistances thermiques d'interface, ainsi que les conditions à satisfaire pour utiliser des modèles thermiques simples ou plus complexes.

Le **Chapitre 4** retrace plusieurs hypothèses qui sont généralement faites dans la littérature, et que nous avons faites dans le Chapitre 3, concernant le modèle thermique qui est utilisé afin de déduire les propriétés thermiques à partir des données expérimentales obtenues lors des mesures 3ω. En particulier, nous quantifions, à l'aide de la modélisation par éléments finis, l'effet de la conduction de la chaleur dans l'élément chauffant, en fonction de sa géométrie et de ses propriétés thermiques. Un modèle analytique en 3D pour des expériences de 3ω est proposé pour les structures multicouches, à partir duquel nous dérivons un critère supplémentaire pour utiliser la méthode dite "de la pente" (plus communément "slope method" dans la litérature) pour déterminer la conductivité thermique d'un substrat avec une erreur minimale.

Le **Chapitre 5** est consacré à la méthode dite 2ω, une technique plus récente introduite par Ramu et Bowers[1] permettant de mesurer les propriétés thermiques anisotropes d'échantillons massifs. Nous utilisons la dérivation du modèle thermique pour la géométrie 3ω et l'adaptons à la géométrie 2ω, et fournissons une solution analytique pour l'oscillation de température mesurée dans une géométrie 2ω, pour les systèmes multicouches. Nous montrons par des moyens analytiques que cette méthode est insensible à la résistance thermique à l'interface chauffage/substrat. Sur la base de la solution multicouche dérivée dans la géométrie 2ω, nous proposons une "frequency-dependent heat spreader method", adaptée des Refs. 2,3, pour mesurer la conductivité thermique des couches minces à l'aide de la méthode 2ω.

Le **Chapitre 6** présente toutes les mesures de conductivité thermique qui ont été effectuées au cours de cette thèse. Les matériaux qui ont été étudiés varient en termes de taille, de structure et de propriétés thermiques. Parmi d'autres matériaux, nous avons utilisé la méthode 3ω pour mesurer la conductivité thermique de couches minces d'oxyde d'aluminium amorphe d'une épaisseur allant de 17 nm à 120 nm, ainsi que les résistances thermiques d'interface des systèmes Pt/Al_2O_3/saphir et Pt/Al_2O_3/germanium. En outre, la conductivité thermique de deux matériaux nanostructurés à base de germanium, une matrice de germanium avec des nano-inclusions de Ge_3Mn_5, et un alliage de GeTe dopé au carbone, a été étudiée car la structure interne et la nanostructuration innovante de ces deux matériaux peuvent être considérées comme des modèles pour l'étude de la diffusion des phonons en présence de bords, de dopage, d'inclusions sphériques et de grains. Enfin, nous présentons un exemple de mesure d'anisotropie thermique par la méthode des 2ω, sur un substrat de saphir.

1 Heat conduction in solids : from bulk materials to interfaces

1.1 Historical introduction


Joseph Fourier (1768-1830)

Among other eighteenth century scientists who worked on the study of the rather broad concept of *heat* such as Joseph Black, Antoine Lavoisier or Pierre Simon Laplace ; Benjamin Franklin was a pioneer when he designed an experiment intended to comparatively measure how efficient different metals were for conducting heat.[4] Ingen-Housz, encouraged by Franklin, coated several wires of different metals with wax, and then proceeded to tighten them between blocks of wood maintained at different temperatures. The difference in melting propagation speed among different metals allowed him to qualitatively compare metals in terms of their relative ability to "conduct" heat. There was, however, no distinction made between the ability of a material to *store* heat to its ability to *conduct* heat.

The first measurement of a material's thermal *conductivity* was made by Joseph Fourier. His success in establishing a rigorous analytical theory of heat propagation in medium in his masterpiece *Théorie analytique de la chaleur*[5] from 1822 allowed him to estimate the thermal conductivity of steel, by performing two experiments on macroscopic samples having different geometries, in steady-state or time-dependent configurations, which astutely alleviated the need of accurately measuring the amount of heat lost by radiation.

It is interesting to note that one of his main motive was the understanding of *diurnal* temperature variations, that is, temperature variations at Earth's surface that occur within a day that result from the relative position of the sun. In particular, he was intrigued by the fact that temperature variations from Earth's surface only propagate within a few meters inside Earth's crust – such a small distance when compared to Earth's radius. However, the temperature variations within Earth's crust induced by *seasonal* temperature variations, propagate to around 60 meters deep. This suggested that for a medium which is periodically heated, the depth at which the resulting temperature oscillation becomes negligible is inversely proportional to the heating frequency – a phenomenon that his theory successfully explained, and that we can turn in our favour to measure the thermal conductivity of small samples, as we will explain in Chapter 2.

Interestingly, Fourier's theory did not rely upon any assumed "nature" of heat, i.e. if it was a "motion" or a "fluid", since there was no consensus about the definition of heat at that time. It was only almost a century later through the emergence of a new kind of science that an acceptable definition and understanding of how heat propagates in solids was proposed. For some reason, scientists at the end of the nineteenth century started to have an obsession with putting particles in boxes and see what would result after performing some calculations. Luckily, it lead to the birth of quantum mechanics, started by Planck, and to Debye's quantum description of lattice vibrations.


Peter Debye (1884-1966)

In 1912, Debye's theory[6] of specific heat in dielectric crystals – successful at low temperature, as opposed to Einstein's model – assumed the crystal energy to be distributed among *collective* mode of vibrations of the atoms, which were later called phonons. They are quasi-particles that extend throughout the entire crystal and carry a finite amount of energy, which are responsible for propagating heat. The quantum description of a crystal, which represents a milestone in solid state physics, paved the way to several physicists, starting with Peierls[7], to gain a deeper understanding of the mechanisms responsible for the temperature dependence of thermal conductivity in both crystals and amorphous materials. The wave-particle picture of phonons, obeying well-defined statistical rules, allowed for the elaboration of a robust framework for describing the various scattering processes existing between phonons and their environment, as will be described in more detail in this chapter.

Importantly, several length-scales emerged from the understanding that heat-carriers could be seen as wave and/or particles. The phonon mean free path and dominant phonon wavelength appeared to be important parameters to play with[8] if one is interested in *tuning* the thermal properties of a material, at appropriate temperature and phonon frequency ranges.

These quantities serve as guidelines for defining the dominant phonon scattering processes that occur within a crystal and, importantly, can be used to better define the heat transport regime in which an experiment is conducted, based on the sample's dimensions. For example, in the context of phonon heat transport, one can say that a material has low dimensions when the phonon mean free path or phonon dominant wavelength is comparable to the size of the material. In this case, the heat transport regime is referred to as ballistic, as opposed to diffusive. Such an improved understanding of heat conduction at the very fundamental level is of course satisfying from a theoretical standpoint, but appears to be extremely valuable for the efficient design of applications that strongly rely on their thermal performances. For example, in such applications as thermoelectricity or phase-change memory devices, better performances are obtained for *thermally insulating materials*. Reducing the size of a material, or engineering it by intentionally adding further phonon scattering centers, are the directions that have proven effective in degrading a material's ability to conduct heat, and is still the approach that is widely used up to this day.[9,10]


Rudolf Peierls (1907-1995)

On the other hand, the incorporation of efficient *heat spreaders* in novel electronic devices is of consequent technological importance for systems producing large heating power that needs to be evacuated efficiently, such as for high-power electronics and optoelectronics applications. The accurate description of phonon scattering processes appears to be critical in the comprehension of ultra-high thermal conductivity materials, such as diamond, graphene, graphite, boron nitride or boron arsenide to name a few.

For these reasons, the nanoscale heat transfer community has grown rapidly for the last couple of decades, leading to an abundant quantity of novel research publications, along with several celebrated textbooks and other PhD dissertations, covering a breadth of nanoscale-heat-transfer-related topics – from which this introductory chapter is based upon. In particular, we used Refs. 11–15 as primary sources, which the reader is referred to for more details.

In this first chapter, we shall only discuss particular topics that are, from near or from afar, related to the measurement and to the understanding of the thermal conductivity of materials that were studied in this work. We will first present a macroscopic picture of heat transfer in solids, which primarily serves as an introduction to fundamental quantities such as heat flux, temperature gradient and thermal conductivity. Besides, it provides the basis upon which our measurement methodology relies on. Then, we will provide a microscopic description of thermal conductivity, with an emphasis on the scattering processes that dictate the temperature dependence of thermal conductivity. We will then move on to define thermal boundary resistances, which are relevant from both experimental and fundamental perspectives.

1.2 The macroscopic picture : Fourier's law and the heat diffusion equation

1.2.1 Fourier's law

Heat is thermal energy in transit due to a spatial temperature difference.[14] There are three basic heat transfer processes that can occur whenever a temperature gradient exists within a medium or between media. The first mode is referred to as *conduction* when heat transfer occurs across a solid or fluid subjected to a temperature difference. Secondly, if the temperature of a surface is different from that of a surrounding moving fluid, heat transfer will occur by a process referred to as *convection*. Lastly, whenever there exists a temperature difference between two surfaces, heat transfer can also occur without any media between the surfaces (i.e. in vacuum), through *radiation*. In this case, energy is emitted by the surface in the form of electromagnetic waves.

We shall only focus on heat transfer by *conduction* in this section, as we are solely interested in thermal properties of solids, without moving fluid and where thermal radiation is unimportant.

It is important to underline that Fourier's law is empirical. Himself and earlier scientists observed that the heat flux resulting from thermal conduction is proportional to the magnitude of the temperature gradient, through an intrinsic property of the material, its thermal conductivity k. Because temperature tends to go from hot to cold regions, a minus sign is added to relate the heat flux ϕ to the temperature gradient $\vec{\nabla}T$:

$$\vec{\phi} = -k\vec{\nabla}T \tag{1.1}$$

The heat flux ϕ has units of $\mathrm{W/m^2}$, the thermal conductivity k has units of W/(m.K) and the gradient operator is defined as usual, such that

$$\vec{\nabla}T(x,y,z) \equiv \frac{\partial T}{\partial x}\vec{n_x} + \frac{\partial T}{\partial y}\vec{n_y} + \frac{\partial T}{\partial z}\vec{n_z}$$

where $\{\vec{n_x}, \vec{n_y}, \vec{n_z}\}$ are the unit vectors in Cartesian coordinates. Eq.(1.1) relates the heat flux across a surface to the temperature gradient perpendicular to that surface. It seems rather difficult from this equation alone to infer the temperature distribution within a medium, since both the temperature and heat fluxes are unknown. The law of conservation of energy is used, which provides the second ingredient along with Fourier's law, allowing for the derivation of what is known as the heat diffusion equation.

1.2.2 The heat diffusion equation

We consider a medium whose temperature distribution $T(x,y,z)$ is unknown, and that we wish to express.[14] As we are seeking for a differential equation, we first define an infinitely small differential volume $dxdydz$, as shown in Figure 1.1. The conduction heat rate (in W) across each surface at the x, y and z coordinates of the infinitely small volume, are expressed as q_x, q_y and q_z. At opposite surfaces, first order Taylor expansion leads to the expression of the conduction heat rates at distances $x+dx$, $y+dy$ and $z+dz$:

$$q_{x+dx} = q_x + \frac{\partial q_x}{\partial x}dx \qquad q_{y+dy} = q_y + \frac{\partial q_y}{\partial y}dy \qquad q_{z+dz} = q_z + \frac{\partial q_z}{\partial z}dz \tag{1.2}$$

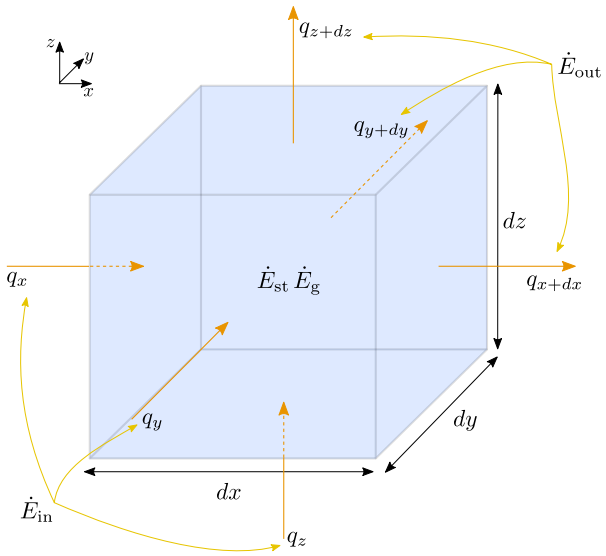

Figure 1.1: Infinitesimal volume $dxdydz$, into which thermal energy enters and leaves by conduction, is stored, and generated. Conservation of energy requires that $\dot{E}_{\text{in}} + \dot{E}_{\text{g}} - \dot{E}_{\text{out}} = \dot{E}_{\text{st}}$. Adapted from Ref. 14.

Importantly, the medium can store energy and there may be as well energy produced or consumed by the medium. As we are dealing with heat rates expressed in Watt we shall also express the *rate* of energy that is stored, produced or consumed using the same units. The rate of energy generated within the volume $dxdydz$ can be therefore written as

$$\dot{E}_{\text{g}} = q_V dxdydz \tag{1.3}$$

where the upper dot refers to a time derivative, and q_V, which has units of W/m^3, represents a volumetric power source. For example, it can be the volumetric power that is produced by Joule heating within a metal. The rate of energy that is stored within the medium, neglecting latent energy effects, is given by

$$\dot{E}_{\text{st}} = \frac{\partial U}{\partial t} dxdydz = \frac{\partial U}{\partial T}\frac{\partial T}{\partial t} dxdydz = \rho C_p \frac{\partial T}{\partial t} dxdydz \tag{1.4}$$

where we use the definition of the specific heat C_p with units of J/(g.K), that is, the amount of energy needed to increase the temperature of a material by one degree. For homogeneity, it is multiplied by the material's density ρ, which has units of g/m^3. Eventually, the conservation of energy requires that the energy rates entering, leaving, that is produced, and stored to be balanced. This is written as

$$\dot{E}_{\text{in}} + \dot{E}_{\text{g}} - \dot{E}_{\text{out}} = \dot{E}_{\text{st}} \tag{1.5}$$

The energy entering and leaving the volume, $\dot{E}_{\text{in}}$ and $\dot{E}_{\text{out}}$, respectively, does so by conduction across the surfaces, for which we have expressed the conduction heat rates entering the medium as q_x, q_y and q_z and that leaving the medium as q_{x+dx}, q_{y+dy} and q_{z+dz}, as shown in Figure 1.1. Therefore, using the above expression for the energy rates, Eq.(1.5) can be written as

$$q_x + q_y + q_z + q_V dxdydz - q_{x+dx} - q_{y+dy} - q_{z+dz} = \rho C_p \frac{\partial T}{\partial t} dxdydz \tag{1.6}$$

and upon substituting the conduction rates using Eq.(1.2), leads to

$$-\frac{\partial q_x}{\partial x}dx - \frac{\partial q_y}{\partial y}dy - \frac{\partial q_z}{\partial z}dz + q_V dxdydz = \rho C_p \frac{\partial T}{\partial t} dxdydz \tag{1.7}$$

The heat fluxes (in $\mathrm{W/m^2}$) across differential surfaces are obtained using Fourier's law (Eq.(1.1)) :

$$\frac{q_x}{dydz} = -k_x \frac{\partial T}{\partial x} \qquad \frac{q_y}{dxdz} = -k_y \frac{\partial T}{\partial y} \qquad \frac{q_z}{dxdy} = -k_z \frac{\partial T}{\partial z} \tag{1.8}$$

Plugging Eq.(1.8) into Eq.(1.7) leads to the general form of the heat diffusion equation in Cartesian coordinates, it reduces to

$$\frac{\partial}{\partial x}\left(k_x \frac{\partial T}{\partial x}\right) + \frac{\partial}{\partial y}\left(k_y \frac{\partial T}{\partial y}\right) + \frac{\partial}{\partial z}\left(k_z \frac{\partial T}{\partial z}\right) + q_V = \rho C_p \frac{\partial T}{\partial t}$$

and if the thermal conductivity is constant along each coordinate

$$k_x \frac{\partial^2 T}{\partial x^2} + k_y \frac{\partial^2 T}{\partial y^2} + k_z \frac{\partial^2 T}{\partial z^2} + q_V = \rho C_p \frac{\partial T}{\partial t} \tag{1.9}$$

In this thesis, temperature measurements will be compared to the solution of the heat equation as it is expressed above in order to infer the thermal conductivity of several structures. The derivation presented above can be found in many heat-transfer textbooks, such as Ref. 14 and is displayed here for better understanding how the heat diffusion equation is derived. The energy balance along with the phenomenological Fourier's law are the two main ingredients.

We put emphasis on this particular aspect since recent frequency-dependent thermal conductivity measurements failed to be correctly explained using Fourier's law and the classical heat equation, for heat sources whose sizes become commensurate to the heat-carrier mean free paths.[16–18] Besides, the thermal conductivity of films measured using time-dependent thermoreflectance (TDTR) have been shown to be dependent on the frequency driving the experiment, for alloys.[19,20] These results have led to several theoretical works intended to provide new tools that allow to model and explain experimental data obtained in the aforementioned conditions. These tools take the form of modified heat transport equations, to go beyond the heat diffusion equation that assumes the temperature gradient to « nondiffusive »[21], « Enhanced Fourier Law »[22] or « hydrodynamic »[23,24] transport models are some examples of so-called « non-Fourier » heat conduction models. Most of these models rely on the fundamental equation describing transport phenomenon, which is the Boltzmann transport equation. The Boltzmann equation requires knowledge of the statistical distribution of the particles making up the system we wish to study. The knowledge of this statistical distribution implies a rigorous mathematical and physical definition of the nature of heat carriers, which has not been rigorously discussed thus far. We will do so in a moment, but before that, a *classical* description of atomic displacement within a crystal has the merits of providing insightful and physically intuitive results.

1.3 Thermal conductivity : the microscopic picture

In solids, heat is carried by electrons and lattice vibrations. In metals, it is primarily carried by electrons whereas in insulators and semi-conductors (depending on the doping level), lattice vibrations are the main carriers. In this section we shall only discuss heat transport by lattice vibrations, as most of the work conducted in this thesis is based on semi-conductors and insulators.

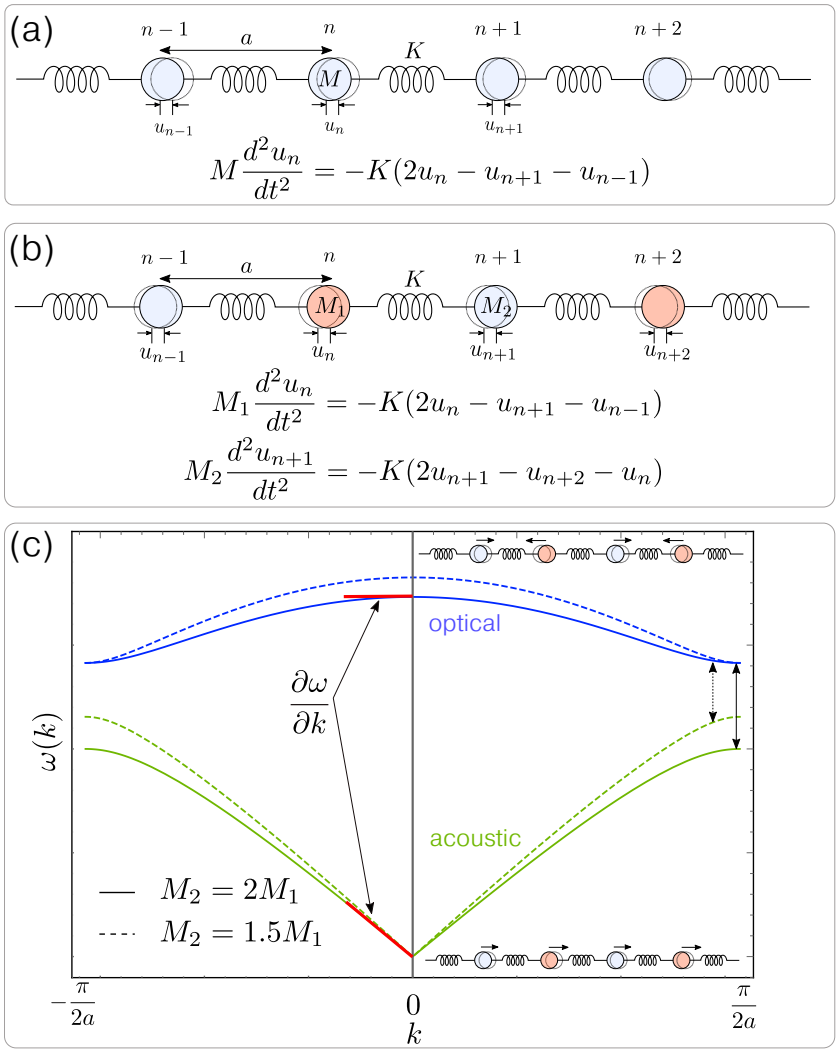

Figure 1.2: (a) 1D diatomic chain with neighbouring atoms having similar masses, and the equation of motion relating atomic displacement and bonding strength, for interaction between first neighbours where the "spring" is assumed massless. (b) Same but for neighbouring atoms with dissimilar masses. (c) The solution of the equation of motion leads to the dispersion relation $\omega = f(k)$, plotted here for a diatomic chain with atoms of different masses, for two M_1/M_2 ratios. In inset is a schematic representation of the atomic displacement for both acoustic and optical phonons, in the limit $k \ll \pi/2a$. The simple mass-spring model gives useful insights into the mechanisms responsible for heat conduction in solids. There is no need to plot the frequency dependence for larger k-values, because it would represent oscillations whose wavelengths are smaller than the interatomic spacing, which is not reasonable physically. Therefore, all the informations are contained within the so-called first Brillouin zone (for each crystallographic direction)

1.3.1 The simple mass-spring model

In crystalline solids, atoms are arranged periodically and hold together through chemical bonds. The periodicity of crystalline solids make the study of heat (and electronic) transport very convenient, since it is only needed to study a small portion of the crystal, the unit cell, that repeats itself throughout the entire lattice, to infer macroscopic transport properties. The periodic arrangement of atoms that are bonded together is often pictured as a spring-mass system[11], such as in Figure 1.2(a), where atoms have the same mass M and are connected by springs of strength K.

Using classical mechanics (Newton's second law), the general solution for the atom dis-

placement u_n is of the form of a travelling wave : $u_n \propto e^{i(kx_n - \omega t)}$ where k is the wavevector of the travelling wave, x_n is the equilibrium position of atom n such that $x_n = na$ in Figure 1.2(a), ω refers to the circular frequency of vibration and t is time. Upon applying proper periodic (Born-Von Karman) boundary conditions, such that the displacement at the end of the atomic chain matches that at the beginning, the oscillation frequency of such a system is given by

$$\omega(k) = \sqrt{\frac{4K}{M}\left|\sin\left(\frac{1}{2}ka\right)\right|} \tag{1.10}$$

The solid green line in Figure 1.2(c) represents the oscillation frequency of the travelling wave as a function of wavevector – the dispersion relation. This simple model (Figure 1.2(a)) captures relatively well the dispersion relation that is measured experimentally, using for instance X-ray, neutron, Brillouin, or Raman scattering. However, it fails to reproduce the upper branch, represented in blue in Figure 1.2(c), that is measured experimentally.

In a slightly improved model where two neighbouring atoms within a unit cell have different masses M_1 and M_2, as shown in Figure 1.2(b), the solution of the equation of motion holds for frequencies such that

$$\omega_{\pm}^2(k) = K\left(\frac{1}{M_1} + \frac{1}{M_2}\right) \pm K\sqrt{\left(\frac{1}{M_1} + \frac{1}{M_2}\right)^2 - \frac{4\sin^2(ka)}{M_1 M_2}} \tag{1.11}$$

The dispersion relation of this improved model possesses two solutions (blue and green in 1.2(c)), in better agreement with experiments.

The dispersion relation is determined using a relatively simple mass-spring system, but is filled with useful informations concerning heat propagation in crystalline solids. In Figure 1.2(c), we make the distinction between the acoustic branch, representing a mode of vibration where two ions within the cell move in phase with one another, and the optical branch, describing a motion in which neighbouring ions are out-of-phase. The name « acoustic » stems from the fact that for small wavevectors, i.e. long wavelength modes, the dispersion relation is of the form $\omega = v_s k$, which is a characteristic dispersion relation for sound (elastic) waves. The label « optical » for the other branch at higher frequency is explained by the fact that the motion of two neighbouring ions can create an oscillating dipole which can interact with electromagnetic radiations in this frequency range. For the general case in three dimensions, if there are p atoms in a unit cell, for each k value there will be $3p$ normal modes. Three of the $3p$ branches are acoustic. One branch representing a travelling wave whose oscillations are parallel to the direction of propagation, referred to as *longitudinal* while the other two represent a travelling wave whose oscillations are perpendicular to the direction of propagation, referred to as *transverse*. The other $3(p-1)$ branches are optical branches.[11] An important quantity that is derived from the dispersion relation is the group velocity of the propagating wave, which we can guess will be strongly related to the efficiency of a crystal to conduct heat. From the form of the solution for the atomic displacement ($u_n \propto e^{i(kx_n - \omega t)}$), the group velocity is obtained as $\partial\omega/\partial k$. Upon calculating this quantity, as displayed in Figure 1.2(c), it becomes evident that the group velocity in the optical branch is negligible, and thus does not contribute significantly to the thermal conductivity. On the other hand, lattice vibrations of the acoustic branch have large group velocity at small k values (long wavelengths), and are therefore the main contributors to heat conduction. In the continuum limit of long wavelengths, the phonon

group velocity is that of the speed of sound v_s, and is readily obtained :

$$\omega_{\text{acoustic},k\to 0} = \left(a\sqrt{\frac{K}{M}}\right)|k| \Leftrightarrow v_s = \frac{\partial\omega}{\partial k} = \left(a\sqrt{\frac{K}{M}}\right)$$

Therefore, large atomic mass and weak chemical bonds lead to small speed of sounds, and therefore lower thermal conductivity. Besides, Eq.(1.11) suggests that the frequency gap between the acoustic and optical branches increases for large difference in atomic masses, as is displayed in Figure 1.2(c). Such a frequency gap would prevent certain lattice vibrations whose frequencies are within this gap to propagate within the crystal. Using this so-called phononic bandgap for manipulating both heat and sound propagation in solids has attracted a regain of interest within the last decade.[25]

However insightful it might be, the spring-mass system has its limitations. For example, it fails to correctly predict the temperature dependence of heat capacity at low temperature, even for increased complexity of the model, such as taking more than the first neighbour in the calculation of the ions' displacement, or solving the problem for a three-dimensional lattice. We must turn to a quantum theory of lattice dynamics to properly explain the observed phenomena that are governed by the lattice vibrations. The fundamental difference with the classical theory is that it requires the energy of the normal modes (the vibrational modes) to take discrete values. In other words, the normal modes are quantized. The quantization of the lattice vibrational energy is called a phonon. A phonon can only have a discrete set of values such that the energy of a particular mode is

$$E_{\vec{k}s} = \left(n + \frac{1}{2}\right)\hbar\omega_s(\vec{k}) \tag{1.12}$$

where n is the excitation number of the normal mode and takes integer values ($n = 0, 1, 2, \dots$), $\hbar$ is the reduced Planck constant and $\omega_s(\vec{k})$ is the frequency of a mode of wavevector $\vec{k}$ with polarization s. The total energy is simply the sum over each individual mode : $E_{\text{total}} = \sum_{\vec{k}s}(n+\frac{1}{2})\hbar\omega_s(\vec{k})$. Importantly, the expected number of phonons of wavevector k and polarization s which are present in thermal equilibrium at temperature T follows Bose-Einstein statistics, such that

$$n_{\vec{k}s} = \frac{1}{\left(e^{\hbar\omega_s(\vec{k})/k_BT} - 1\right)} \tag{1.13}$$

where k_B is the Boltzmann constant.

1.3.2 The Boltzmann equation

Up to this point, lattice vibrations have been conceptually introduced using the spring-mass model, and refined by introducing the quantum nature of these vibrations. Each phonon with wavevector $\vec{k}$ describes the motion of atoms *throughout the entire crystal*. With this picture in mind, it seems difficult for instance to see how a defect, a dislocation, or a nanoinclusion at a specific position within the crystal will affect the lattice vibration. A particle description of the lattice vibration would prove useful in this case. Such a picture is drawn by not only considering one phonon which extends throughout the entire crystal, but rather by taking a superposition of several phonons, whose wavevectors are in the vicinity of $\vec{k}$, which then describes a *wave packet* that has the property of being *localized* on a much smaller scale than the entire crystal.[11] For this reason, one can see phonons as particles with little spatial extent,

which can be useful in the representation of heat transport, and makes the introduction of characteristic lengths such as the phonon mean free path, somewhat easier.

We now have all the ingredients to establish an expression for the thermal conductivity, based on a microscopic description of a crystal, where phonons are treated as quasi-particles. A convenient way of doing so is by using the Boltzmann transport equation, which describes a thermodynamic system that is not in a state of equilibrium. For a statistical distribution function $n = f(\vec{r}, \vec{k}, t)$, describing a large ensemble of particles varying with position $\vec{r}$, wavevector $\vec{k}$ and time t, the Boltzmann equation is written as

$$\left.\frac{\partial n}{\partial t}\right|_{\text{col}} = \frac{\partial n}{\partial \vec{r}} \cdot \vec{v} + \frac{\partial n}{\partial \vec{k}} \cdot \frac{\vec{F}}{\hbar} + \frac{\partial n}{\partial t} \tag{1.14}$$

The right hand side of Eq.(1.14) describes phonon displacement and external forces applied to them, while the left hand side is a so-called collision term that restores equilibrium.[13] We may notice that the right hand side is simply the total derivative of the distribution function :

$$\begin{aligned}\frac{dn}{dt} &= \frac{\partial n}{\partial \vec{r}} \cdot \frac{d\vec{r}}{dt} + \frac{\partial n}{\partial \vec{k}} \cdot \frac{d\vec{k}}{dt} + \frac{\partial n}{\partial t} \\ &= \frac{\partial n}{\partial \vec{r}} \cdot \vec{v} + \frac{\partial n}{\partial \vec{k}} \cdot \frac{\vec{F}}{\hbar} + \frac{\partial n}{\partial t}\end{aligned}$$

where we used $\vec{F} = \partial \vec{p}/\partial t = \hbar \partial \vec{k}/\partial t$, $\vec{p} = \hbar \vec{k}$ being the particle momentum. In such case that no external force is applied to the system, it reduces to

$$\left.\frac{\partial n}{\partial t}\right|_{\text{col}} = \frac{\partial n}{\partial \vec{r}} \cdot \vec{v} + \frac{\partial n}{\partial t} \tag{1.15}$$

The collision term is alas very difficult to describe and often, the relaxation time approximation is used. The relaxation time approximation (RTA) consists in writing the collision term as

$$\left.\frac{\partial n}{\partial t}\right|_{\text{col}} = -\frac{n - n_0}{\tau(\vec{k})} \tag{1.16}$$

where n_0 is the equilibrium distribution of the system following Bose-Einstein statistics, as introduced previously :

$$n_0(\omega, T) = \frac{1}{(e^{\hbar\omega/k_B T} - 1)} \tag{1.17}$$

and τ is the relaxation time. The relaxation time is the time taken by the system driven out of equilibrium to relax back to equilibrium. It does so because of scattering. Once the distribution function is known, the heat flux is obtained as follow :

$$\vec{\phi} = \frac{1}{V} \sum_{\vec{k},s} n(\vec{k}, s) \hbar\omega(\vec{k}, s) \vec{v}(\vec{k}, s) \tag{1.18}$$

In order to use Fourier's law to obtain an expression for the thermal conductivity, we use its fundamental assumption, which is local thermodynamic equilibrium. We can then write $\partial n/\partial \vec{r} = \partial n_0/\partial \vec{r}$, which, under the RTA in addition to the condition that there is no external force applied to the system, leads to the following relation for the distribution function :

$$n = n_0 - \tau \frac{\partial n_0}{\partial \vec{r}} \cdot \vec{v} = n_0 - \tau \frac{\partial n_0}{\partial T} \frac{\partial T}{\partial \vec{r}} \cdot \vec{v} \tag{1.19}$$

Describing heat transport in one dimension for simplicity (the temperature gradient is parallel to the x direction), substituting Eq.(1.19) into Eq.(1.18) leads to the expression[1] for the heat flux :

$$\vec{\phi} = -\frac{1}{V}\sum_{\vec{k},s} v_x(\vec{k},s)\tau(\vec{k},s)\frac{\partial n_0}{\partial T}\frac{\partial T}{\partial x}\hbar\omega(\vec{k},s)\vec{v}(\vec{k},s) \tag{1.20}$$

We compare this equation to Fourier's law :

$$\phi_x = -k\frac{dT}{dx} \tag{1.21}$$

$$= -\frac{1}{V}\sum_{\vec{k},s} v_x^2(\vec{k},s)\tau(\vec{k},s)\frac{\partial n_0}{\partial T}\hbar\omega(\vec{k},s)\frac{\partial T}{\partial x} \tag{1.22}$$

Assuming an isotropic solid, the frequency $\omega(\vec{k})$ and relaxation time $\tau(\vec{k})$ are functions of k only such that we can write $\omega(\vec{k}) = \omega(k)$ and $\tau(\vec{k}) = \tau(k)$. Similarly, for an isotropic solid, the value of v_x^2 averaged over all directions is $v^2/3$. It leads to the following expression for the thermal conductivity :

$$k = \frac{1}{3}\frac{1}{V}\sum_{k,s} v^2(k,s)\tau(k,s)\frac{\partial n_0}{\partial T}\hbar\omega(k,s) \tag{1.23}$$

Upon substituting the discrete summation over k by an integral, we rewrite the above expression as[26] :

$$k = \frac{1}{3}\frac{1}{V}\sum_{s}\int_0^{k_{\max}} v^2(k,s)\tau(k,s)C_{\rm ph}(k,s)D(k,s)dk \tag{1.24}$$

where $D(k,s)$ is the density of phonons in branch s, and $C_{\rm ph}(k,s) = \frac{\partial n_0}{\partial T}\hbar\omega(k,s)$ is the specific heat per normal mode for frequency ω. It is written more explicitly by computing the temperature derivative :

$$C_{\rm ph}(k,s) = \frac{\partial n_0}{\partial T}\hbar\omega(k,s) = k_B x^2 e^x (e^x-1)^{-2} \qquad \text{where} \qquad x = \hbar\omega/k_B T \tag{1.25}$$

In the Debye model, $\omega = vk$ and

$$D(k,s)dk = \frac{4\pi k^2 dk}{(2\pi/L)^3} = \frac{4\pi k^2}{(2\pi/L)^3}\frac{d\omega}{(d\omega/dk)} = \frac{V}{2\pi^2}\frac{\omega^2}{v^3}d\omega \tag{1.26}$$

leading to

$$k = \frac{1}{6\pi^2}\sum_{s}\int_0^{\omega_{\max,s}} \frac{\tau(\omega,s)}{v(\omega,s)}C_{\rm ph}(\omega,s)\omega^2 d\omega \tag{1.27}$$

The highest phonon frequency $\omega_{\max,s}$ is the maximum frequency for the phonon branch s. It is found under the assumption that a phonon cannot have a wavelength smaller than the interatomic spacing and thus there is a minimum wavelength allowed for a phonon, or inversely, a maximum frequency. Following Debye model, it is given by $\omega_{\max} = \omega_{\rm D} = (6\pi^2 v_s^3\rho)^{1/3}$, where v_s is the speed of sound and ρ is the atomic density. Above this frequency, all phonons begin to be excited. Equivalently, above the Debye temperature defined as $\theta_{\rm D} = \hbar\omega_{\rm D}/k_B$, all the phonons are excited.

We notice from Eq.(1.24) that if both τ and v are assumed to be wave-vector-independent, we obtain a relation for the thermal conductivity of the form

$$k \propto \frac{1}{3}C_p v^2\tau = \frac{1}{3}C_p v\Lambda \tag{1.28}$$

[1]The n_0 term in Eq. (1.19) drops out because there is no heat current if the phonon distribution function is not perturbed, i.e. isotropic.

which is the kinetic formula, where $\Lambda = v\tau$ is the phonon mean free path, i.e. the average distance travelled by a phonon between two collisions. We will shortly see that the relaxation time is far from being k-independent, or frequency-independent, but the simple form of the kinetic formula provides some insights on the quantities that define the thermal conductivity of a material, and importantly the quantities that we can play with in order to tune it.

In order to tune the thermal conductivity of a material, one can try to tune the material's heat capacity, phonon group velocity and relaxation time (or equivalently the phonon mean free path). The heat capacity is mostly material-dependent and can be modified only by drastically reducing the sample size (2D materials and nanowires) such that the phonon density of states is modified. The maximum value for the phonon group velocity is given by the speed of sound, and is related to the mass and bonding strength of the atoms constituting the material, as explained before. Similarly, it can be reduced by strongly reducing the size of the system (for example, a quantum dot[27] or a nanowire[28]). Therefore, it is rather difficult to reduce a material's thermal conductivity using these two quantities because tuning the phonon group velocity or heat capacity of a material requires to reduce its dimensions to the smallest scale.

The phonon mean free path, however, will strongly depend upon the scattering processes that the heat carriers are subjected to. While reducing the dimensions of a material can indeed reduce the phonon mean free path, there are other ways to reduce the ability of a material to conduct heat. Reducing the thermal conductivity by adding new scattering centers within a material have been the main direction toward which research has focused on within the last two decades. There are many types of scattering processes experienced by phonons, which we describe now.

1.3.3 Scattering processes

General scattering processes in bulk materials

Phonon scattering is the reason for the finite thermal conductivity of solids.[7] There are many scattering processes that take place in a crystal, which we can first try to list solely based on our knowledge of what a crystal is made of. In the general case, there are electrons, other phonons, impurities, dislocations, boundaries and isotopes. There can also be, depending on the material, scattering between phonons and magnons[29], grain boundaries[30,31], interfaces (for superlattices[32]) and other quasiparticles.[33] Therefore it seems that there is a large variety of scattering processes which, we assume, can lead to a degradation of the lattice thermal conductivity. Theses processes are schematically presented in Figure 1.3.

The implicit assumption behind this reasoning is that scattering between two phonons effectively poses thermal resistance to thermal energy flow. This is the case for scattering processes that are called Umklapp (U) processes, for which the energy is conserved, but the crystal momentum is conserved only if a reciprocal lattice vector is added[7], as explained in Figure 1.4(c).[2] U processes redistribute phonon frequencies and, most importantly, change the direction of propagations of phonons and thus create thermal resistance. The other type of processes are called Normal (N) processes, which conserve both energy and crystal momentum (see Figure 1.4(b)). Although they do not contribute *directly* to the thermal resistance, they

[2]The reason for adding a reciprocal lattice vector relies on the same argument that we used before to define a maximum phonon frequency : the phonon wavelength cannot be smaller that the interatomic distance, and therefore any wavevector that goes beyond the first Brillouin zone should be replaced by an equivalent wavevector which fits within the first Brillouin zone.

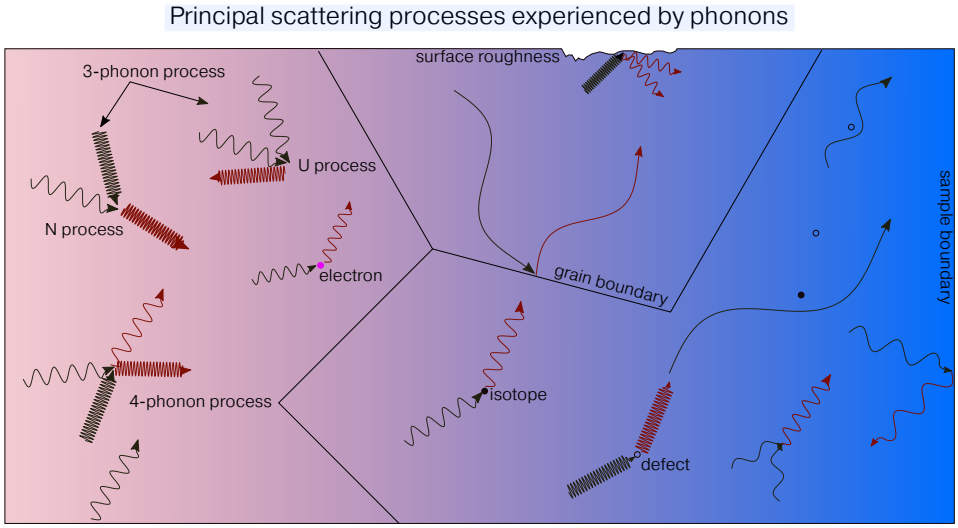

Figure 1.3: Schematic representation of the general scattering processes experienced by phonons. The relaxation time for each process is closely related to the phonon frequency and temperature, as explained in the text.

are essential in spreading out the influence of other processes – that are resistive – to the entire phonon spectrum.[34]

General trend

Before detailing how each scattering process scales with frequency and temperature, we discuss the general trend of the temperature dependence of the thermal conductivity of germanium, as presented in Figure 1.4(a), which is taken from Ref. 34. We observe three regimes for the temperature dependence of thermal conductivity. From sub-Kelvin temperatures up to ≈ 20 K, the thermal conductivity increases until it reaches a plateau, and then decreases indefinitely. When speaking of high and low temperatures as we will do in the following, the implicit reference temperature is the Debye temperature θ_{D}, above which all phonons are excited, and below which some are frozen out, as mentioned previously.[11]

For the high-temperature limit, we can assume that the more phonons there are, the more probable is a collision between phonons and consequently the smaller the thermal conductivity is, assuming U processes. At high temperature, i.e. $T \gg \theta_{\mathrm{D}}$, the total number of phonons is approximated as $n_s(\vec{k}) = 1/(\exp(\theta_{\mathrm{D}}/T) - 1) \approx T/\theta_{\mathrm{D}} = k_B T/\hbar\omega_s(\vec{k})$ and thus the relaxation time is expected to decrease linearly with temperature since the phonon population increases linearly with temperature. This reasoning holds because at high temperature, the heat capacity is temperature-independent following Dulong and Petit law. This is what is generally observed experimentally. The thermal conductivity is inversely proportional to temperature, $k \propto T^{-a}$, where a usually lies between 1 and 2, as shown in Figure 1.4(a).

As temperature decreases, the thermal conductivity does not go to infinity but reaches a peak before decreasing. The peak in the thermal conductivity of germanium, at about 20 K in Figure 1.4(a), is strongly dependent on the isotopic concentration of the material. The isotopic concentration does not seem to greatly affect the temperature at which the peak appears, but it does reduce the thermal conductivity amplitude at the peak position. In this temperature region, phonon scattering by isotopes, defects and dislocations reduce the phonon mean free path and are thus responsible for decreasing the thermal conductivity. As the size

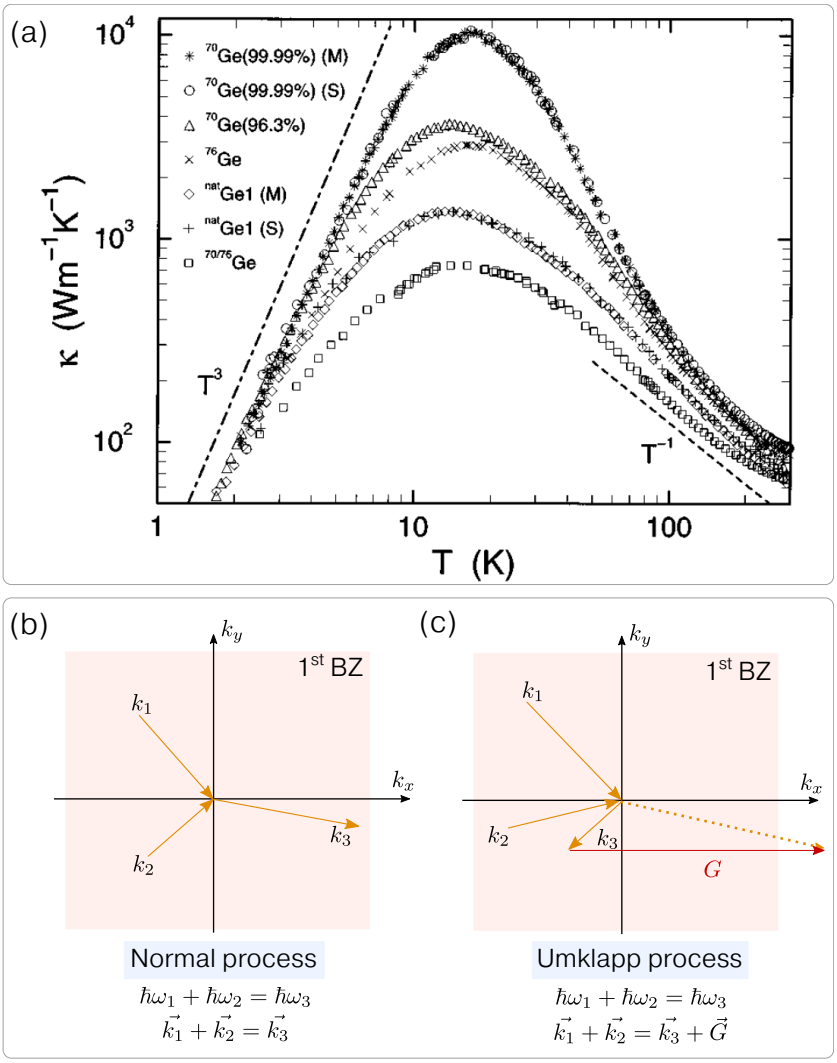

Figure 1.4: (a) Thermal conductivity of germanium, taken from Ref. 34, for different isotopic concentrations. Percentages in parentheses represent sample purity, M and S refer to samples measured using different setups. (b) Normal (N) and (c) Umklapp (U) processes. The pale red area represents the first Brillouin zone for a two-dimensional square lattice. Both processes conserve energy, however U processes do not conserve crystal momentum without the addition of a reciprocal lattice vector G. Such processes are called "three-phonon" processes because of the number of phonon involved in the scattering event.

of such scatterers are of the order of the atomic scale, we can assume from Rayleigh's theory that theses processes will be strongly frequency-dependent when the phonons' wavelengths are greater than the interatomic distance.

At temperatures below the peak position, anharmonic processes are no longer the main source of thermal resistance and thus do not define the phonon mean free path anymore. The phonon mean free path is set by temperature-independent parameters, such as the spatial distribution of imperfections or the sample's size.

To understand this last statement, it might be useful to think of a crystal as a black-body which has a spectral distribution of phonons, obeying Bose-Einstein statistics. Wien's displacement law states that at any temperature, the maximum phonon wavelength increases as temperature decreases such that $\lambda_{\max} T$ = constant. Therefore, one can define at each temperature a so-called *dominant* phonon wavelength, readily obtained by calculating the wavelength for which the phonon spectral density is maximum[35] – exactly as in Wien's law for photons. The dominant phonon wavelength is then expressed as

$$\lambda_{\text{dom}} = \frac{hv}{2.82 k_B T}$$

where v refers to the phonon group velocity. Therefore, at low temperature, most phonons have long wavelengths and thus start being immune to small defects, impurities, isotopes and the like. Consequently, the important length scale that will eventually sets an upper limit to the phonon mean free path at low temperature is the geometry of the sample, which is fixed.[36] The T^3 dependence of the thermal conductivity that is observed as temperature decreases below the peak in Figure 1.4(a) stems from the T^3 temperature dependence of the specific heat for 3D systems, as derived in the Debye model. For systems of lower dimensions, the temperature dependence changes, with $C_p \propto T$ for 1D systems and $C_p \propto T^2$ for 2D systems.

Relaxation times

The relaxation times due to the aforementioned scattering processes have been calculated by several 20$^{\text{th}}$ century physicists, pioneers in the field of heat conduction in solids. Chronologically, Casimir[36] in 1938, following Peierls's work[7] of 1929, derived an expression for the relaxation time due to boundary scattering, τ_b. Klemens[37] provided an expression for the relaxation time due to U processes, τ_u, in 1951, which was suggested by Peierls[7]. Herring[38] calculated the relaxation time for N processes, τ_n in 1954. In 1955, Klemens derived an expression of the relaxation time due to phonon scattering by static imperfections, which in his seminal work[39] separated into three components : points imperfections τ_i, defects τ_d and grain boundaries τ_{gb} (which are considered as an array of dislocations lying in the plane of the boundary). Four-phonons (4p) processes, which were first considered by Pomeranchuk[40], were studied as well by Ecsedy and Klemens.[41] The temperature and frequency dependence of the relaxation times for these scattering events are listed below :

$$\begin{aligned}
\tau_{u,\text{low T}}^{-1} &= B_u e^{-\theta_D/bT} T^3 \omega^2 & \tau_d^{-1} &= B_d \omega \\
\tau_{u,\text{high T}}^{-1} &= B'_u \omega^2 T & \tau_{gb}^{-1} &= B_{gb}/L_g \\
\tau_n^{-1} &= B_n \omega^2 T^3 & \tau_b^{-1} &= vj/L_s \\
\tau_i^{-1} &= B_i \omega^4 & \tau_{4p}^{-1} &= B_{4p} \omega^2 T^2
\end{aligned}$$

B_j are constants related to the material's intrinsic properties, but often need to be adjusted by fitting the temperature dependence of the thermal conductivity to experimental data. ω refers to phonon frequency, T is the temperature, and v is the phonon group velocity. In the expression of the relaxation time due to boundary, L_s is the characteristic length of the sample (such as the diameter for nanowires, thickness for thin films, etc.), and j is a so-called shape factor. For grain boundary scattering, L_g is the grain size. We note that Slack and Galginatis[42] found better agreement with their experimental data using a relaxation time for U processes of the form $\tau_u^{-1} = B_u e^{-\theta_D/3T} T\omega^2$, and suggested that in general $\tau_u^{-1} = B_u e^{-\theta_D/3T} (T/\theta_D)^\beta \omega^\alpha$, with $\alpha \leq 2$ and for $T > \theta_D$, $\beta = 1$.

In 1994, Klemens refined his calculation considering phonon scattering by grain boundaries.[31] He included a disorder layer between grains, leading to a frequency dependence of the relaxation time, such that $\tau_{gb}^{-1} \propto B_{gb}\omega^2/L_g$. However, a more recent work by Wang *et al.* found that a relaxation time for phonon-grain boundaries scattering of the form $\tau_{gb}^{-1} \propto B_{gb}\omega/L_g$ better described their experimental data.[43]

To eventually calculate the thermal conductivity using all these scattering rates, Callaway[44] considered all the resistive scattering processes to be independent and thus additive, allowing to use the Mathiessen rule for expressing the total relaxation time as

$$\frac{1}{\tau} = \sum_j \frac{1}{\tau_j} \tag{1.29}$$

Holland[26] then a few years later in 1963 made the distinction between longitudinal (l) and transverse (t) modes for calculating the relaxation times, which was not taken into account by Klemens and Callaway. They are expressed as :

$$\text{low T} \begin{cases} \tau_{n,l}^{-1} = B_{n,l}\omega^2 T^3 \\ \tau_{n,t}^{-1} = B_{n,t}\omega T^4 \end{cases} \quad \text{high T} \begin{cases} \tau_{n,l}^{-1} = B'_{n,l}\omega^2 T \\ \tau_{n,t}^{-1} = B'_{n,t}\omega T \end{cases} \quad \tau_{u,t}^{-1} = B_{t,u}\omega^2/\sinh(\theta_D/T)$$

Even though these rather compact expressions for scattering rates are usually based on several assumptions concerning the phonon dispersion, density of states and phonon energies[12], they are very good indicators for describing the temperature dependence of thermal conductivity[34,45], and are actually used for determining the thermal conductivity of materials by solving the Boltzmann equation under the RTA, using a Monte Carlo method for example, provided that all the constant pre-factors B_j are known/fitted from other measurements.[46] Moreover, using these scattering rates can prove useful in estimating which processes are important according to the phonon frequencies and the sample's temperature.

The form of the relaxation times surely inform us that introducing phonon scattering centers at different length scales (adding impurities, grains boundaries or simply reducing the sample size) can eventually reduce the thermal conductivity of the material, depending on the material's temperature and phonon frequency. This has been an extensive research focus within the last three decades[47] for achieving high performances in thermoelectric applications for instance. The performances of thermoelectric materials are increased if they possess low thermal conductivity, high electrical conductivity, and are capable of efficiently converting a temperature gradient into an voltage difference. Indeed, the thermoelectric performance at an operating temperature T is given by the figure of merit $ZT = \sigma S^2/(k_{\text{el}} + k_{\text{lat}})$, where σ is the electrical conductivity, S is the Seebeck coefficient while $k_{\text{el}} + k_{\text{lat}}$ refers to the sum of the electronic and lattice contribution to the thermal conductivity. Since the electronic

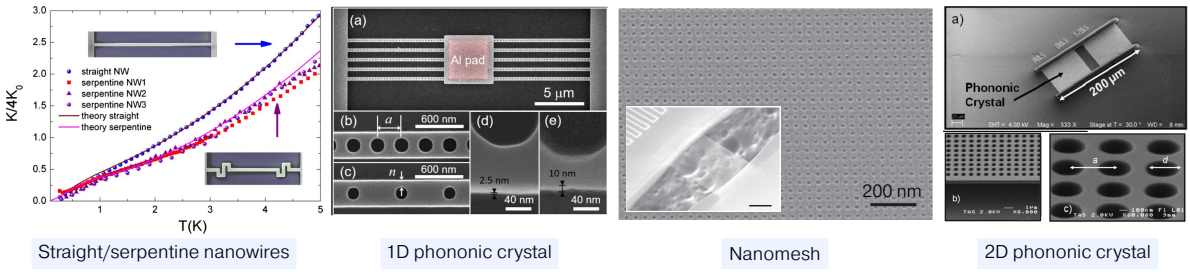

Straight/serpentine nanowires | 1D phononic crystal | Nanomesh | 2D phononic crystal

Figure 1.5: Some examples of material nanostructuration intended to reduce the lattice contribution to the thermal conductivity, for 1D and 2D systems. Images are reprinted with permission from Refs. 48–51. Importantly, the constrictions/holes are designed in such a way that their size match the material's phonon mean free path or wavelength. For this reason, the efficiency of thermal conductivity reduction strongly depends on temperature.

contribution to the thermal conductivity is related to its electrical conductivity through the Wiedemann-Franz law, $k_{\mathrm{el}}/(T\sigma) = L =$ constant, where L is the Lorenz number, the overall gain in one of the two parameters is counterbalanced by a reduction of the other one, and thus the figure of merit remains relatively unchanged by only playing with the electrical properties of a system. An effective approach to increase the figure of merit is thus to reduce the lattice contribution to the thermal conductivity, through for instance, nanostructuration.

1.3.4 Phonon scattering in nanostructured materials

1D and 2D nanostructures

State-of-the-art nanofabrication methods have opened up new possibilities for creating structures whose length scales are close to the characteristic lengths governing heat conduction. Phonon transport can be tuned for example, by simply playing with the geometry of the structure, as shown in Figure 1.5.

One of the most prominent example is the nanowire, whose thermal conductivity is drastically reduced because of enhanced phonon-boundary scattering. Even at room temperature, the thermal conductivity of silicon nanowires have been measured to be significantly lower than their bulk counterpart, because their diameter is below the bulk phonon mean free path.[52–55] In this case, the new phonon mean free path is simply the characteristic length of the nanowire, i.e. its diameter, as proposed by Casimir. We note that in these structures, the thermal transport is also dependent on the surface roughness[35,56], as well as the crystalline quality of their outer layer[57] (in most cases, there is a thin amorphous layer around the nanowire due to oxidation). Notable thermal conductivity reduction in nanowires only due to size effects have been reported for narrow[52], rough[58], modulated[59], scalloped-shaped[60] or serpentine-shaped nanowires.[48] Using the diameter of a nanowire in addition to a combined engineering of crystal phase and isotope disorder has been reported to strongly reduce the thermal conductivity as well.[61]

For membranes, the thermal conductivity is partly reduced by the thickness of the membrane, though the thickness of the membrane alone does not define the phonon mean free path, as it is the case for NWs.[62] Moreover, it can be further reduced by including new phonon scattering centers, which take the form of holes. Fabricating structures that can effectively reduce phonon transport has been made possible primarily because of relentless efforts made in the

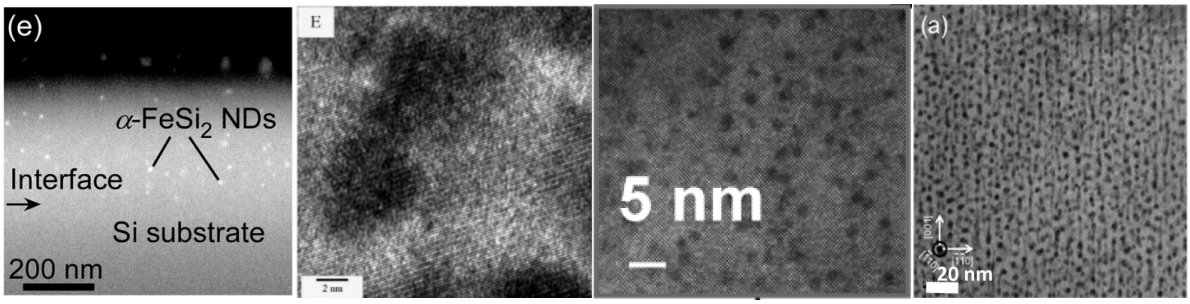

Figure 1.6: Several example of structures whose thermal conductivities have been reduced because of the incorporation of nanoparticle/nanodots within the host material. TEM images reprinted with permission from Refs. 70–73.

field of nano-fabrication. For instance, the realization of holes whose sizes are commensurate to the phonon mean free path or wavelength has been made possible because of the development of electron beam lithography. Such structures as nanomeshes[50] or holey silicon[63] have been reported to significantly reduce the lattice thermal conductivity at room temperature and below. At lower temperature (around 4K), the dominant phonon wavelength starts to become "large" enough such that structures of comparable sizes can be effectively built using modern fabrication techniques. Structures built with such characteristics are often referred to as phononic crystals, and have been extensively studied lately.[64–68]

3D structures

Increasing phonon scattering in 3D structures, i.e. structures where all the dimensions are taken to be greater than the phonon mean free path, seems challenging since growing 3D structures with nanoscale cavities is, technologically speaking, an arduous task. There have been nonetheless theoretical predictions of reduced thermal conductivity in such hypothetical structures.[69] A common substitute to growing materials with nanoscale air gaps is the incorporation of nanodots (NDs)[70], nanoparticles (NPs)[71–75] or nanoinclusions[3] (NIs)[76] using materials different from the host, within the 3D structure (alloy or single crystal), as shown in Figure 1.6. Such phonon scatterers differ from *grains* primarily because of their reduced size, but are still larger than impurities and point defects. The general idea is that while grains would effectively scatter long wavelength phonons and point defects that of short-wavelength phonons, nanoparticles provide an additional scattering mechanism for the mid-to-long-wavelength phonons.[72] Pushing further this reasoning, it seems reasonable to assume that the *broader* the size distribution of nano-inclusions within a material, the more *effective* the scattering will be since nano-inclusions of different sizes will scatter with a larger portion of the phonon spectrum. The relaxation time τ_{ni} due to scattering by a distribution of nano-inclusions is expressed, according to kinetic theory as[77]

$$\tau_{ni}^{-1} = v\sigma_{\mathrm{sct}}(\chi)\eta \tag{1.30}$$

where v is the phonon group velocity, η represents the particle concentration and $\sigma_{\mathrm{sct}}(\chi)$ is the scattering cross-section, which depends on the so-called size parameter χ. The size parameter

[3] The difference between NDs, NPs and NIs might simply be a matter of vocabulary.

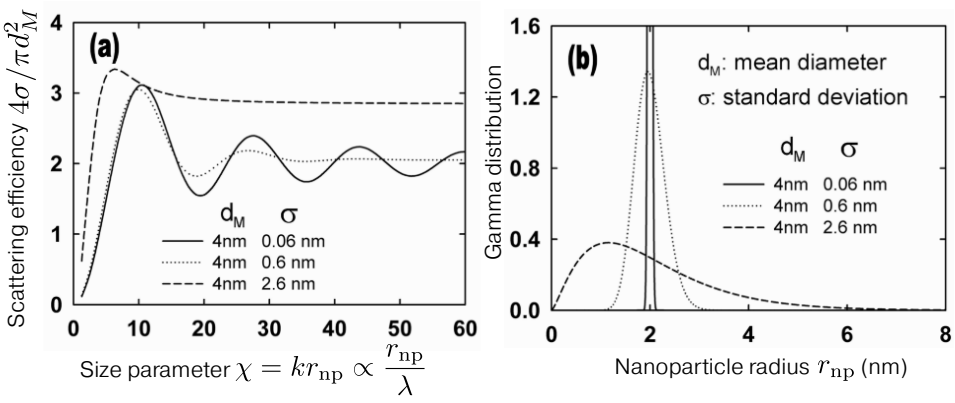

Figure 1.7: Scattering efficiency for several Gamma distributions of the nanoparticle size, with fixed diameter and increasing standard deviations, reprinted with permission from Ref. 77. According to this calculation, a more efficient phonon scattering is obtained for a broader size distribution of nanoparticles.

is a dimensionless parameter that relates the phonon wavevector k to the radius of the scatterer $r_{ni} = d_{ni}/2$ via $\chi = kr_{ni}$. In the limit $\chi \to 0$, we have $\sigma_{sct} \propto r_{ni}^6/\lambda^4$, λ referring to the phonon wavelength, a result first derived by Rayleigh in his study of light scattering with particles whose sizes are much smaller than the wavelength of electromagnetic radiations. This is in accordance with the relaxation time due to impurity scattering, which scale as $\tau_i^{-1} \propto \omega^4$.

Kim and Majumdar[77] provided an approximate analytical solution to estimate the phonon scattering cross section of polydispersed spherical nanoparticles, allowing to estimate how efficient a particle distribution is for impeding thermal flow. In particular, the standard deviation of the distribution function seems to be one important parameter driving the phonon scattering efficiency. This is in agreement with the reasoning that a *broad* NIs size distribution (i.e. with a large standard deviation) would scatter a broader part of the phonon frequency spectrum, thus reducing thermal conductivity more efficiently. The scattering efficiency for several size distributions with several standard deviations are plotted as a function of the size parameter in Figure 1.7(a), which is taken from Ref. 77. This result indeed suggests that a *broad* size distribution of nanoparticles scatters phonons more efficiently. We notice in Figure 1.7(a) that the scattering cross-section presents an oscillatory behavior as a function of size parameter, however this would be averaged out when integrating over the entire phonon spectrum.

Zhang and Minnich have recently suggested, using advanced computational methods, that a broad NPs size distribution was not the most efficient way of reducing phonon transport, but rather discrete peaks at well-chosen nanoparticle radii.[78] However, reports of thermal conductivity measurements in materials with a controlled NPs size distribution are not abundant, primarily because of the difficulty of growing such structures. Even though the continuous or discrete nature of the NP size distribution that would lead to the most efficient reduction in thermal conductivity differ in Kim and Zhang's approaches, both predictions suggest that phonon scattering is enhanced for embedded NPs of different sizes.

Lastly, a design that is somewhere between 2D and 3D structures is that of *superlattices*. A superlattice is a periodic structure of layers of two or more materials, whose thicknesses are of the order of a few tens of nanometers or less. Superlattices show a significant thermal conductivity reduction in the cross-plane direction (see Figure 1.8) primarily because planar interfaces in these structures act as new phonon scattering centers which, when put in series,

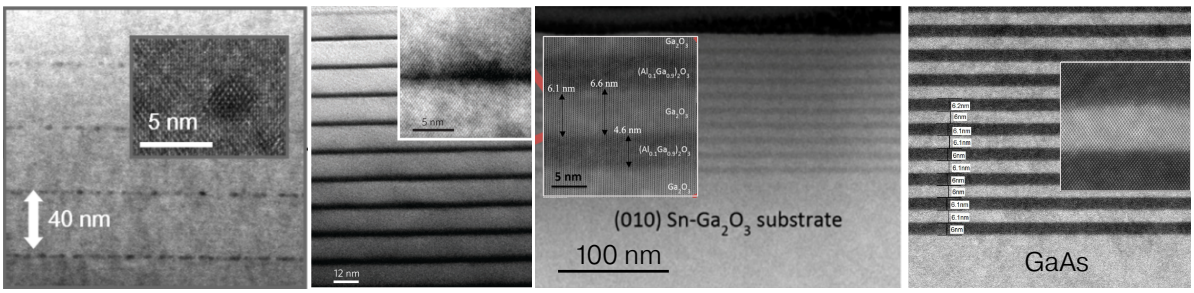

Figure 1.8: Several superlattices structures with reported significant cross-plane thermal conductivity reduction (the cross-plane direction represents the vertical axis in theses TEM images). Reprinted with permission from Refs. 72,80–82.

greatly reduce the effective thermal conductivity of the superlattice.[32] Additionally, large mass difference in two intercalated layers, or weakened interactions across the interface between layers result in reduced thermal conductivity.[79] For superlattices with very thin interlayer spacing, phonon transport within each layer is essentially ballistic and the thermal boundary resistance between each layer becomes the principal source of thermal resistance.[32] An essential parameter for these structures is thus the inter-spacing distance between the layers, compared to the phonon mean free path. A vast majority of literature studies have essentially been focused on the thermal characterization and theoretical study of Si/Ge, Si/SiGe superlattices[32,83–87], superlattices with quantum dots between each two layers (Quantum Dots Superlattices, QDSL)[80,88,89], or even nanowire Si/SiGe superlattices[90,91] but other compositions are very promising in providing materials with enhanced thermoelectric properties.[81,82,92–98] Some examples of these structures are shown in Figure 1.8. Besides, theoretical efforts have been made to quantify how the interface quality[99] and crystallinity[100,101] may impact thermal flow across theses structures.

On the thermal perspective, the impact of interfaces is not solely relevant for increasing a superlattice ability to impede thermal flow. The thermal weight of thermal boundary resistances (TBRs) can be substantial in many measurement configurations that are performed on multilayer systems. This is the case in a majority of popular thermal conductivity measurement techniques such as time-domain thermoreflectance[102], where a metallic layer whose reflectivity is probed to monitor the sample's temperature is deposited on top of the sample of interest, thus creating an interface. Similarly, as will be discussed in the next chapter, the 3ω measurement technique is very sensitive to thermal boundary resistances, which can be detrimental to the accuracy of the measurement. For this reason, we will introduce in the following section the general concept of thermal boundary resistance, and some common models that are used to evaluate it.

1.4 Thermal boundary resistance

Any interface made of two dissimilar materials, or of the same material with different crystallographic orientation, will hamper a thermal flux that is applied across it – even if the interface is smooth at the atomic level. The thermal boundary resistance R_{int} between two materials

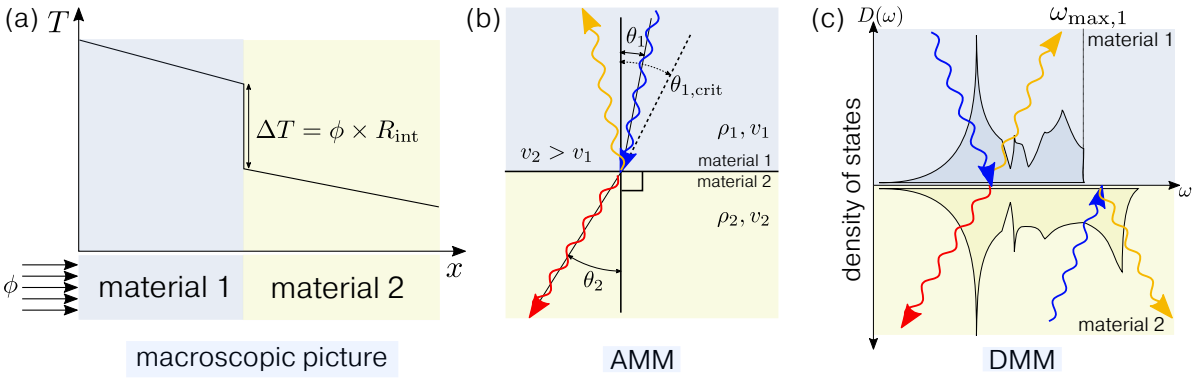

Figure 1.9: (a) Macroscopic picture of the concept of thermal boundary resistance. The TBR causes a temperature jump at the interface. (b) General idea behind the acoustic mismatch model (AMM), it is analogous to Snell-Descartes's law for sound waves. An incident phonon (blue) can be transmitted (red) or reflected (orange), according to the acoustic mismatch between both materials. (c) General idea behind the diffuse mismatch model (DMM), the probability for a phonon to transmit across the interface depends on the phonon density of states of the other material. In this example, the incident phonon from material 2 cannot cross the interface because the density of states in material 1 is null at this particular frequency, and is thus reflected back. More generally, in this model, the material with the lower phonon maximum frequency, or similarly, the lower Debye temperature, will dictate the temperature dependence of the TBR. In particular, above the Debye temperature of the material with lower Debye temperature, the TBR should remain constant when temperature increases.

relates the temperature discontinuity ΔT measured at the interface to the heat flux ϕ that is applied across it, as shown in Figure 1.9(a) :

$$R_{\text{int}} = \frac{\Delta T}{\phi} \tag{1.31}$$

where R_{int} has units of $\text{m}^2.\text{K.W}^{-1}$. It was first reported experimentally by Kapitza in 1941 [103], between liquid helium and copper. Historically, the first models that have been used to estimate the TBR amplitude are the acoustic mismatch model (AMM), diffuse mismatch model (DMM) and the phonon radiation limit (RL). [104,105] The important parameters required to describe the net heat flux of carriers crossing an interface are the flux of energy carriers irradiating the surface, and how well they transmit across the interface.

We shall therefore return to the microscopic picture of the heat flux, which describes the thermal energy that is carried by phonons, but this time accounting for the fact that they can be transmitted or reflected at the interface. This is achieved by adding a *transmission coefficient*, $\alpha_{1\to2}$, describing the probability of an energy carrier to transmit across the interface. Taking into account phonons incident from all directions in the upper half-plane above the interface, the heat flux from material 1 of the interface to material 2 is written as [104]

$$\phi_{1\to2} = \frac{1}{2}\sum_s \int_0^{\pi/2} \int_0^{\omega_{\text{max}}} \hbar\omega v_s(\omega) n(\omega_s, T) D(\omega) \alpha_{1\to2}(\theta, \omega_s) \cos(\theta) \sin(\theta) d\theta d\omega \tag{1.32}$$

where the integral over azimuthal angle φ contributed 2π, and θ is the angle between the incident phonon wavevector and the normal to the interface. Material 1 is defined by convention as the material with the lowest maximum frequency ω_{max} (i.e. lowest Debye temperature). For small temperature difference $\Delta T = (T_2 - T_1) \to 0$, we can replace

$$R_{\text{int}} = \frac{T_2 - T_1}{\phi_{1\to2}(T_2) - \phi_{1\to2}(T_1)} \tag{1.33}$$

using its derivative :

$$\frac{1}{R_{\text{int}}} = \frac{\partial \phi_{1\to 2}}{\partial T} \tag{1.34}$$

and thus, since only the occupation number is temperature dependent, we write

$$\frac{1}{R_{\text{int}}} = \frac{1}{2}\sum_s \int_0^{\pi/2} \int_0^{\omega_{\max}} \hbar\omega v_s(\omega) \frac{\partial n(\omega_s, T)}{\partial T} D(\omega)\alpha_{1\to 2}(\theta, \omega_s)\cos(\theta)\sin(\theta) d\theta d\omega \tag{1.35}$$

The most important and difficult parameter to determine in the above formulation of TBR is the transmission coefficient. The AMM, DMM and RL are the three general models that provide a relatively easy way of calculating the transmission coefficient, under several assumptions which will be introduced.

1.4.1 Acoustic Mismatch Model

The AMM was formulated by Little in 1959.[106] In this model, the transmission coefficient is derived using an acoustic analogous to Snell-Descartes's law for the refraction of light. Phonons are assumed to be deflected at the interface, and the transmission probability depends on their angle of incidence along with the acoustic mismatch between the two media, as shown in Figure 1.9(b). Above a critical angle, phonons are reflected and conversely, they are transmitted below the same critical angle, $\theta_{1,\text{crit}} = \sin^{-1}(v_1/v_2)$, assuming $v_2 > v_1$. The transmission coefficient is given by

$$\alpha_{1\to 2} = \frac{4\frac{\rho_2 v_{p,2}}{\rho_1 v_{p,1}}\frac{\cos(\theta_{p,2})}{\cos(\theta_{p,1})}}{\left(\frac{\rho_2 v_{p,2}}{\rho_1 v_{p,1}} + \frac{\cos(\theta_{p,2})}{\cos(\theta_{p,1})}\right)^2} \tag{1.36}$$

where the angles are related through $\frac{\sin(\theta_1)}{v_1} = \frac{\sin(\theta_2)}{v_2}$, i.e. the acoustic version of Snell-Descartes's law. In this model, the transmission coefficient is derived by solving the continuum elasticity equations and the interface is assumed to be a smooth plane ; any granularity or imperfections at the interface are thus discarded. For this reason, this model is only relevant in the case where phonons do not see any irregularities at the interface. A case that approaches this limit and where the AMM model is successful is at low temperature ($T < 30$ K), where most phonons have low energy and thus long wavelength.[104]

1.4.2 Diffuse Mismatch Model

Diffuse Mismatch Model for phonons

The second model, named Diffuse Mismatch Model or DMM, has been introduced by Swartz and Pohl[104], and the complete specularity (i.e. zero scattering) that is assumed in the AMM, is replaced by the opposite extreme : all phonons are *diffusively* scattered at the interface. In the process of scattering, phonons lose memory of their direction (thus wavevector $\vec{k}$), polarization s, and material of origin such that there is now way to tell if a phonon leaving the interface is due to reflection from the same side or transmission from the other side.[32,104] However, the transmitted phonon keeps the same frequency ω as that of the incident phonon. The probability for a phonon with frequency ω from one side to cross the interface depends on the phonon density of states *at the same frequency* ω of the material on the other side of the interface. For a phonon coming from material 1, the more phonon states at a particular frequency ω there is in material 2, the more likely the phonon will cross the boundary ("forward

scatter") instead of being reflected back into material 1. This also implies that, since a phonon from one material can only transmit energy to another phonon of the other material with the *same* frequency, the material with the lowest allowed maximum frequency (or lowest Debye temperature) will eventually dictate the temperature dependence of the TBR, as shown in Figure 1.9(c). In particular, above the Debye temperature of the material with the lowest Debye temperature, the TBR should be constant when temperature increases.[107]

In this model, the probability of phonon reflection from one side must equal the probability of transmission from the other side :

$$\alpha_{1\to2}(\omega) = 1 - \alpha_{2\to1}(\omega) \tag{1.37}$$

This models suggests that the TBR depends on the density of states $D(\omega)$ of both materials, and their dispersion relation $\omega = f(k)$ – quantities calculated using the material's bulk properties. However, it does not depend on the phonons' angle of incidence. The transmission coefficient is obtained using the detailed balance principle, such that the number of phonons leaving one side of the interface must equal the number of phonons transmitting from the other side of the interface when both sides are at the same temperature[104] :

$$\sum_s \int_0^{2\pi} \int_0^{\pi/2} v_{1,s} n_{1,s}(\omega, T) D_1(\omega) \alpha_{1\to2}(\omega) d\phi \cos(\theta) d\theta \tag{1.38}$$

$$= \sum_s \int_0^{2\pi} \int_0^{\pi/2} v_{2,s} n_{2,s}(\omega, T) D_2(\omega) \alpha_{2\to1}(\omega) d\phi \cos(\theta) d\theta \tag{1.39}$$

Along with Eq.(1.37) and upon integrating over spherical coordinates, it leads to

$$\alpha_{1\to2}(\omega) = \frac{\sum_s v_{2,s} n_{2,s}(\omega, T) D_2(\omega)}{\sum_s v_{1,s} n_{1,s}(\omega, T) D_1(\omega) + \sum_s v_{2,s} n_{2,s}(\omega, T) D_2(\omega)} \tag{1.40}$$

Using the Debye model for the density of states and dispersion relation, it is further reduced to

$$\alpha_{1\to2}(\omega) = \alpha_{1\to2} = \frac{\sum_s v_{2,s}^{-2}}{\sum_s v_{1,s}^{-2} + \sum_s v_{2,s}^{-2}} \tag{1.41}$$

where the $v_{i,s}$ refer to the materials' phonon group velocities, for the three phonon polarizations (two transverse, one longitudinal). The TBR is inferred by plugging the transmission coefficient into Eq.(1.35). It leads to

$$\frac{1}{R_{\text{int}}} = \frac{1}{2} \sum_s \int_0^{\pi/2} \int_0^{\omega_{\max,1}} \hbar\omega v_s \frac{\partial n(\omega_s, T)}{\partial T} D(\omega) \frac{\sum_s v_{2,s}^{-2}}{\sum_s v_{1,s}^{-2} + \sum_s v_{2,s}^{-2}} \cos(\theta) \sin(\theta) d\theta d\omega \tag{1.42}$$

$$= \frac{1}{8\pi^2} \sum_s \int_0^{\omega_{\max,1}} \hbar\omega^3 v_{s,1}^{-2} \frac{\partial n(\omega_s, T)}{\partial T} \frac{\sum_s v_{2,s}^{-2}}{\sum_s v_{1,s}^{-2} + \sum_s v_{2,s}^{-2}} d\omega \tag{1.43}$$

where the Debye density of states is used from the first to second line. In general, the DMM is often seen as more appropriate than the AMM at high temperature. The reason is that at high temperature, most phonons have short wavelength and therefore are more prone to see the atomic imperfections of the interface, and therefore more likely to be scattered, which is the underlying assumption of the DMM.

Diffuse Mismatch Model for electrons

So far, only the thermal resistance due to phonons has been considered. Electrons participate as well in the overall heat transport across interfaces, if at least one of both materials is

metallic, or semi-conducting with sufficient doping. Gundrum *et al.*[108] have used exactly the same assumptions used in the DMM for estimating the thermal boundary resistance due to electrons, for metal-metal interfaces. The transmission coefficient for phonons is replaced by a transmission coefficient for electrons, by taking the Fermi-Dirac distribution rather than the Bose-Einstein one, and replacing the phonon group velocity by the Fermi velocity of electrons. The thermal boundary resistance only due to electrons is written as

$$\frac{1}{R_{\text{int}}} = \frac{Z_{e^-,1} Z_{e^-,2}}{4(Z_{e^-,1} + Z_{e^-,2})} \tag{1.44}$$

where $Z_{e^-,i}$ is given by the product of electronic heat capacity per unit volume $C_{e^-} = (\pi^2/3) D(E_{\text{F}}) k_b^2 T = \gamma T$ and Fermi velocity v_{F} : $Z_{e^-,i} = \gamma v_{\text{F}} T$. This simple models led to quite good agreement with experimental measurements for metal-metal interfaces.[108,109]

1.4.3 Phonon radiation limit

Even though the general trend is respected in terms of how resistive an interface will be regarding the materials' acoustic mismatch and weighted density of states, the AMM and DMM usually overestimate the TBR when compared to experimental results. One could wonder what is the *lowest* resistance that can be achieved, given an interface made of dissimilar materials. Snyder[110] has introduced the phonon radiation limit in which all phonons from the side with the lower density of states are assumed to be transmitted[104], granted that the density of states of the other material is not zero. Phonons from the other material also transmit into the material with lower density of states such that the principle of detailed balance is maintained. The TBR is then obtained by setting the transmission of the lower density of states material (at a particular frequency) to 1 :

$$\frac{1}{R_{\text{int}}} = \frac{1}{2} \sum_s \int_0^{\pi/2} \int_0^{\omega_{\max,1}} \hbar \omega v_{s,2} \frac{\partial n(\omega_s, T)}{\partial T} D(\omega) \cos(\theta) \sin(\theta) d\theta d\omega \tag{1.45}$$

$$= \frac{1}{8\pi^2} \sum_s \int_0^{\omega_{\max,1}} \hbar \omega^3 v_{s,2}^{-2} \frac{\partial n(\omega_s, T)}{\partial T} d\omega \tag{1.46}$$

where the Debye density of states is used from the first to second line. We underline that this limit is not physically justified as opposed to the other two models, but provides a lower bound for TBR.

1.4.4 Other approaches

The three aforementioned models/limit often use approximations in order to provide an easy way of estimating TBR between materials, using informations that can be found in literature, such as the material's Debye temperature or sound velocity. This kind of approach is limited, primarily because the dispersion relation and density of states are often simply taken to be that derived in the Debye model, which does not accurately describe phonons at the edge of the first Brillouin zone (whose group velocity are lower than that predicted in the Debye approximation). Some improvements have led to somewhat better agreement with experiments ; for example, the Debye dispersion relation has been replaced by a more accurate sine-type dispersion relation[111], or using a truncated Debye model.[112] Another approach consists in using the AMM or DMM with dispersion relation and density of states that have been measured experimentally.[113]

Eventually, more realistic approaches that do not rely on these models are computational approaches, such as lattice dynamics and molecular dynamics (MD).[100,107,114–116] These approaches allow to more rigorously explain the factors governing TBR, beyond the dispersion relation and acoustic mismatch, such as the interfacial bonding strength and stiffness, crystallographic orientation, interfacial roughness, or hydrostatic pressure.[105] For a recent review of computational advances in nanoscale thermal transport across interfaces, the reader is referred to Ref. 107. These models usually provide correct qualitative results, but with a restricted quantitative accuracy. Instead of calculating TBR values using the models presented hereinabove, we provide *experimental reports* of thermal boundary resistances for several combinations of materials in Figure 1.10, which is adapted from Ref. 117. As we will discuss in the following chapters, the thermal weight of TBRs, in comparison to the thermal weight of thin films, can become the dominant source of uncertainty when measuring the thermal conductivity of a thin film in a multilayer system. Thermal boundary resistances span about three orders of magnitude, from around 10^{-10} to 10^{-7} m^2.K/W at room temperature. In comparison, a thin film with thermal conductivity $k_f = 1$ W/m.K and thickness $d_f = 10$ nm has a thermal resistance $R_f = d_f/k_f = 10^{-8}$m^2.K/W, which is the same order of magnitude. This simple comparison underlines the difficulty of measuring the thermal conductivity of supported films which are very thin, thermally conductive, or both.

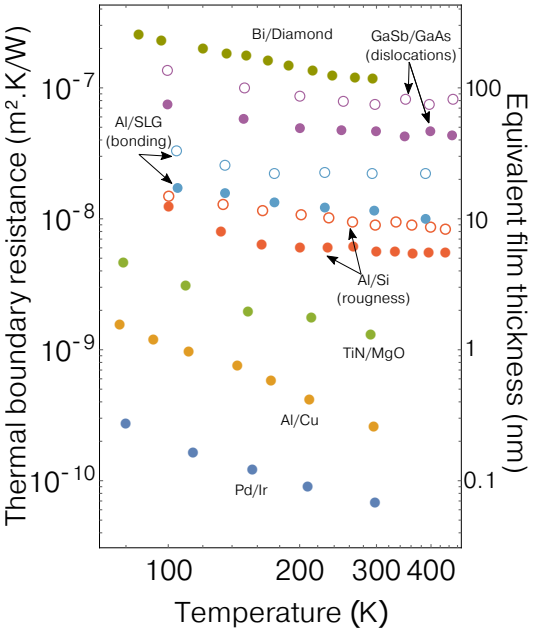

Figure 1.10: Measured TBRs as a function of temperature, adapted from Ref. 117. The scale on the right represents the thickness of a film with thermal conductivity k_f=1 W/m.K whose computed thermal resistance would lead to the same TBR as that on the left scale.

In the next chapters, we will describe the measurement technique – the 3ω method – that have been implemented and used for determining the thermal conductivity of films and substrates, which differ in terms of size and thermal properties, and where TBRs can greatly affect the accuracy of the measurement. The technique is used to measure the thermal conductivity of films that have been nanostructured, such that we expect a reduced thermal conductivity because of the scattering events experienced by phonons, as introduced in Section 1.3.3 of this chapter.

2 The 3ω method : principle and implementation

2.1 The 3ω method

2.1.1 Introduction

The ever-decreasing size of structures implemented in next-generation electronic devices has led to the development of measurement techniques which are adapted to such reduced sizes. For thermal measurements, the heat source and temperature sensor are scaled to match the size of the sample of interest. For example, in pump-probe experiments such as opto-thermal Raman spectroscopy[118] or time-domain thermoreflectance[102], the spot size of lasers used to provide the heat flux and read the temperature response are of the order of a few micrometers.[1] In electro-thermal measurement techniques, the heating element and temperature sensor are thin films which are hundred of nanometer thick and a few μm large. The heat flux is created by Joule heating while the temperature is monitored by reading the temperature-dependent resistance of the metallic thin film.

The 3ω method is an electro-thermal method which can be used to measure the thermal conductivity of bulk substrates, thin films, membranes, nanowires and under certain conditions, thermal boundary resistances. It has been popularized by Cahill in 1990[119], who extended the

[1] In time-domain thermoreflectance, the pump laser is heating a metallic film deposited on top of the sample, which in turn serves as a heat source for the sample underneath. The laser does not directly heat the sample.

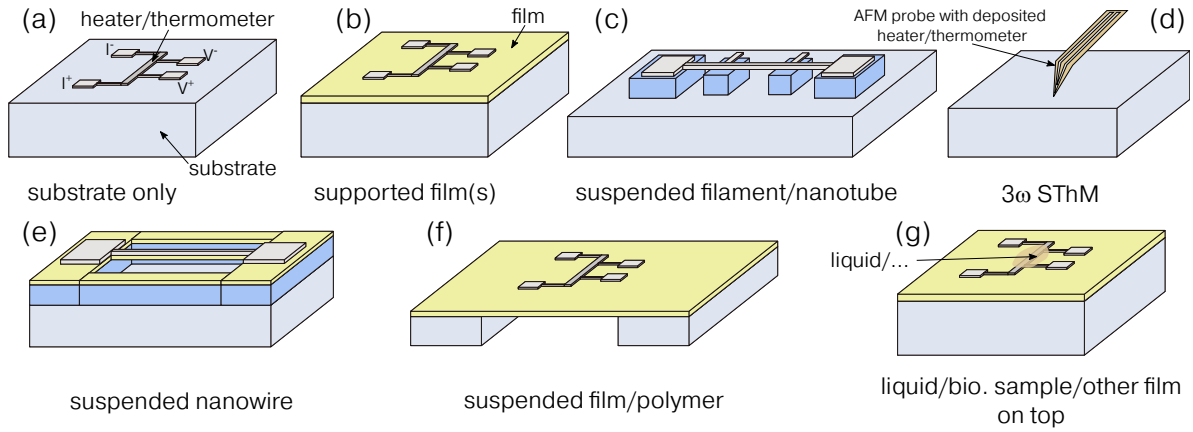

Figure 2.1: Principal geometries that have been used to measure the thermal conductivity of films and other structures using the 3ω method.

measurement method proposed by Birge and Nagel that was aimed to measure the specific heat of liquids.[120] The 3ω method is widely used in the heat-transfer community, primarily because it is (historically) among the first methods to be essentially immune to errors due to black-body radiation since the effective heated area is small (with an order of magnitude of $\approx$ 100 μm), and does not suffer from long thermalisation times. Besides, it is an *electro*-thermal method, which is well mastered and relatively easy to set up, and since it is also a frequency-dependent technique, it can take advantage of lock-in amplifier technology to read the system's frequency response with great accuracy.

The 3ω method has been used to measure the thermal properties of a large variety of materials with different geometries, for different purposes, as can be seen in Figure 2.1. Whatever the geometry of the structure to be studied, the method relies on the frequency-dependent thermal response of a self-heated single metallic element which serves both as a heater and a thermometer. Thermal properties of the surroundings of the heater/thermometer, or of the heater/thermometer itself, are inferred by monitoring its thermal response as a function of driving frequency. It was first used by Cahill to measure the thermal conductivity of thick, electrically insulating substrates[119] (Figure 2.1(a)) and later, amorphous thin films[121] (Figure 2.1(b)). The thermal conductivity of an anisotropic multi-wall carbon nanotube strands has been measured several years later[122], which took advantage of a more accurate thermal model for 3ω experiments[123] conducted in a multilayer-on-substrate configuration (Figure 2.1 (b)). Then, the thermal conductivity of suspended filaments/nanotubes[124] (Figure 2.1(c)) and nanowires[54,125] (Figure 2.1(e)) have been measured by suspending the structure such that the thermal flux leaks into the nanowire rather than directly into the substrate. Similarly, the thermal conductivity of suspended membranes and polymers have been measured using the geometry of Figure 2.1(f).[126–129]

Lefèvre and Volz[130] provided a thermal model for using the 3ω method when the heater/thermometer is placed at the tip of a AFM probe (Figure 2.1(d)), providing a better spatial resolution for temperature measurements. The thermal conductivity of liquids was then measured by Choi *et al.*[131], by placing a small amount of liquid on top of the heater/thermometer (Figure 2.1(g)) and measuring its thermal contribution – a method also used for measuring the thermal conductivity of other types of systems (gas[132], biological tissues[133] or other films with applied pressure[134]).

Additionally, the technique has been used for purposes other than measuring the thermal conductivity of materials. For example, it has recently been used for tracking moving phase boundaries[135] or determining the extent of a freezing region surrounding a cryoprobe.[136]

In this work, we will use the geometry of Figure 2.1(a) and (b) for measuring the thermal conductivity of thin films and substrates when using the 3ω method, which is the simplest geometry we can think of, and the easiest to achieve in terms of fabrication. However, the simplicity in fabrication does not translate into simplicity in data modelling. We will focus this chapter and the two following ones in explaining the principle of the 3ω method, how it has been implemented during this thesis, and the thermal model used to determine important thermal properties in a supported multilayer system.

2.1.2 Principle

The 3ω method consists in measuring the thermal impedance created by a specimen of interest, when submitted to a periodic heat flux. The periodic heat flux is created by applying an alternative current of frequency $1\omega_e$ across a metallic line microfabricated on top of the specimen, as depicted in Figure 2.2(a). Joule heating occurring at $2\omega_e$ induces a temperature oscillation at the same frequency, which, coupled with the metallic line's temperature coefficient of resistance (TCR), leads to a periodic change of the metallic line resistance at $2\omega_e$. Consequently, a voltage at frequency $3\omega_e$ that is proportional to the temperature oscillation $\Delta T_{2\omega_e}$ develops across the metallic line, as displayed in Figure 2.3. It is from this temperature oscillation that we infer thermal properties of the system beneath the metallic line.

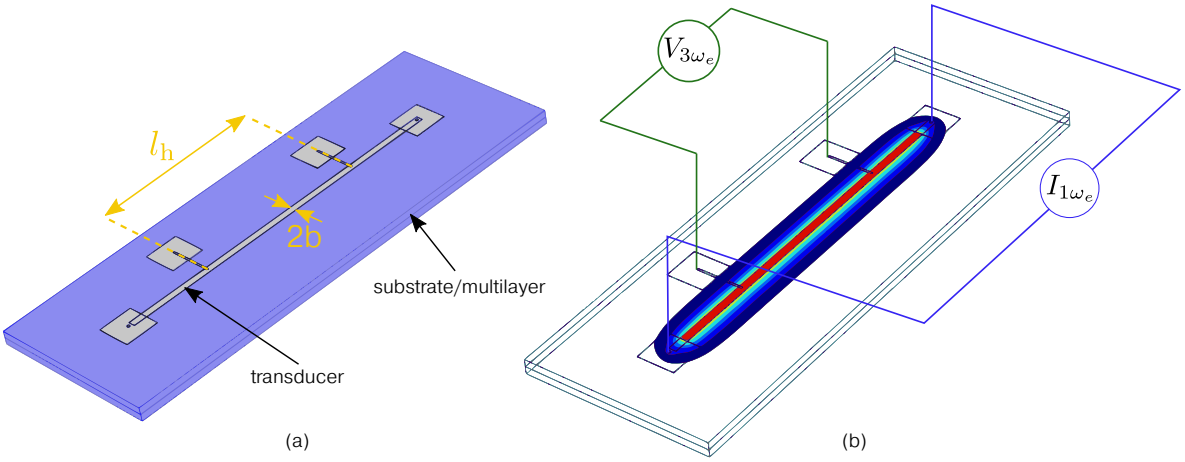

Figure 2.2: (a) Schematic of the metallic transducer on a substrate/multilayer with important geometry parameters (length l_h and width $2b$). (b) Illustration of the principle of the 3ω method : $V_{3\omega_e}$ is read to infer the temperature oscillations sensed by the transducer which in turn gives informations about the thermal properties of the system.

We remind that in this geometry, the metallic line serves both as a heater and temperature sensor : it will be hence often referred to as a *transducer* in this manuscript. Prior to discussing the mathematics involved in the determination of thermal properties of materials using the 3ω method, it is important to grasp a few important key points related to the method.

Firstly, the 3ω method relies upon the measurement of a temperature oscillation that is a consequence of the finite thermal impedance of a material submitted to a periodic heat flux. Importantly, the temperature oscillation is sensed at the same position where the heat flux is

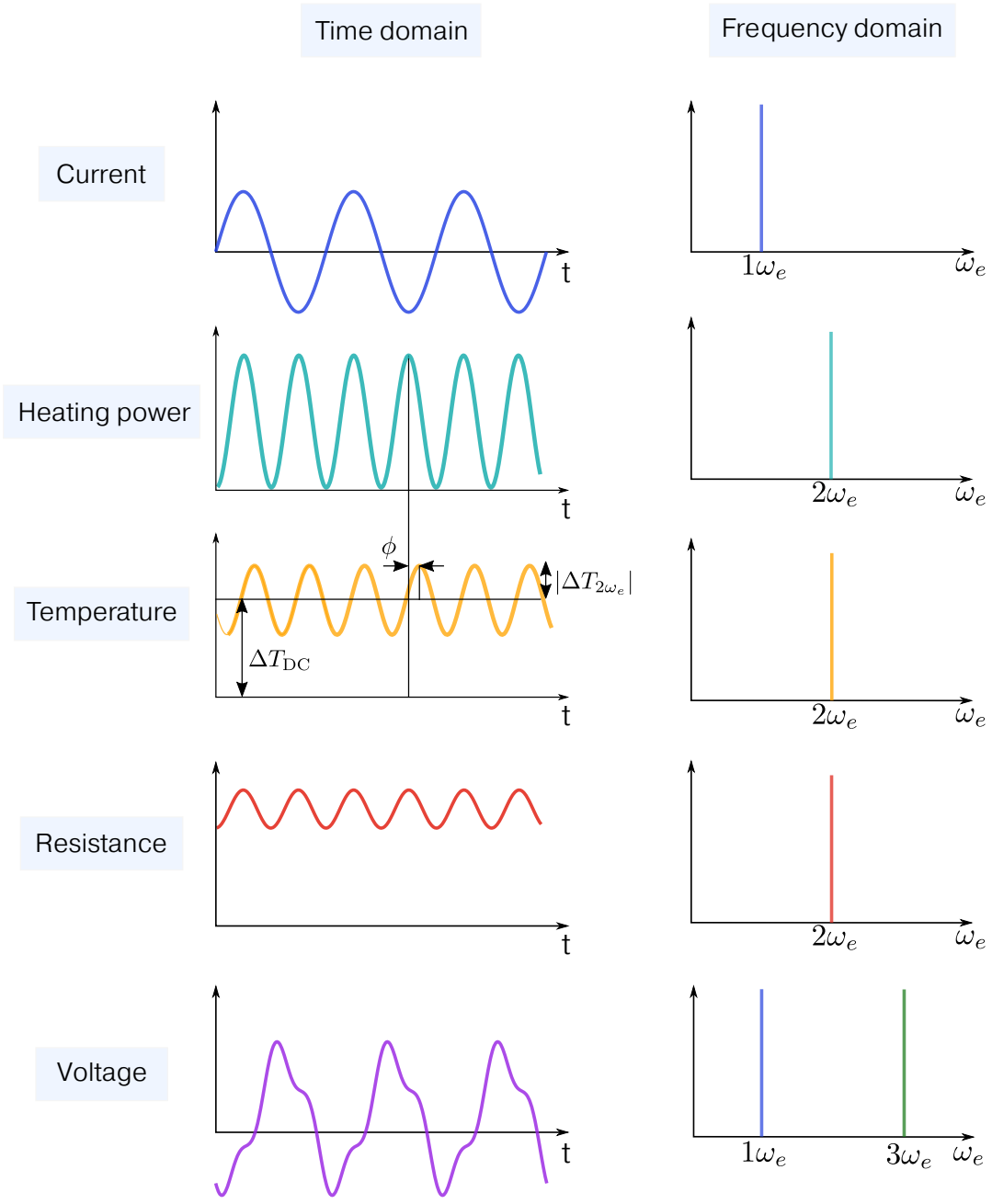

Figure 2.3: Schematic representation of the time-varying quantities of interest during a 3ω experiment.

produced. If the material is thermally insulating (such as amorphous materials, polymers, etc.), heat won't propagate easily through the material, and therefore the temperature oscillation sensed by the transducer will be large, thus relatively easy to measure. Conversely, a material with large thermal conductivity (such as metals, semi-conductors, etc.) will easily spread heat coming from the transducer. For the same applied power, the temperature oscillation measured across the transducer will therefore be very small and difficult to measure. Using the geometry depicted in Figure 2.2, it is then easier to measure a thermally insulating material.

Secondly, the wording thermal « impedance » suggests that the temperature oscillation is complex and therefore has a magnitude and phase. We must recall that the temperature oscillation is a consequence of an oscillating heat source, which also has an amplitude and phase. When the heat wave coming from the periodic joule heating flows across the system of interest, its amplitude and phase will change according to the system's thermal properties (see Figure 2.3). Consequently, there is a difference in amplitude and phase between the heat source excitation and the temperature response. That way we can define two orthogonal components, the real part of the complex temperature oscillation which is in phase with the heat, and the imaginary part, out of phase with the heat. This aspect is important since it is directly related to quantities we have access to experimentally, i.e., oscillating voltage that have in-phase and out-of-phase components.

Lastly, we only have access to the temperature oscillation at one position (on top of the specimen), averaged across the transducer's dimensions, to infer thermal informations of the underlying material(s). Since we accurately know the power P that is supplied, the measured temperature oscillation $\Delta T_{2\omega_e}$ can be translated into an *effective* thermal impedance Z_{eff}, since $\Delta T_{2\omega_e} = Z_{\text{eff}} \times P$. It is *effective* since it is the impedance of the *complete* thermal circuit (heater, film, substrate, thermal boundary resistances, etc.). For this reason, it does not seem straightforward to infer the thermal properties of a complex system made of many layers with different thermal properties, since we only measure the temperature at one position, which reflects the effective thermal impedance of the system. For a film-on-substrate system, how is it possible to separate the thermal contribution of the substrate to the total thermal impedance, which we can reasonably assume will be large, from that of the film deposited onto the substrate, which we can assume will be small ? Similarly, since we are dealing with small samples, typically several hundred of microns thick for most substrates, will the experiment be sensitive to the thermal contact between the sample and the sample holder ? These questions have several answers, which rely upon the core of the 3ω method : it is a frequency-dependent technique and it is therefore possible to tune the depth at which the temperature gradient extends within the material of interest by varying the heat source excitation frequency (remember Fourier and the temperature propagation within Earth's crust from Chapter 1). In practice, this is achieved by varying the frequency of the current flowing through the transducer. The relationship between frequency and heating depth brings the need to define the notion of thermal penetration depth.

2.1.3 Thermal penetration depth

The thermal penetration depth is a simple, yet important notion in frequency-dependent thermal measurements that needs to be conceptually understood. To do so, we start from the simple case of heat conduction in one dimension, with no *internal* heat generation. The heat

equation is written as

$$\rho C_p \frac{\partial T(y,t)}{\partial t} = k_y \frac{\partial^2 T(y,t)}{\partial y^2}$$

If the heat source is periodic with a characteristic frequency ω, it is reasonable to assume that temperature oscillates at frequency ω as well, and therefore we write $T(y,t) = T(y)e^{i\omega t}$. Applying boundary conditions such that $T(y)_{y\to\infty} = 0$ and introducing the heat source as a boundary heat flux ϕ such that $-k_y \partial T(y)/\partial y|_{y=0} = \phi$, the temperature oscillation as a function of coordinate y is of the form[2]

$$T(y) = \frac{\phi}{q k_y} e^{-qy} \tag{2.1}$$

where we have defined

$$q \equiv \sqrt{\frac{i\rho C_p \omega}{k_y}}$$

This definition of q will be used henceforward. We underline that ω represents the frequency at which the temperature is oscillating. Therefore, when the temperature oscillation comes from Joule heating at electrical frequency $\omega_e = 2\pi f$, the heating frequency is written $\omega = 2 \times \omega_e = 2 \times 2\pi \times f$. From Eq. (2.1), we understand that temperature is decaying exponentially as a function of position, over a characteristic length $|1/q|$. This length will be henceforth referred to as the thermal penetration depth (TPD), since it represents the characteristic length over which the temperature amplitude decays towards zero.

$$\text{Thermal penetration depth (TPD)} = \lambda_{\text{tpd}} = \left|\frac{1}{q}\right| = \sqrt{\frac{k_y}{\rho C_p \omega}} = [\text{m}] \tag{2.2}$$

In this example in one dimension, it represents the length at which the temperature amplitude has dampened by $1/e \approx 37\%$ from its initial value. Indeed

$$\frac{T(y = |1/q|)}{T(y = 0)} = \exp(-1) = 1/e$$

This is derived for the case of heat conduction in one dimension so that the familiar exponential decay and characteristic length appear clearly. The result is similar in essence for higher dimensions[3], as shown in two dimensions in Figure 2.4, for a heat source of finite width dissipating heat inside a material underneath. The TPD is inversely proportional to the heating frequency, meaning that the length over which the material of interest is heated decreases as the heater frequency increases. This is of major importance, because we can devise experiments to probe in depth a material by changing the heat source oscillation frequency – thereby being immune to end effects due to the finite size of samples, which can be important in DC measurements. This is the starting point for many frequency-dependent thermal measurement schemes. As we will discuss later, it also entails limitations for the heating frequency range to use when performing an experiment.

[2] dropping the time dependent part

[3] The exact solution for an infinitely narrow line dissipating inside a material in two dimensions is written using a modified Bessel function of the second kind.[137] The temperature decreases over the same characteristic length as defined in the text, however it represents the length at which the temperature amplitude dampens by $K_0(1) \approx 42\%$ from its initial value.

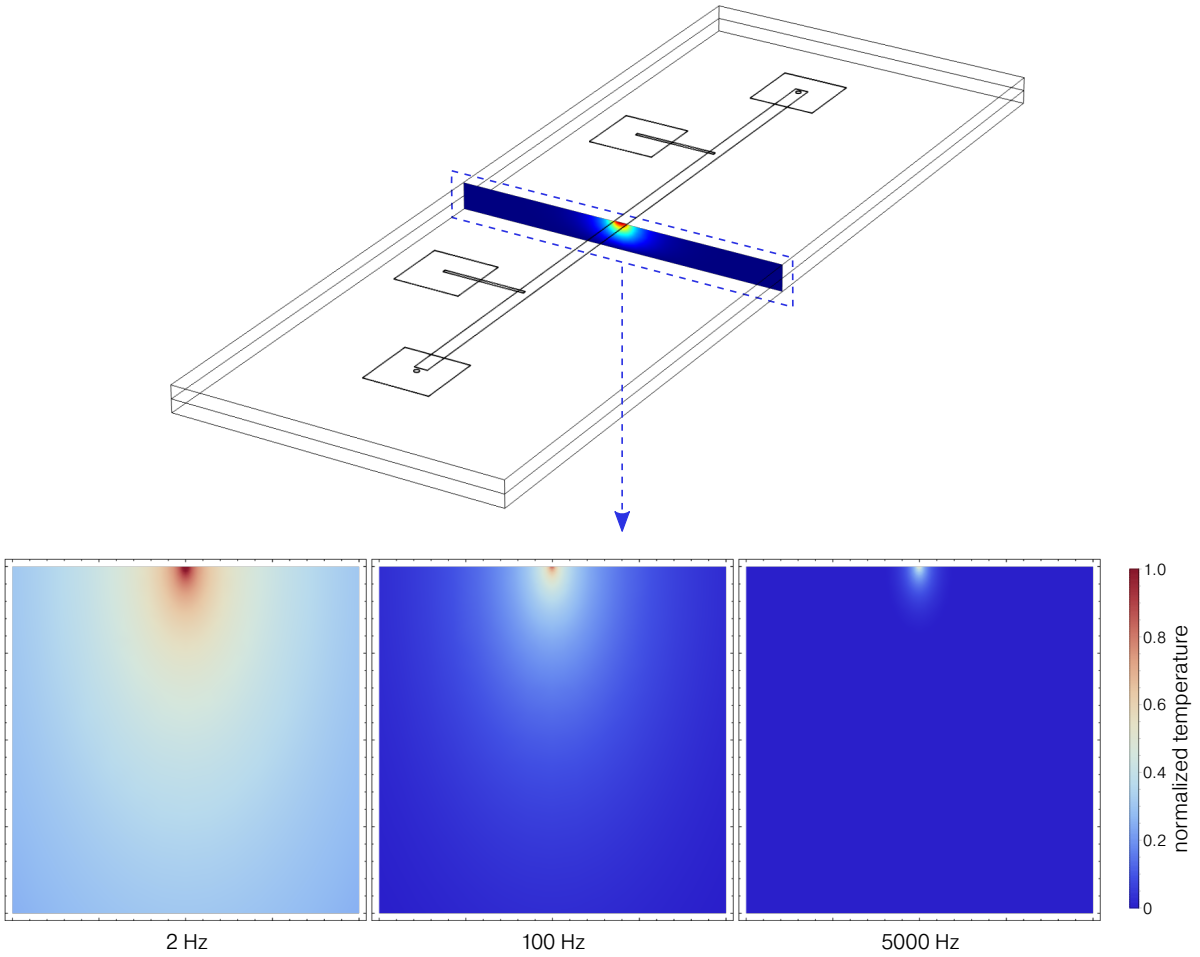

Figure 2.4: Calculated amplitude of the temperature *oscillation* at $2\omega_e$ in two dimensions in a germanium substrate, for several excitation frequencies. The heat source is a boundary heat source, mimicking a heater of negligible thickness deposited onto the substrate. Increasing the frequency makes the thermal penetration depth smaller and thus playing with the excitation frequency allows to probe in depth a material of interest. The size of the plots is 200×200 μm^2. There always is a DC component of the temperature, which is superposed to the temperature oscillation at $2\omega_e$. It has been removed in these plots for clarity.

Consequently, the 3ω method consists in heating the sample using the transducer, and measuring the temperature response of this transducer as a function of its excitation frequency in order to probe the material in depth. Fitting the thermal response of the calibrated transducer using an adapted heat conduction model allows to infer several thermal properties of the system under study.

As we will see in the following section, the measurement of the temperature oscillation $\Delta T_{2\omega_e}$ is straightforward using experimental quantities that are very well controlled or measured. To infer thermal properties from this temperature oscillation is, however, more demanding.

2.1.4 Measuring the temperature oscillation

In this section, we wish to express the temperature oscillation, related to the thermal impedance of the system of interest which contains useful thermal informations, in terms of the quantities that are driving our electro-thermal experiment, i.e. the voltage, current and power produced

by Joule heating. A sinusoidal current

$$I_{1\omega} = I_1 \cos(\omega_e t) \tag{2.3}$$

is flowing through the metallic transducer, whose electrical resistance variation with temperature is written as

$$R_e = R_{e,0}(1 + \beta \Delta T_{\text{tot}}) \tag{2.4}$$

where

$$\beta = \frac{1}{R_{e,0}} \frac{dR_e}{dT} \tag{2.5}$$

is its temperature coefficient of resistance (TCR). Because $\beta \Delta T_{\text{tot}} \ll 1$, to leading order, Joule heating can be approximated as[138,139]

$$P = R_{e,0} \times I_{1\omega}^2$$

The temperature variation resulting from the metallic line dissipating power through Joule heating is

$$\begin{aligned} \Delta T_{\text{tot}} &= P \times Z_{th} \\ &= R_{e,0} \left(I_1 \cos(\omega_e t)\right)^2 \times Z_{th} \\ &= R_{e,0} Z_{th} \frac{I_1^2}{2} (1 + \cos(2\omega_e t)) \\ &= \underbrace{\Delta T}_{\Delta T_{\text{DC}}} + \underbrace{\Delta T \cos(2\omega_e t + \phi)}_{\Delta T_{2\omega_e}} \end{aligned} \tag{2.6}$$

where Z_{th} represents the *thermal impedance* of the specimen under study. Importantly, it can be complex and frequency dependent and cause a phase lag ϕ between the periodic heating and the temperature response (see Figure 2.3). In some cases, it is not frequency dependent ; it is then referred to as a thermal *resistance*. The voltage across the transducer reads

$$\begin{aligned} V &= R_e \times I_{1\omega} \\ &= R_{e,0}(1 + \beta \Delta T_{\text{tot}}) \times I_1 \cos(\omega_e t) \\ &= R_{e,0} I_1 [1 + \beta \left(\Delta T + \Delta T \cos(2\omega_e t + \phi)\right)] \cos(\omega_e t) \\ &= R_{e,0} I_1 \cos(\omega_e t) + R_{e,0} I_1 \beta \Delta T \cos(\omega_e t + \phi) + R_{e,0} I_1 \beta \Delta T \cos(\omega_e t) \cos(2\omega_e t + \phi) \\ &= \underbrace{\left[R_{e,0} I_1 \cos(\omega_e t) + \frac{3}{2} R_{e,0} I_1 \beta \Delta T \cos(\omega_e t + \phi)\right]}_{V_{1\omega_e}} + \underbrace{\left[\frac{1}{2} R_{e,0} I_1 \beta \Delta T\right] \cos(3\omega_e t + \phi)}_{V_{3\omega_e}} \end{aligned} \tag{2.7}$$

For simplicity, we will now write harmonics of the voltage $V_{1\omega_e}$ and $V_{3\omega_e}$ as $V_{1\omega}$ and $V_{3\omega}$. Since we use a lock-in amplifier to measure $V_{3\omega}$, we express important quantities in terms of root-mean-square (rms) values, as read by the lock-in :

$$\Delta T = \frac{2 V_{3\omega,\text{rms}}}{R_{e,0} I_{1\omega,\text{rms}} \beta}$$

We have kept the peak value of the temperature oscillation, since in the data reduction process that is described later on, we use the peak value of the dissipated power to fit the measured temperature oscillation data to a thermal model. The temperature oscillation has in-phase (with the heating) and out-of-phase components, which can be readily determined using the

in-phase and out-of-phase components of $V_{3\omega}$. The temperature oscillation in-phase with the heating is therefore readily inferred from quantities that can be accurately measured : the ac current, the transducer resistance and its temperature coefficient of resistance. It can be useful to re-write Eq.(2.7), using the expression of ΔT in Eq. (2.6) :

$$\begin{aligned} V &= \left[R_{e,0}I_1 + \frac{3}{2}R_{e,0}I_1\beta\left(R_{e,0}Z_{th}\frac{I_1^2}{2}\right)\right]\cos(\omega_e t) + \left[\frac{1}{2}R_{e,0}I_1\beta\left(R_{e,0}Z_{th}\frac{I_1^2}{2}\right)\right]\cos(3\omega_e t) \\ &= \left[R_{e,0}I_1 + \frac{3}{4}R_{e,0}^2I_1^3\beta Z_{th}\right]\cos(\omega_e t) + \left[\frac{1}{4}R_{e,0}^2I_1^3\beta Z_{th}\right]\cos(3\omega_e t) \end{aligned} \tag{2.8}$$

This expression exhibits an explicit relation between the third harmonic of the voltage and the current's third power. Checking the relation $V_{3\omega} \propto I_1^3$ has been very useful throughout all the experiments carried out in this work, since it acts as a probe for many of the inconveniences that can be present during an experiment, such as electrical leakage through the sample that can be due to faulty electrical insulation.

From Eq. (2.7) or (2.8), we notice that both the first and third harmonics of the voltage contain informations about the temperature oscillation amplitude sensed by the transducer. $V_{1\omega}$ has two components, one which is orders of magnitude larger than the other. It is uncommon to infer the temperature oscillation from the first harmonic of the voltage since it is an arduous task to separate its small contribution from that of the much larger ohmic voltage. Similarly, $V_{3\omega}$ is buried within the large ohmic background voltage $V_{1\omega}$ that lessen the accuracy of the voltage reading. It scales as

$$\frac{V_{1\omega}}{V_{3\omega}} \approx \frac{2}{\beta\Delta T}$$

The temperature oscillation amplitude usually lies within the range of 0.1-3 K whereas the TCR of metallic films has an order of magnitude of 10^{-3} K^{-1}, leading to a ratio $V_{1\omega}/V_{3\omega}$ as large as 10^4. From this consideration, we can either rely upon the dynamic reserve of our lock-in amplifier to read the small third harmonic of the voltage[124,138], or try to attenuate $V_{1\omega}$ while keeping $V_{3\omega}$ intact with the help of a nullifying bridge. Most of literature studies have chosen the second option, and we do so as well in this work, for reasons that will be explained hereafter. This requires a specific instrumentation and calibration, which we will describe and discuss in the following section, along with the sample mounting.

2.2 Instrumentation and sample mounting

The instrumentation required to perform a 3ω measurement is relatively simple, when compared to other thermal measurement technique setups such as those used for Raman spectroscopy or time-domain thermoreflectance. The most important item is the lock-in amplifier which, in our setup, both provides the oscillating current and reads the 3ω voltage. As in any thermal measurement scheme, the heating power provided to the system and the resulting temperature response are two quantities that must be accurately quantified to infer the system's relevant thermal characteristics. In a 3ω experiment, it translates to the transducer resistance, the oscillating current and the temperature coefficient of resistance of the transducer – quantities that are relatively easy to measure or calculate.

To measure the transducer's TCR, we apply a current across its outer pads and measure the resulting voltage between its inner pads (as in the geometry of Figure 2.2(a)), using a four-probe geometry, as a function of temperature. In this work we used a device developed

at Institut Néel (named MMR3) that allows to measure up to three resistances simultaneously using very low currents, with high resolution and very low noise (see Figure 2.5). All the calibrations have been carried out for each transducer, using a current ranging from $\sim$ 5-30 μA. When possible, calibrations of different transducers were performed simultaneously.

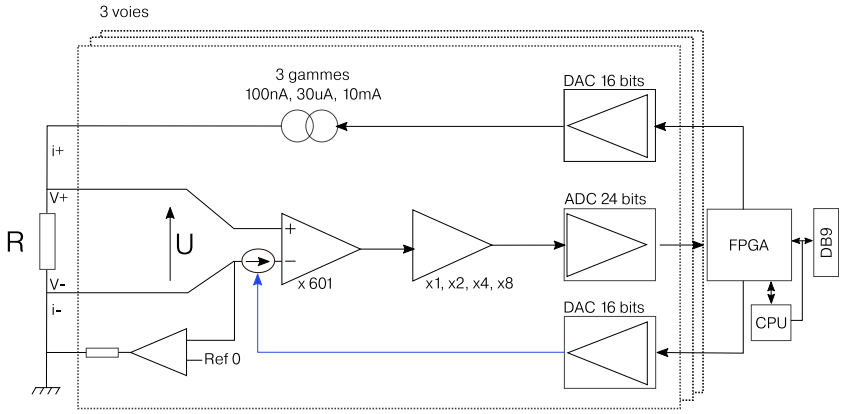

Figure 2.5: Detailed schematic of the MMR3 device used to measure the resistance of the transducers. An alternative current passes through the resistance and the resulting voltage is read in a 4-wire configuration. Its accuracy on the measured resistance is 0.05%. Source : http://neel-2007-2019.neel.cnrs.fr/spip.php?rubrique840

After the calibration of the transducer, the second step of the experiment consists in measuring $V_{3\omega}$ as a function of the excitation frequency.

2.2.1 Lock-in amplifier and differential bridge

As discussed above and underlined in Figure 2.3, though it can be omitted[124,138], it is preferred to remove the large $V_{1\omega}$ in order to measure $V_{3\omega}$ with better precision. This permits to be well above the detection limit of the lock-in amplifier. The limits of a digital lock-in amplifier are mainly dictated by its dynamic reserve, which is related to the performance of its main Analog to Digital Converter (ADC).[140] In this work, the lock-in ADC has a resolution of 16 bits, meaning that it can encode an analog input to one in 65536 different levels (2^{16}=65536). For example, if the voltage at the lock-in input is 1V (10 mA flowing through a 100 Ω resistance) and the full scale sensitivity is accordingly set to 1V, then the discrete digitization of the signal from the ADC will impose a resolution of $1V/2^{16} = 15.26\ \mu V$, which could become a significant portion of the thermal $V_{3\omega}$ signal, especially for thermally conductive samples that produce weak $V_{3\omega}$ signals. Another benefit of removing $V_{1\omega}$ is to perform measurements at a higher current to produce larger heating power – leading to temperature oscillations that are well above the minimum temperature change that can be sensed by the thermometer. Indeed, since the lock-in amplifier has a finite maximum voltage input $V_{\max}$, it imposes a limit upon the maximum current that can flow through the circuit : a current too high will produce an ohmic voltage $V_{1\omega}$ through the metallic line that could overload the lock-in amplifier (i.e. $V_{1\omega} > V_{\max}$).

To remove the large $V_{1\omega}$ background voltage, there has been mainly two different approaches in the literature. The first one has been introduced by Cahill in his original paper presenting the 3ω method[119], who used a differential bridge. The second one is to use a Wheatstone bridge.

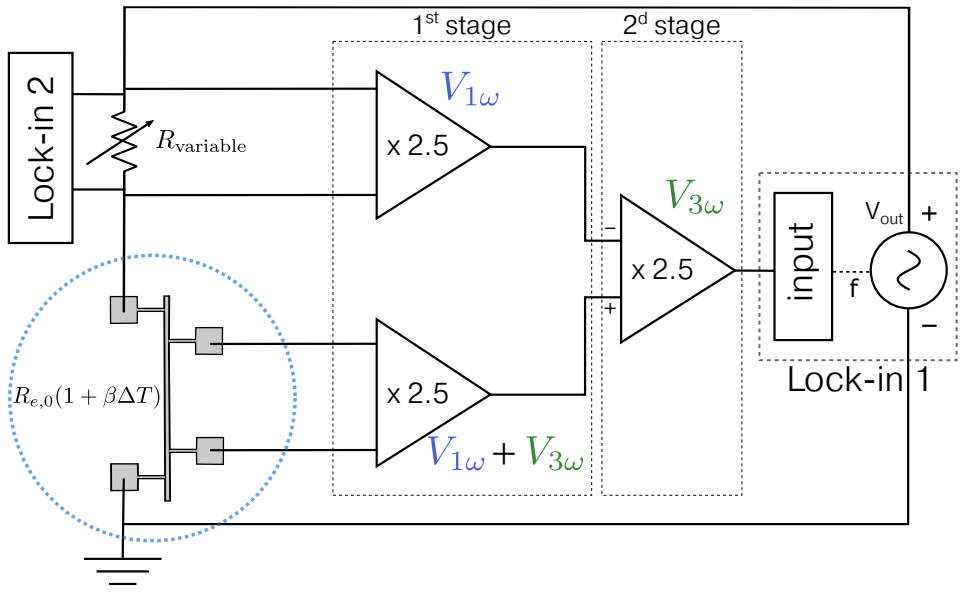

Figure 2.6: Simplified schematic of the setup used for a 3ω experiment as described in the text. Part of the circuit (within the blue-dashed circle) is immersed inside a cryostat and put under vacuum ($\approx 10^{-5}$ mbar). The circuit is controlled from a computer such that the programmable resistance is automatically changed to match that of the transducer when the experiment is run as a function of temperature. Everything is controlled using a home-made LabView program (see Appendix E).

In this work, we use a differential bridge as depicted in Figure 2.6. We use lock-in 1 (AMETEK 7230) output voltage to source the circuit. A variable resistance (IET PRS-B-7.001), denoted R_{variable} in Figure 2.6, is placed in series and set to match the transducer's resistance $R_{e,0}$. It is further used to read the current flowing through the circuit, using lock-in 2.

The differential bridge is built from three INA103 instrumentation amplifiers, with the purpose of considerably lessening the ohmic 1ω voltage. In the first stage of the bridge, the same voltage drops across both the transducer and the variable resistance, the latter assumed to have negligible temperature coefficient of resistance. Consequently, the output voltage in the second stage of the bridge contains the small $V_{3\omega}$ immune from the large ohmic background. Amplification has been chosen so as to increase the signal for easier detection while keeping it low enough for the second stage of the bridge *and* the lock-in input not to overload.[4] The resulting signal is read using lock-in 1, which can inherently read up to two different harmonics of the voltage using two distinct demodulators.

The use of lock-in 1 output voltage to provide an oscillating current has the disadvantage of not knowing directly the current that is flowing through the circuit. A stable current source, or a voltage-to-current converter could be used instead, which would remove the need of a second lock-in to measure the current. During this thesis, we have tried both approaches. However, the home-made voltage-to-current converter that was available suffered from a restricted bandwidth ($f_{-3\text{db}} \approx 14$ kHz), which prevented its use for accurate 3ω measurements at frequencies above 10 kHz. We have then used the commercially available current source Keithley 6221 which worked great but suffered from harmonic distortion at relatively low frequencies, in com-

[4] In practice, we have found that the second stage of the bridge is important because operational amplifiers have in general a higher input voltage range than lock-in amplifiers and therefore we can apply higher current in the circuit without overloading the lock-in amplifier.

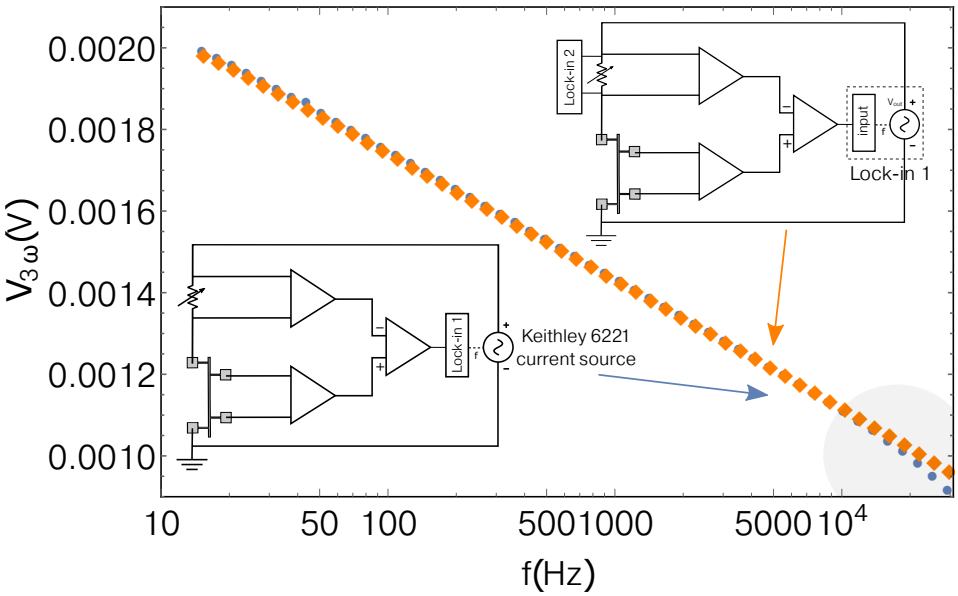

Figure 2.7: Measurement of the third harmonic of the voltage, $V_{3\omega}$, as a function of electrical frequency using the lock-in output voltage as a current source (orange diamonds), and using a Keithley 6221 current source (filled blue circles). At high frequency, using the lock-in voltage output as a current source seems to provide more reliable results. Indeed, the experiment was carried out on a thick sapphire substrate where we expect a linear relation $V_{3\omega} = \mathrm{f}(\ln(\omega))$, until at least 50 kHz.

parison to its specifications. The use of this external current source also required to externally lock its reference frequency to the lock-in amplifier, which, we assume, caused some measured phase jumps at around $3f = 10$ kHz. A similar behavior was reported in Ref. 141, using the same current source. The measured *amplitude* of the third harmonic of the voltage was less prone to such errors, but we found that it still did not behave as expected when using this current source, at higher frequency.

In Figure 2.7, we plot the measured third harmonic of the voltage as a function of electrical frequency, using as a current source, either lock-in 1 output voltage (first measurement, orange diamonds), or the Keithley 6221 current source (second measurement, blue filled circles). When using the voltage output of lock-in 1, the current is calculated using lock-in 2 and the known resistance R_{variable}, as explained above and depicted in Figure 2.6. When using the Keithley 6221 current source, we set the current to be equal to the current that has been calculated using lock-in 2 in the first measurement, such that the amplitude of $V_{3\omega}$ is similar in both measurements. Two conclusions can be drawn from these measurements. First, in both setups, the measured $V_{3\omega}$ are indeed very similar. This means that the current read from lock-in 2 is in excellent agreement with the current provided by the Keithley 6221 current source. Second, the frequency behavior of $V_{3\omega} = \mathrm{f}(\ln(\omega))$ is better for the setup using the lock-in output as a current source, for the following reason. The measurement was performed on a thick sapphire substrate, where we expect $V_{3\omega} = \mathrm{f}(\ln(\omega))$ to be linear, on the frequency range that is studied. From around $f = 10$ kHz, such a linear behavior is no longer observed, which we attribute to problems coming from the current source itself, or the phase-locking between the current source and the lock-in amplifier. Importantly, the frequency at which the voltage diverges from its linear behavior does not seem to be reproducible from sample to sample. Therefore, measurements were preferably performed using the setup shown in Figure 2.6, if the highest frequency that is reached during the experiment is above 10 kHz.

2.2.1.1 Operational amplifier bandwidth

When using an operational amplifier while performing a frequency dependent experiment, the very first step is to ensure that the amplifier bandwidth is large enough to cover the frequency range that will be spanned during the experiment. In particular, since we are interested in measuring the third harmonic ($3f$) of the voltage, the bandwidth should be *at least* three times larger than the frequency range spanned at $1f$ during the measurement. In practice, it is better if the frequency cutoff of the amplifier, commonly referred to as $f_{\text{-3dB}}$ in the literature, is several orders of magnitude higher than the highest frequency we want to reach during the experiment. This is because the cut-off frequency represents the frequency at which the output signal of the amplifier is already attenuated by $\sqrt{2}$ from its nominal value. Therefore we want to be very far from this frequency.

Figure 2.8 displays the gain-frequency and noise-frequency characteristics, often referred to as Bode diagrams, of the operational amplifiers used to build the differential bridge. A stable, constant gain is achieved when the gain is the lowest, but comes with a higher noise. Hence a compromise should be made, according to the experimental needs. In this work, we used two amplifiers with a gain of 2.5 as shown in Figure 2.6, leading to a total gain of $2.5^2 = 6.25$. This corresponds, for each amplifier, to a gain in decibel of $20 \times \log(2.5) \approx 8$ dB. According to the instrument's Bode diagram depicted in Figure 2.8(a), it sets the cutoff frequency between 2-4 MHz, hence the electrical frequency $1f$ should be lower than 0.6-1.3 MHz when reading the third harmonic $3f$ up to 2-4 MHz. This is more than enough for all the measurements carried out in this thesis. What is not displayed, and often not provided on the amplifier datasheet, is the phase-frequency characteristic of the amplifier. It is as well strongly frequency dependent, as any filter, and therefore should be checked carefully. Such characteristics are very general and apply to any amplifier. In particular, it is to be evaluated when using amplifiers to build a home-made voltage-to-current converter that would be as well restricted by a finite bandwidth.

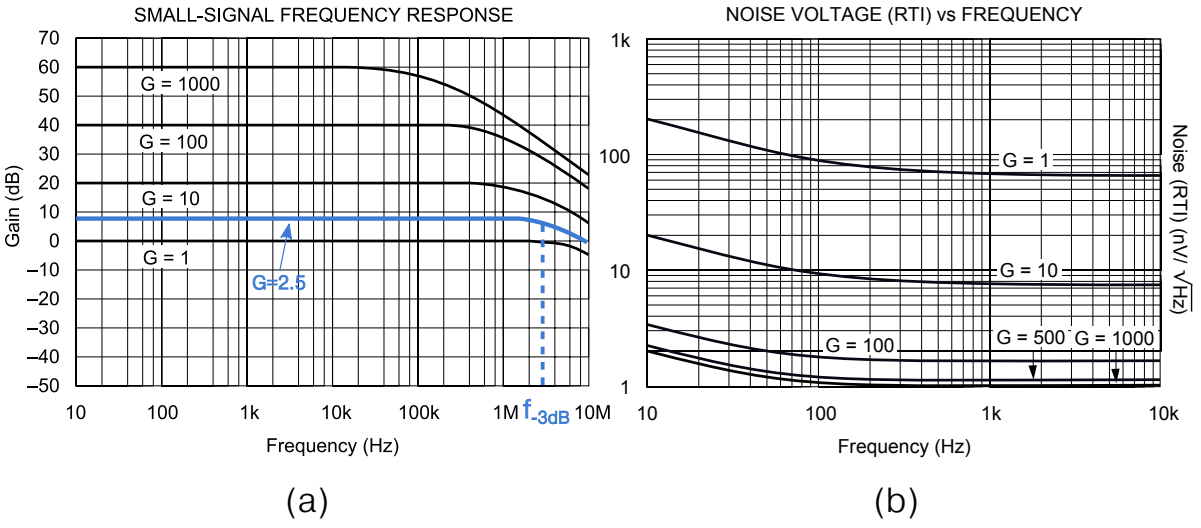

Figure 2.8: (a) Bode diagram of the operational amplifier (model INA103 from Burr-Brown) used to build the differential bridge. The blue line has been drawn by hand to estimate the frequency response of the amplifier for the gain we use. From this estimation, a gain of G = 2.5, corresponding to 8 dB, is estimated to have a frequency cutoff between 2 and 4 MHz. (b) Noise voltage versus frequency for different gains of the amplifier. A lower gain leads to higher noise. Source : https://www.ti.com/lit/ds/symlink/ina103.pdf

Then, strictly speaking about the instrumentation, the upper frequency limit will eventually be dictated by the lock-in frequency bandwidth. In this work, the upper frequency of the lock-in amplifier is 250 kHz. Since it is used both for sourcing the circuit and reading the voltage, it can be used to provide an AC current until frequency $1f = 250/3 \approx 83$ kHz in order to read the voltage at $3f = 250$ kHz.

2.2.1.2 Harmonic distortion

The inherent total harmonic distortion of the instruments, referred to as either THD or THD+N (Total Harmonic Distortion + Noise) is another specification that should be quantified prior to performing a 3ω experiment. It is defined as[5]

$$\text{THD}=\frac{\sqrt{\sum_{n=2}^{\infty} V_{n,\text{rms}}^2}}{V_{1,\text{rms}}}$$

where V_n represents the voltage signal at harmonic n and $V_{1,\text{rms}}$ refers to the rms voltage signal at the fundamental frequency. It should therefore be as small as possible, to prevent any harmonics that are non-thermal to propagate inside the experiment. A parasitic voltage at $3f$ in the first stage of the differential bridge – if its amplitude is equal in both amplifiers – would be removed in the second stage of the bridge. However, a parasitic voltage at $3f$ produced in the second stage of the bridge would be superposed to the thermal $V_{3\omega}$ signal and enters the measurement with no attenuation. For the three amplifiers building the bridge, THD+N $< 0.003\%$ for $f < 20$ kHz.

As mentioned previously, the lock-in amplifier both provides the oscillating current and reads the voltage. Therefore the two specifications that are relevant are distortion from its output voltage (the lock-in internal oscillator) and distortion that is produced when the voltage is read by the lock-in amplifier. The output voltage used to drive the experiment is digitally synthesised using the lock-in Digital to Analog Converter (DAC), and therefore is not a pure sinusoid but rather a stepped approximation to one.[140] It is then filtered to reduce the harmonic distortion to a level of THD=-80 dB at 1kHz and 100 mV_{rms}, which represents 0.01% of the signal.[142] Let us examine how distortion influences the accuracy of the measurement. If the current is not a pure sinusoid, but contains spurious harmonics, we may write it as

$$\begin{aligned} I &= I_1 \cos(2\pi f t) + \sum_{i=2}^{n} I_i \cos(i \times 2\pi f t) \\ &= I_{1f} + \sum_{i=2}^{n} I_{if} \end{aligned}$$

where the summation is performed over the harmonics of the current. This current flows through the following resistances, present in the circuit shown in Figure 2.6 :

$$\begin{aligned} R_{\text{transducer}} &= R_{e,0} + R_{e,0}\beta\Delta T_{2f} = R_{e,0} + R_{2f} \\ R_{\text{variable}} &= R_{e,0} \end{aligned}$$

leading to the following voltage across the transducer :

$$V_{\text{transducer}} = R_{e,0} I_{1f} + R_{2f} I_{1f} + (R_{e,0} + R_{2f}) \sum_{i=2}^{n} I_{if}$$

[5] for THD+N, the noise is taken into account in the numerator and is therefore always higher than the THD.

Only specific harmonics would lead to additional voltages at $3f$. I_{1f} mixes with R_{2f} which produces the main component V_{3f} (in addition to the large ohmic V_{1f}). I_{3f} mixes with $R_{e,0}$, and I_{5f} mixes with R_{2f} producing two harmonics (the sum and the difference) of the voltage, V_{3f} and V_{7f}. All other harmonics of the current would not contribute to V_{3f}. The resulting voltage at $3f$ read across the transducer is therefore :

$$V_{3f,\text{transducer}} = \frac{1}{2}R_{e,0}I_1\beta\Delta T_{2f} + R_{e,0}I_{3f} + \frac{1}{2}R_{e,0}I_5\beta\Delta T_{2f} \tag{2.9}$$

The voltage across the variable resistance, set to match the resistance of the transducer is simply :

$$V_{3f,\text{var.}} = R_{\text{variable}}I_{3f} = R_{e,0}I_{3f}$$

Therefore, after the differential bridge which subtracts both voltages, it reads

$$V_{3f,\text{aft.brdge}} = \frac{1}{2}R_{e,0}I_1\beta\Delta T_{2f} + \frac{1}{2}R_{e,0}I_5\beta\Delta T_{2f}$$

Therefore, when using a differential bridge, only the contribution from I_{5f} enters the experiment and affects the reading at V_{3f}. The error scales as I_{1f}/I_{5f}, which can be estimated using the harmonic distortion, not total, but rather "per harmonic". Using the THD figure provided by the lock-in manufacturer, it is therefore not straightforward to accurately estimate the relative contribution of I_{5f} to $V_{3\omega}$, since it comprises *all* harmonics. To quantify the contribution from I_{5f}, we may use a spectrum analyser to measure V_{5f} produced by the lock-in output (which would translate to I_{5f} since we use the lock-in output voltage as a current source). Such an instrument would remove the first harmonic of the voltage using a notch filter and therefore allocate the maximum of its dynamic reserve to read all other harmonics. We do not possess such instrument and instead, use our lock-in built-in harmonic detection to measure its own distortion. This has the disadvantage of adding error coming from its DAC which also add distortion, and not allocating the instrument maximum dynamic reserve, but is a reasonable conservative estimate. We apply a voltage V_{1f} in its input, and read the resulting voltage at the fifth harmonic, V_{5f}. From this simple experiment, we find that the harmonic distortion at $5f$ varies from 0.0017% at $1f$=20 kHz up to 0.007% at $1f$=50 kHz, for an applied voltage of 1 $V_{1f,\text{rms}}$. Figure 2.9 displays the measured distortion of the lock-in output, per harmonic, for several harmonics and frequencies. Therefore

$$V_{3f} = \frac{1}{2}R_{e,0}I_1\beta\Delta T_{2f} + \frac{1}{2}R_{e,0}I_5\beta\Delta T_{2f} \quad \text{with} \quad \frac{I_5}{I_1} < 7.10^{-5}$$

and the contribution from I_{5f} can be safely neglected.

We note that if the cancellation bridge is omitted, we see from Eq. (2.9) that the relative error coming from I_{3f} scales as

$$\frac{V_{3f,\text{distortion}}}{V_{3f,\text{thermal}}} = \frac{R_{e,0}I_{3f}}{(1/2)R_{e,0}I_{1f}\beta\Delta T} = \frac{I_{3f}}{I_{1f}}\frac{2}{\beta\Delta T} \tag{2.10}$$

Because of small values of β and ΔT, typically $\approx 10^{-3}$ K^{-1} and $\Delta T \approx 0.1 - 3\text{K}$, an extremely low harmonic distortion is needed in order for the contribution of I_5 to V_{3f} to be negligible. For example, for ultra-low distortion generators with THD< -100 dB, in this case $I_{3f}/I_{1f} = 10^{-5}$ and the distortion would account for about 1% of the signal, using $\beta\Delta T = 2.10^{-3}$. For lower $\beta\Delta T$ values, the contribution would increase. This, in addition to the removal of V_{1f}, suggests that a nullifying bridge is recommended to perform an accurate measurement.

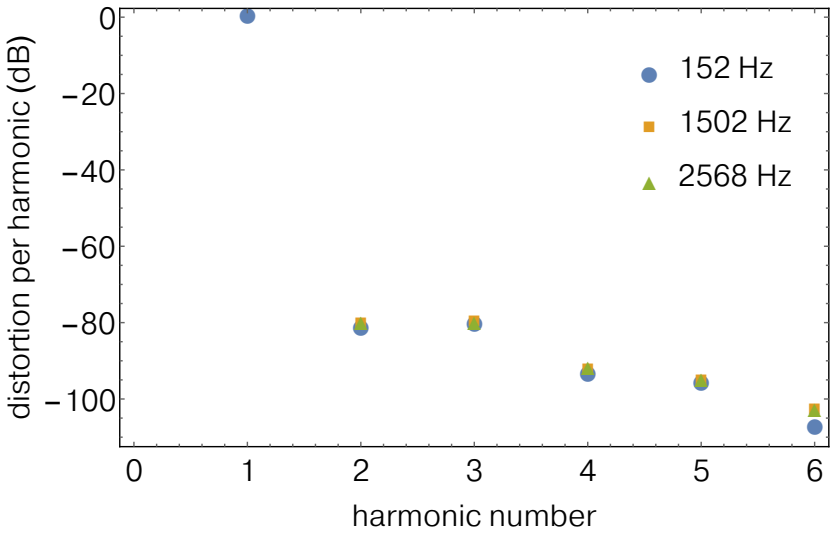

Figure 2.9: Harmonic distortion per harmonic of the lock-in amplifier measured by plugging its output voltage to its input and reading the contribution from different harmonics using its own demodulator. The applied voltage is $1V_{\mathrm{rms}}$. This measurement agrees well with the specified THD of -80 dB.

Lastly, as we have explained in the previous part, the lock-in ADC produces distortion as well, with THD = -90 dB at 1 kHz, which represents 0.0032% of the signal (which was somehow taken into account when measuring its own distortion). When compared to other sources of uncertainty present in a typical experiment, the distortion from all instruments is relatively small and therefore is neglected in this work.

2.2.1.3 Stray capacitances and inductances

The aforementioned limitations are only given from instruments datasheets. In practice, we have found that high frequency discrepancies, appearing before instrumentation limits, are mainly due to the presence of stray capacitances (C) and/or inductances (L) in the electrical circuit. A simple model of the differential bridge, containing capacitances and inductances is presented in Figure 2.10a. The electrical impedances $Z_{e,1}$ and $Z_{e,2}$ which take into account these capacitances and inductances are written as :

$$Z_{e,1} = i\omega L_1 + \frac{R_1}{1 + i\omega R_1 C_1} \text{ and } Z_{e,2} = i\omega L_2 + \frac{R_2}{1 + i\omega R_2 C_2} \tag{2.11}$$

The current I flowing through the circuit is related to the total electrical impedance of the circuit. Following the notation of Figure 2.10a :

$$I = \frac{V_{\mathrm{in}}}{Z_{e,1} + Z_{e,2} + \sum R_{\mathrm{leads}}} \tag{2.12}$$

where the resistances coming from the electrical leads (including electrical contact resistances) are taken into account in $\sum R_{\mathrm{leads}}$. V_{in} is the voltage used to source the circuit, typically $5\mathrm{V}_{\mathrm{rms}}$ using the lock-in amplifier's output voltage.

In order to estimate capacitances and inductances present in the circuit, we have performed voltage measurements as a function of electrical frequency at two different locations in the circuit, denoted V_{A} and V_{B} in Figure 2.10a. We chose these two locations to read the voltage because V_{A} is the voltage read across a known resistance to infer the current flowing through the

circuit and V_{B} is the voltage read at the end of the differential bridge during a 3ω experiment, thus providing $V_{3\omega}$. Fitting the amplitude and phase of the recorded voltages permits, at least qualitatively, to confirm the electrical circuit proposed in Figure 2.10a. Since the impedance is complex, the amplitude $|V_{\mathrm{i}}|$ and phase ϕ_i of the AC voltage are written as :

$$|V_{\mathrm{A}}| = |I \times Z_{\mathrm{e},1}| \qquad |V_{\mathrm{B}}| = |I \times (Z_{\mathrm{e},2} - Z_{\mathrm{e},1})| \tag{2.13}$$

$$\phi_A = \arg\left(I \times Z_{e,1}\right) \qquad \phi_B = \arg\left(I \times (Z_{e,2} - Z_{e,1})\right) \tag{2.14}$$

The measurements of the first harmonic of the voltage and their best fit using Equations (2.11)-(2.14) are displayed in Figure 2.10b. Every filter of the lock-in amplifier is turned off and the lock-in input coupling is set to "DC". R_1 is the variable electrical resistance and therefore can be tuned at will : we used three different values of R_1 to produce reliable measurements ($R_1 = R_2$, $R_1 > R_2$ and $R_1 < R_2$). R_2 is the electrical resistance of a transducer from a real sample that is mounted inside our probe. This allows to quantify the capacitances and inductances that are present during a real experiment using exactly the same conditions and wiring. The resistance of the transducer is measured to be $\mathrm{R}_2 = 130\ \Omega$. The agreement between the simple model displayed in Figure 2.10a and the measurements depicted in Figure 2.10b is qualitatively satisfying. However, we could not reliably fit all the measured values (amplitude and phase from V_{A} and V_{B}) with the same pair of C_1 and C_2. In principle the same pair of C_1 and C_2 should fit every measurement if the proposed model was the good one. In our case, the values of capacitances that best fit our data need to be adjusted between 1 to 4 nF. Inductances were changed from a few nH to tens of μH with no effect, therefore we set L_1=L_2=0. We concluded that the frequency behavior of the impedance was mostly caused by stray capacitances rather than inductances.

The agreement between data and the model is not perfect, especially for ϕ_B, however it is expected since the proposed circuit is relatively simple. A more detailed model should be used for a better description, taking the frequency response of the three individual amplifiers into account, for example. We will not venture into doing so in this work, since the global picture seems to be well captured using this simple model. Besides, as measurements were performed using a real sample which produces frequency-dependent signals, the results shown in Figure 2.10b do not distinguish thermal signals (from the transducer's heat capacity for example) from purely electrical signals (parasitic capacitances). To remove this ambiguity, similar measurements were carried out, replacing the transducer (with resistance R_1) with a stable, known resistance, with negligible temperature coefficient of resistance. The results were similar, comforting us with the parasitic origin of the measured frequency behavior.

One important result from these measurements is the frequency response of the current flowing across the circuit. Amplitude and phase deviate from their "ideal" behavior around 30-40 kHz, which is not something desirable for our study. As a consequence, we have monitored in this work the frequency response of the current, using lock-in 2 as depicted in Figure 2.6. The fitting of thermal properties is carried out in a frequency window where the current is stable with frequency.

Before moving on to the heat transfer model that is used to infer thermal properties in 3ω measurements, we describe the environment into which all the samples measured in this work have been mounted.

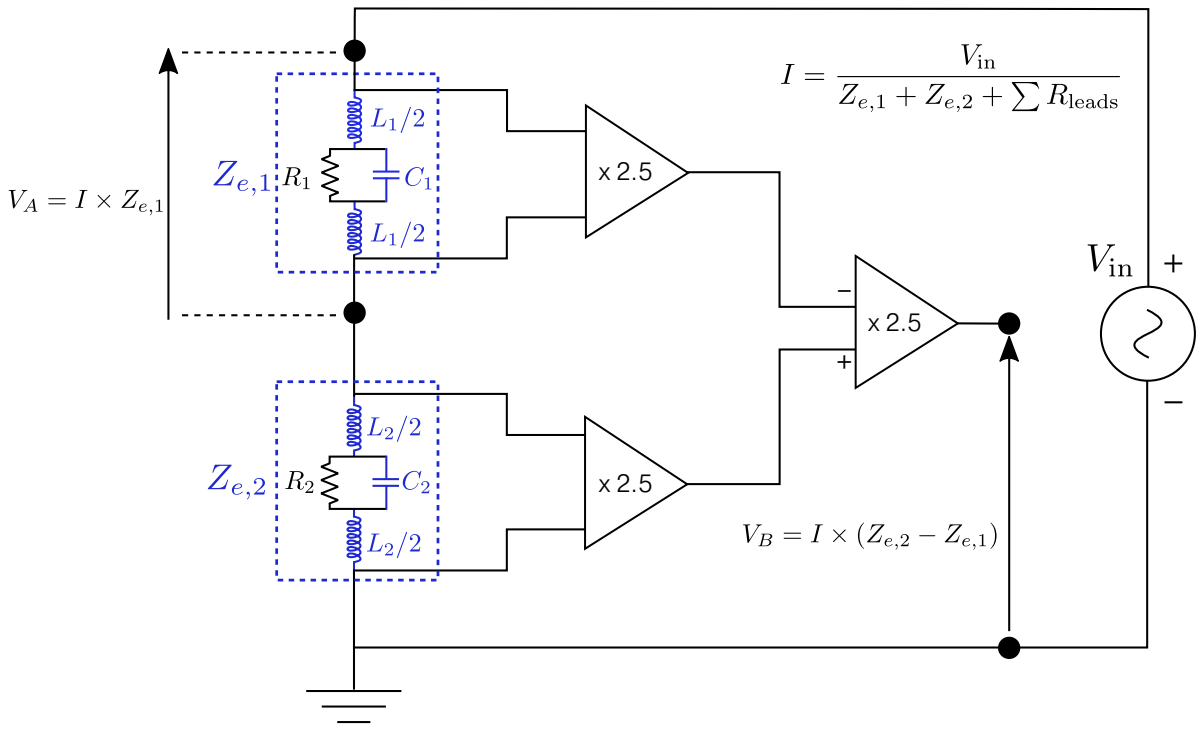

(a)

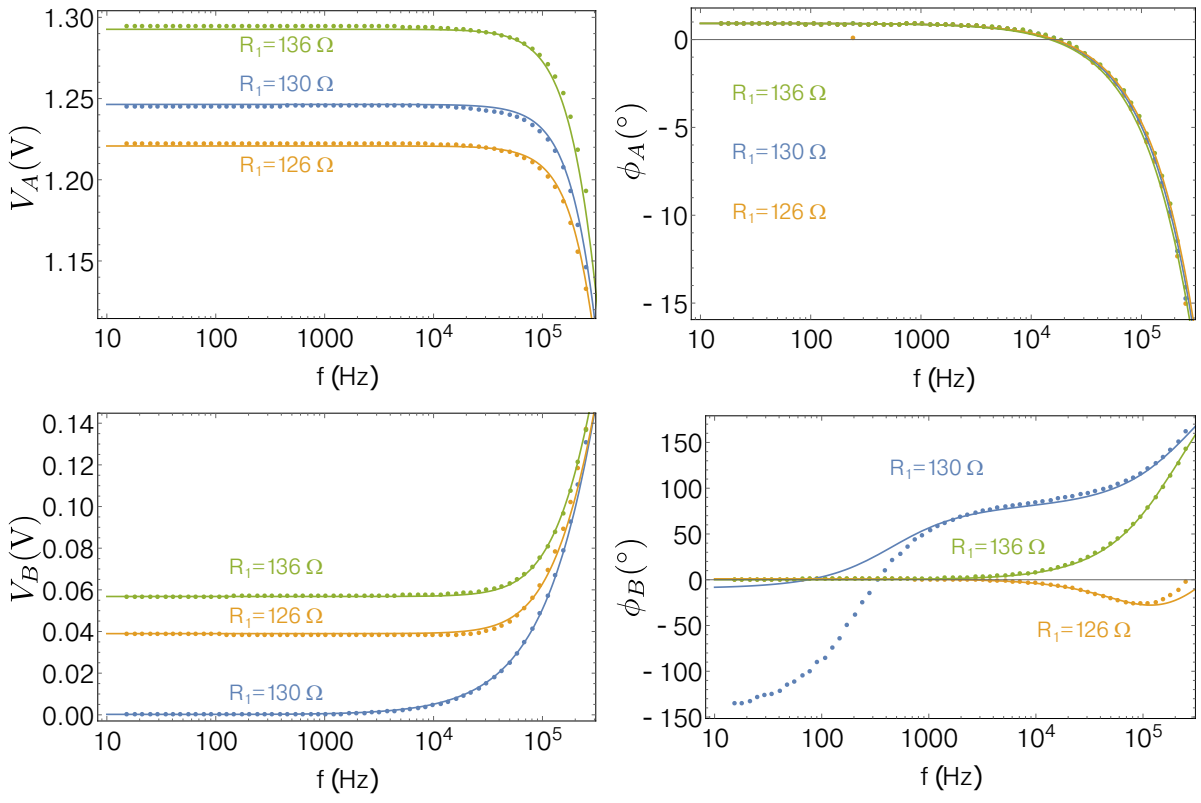

(b)

Figure 2.10: (a) Proposed electrical circuit accounting for stray inductances and capacitances. V_A and V_B are measured using lock-in amplifiers. (b) Solid circles are the amplitude and phase response of the first harmonic of the voltage, measured as depicted in the electrical circuit above. Solid lines are the expected voltage computed using Eq. (2.11) and Eq. (2.12). The overall agreement is qualitatively good with the proposed model for capacitances present in the circuit, using the measured value for the transducer thermometer $R_2 = 130\ \Omega$, C_1 and C_2 between 1 to 4 nF and $L_1 = L_2 = 0$.

2.2.2 Sample mounting

The 3ω method can be used in quite a large temperature window. It will be constrained mostly by the TCR of the transducer used to perform the experiment. When using a metallic transducer such as gold, aluminium or platinum, the TCR will decrease towards zero at temperature around 10-30 K and hence the 3ω method won't be applicable anymore. At very high temperature, the TCR won't vanish but will be increasingly smaller because of the larger resistance at high temperature. Another consideration to take into account at higher temperature (say, $> 500°C$) is the possible diffusion of the metallic transducer material into the layer underneath that could hinder the measurement.[143] Lastly, the radiation will play a role at extremely elevated temperatures ($> 750°C$), especially for low diffusivity materials that radiate out most of the flux coming from the transducer – though it can be accurately quantified.[119] Most of the results of this thesis were performed in the temperature range of 90-320 K where liquid nitrogen have been used to cool down the system.

The setup used in this thesis is summed up in Figure 2.11. Samples were mounted onto a sample holder that is shown in Figure 2.11(b). We used silver paint or resist on their backside to make sure they were well attached. Silver paint is preferred for better thermal coupling (it has a large thermal conductivity), but when removing the samples, a large amount of small silver particles spread on the sample holder – eventually leading to shortcuts between the sample holder's electrical pads. We then used mechanical clips, pressing samples from the top to make them hold tightly.

To connect the transducer pads to the sample holder, we did not use micro-bonding since it was shown (thanks to the previous PhD student Yanqing Liu) to break thin electrically insulating layers deposited on top of the samples (e.g. Al_2O_3 deposited by Atomic Layer Deposition). Instead, we used a softer approach, spreading a small amount of electrically conductive silver paint on the pads, and then depositing aluminium wires (with diameter ≈ 25 μm) onto it. After annealing at $\approx 100°C$, the silver paint dried and the contacts were working. Other useful ingredients were shake-free hands and patience.

Once the circular sample holder is screwed to the main body of the probe (Figure 2.11(a-b)), the sample stage is then covered using a copper shield, preventing from radiations as depicted in Figure 2.11 (d). The temperature of the probe is regulated using a resistive heater and a commercially available Cernox© thermometer, using a PID controller (MGC3 from Institut Néel). The thermal contact between the probe and the sample holder is ensured using four gold screws (Figure 2.11(b)) that maintain the body of the probe to the sample holder through four copper contacts (Figure 2.11(a)). As depicted in Figure 2.11(e), a stainless steel cover is attached to the body of the probe and then sealed using an indium wire and thermal grease. The probe is then put under vacuum using a turbo pumb, until it reaches $\approx 10^{-5}$ mbar. All the leads are passing through the length of the probe, and then connected to 6-pins Jaeger sockets. The connections between the probe and the instruments (lock-in and operational amplifiers) were made using home-made adaptors (from Jaeger to BNC jacks), and commercially available BNC cables.

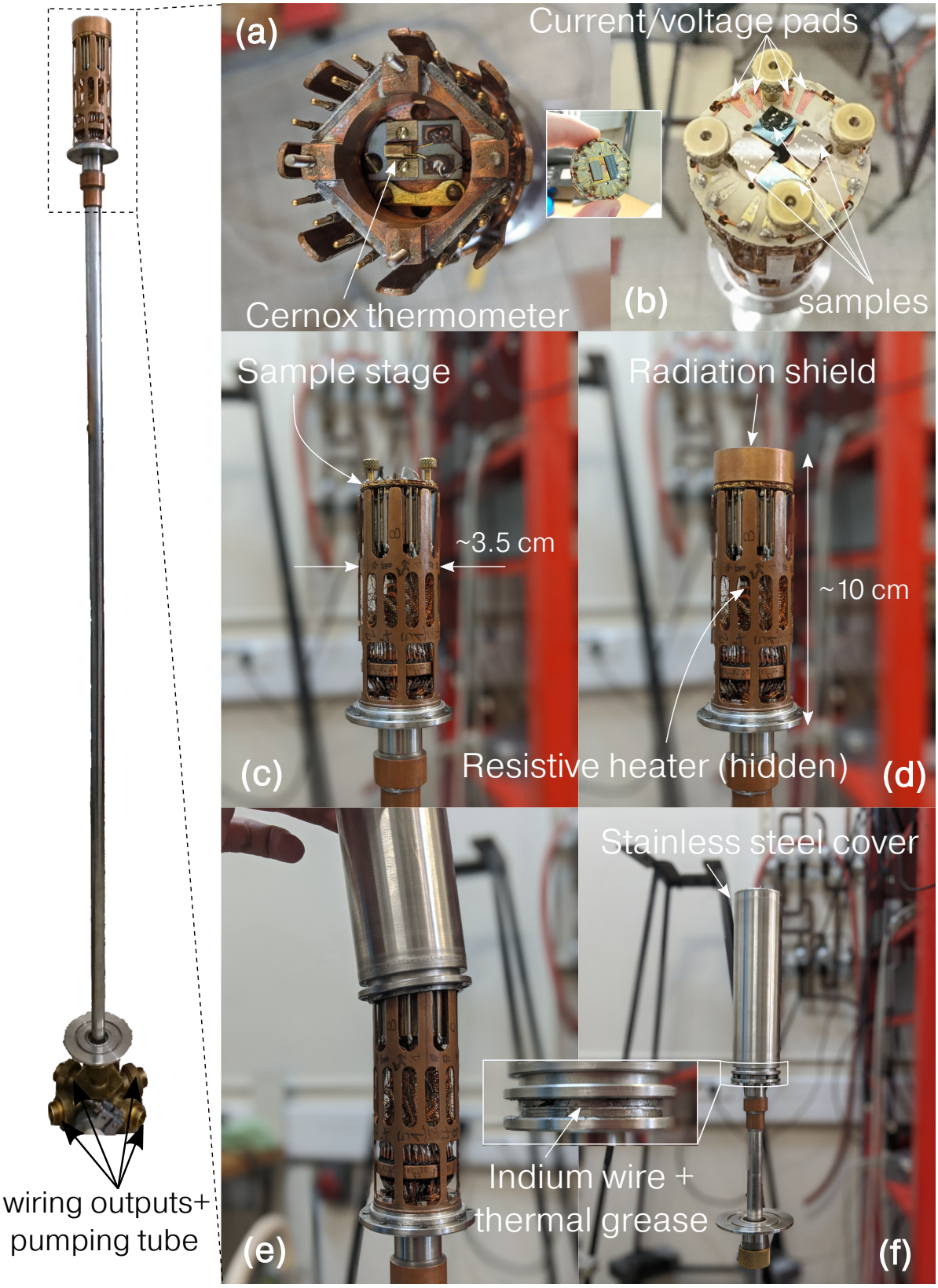

Figure 2.11: Pictures of the instrumentation used for the sample mounting. The probe is shaped as a long cylindrical tube to fit inside a cryostat. Samples are attached on a circular sample holder as seen on (b) that can be removed from the probe. Gold pads, highlighted in red in (b) are used to electrically connect the transducers from the sample to the probe. Wires then go along the length of the tube and come out in Jaeger sockets. 4×4 pads are present, to measure four samples (I^+, I^-, V^+, V^-). The probe's temperature is regulated using a Cernox thermometer (2-320 K) and a resistive heater, using a PID controller. (d) After screwing the copper shield to the sample holder, a stainless steel cover is screwed and sealed using an indium wire (e-f). The probe is then put under vacuum using a turbo pump.

3 Heat transfer model for 3ω experiments

Once all the troubles related to the measurement of the temperature oscillation have been worked out and the measurement performed, the next natural step is to compare experimental data to a thermal model, allowing to extract thermal informations about the system of interest. Thermal models of increased accuracy and complexity have been derived in the last two decades for the general 3ω geometry, for a semi-infinite substrate[119], a film-on-substrate system[144], and a multilayer system.[123,145,146] Heat conduction within the heater is neglected in these models – it has been considered later analytically in Refs. 147,148.

The purpose of this chapter is to provide a step by step derivation of the temperature rise sensed by a transducer deposited on top of system of interest when heated periodically. We will start from the simple case of a bare substrate and then move on to the more general case of a multilayer system. From these models, we will explain how to extract thermal informations about the system, from the thermal conductivity of the substrate to that of the films, and thermal boundary resistances that are inherently present between layers. Additionally, the "slope method" and "differential method" for determining the substrate and film's thermal conductivities are described, and the conditions for their use are detailed following the work of Borca-Tasciuc *et al.*.[123]

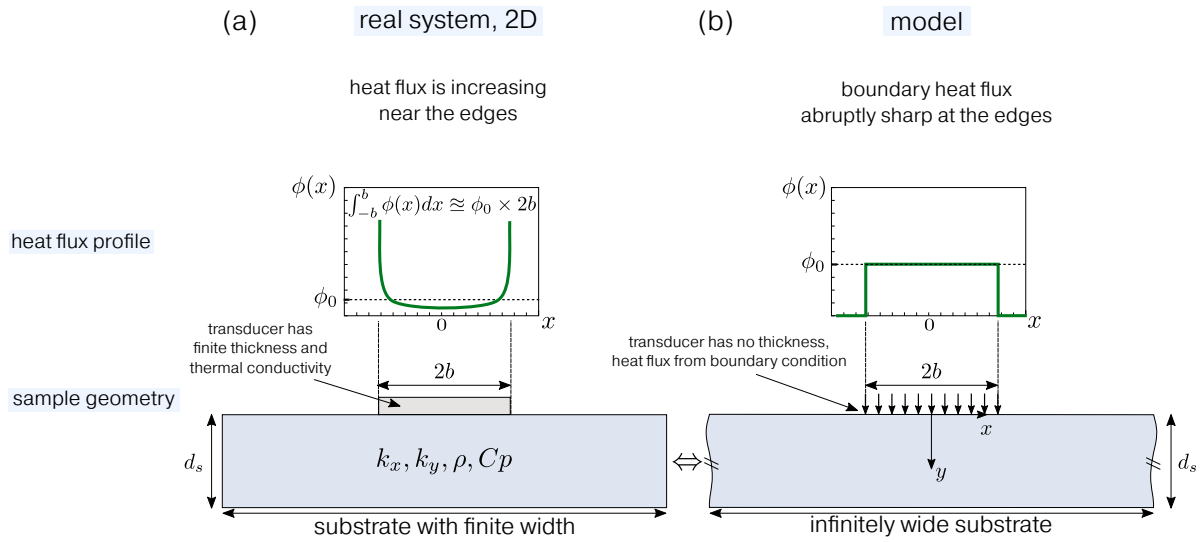

Figure 3.1: (a) Schematic of the system that is studied (b) and its approximation. One important assumption concerns the heat flux, taken to be constant along the heater width which might not be the case for a heater with finite thickness and non-zero thermal conductivity. The shape of the flux in the real system (a) is sketched by hand, following calculations provided in Ref. 147. Note that it can be recovered using FEM as well.

3.1 Transducer on substrate

Solving the heat equation

In two dimensions, temperature inside an anisotropic material with no internal heat generation evolves with respect to time and position following the heat diffusion equation :

$$\rho C_p \frac{\partial T(x,y,t)}{\partial t} = k_x \frac{\partial^2 T(x,y,t)}{\partial x^2} + k_y \frac{\partial^2 T(x,y,t)}{\partial y^2} \tag{3.1}$$

where ρ is the material density in g.m^{-3}, C_p the specific heat in J.g^{-1}.K^{-1}, T the temperature in K, and k_x and k_y are the in-plane and cross-plane components of the thermal conductivity in W.m^{-1}.K^{-1}, respectively. The geometry of the problem is shown in Figure 3.1. Dividing Eq. (3.1) by k_y we get

$$\frac{\rho C_p}{k_y} \frac{\partial T(x,y,t)}{\partial t} = k_{xy} \frac{\partial^2 T(x,y,t)}{\partial x^2} + \frac{\partial^2 T(x,y,t)}{\partial y^2} \tag{3.2}$$

where we have defined $\frac{k_x}{k_y} = k_{xy}$, often referred to as the thermal anisotropy ratio or simply thermal anisotropy. Applying an oscillating current at angular frequency ω_e leads to Joule heating at frequency $\omega = 2 \times \omega_e$. Because the response in the thermal domain is linear[138], this periodic Joule heating at frequency ω induces temperature oscillation at the same frequency. Therefore, we write

$$T(x,y,t) = T(x,y)e^{i\omega t} \tag{3.3}$$

Plotting Eq.(3.3) in Eq.(3.2) leads to

$$\frac{\rho C_p}{k_y} i\omega T(x,y)e^{i\omega t} = k_{xy} \frac{\partial^2}{\partial x^2} T(x,y)e^{i\omega t} + \frac{\partial^2}{\partial y^2} T(x,y)e^{i\omega t}$$

dividing by $e^{i\omega t}$ and rearranging

$$k_{xy}\frac{\partial^2}{\partial x^2}T(x,y)+\frac{\partial^2}{\partial y^2}T(x,y)-\frac{\rho C_p}{k_y}i\omega T(x,y)=0$$

We have reduced the initial three variables (x,y,t) partial differential equation to a two variables (x,y) partial differential equation. To further simplify this equation, we take its Fourier Transform (FT) with respect to x[137]:

- integrating by parts, the first term becomes

$$\int_{-\infty}^{\infty}k_{xy}\frac{\partial^2}{\partial x^2}T(x,y)e^{-i\lambda x}dx=\left[k_{xy}\frac{\partial T(x,y)}{\partial x}e^{-i\lambda x}\right]_{-\infty}^{\infty}+i\lambda\int_{-\infty}^{\infty}k_{xy}\frac{\partial T(x,y)}{\partial x}e^{-i\lambda x}dx$$

  The first term of the right hand side vanishes as $\partial_x T(x,y)_{x\to\pm\infty}=0$. We are left with

$$\begin{aligned}i\lambda\int_{-\infty}^{\infty}k_{xy}\frac{\partial T(x,y)}{\partial x}e^{-i\lambda x}dx&=k_{xy}i\lambda\left\{\left[T(x,y)e^{-i\lambda x}\right]_{-\infty}^{\infty}+i\lambda\int_{-\infty}^{\infty}T(x,y)e^{-i\lambda x}dx\right\}\\&=k_{xy}(i\lambda)^2\int_{-\infty}^{\infty}T(x,y)e^{-i\lambda x}dx\\&=k_{xy}(i\lambda)^2\widehat{T}(\lambda,y)\end{aligned}$$

  where the notation $\widehat{T}(\lambda,y)$ denotes the Fourier transform with respect to x of the function $T(x,y)$ in λ-space.

- the second term contains a derivative with respect to y, we put it outside the integral, leading to

$$\int_{-\infty}^{\infty}\frac{\partial^2}{\partial y^2}T(x,y)e^{-i\lambda x}dx=\frac{\partial^2}{\partial y^2}\widehat{T}(\lambda,y)$$

- similarly, the third term is

$$i\omega\frac{\rho C_p}{k_y}\int_{-\infty}^{\infty}T(x,y)e^{-i\lambda x}dx=i\omega\frac{\rho C_p}{k_y}\widehat{T}(\lambda,y)$$

At this point, we emphasize that the Fourier Transform in the x direction is carried out from $-\infty$ to ∞, and we assumed $T(x,y)_{x\to\infty}=0$. This means that the problem is considered infinite along the x direction. It is a reasonable assumption, since the heat source is usually tens of microns large, whereas samples usually are about a centimeter large. Most importantly, the thermal penetration depth, as will be discussed later on, is at most a few millimeters. End effects in the x direction are thus neglected and the problem can be modeled as infinite along the x direction, as shown in Figure 3.1(b).

The new equation to solve is

$$\frac{\partial^2}{\partial y^2}\widehat{T}(\lambda,y)-\underbrace{\left(k_{xy}\lambda^2+i\omega\frac{\rho C_p}{k_y}\right)}_{\gamma^2}\widehat{T}(\lambda,y)=0 \tag{3.4}$$

The equation is now an ordinary, homogeneous, linear differential equation. The general solution is of the form :

$$\widehat{T}(\lambda,y)=C_1e^{\gamma y}+C_2e^{-\gamma y} \tag{3.5a}$$

$$\gamma=\sqrt{k_{xy}\lambda^2+i\omega\frac{\rho C_p}{k_y}} \tag{3.5b}$$

To determine C_1 and C_2, we need two boundary conditions. The boundary condition at $y = 0$ is a prescribed heat flux[1] :

$$-k_y \left.\frac{\partial T(x,y)}{\partial y}\right|_{y=0} = \phi(x, y = 0)$$

At the bottom of the substrate $y = d_\mathrm{s}$, the boundary condition is written as (for adiabatic or isothermal boundary conditions) :

$$\text{adiabatic b.c. : } \left.\frac{\partial T(x,y)}{\partial y}\right|_{y=d_\mathrm{s}} = 0$$

$$\text{isothermal b.c. : } T(x,y)|_{y=d_\mathrm{s}} = 0$$

We remind here that we are dealing with the oscillating part of the temperature. Hence, the isothermal boundary condition (Dirichlet boundary condition, b.c.) set to zero means that there is no more oscillation at $y = d_s$, but of course the sample's temperature is not zero. Adiabatic boundary condition (Neumann boundary condition) refers to a perfectly insulated surface (the substrate's bottom), across which the heat flux is zero. Taking the Fourier Transform of the boundary condition at $y = 0$ leads to

$$-k_y \left.\frac{\partial \widehat{T}(\lambda,y)}{\partial y}\right|_{y=0} = \widehat{\phi}(\lambda, 0)$$

where $\widehat{\phi}(\lambda, 0)$ is the FT of $\phi(x, 0)$. At $y = d_s$, it gives

$$\text{adiabatic b.c. : } \left.\frac{\partial \widehat{T}(\lambda,y)}{\partial y}\right|_{y=d_\mathrm{s}} = 0$$

$$\text{isothermal b.c. : } \left.\widehat{T}(\lambda,y)\right|_{y=d_\mathrm{s}} = 0$$

The first boundary condition leads to

$$\begin{aligned} -k_y C_1 \gamma\, e^{\gamma y}|_{y=0} + k_y C_2 \gamma\, e^{\gamma y}|_{y=0} &= \widehat{\phi}(\lambda, 0) \\ \gamma k_y \left(1 - \frac{C_1}{C_2}\right) &= \frac{\widehat{\phi}(\lambda, 0)}{C_2} \end{aligned}$$

while the second one gives

$$\begin{aligned} \text{adiabatic b.c. : } C_1\gamma e^{\lambda d_\mathrm{s}} - C_2\gamma e^{-\lambda d_\mathrm{s}} = 0 \Leftrightarrow \frac{C_1}{C_2} &= +e^{-2\gamma d_\mathrm{s}} \\ \text{isothermal b.c. : } C_1 e^{\lambda d_\mathrm{s}} + C_2 e^{-\lambda d_\mathrm{s}} = 0 \Leftrightarrow \frac{C_1}{C_2} &= -e^{-2\gamma d_\mathrm{s}} \end{aligned}$$

Hence, we deduce

$$\begin{aligned} \text{adiabatic b.c. : } \widehat{T}(\lambda, y) &= \frac{\widehat{\phi}(\lambda)}{\gamma k_y} \left(e^{-\gamma y} + e^{-2\gamma d_\mathrm{s}} e^{\gamma y}\right) \left(1 - e^{-2\gamma d_\mathrm{s}}\right)^{-1} \\ \text{isothermal b.c. : } \widehat{T}(\lambda, y) &= \frac{\widehat{\phi}(\lambda)}{\gamma k_y} \left(e^{-\gamma y} - e^{-2\gamma d_\mathrm{s}} e^{\gamma y}\right) \left(1 + e^{-2\gamma d_\mathrm{s}}\right)^{-1} \end{aligned}$$

[1] From now on, we will discard the time dependence of the heat flux for ease of reading, and set $\phi(x, y = 0, t) \equiv \phi(x, y = 0)$

We still have to express the quantity $\widehat{\phi}(\lambda,0)$, the Fourier Transform of the heat flux $\phi(x,0)$. Assuming a sharp heat flux from the heater of width $2b$, as displayed in Figure 3.1(b), we write

$$\phi(x,0) = \begin{cases} \phi_0 & \text{if } -b < x < b \\ 0 & \text{otherwise} \end{cases}$$

which is the definition of a Heaviside function (or rectangular function). In other words, we assume that the heat flux is evenly entering over the width of the transducer, and that it is abruptly sharp at its edges. The Fourier Transform is then

$$\widehat{\phi}(\lambda,0) = 0 + \int_{-b}^{b} \phi_0 e^{-i\lambda x} dx + 0 = \left[\frac{\phi_0 e^{-i\lambda x}}{-i\lambda}\right]_{-b}^{b} = \frac{2\phi_0 \sin(\lambda b)}{\lambda} \tag{3.6}$$

In order to recover our function $T(x,y)$, we take the inverse Fourier Transform of $\widehat{T}(\lambda,y)$:

$$\begin{aligned} T(x,y) &= \frac{1}{2\pi}\int_{-\infty}^{\infty} \widehat{T}(\lambda,y) e^{i\lambda x} d\lambda \\ &= \frac{1}{2\pi}\int_{-\infty}^{\infty} \frac{2\phi_0 \sin(\lambda b)}{\lambda\gamma k_y} \frac{\left(1 \pm e^{-2\gamma(d_s - y)}\right)}{(1 \mp e^{-2\gamma d_s})} e^{-\gamma y} e^{i\lambda x} d\lambda \end{aligned}$$

Omitting the time-dependent part ($e^{i\omega t}$), this is the general solution for the temperature distribution in two dimensions inside a material of thickness d_s, with constant heat flux ϕ_0 applied at $y = 0$ over the width $-b < x < b$. Signs depend upon the boundary condition at the bottom of the material (+ and − for adiabatic, − and + for isothermal).

3.1.1 What is sensed by the transducer

The transducer, both providing heat to the system and measuring the temperature oscillation, is deposited on top of the material of interest. Hence, we are interested in what is happening at $y = 0$, following the geometry shown in Figure 3.1 :

$$\begin{aligned} T(x,y=0) &= \frac{1}{2\pi}\int_{-\infty}^{\infty} \frac{2\phi_0 \sin(\lambda b)}{\lambda\gamma k_y} \frac{\left(1 \pm e^{-2\gamma d_s}\right)}{(1 \mp e^{-2\gamma d_s})} e^{i\lambda x} d\lambda \\ &= \frac{1}{2\pi}\int_{-\infty}^{\infty} \frac{2\phi_0 \sin(\lambda b)}{\lambda\gamma k_y} \tanh^a(\gamma d_s) e^{i\lambda x} d\lambda \end{aligned}$$

$$\text{with } a = \begin{cases} -1 & \text{adiabatic b.c.} \\ 1 & \text{isothermal b.c.} \end{cases}$$

For a semi-infinite substrate, i.e. letting $d_s \to \infty$, it reduces to

$$\begin{aligned} T(x,y=0) &= \frac{1}{2\pi}\int_{-\infty}^{\infty} \frac{2\phi_0 \sin(\lambda b)}{\lambda\gamma k_y} e^{i\lambda x} d\lambda \\ T(x,y=0) &= \frac{P}{\pi l_h b k_y}\int_{0}^{\infty} \frac{\sin(\lambda b)}{\lambda\gamma} \cos(\lambda x) d\lambda \end{aligned} \tag{3.7}$$

where we used the definition of the heat flux ϕ_0 produced by Joule heating :

$$\phi_0 = \frac{P}{2b \times l_h} = \left[\text{W.m}^{-2}\right]$$

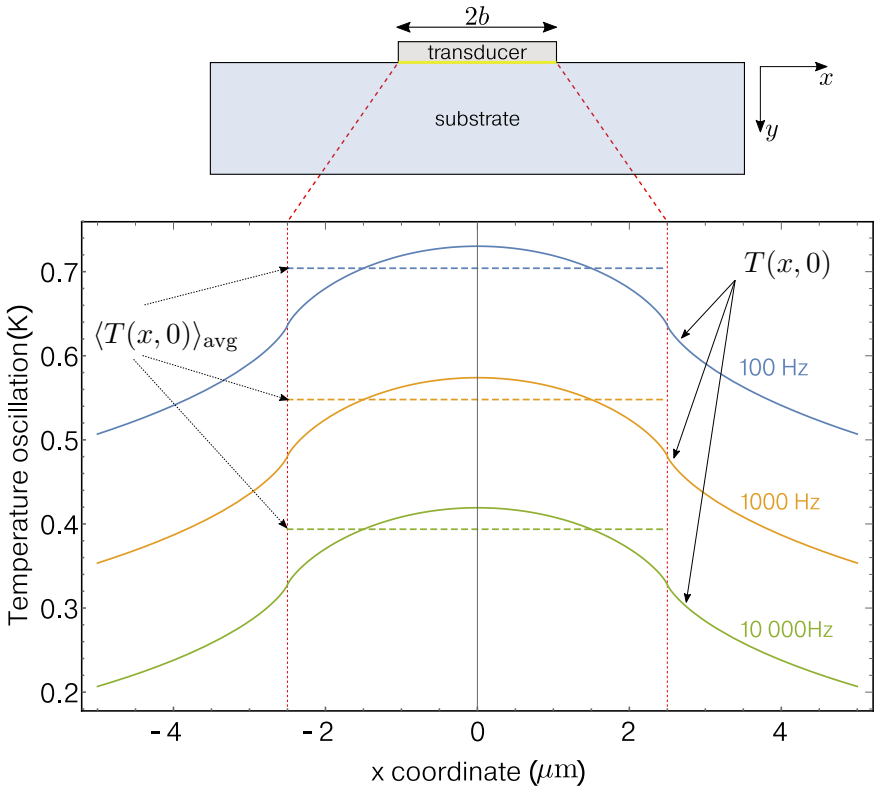

Figure 3.2: Temperature oscillation amplitude at $y = 0$, as a function of lateral coordinate x, plotted for different frequencies using $2b = 5\mu$m. Solid lines represent the amplitude of the temperature oscillation computed using Eq. (3.7) whereas dashed, constant lines represent the spatially averaged temperature oscillation computed using Eq. (3.9). We remind that the present model assumes a constant heat flux at the heater/substrate interface along the heater width.

l_h refers to the length of the transducer[2], $2b$ its width and $P = R_{e,0} I_1^2/2 = R_{e,0} I_{1,\mathrm{rms}}^2$ is the electrical power. We underline that the heater's length l_h only enters the calculation when coupled to the dissipated power P, as can be noticed above. Since the thermal model is two dimensional, the effect of the heater's length on the temperature oscillation should not enter the calculation, this 2D model actually assumes that the heater is infinitely long. Therefore, it makes more sense to display the power *per unit length*, which we write P_l, with units of W/m.

By plotting Eq. (3.7) as a function of lateral coordinate x, as depicted in Figure 3.2, we observe the effect of the transducer width on the temperature profile at $y = 0$. Experimentally, we only have access to the spatially averaged value of the temperature oscillation when measuring the transducer's resistance oscillation. In the present two dimensional model, we assume the transducer to have no thickness, i.e. we neglect heat conduction within it. This is implicitly assumed since the heat source only appears as a heat flux boundary condition.

[2]Importantly, the length that is considered to calculate the power per unit length P_l should be the same length that is used to measure the resistance of the heater/thermometer. Therefore in a 4-wire configuration, if the resistance is read across the inner voltage leads of the thermometer, the power per unit length is then calculated by considering the distance between the inner voltage leads rather than the full length of the heater/thermometer.

Therefore, we express the spatial average of the temperature only over its width :

$$\begin{aligned}
\langle T(x,0)\rangle_{\text{avg}} &= \frac{1}{2b}\int_{-b}^{b}\{T(x,0)\}\,dx \\
&= \frac{1}{2b}\int_{-b}^{b}\left\{\frac{1}{2\pi}\int_{-\infty}^{\infty}\frac{2\phi_0\sin(\lambda b)}{\lambda\gamma k_y}\tanh^a(\gamma d_{\text{s}})e^{i\lambda x}d\lambda\right\}dx \\
&= \frac{1}{2\pi}\int_{-\infty}^{\infty}\frac{2\phi_0\sin(\lambda b)}{\lambda\gamma k_y}\tanh^a(\gamma d_{\text{s}})\frac{1}{2b}\int_{-b}^{b}e^{i\lambda x}dxd\lambda \\
&= \frac{1}{2\pi}\int_{-\infty}^{\infty}\frac{2\phi_0\sin(\lambda b)}{\lambda\gamma k_y}\tanh^a(\gamma d_{\text{s}})\frac{1}{2b}\frac{2\sin(\lambda b)}{\lambda}d\lambda \\
&= \frac{\phi_0}{\pi k_y}\int_{-\infty}^{\infty}\frac{\sin^2(\lambda b)}{\gamma\lambda^2 b}\tanh^a(\gamma d_{\text{s}})d\lambda \\
&= \frac{2\phi_0}{\pi k_y}\int_{0}^{\infty}\frac{\sin^2(\lambda b)}{\gamma\lambda^2 b}\tanh^a(\gamma d_{\text{s}})d\lambda
\end{aligned}$$

The temperature rise sensed by the transducer dissipating inside a material of thickness d_{s} with cross plane thermal conductivity k_y and anisotropy k_{xy} is then

$$\langle T\rangle = \frac{P_l}{\pi k_y}\int_0^{\infty}\frac{\sin^2(\lambda b)}{(\lambda b)^2}\frac{\tanh^a\left(\sqrt{k_{xy}\lambda^2+i\omega\frac{\rho C_p}{k_y}}d_{\text{s}}\right)}{\sqrt{k_{xy}\lambda^2+i\omega\frac{\rho C_p}{k_y}}}d\lambda \tag{3.8}$$

with

$$a = \begin{cases} -1 & \text{adiabatic b.c.} \\ 1 & \text{isothermal b.c.} \end{cases}$$

where we remind that b.c. stands for the boundary condition at the bottom of the substrate (at the sample holder/sample interface). For a semi-infinite substrate, i.e. letting $d_s \to \infty$, it reduces to

$$\langle T\rangle = \frac{P_l}{\pi k_y}\int_0^{\infty}\frac{\sin^2(\lambda b)}{(\lambda b)^2}\frac{1}{\sqrt{k_{xy}\lambda^2+i\omega\frac{\rho C_p}{k_y}}}d\lambda \tag{3.9}$$

which, upon setting $k_{xy}=1$, corresponds to the solution derived by Cahill.[119]

3.1.2 Extracting the substrate's thermal conductivity

Even though numerical integration softwares allow to evaluate a large variety of integrals of increased complexity, the derived expression for the temperature oscillation amplitude (Eq.(3.9)) is not the most widely used in the literature. A more attractive form of Eq.(3.9) is used most of the time out of simplicity and to avoid numerical integration. Besides, it gives a clear picture on how to extract the thermal conductivity of the substrate that is studied. Let us write Eq.(3.9) in a more appealing form. Starting off with Eq.(3.9) where, for ease of reading, we use the previous definition $q^2 = i\omega\rho C_p/k_y$:

$$\langle T\rangle = \frac{P_l}{\pi k_y}\int_0^{\infty}\frac{\sin^2(\lambda b)}{(\lambda b)^2}\frac{1}{\sqrt{k_{xy}\lambda^2+q^2}}d\lambda$$

using substitution, setting $\xi^2 = k_{xy}\lambda^2 \Leftrightarrow d\xi = \sqrt{k_{xy}}d\lambda$ leads to :

$$\langle T\rangle = \frac{P_l}{\pi k_y}\frac{1}{\sqrt{k_{xy}}}\int_0^{\infty}\frac{\sin^2\left(\xi b/\sqrt{k_{xy}}\right)}{\left(\xi b/\sqrt{k_{xy}}\right)^2}\frac{1}{\sqrt{\xi^2+q^2}}d\xi$$

If we are in the limit where $|1/q| \gg b/\sqrt{k_{xy}}$, meaning that the thermal penetration depth is much larger than the transducer half-width (to anisotropy ratio), the integral is dominated by values such that $0 < \xi < \sqrt{k_{xy}}/b$. It follows that $\xi b/\sqrt{k_{xy}} \ll 1$ and therefore we approximate the integral using $\sin\left(\xi b/\sqrt{k_{xy}}\right)/\left(\xi b/\sqrt{k_{xy}}\right) = 1$, as suggested by Cahill.[119] The integral reduces to

$$\langle T \rangle = \frac{P_l}{\pi k_y} \frac{1}{\sqrt{k_{xy}}} \int_0^{\sqrt{k_{xy}}/b} \frac{1}{\sqrt{\xi^2 + q^2}} d\xi$$

Again, using substitution, setting $\eta = \xi/q \Leftrightarrow d\eta = d\xi/q$,

$$\begin{aligned}
\langle T \rangle &= \frac{P_l}{\pi k_y} \frac{1}{\sqrt{k_{xy}}} \int_0^{\sqrt{k_{xy}}/bq} \frac{1}{\sqrt{1+\eta^2}} d\eta \\
&= \frac{P_l}{\pi k_y} \frac{1}{\sqrt{k_{xy}}} \left[\ln\left(\sqrt{\eta^2+1} + \eta \right) \right]_0^{\frac{\sqrt{k_{xy}}}{bq}} \\
&= \frac{P_l}{\pi k_y} \frac{1}{\sqrt{k_{xy}}} \ln\left(\frac{\sqrt{k_{xy}}}{bq} + \sqrt{\left(\frac{\sqrt{k_{xy}}}{bq}\right)^2 + 1} \right) \\
&\approx \frac{P_l}{\pi k_y} \frac{1}{\sqrt{k_{xy}}} \ln\left(2\frac{\sqrt{k_{xy}}}{bq} \right)
\end{aligned}$$

In the last step, we used the fact that we are in the limit where $\sqrt{k_{xy}}/b|q| \gg 1$. Hence, making explicit the frequency dependence of the temperature oscillation :

$$\langle T \rangle = \frac{P_l}{\pi\sqrt{k_x k_y}} \left[\ln\left(\frac{\lambda_{\text{tpd}}}{b}\right) + \frac{1}{2}\ln\left(k_{xy}\right) - i\frac{\pi}{4} + \eta \right] \tag{3.10a}$$

$$= \frac{P_l}{\pi\sqrt{k_x k_y}} \left[-\frac{1}{2}\ln(\omega) + \frac{1}{2}\ln\left(\frac{k_y}{\rho C_p}\right) + \ln\left(\frac{\sqrt{k_{xy}}}{b}\right) - i\frac{\pi}{4} + \eta \right] \tag{3.10b}$$

where η is a numerical constant. When comparing Eq. (3.9) to its approximation Eq. (3.10), η is numerically evaluated to $\eta \approx 0.923$. Duquesne *et al.* further showed in 2010 that Eq. (3.9) can be written as a Meijer-G function, and explicitly derived η by examining the limit where the thermal penetration depth is much larger than the transducer half-width.[149] In this limit, they found $\eta = 3/2 - \gamma \approx 0.923$ where γ is the Euler-Mascheroni constant.

Eq.(3.10) is extensively used to extract the thermal conductivity of a material which is considered semi-infinite, such as a thick substrate. It is now much more intuitive as how to derive the thermal conductivity of a material, using Eq.(3.10). Indeed, measuring the temperature oscillation as a function of excitation frequency and taking its slope with respect to $\ln(\omega)$, it is straightforward to infer $\sqrt{k_x k_y}$. This way of extracting a material's thermal conductivity is often referred to as the "slope method" in the literature. The slope method will often be discussed in this manuscript, and therefore we emphasize that it consists in taking the derivative (slope) of $\langle T \rangle = \text{f}(\ln(\omega))$ to extract the thermal conductivity of a material, rather than fitting the amplitude of $\langle T \rangle$ at each frequency, which implies to input more (possibly unknown) parameters (samples's heat capacity, thermometer width, etc.). Proceeding in this way leads to

$$\sqrt{k_x k_y} = \frac{-P_l}{2\pi} \frac{1}{\frac{\partial\langle T \rangle}{\partial(\ln(\omega))}} \tag{3.11}$$

We note that when using the slope method, we are sensitive to $\sqrt{k_x k_y}$, a geometric *average* of the in-plane and out-of-plane components of the thermal conductivity, not only the cross-plane thermal conductivity k_y, as shown by several authors.[123,150,151]

We remind the reader that we assumed a perfect contact between the transducer and the substrate, i.e. we have neglected the thermal boundary resistance between both materials. As we will see later, the thermal boundary resistance only adds a frequency independent term to the temperature oscillation, therefore making the slope method still applicable.

Examining Eq.(3.11), we understand that it is not a prerequisite to know the specific heat of the material, nor the transducer width, to extract its thermal conductivity using the slope method. The explanation for this is uniquely related to the geometry of the transducer, seen as an infinite line with finite width, which imply cylindrical symmetry around the "infinite" axis. As remarked in Ref. 152, the general solution for the temperature field in a cylinder is a function of the logarithm of the ratio between its inner and outer radii, while for the 3ω geometry, it is a function of the logarithm of the ratio between the thermal penetration depth and heater half-width, as can be seen from Eq. (3.10a). This logarithmic dependency in turn allows to separate the contribution from frequency and diffusivity, as shown in Eq.(3.10b), hence making the "slope method" possible. If the heat source were to be spherical, it would probably not be possible to use a similar "slope method", and therefore the specific heat would have to be known in order to extract the material's thermal conductivity. For this reason, the 3ω method is a very robust technique to measure the thermal conductivity of thick materials (say, > 300 μm). Indeed, the length of the transducer and the power supplied – which are the only quantities needed to extract the material's thermal conductivity – are readily measured and determined with great accuracy.

3.1.3 Slope method : range of applicability

However powerful the slope method is, care has to be taken when it is used in order to satisfy the approximations made when the approximate solution of the temperature oscillation was derived. In the previous derivation, we have stated that the heater half-width to anisotropy ratio should be much smaller than the TPD : $b/(k_{xy})^{1/2} \ll \lambda_{\text{tpd}} = |1/q|$. The other condition is that, since the approximation is only valid for semi-infinite substrates, which is not true in nature, we must specify some conditions on whether or not the substrate can be considered semi-infinite. Qualitatively, this condition can be met if the TPD is much smaller than the substrate thickness : $\lambda_{\text{tpd}} = |1/q| \ll d_s$. This gives two qualitative limits in order for the slope method to be used reasonably. Borca-Tasciuc *et al.* thoroughly discussed that matter[123] and provided quantitative criteria to make the slope method applicable by comparing the slope (with respect to logarithm frequency) of Eq. (3.8) to that of Eq. (3.10).

Normalized by $(-P_l/(2\pi\sqrt{k_x k_y}))$, the slope of the real part of Eq. (3.10) versus $\ln(\omega)$ has the constant value of 1 :

$$\frac{1}{(-P_l/(2\pi\sqrt{k_x k_y}))}\frac{\partial \,\text{Re}\{\langle T\rangle_{\text{approx}}\}}{\partial(\ln(\omega))} = 1 \tag{3.12}$$

whereas the slope of Eq. (3.8) has to be computed. For adiabatic boundary conditions at the bottom of the substrate, it is given by :

$$\frac{1}{(-P_l/(2\pi\sqrt{k_x k_y}))}\frac{\partial\langle T\rangle_{\text{exact}}}{\partial(\ln(\omega))} = \int_0^\infty \frac{z^2}{\tanh(\beta_S B_S)B_S^3}\left(1+\frac{4\beta_S B_S}{e^{2\beta_S B_S}-e^{-2\beta_S B_S}}\right)\frac{\sin^2(\lambda)}{\lambda^2}d\lambda \tag{3.13}$$

where $z = qb/\sqrt{k_{xy}}$, $\beta_S = \sqrt{k_{xy}}(d_s/b)$ and $B_S = \sqrt{\lambda^2 + z^2}$. The two quantities z and β_s are parameters that allow to examine the two limits introduced previously. Indeed, a small value of z reflects a large TPD when compared to the heater half-width (to substrate anisotropy ratio) whereas a large value of $z\beta_S = qd_s$ represents the limit where the substrate's thickness is large compared to the TPD ($d_s > \lambda_{tpd}$). Therefore, as the authors of Ref. 123 discussed, it is interesting to plot the computed slope as a function of these two quantities, z and $z\beta_s = qd_s$, and examine the limits where it matches the slope of the approximate solution. This is shown in Figure 3.3(a-b). Colored curves are the real part of Eq. (3.13) for different values of β_S and will be equal to 1 if they match the approximation Eq. (3.12). We further plot the relative error that is made when taking the slope of the approximate solution instead of that of the exact one. It is defined as :

$$\text{error } (\%) = 100 \times \frac{\left|\text{Re}\left\{\frac{\partial\langle T\rangle_{\text{approx}}}{\partial(\ln(\omega))}\right\} - \text{Re}\left\{\frac{\partial\langle T\rangle_{\text{exact}}}{\partial(\ln(\omega))}\right\}\right|}{\text{Re}\left\{\frac{\partial\langle T\rangle_{\text{exact}}}{\partial(\ln(\omega))}\right\}}$$

and is plotted in Figure 3.3(c-d).

We observe from these plots that, for any β_S, it is not possible to have a relative error of less than 1% if $z > 0.2$ and $|q|d_s < 5$ when using the slope method.[3] We also observe in Figure 3.3(c) that for $\beta_s = 10$ (the blue curve), there is no range that would lead to an error smaller than 1%. Actually, there is no range of applicability of the slope method for $\beta_S < 25$ that would lead to less than 1% error.[123] Therefore, when using the slope method, the thermal penetration depth λ_{tpd} should be restricted to values satisfying

$$\lambda_{tpd} > \frac{5b}{\sqrt{k_{xy}}} \quad \text{and} \quad \lambda_{tpd} < \frac{d_s}{5}$$

in order for the error on the substrate's thermal conductivity to be less than a percent. Making explicit the electrical frequency dependence :

$$\frac{25\alpha_s}{4\pi d_s^2} < f < \frac{\alpha_s k_{xy}}{100\pi b^2} \tag{3.14}$$

where α_s stands for the substrate's diffusivity. These conditions allow to choose the appropriate frequency range depending on the material diffusivity and to adjust the transducer width, if necessary, prior to performing an experiment. Note that taking the slope of the *amplitude* of the temperature versus logarithm of frequency instead of its real part is possible and leads to the same conditions to be respected for achieving less than 1% error on the substrate's thermal conductivity (i.e. Eq.(3.14)). This is verified by comparing the slope of the amplitude of the approximate solution as a function of logarithm of frequency, to the slope of the amplitude of the exact solution as a function of logarithm of frequency.

As an example, we have plotted in Figure 3.3(e), both the exact and approximate real part of the temperature oscillation derived previously (Eqs. (3.8) and (3.10)). It might appear more clearly as where the slope method is applicable by looking at this graph as the two curves are plotted over an intentionally very large frequency range, which contains the two limits ($\lambda_{tpd} < 2b$ and $\lambda_{tpd} > d_s$) where both expressions differ greatly. In the light red areas, the conditions stated above are not met and therefore the slope method cannot be used with great accuracy. For this example, we used a germanium substrate with diffusivity

[3] Numerically, $qd_s \lessapprox 4.7$ is sufficient but we will keep the value of 5 as it gives a good rule of thumb.

$\alpha_s = 3.02 \times 10^{-5}$ m^2.s^{-1}, thickness $d_\mathrm{s} = 500$ μm, anisotropy $k_{xy} = 1$ and transducer width $2b = 2$ μm. This led to the following conditions in terms of electrical frequency

$$240 \text{ Hz} < f < 96.2 \text{ kHz}$$

as can be seen in Figure 3.3(e-f). Furthermore, we see from Figure 3.3(f) that there exists a frequency window (300 Hz $< f <$ 9263 Hz) where the error coming from using the slope method caps to no more than 0.1%.

As bulk materials are not the most attractive playground for studying atypical properties of heat conduction, the next step in this chapter is to provide a rigorous thermal model which can be used for systems made of several layers. Specific attention will be given for the case of a film-on-substrate system.

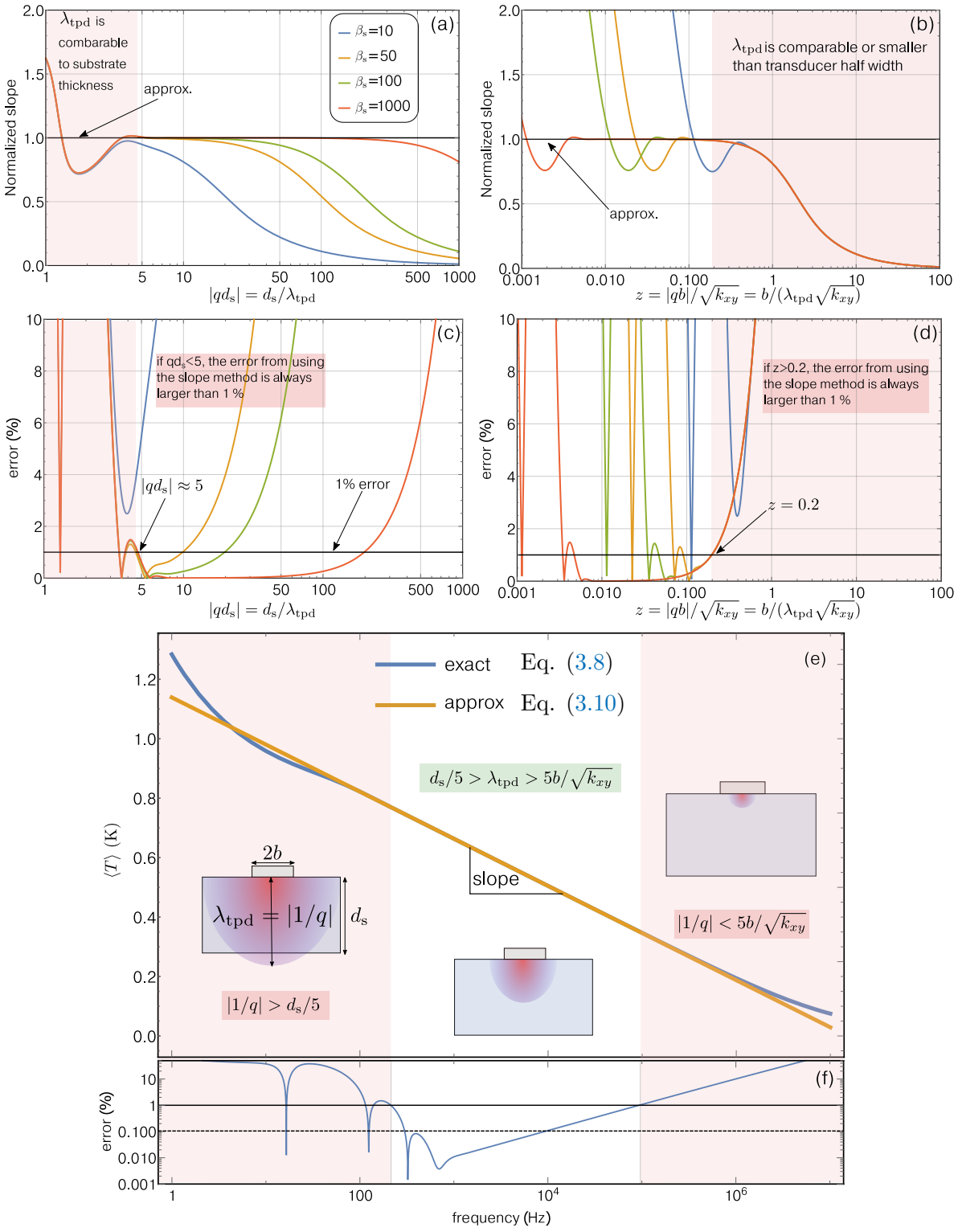

Figure 3.3: Range of applicability of the slope method for extracting a substrate's thermal conductivity. (a-b) The normalized slope (Eq.(3.12)) of the approximate solution is plotted as a constant equal to 1 as a solid black line, whereas colored curves represent the slope (Eq.(3.13)) of the exact solution, for several values of $\beta_s = \sqrt{k_{xy}} d_s/b$. The slope of the approximate solution can be safely used when it matches that of the exact solution. (c-d) Relative error (in %) on the substrate's thermal conductivity made when using the slope method, as a function of two non-dimensional parameters $|q|d_s$ and $|q|b/(k_{xy})^{1/2}$. The error is smaller than 1% if both $|q|d_s > 5$ and $|q|b/(k_{xy})^{1/2} < 0.2$. (e) Comparison of the two expressions of the temperature oscillation derived in the main text (exact and approximate solution). It is clear that in both high and low frequency limits, the slope of the two curves are dissimilar, and therefore the slope of the approximate solution cannot be used to determine the substrate's thermal conductivity, as can be seen from the relative error plotted on the bottom panel (f).

3.2 Transducer on a multilayer system

Most systems of interest for thermal characterization are shrinking in size. A plethora of materials and complex structures such as thin films, superlattices, forest of nanowires or quantum dots are now a step closer to being integrated into functional devices. They are, in most cases, deposited onto substrates and therefore measurements are performed on a system made of several materials whose thermal properties can be dissimilar. It is rather cumbersome to derive a general expression for the temperature rise sensed by the transducer for a system consisting of many layers using the aforementioned method. Consequently, a detailed model of the two-dimensional heat flow for a multilayer system will be presented hereafter, using a different approach from that of the first part.

The "thermal quadrupole" method, extending the notion of electrical quadrupole, was initially proposed by Carslaw and Jaeger[137] and later improved by Degiovanni (published in french in 1988[153] and in english in 2000[154]). It is also often referred to as the Feldman algorithm, who used the same formalism for the specific case of a heat source periodically heating a stratified medium.[155]

In Figure 3.4 is displayed the geometry of the system, consisting of multiple parallel slabs, with the heater/thermometer on top. The general idea is to express temperature and flux from the

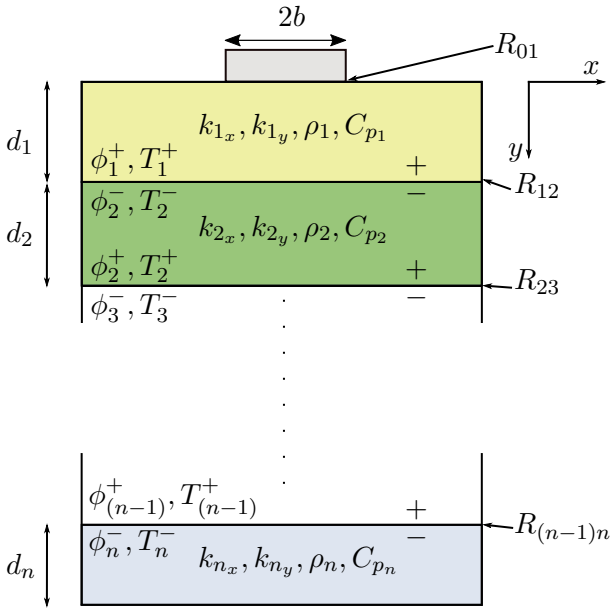

Figure 3.4: Schematic representation of a multilayer system with a metallic layer (grey) deposited on top of the first layer. Each layer has a set of thermal properties, and there is a thermal boundary resistance between every consecutive layer. Each layer has a top and bottom (with respect to y) labelled as $+$ and $-$, following the notation of Eq. (3.20). Note that the metallic layer (the transducer) is not considered in this model as well. The heat flux is considered to be a boundary condition at $y = 0$ and between $-b < x < b$.

top $(+)$ of one slab as a function of temperature and flux at the bottom $(-)$ of the same slab. Temperature and flux at the bottom of a slab will be related to temperature and flux at the top of the next slab, and so on, until the last slab is reached and an adequate boundary condition is applied. These temperature and flux will be expressed as a matrix product, as shown below, and can therefore be readily extended to a system of n layers.

Starting off with the Fourier transformed heat equation Eq.(3.4), derived in the previous section, which we re-write below :

$$\frac{\partial^2}{\partial y^2}\widehat{T}(\lambda, y) - \gamma^2 \widehat{T}(\lambda, y) = 0$$

$$\gamma = \sqrt{k_{xy}\lambda^2 + i\omega\frac{\rho C_p}{k_y}}$$

and its solution

$$\widehat{T}(\lambda, y) = C_1 e^{\gamma y} + C_2 e^{-\gamma y}$$

The following steps are followed from Ref. 137 (p.109-111). Temperature and flux are written as :

$$\widehat{T}(\lambda, y) = C_1 e^{\gamma y} + C_2 e^{-\gamma y} \tag{3.16}$$

$$\widehat{\phi}(\lambda, y) = -k_y \frac{\partial \widehat{T}(\lambda, y)}{\partial y} = -k_y \gamma \left(C_1 e^{\gamma y} - C_2 e^{-\gamma y}\right) \tag{3.17}$$

We evaluate $\widehat{T}(\lambda, 0)$ and $\widehat{\phi}(\lambda, 0)$ in order to infer C_1 and C_2 :

$$\widehat{T}(\lambda, 0) = C_1 + C_2$$

$$\widehat{\phi}(\lambda, 0) = -k_y \left.\frac{\partial \widehat{T}(\lambda, y)}{\partial y}\right|_{y=0} = -k_y \gamma (C_1 - C_2)$$

From these two relations, C_1 and C_2 can be written as :

$$C_1 = \frac{1}{2}\left(\widehat{T}(\lambda, 0) - \frac{\widehat{\phi}(\lambda, 0)}{k_y \gamma}\right) \tag{3.18}$$

$$C_2 = \frac{1}{2}\left(\widehat{T}(\lambda, 0) + \frac{\widehat{\phi}(\lambda, 0)}{k_y \gamma}\right) \tag{3.19}$$

We now express temperature and flux at $y = d$, where d refers to the thickness of a layer, as a function of the temperature and flux at $y = 0$. Writing Eqs.(3.16)-(3.17) at $y = d$ using Eqs.(3.18)-(3.19) :

$$\widehat{T}(\lambda, d) = \widehat{T}(\lambda, 0)\left(\frac{e^{\gamma d} + e^{-\gamma d}}{2}\right) + \widehat{\phi}(\lambda, 0)\frac{1}{k_y \gamma}\left(\frac{e^{-\gamma d} - e^{\gamma d}}{2}\right)$$

$$\widehat{\phi}(\lambda, d) = \widehat{T}(\lambda, 0)\left((-k_y \gamma)\left(\frac{e^{\gamma d} - e^{-\gamma d}}{2}\right)\right) + \widehat{\phi}(\lambda, 0)\left(\frac{e^{-\gamma d} + e^{\gamma d}}{2}\right)$$

In matrix form, expressing exponential identities as hyperbolic sines and cosines :

$$\begin{pmatrix} \widehat{T}(\lambda, d) \\ \widehat{\phi}(\lambda, d) \end{pmatrix} = \begin{pmatrix} \cosh(\gamma d) & \frac{-1}{k_y \gamma}\sinh(\gamma d) \\ -k_y \gamma \sinh(\gamma d) & \cosh(\gamma d) \end{pmatrix} \begin{pmatrix} \widehat{T}(\lambda, 0) \\ \widehat{\phi}(\lambda, 0) \end{pmatrix}$$

Since we are interested in the temperature at $y = 0$, we express $\widehat{T}(\lambda, 0)$ as a function of $\widehat{T}(\lambda, d)$:

$$\begin{pmatrix} \widehat{T}(\lambda, 0) \\ \widehat{\phi}(\lambda, 0) \end{pmatrix} = \begin{pmatrix} \cosh(\gamma d) & \frac{1}{k_y \gamma}\sinh(\gamma d) \\ k_y \gamma \sinh(\gamma d) & \cosh(\gamma d) \end{pmatrix} \begin{pmatrix} \widehat{T}(\lambda, d) \\ \widehat{\phi}(\lambda, d) \end{pmatrix}$$

Thermal boundary resistance between two consecutive layers is readily added to the model. Temperature and flux at any interface between two layers are expressed as :

$$\begin{aligned} T_j^+ - T_{j+1}^- &= R_{j,j+1}\phi_j^+ \\ \phi_j^+ &= \phi_{j+1}^- \end{aligned} \tag{3.20}$$

where $R_{j,j+1}$ is the thermal boundary resistance between layer j and $j+1$ (see Figure 3.4). In matrix form :

$$\begin{pmatrix} T_j^+ \\ \phi_j^+ \end{pmatrix} = \begin{pmatrix} 1 & R_{j,j+1} \\ 0 & 1 \end{pmatrix} \begin{pmatrix} T_{j+1}^- \\ \phi_{j+1}^- \end{pmatrix}$$

For example, temperature $\widehat{T}(\lambda,0)$ and flux $\widehat{\phi}(\lambda,0)$ for a substrate of thickness d_s, with a thermal resistance R_{01} between the transducer and the substrate is written as :

$$\begin{pmatrix} \widehat{T}(\lambda,0) \\ \widehat{\phi}(\lambda,0) \end{pmatrix} = \begin{pmatrix} 1 & R_{01} \\ 0 & 1 \end{pmatrix} \begin{pmatrix} \cosh(\gamma d_s) & \frac{1}{k_y\gamma}\sinh(\gamma d_s) \\ k_y\gamma\sinh(\gamma d) & \cosh(\gamma d_s) \end{pmatrix} \begin{pmatrix} \widehat{T}(\lambda,d_s) \\ \widehat{\phi}(\lambda,d_s) \end{pmatrix} \tag{3.21}$$

$\widehat{T}(\lambda,d_s)$ or $\widehat{\phi}(\lambda,d_s)$ is then set to zero according to the boundary condition that is applied at the bottom of the last layer (isothermal or adiabatic, respectively). The most important feature of this method is that it can be extended to n layers. Repeating Eq.(3.21), it follows that :

$$\begin{aligned} \begin{pmatrix} \widehat{T}(\lambda,0) \\ \widehat{\phi}(\lambda,0) \end{pmatrix} = &\begin{pmatrix} 1 & R_{01} \\ 0 & 1 \end{pmatrix} \begin{pmatrix} \cosh(\gamma_1 d_1) & \frac{1}{k_{1_y}\gamma_1}\sinh(\gamma_1 d_1) \\ k_{1_y}\gamma_1\sinh(\gamma_1 d_1) & \cosh(\gamma_1 d_1) \end{pmatrix} \times \\ &\begin{pmatrix} 1 & R_{12} \\ 0 & 1 \end{pmatrix} \begin{pmatrix} \cosh(\gamma_2 d_2) & \frac{1}{k_{2_y}\gamma_2}\sinh(\gamma_2 d_2) \\ k_{2_y}\gamma_2\sinh(\gamma_2 d_2) & \cosh(\gamma_2 d_2) \end{pmatrix} \times \cdots \times \\ &\begin{pmatrix} 1 & R_{(n-1)n} \\ 0 & 1 \end{pmatrix} \begin{pmatrix} \cosh(\gamma_n d_n) & \frac{1}{k_{n_y}\gamma_n}\sinh(\gamma_n d_n) \\ k_{n_y}\gamma_n\sinh(\gamma_n d_n) & \cosh(\gamma_n d_n) \end{pmatrix} \begin{pmatrix} \widehat{T}(\lambda,d_n) \\ \widehat{\phi}(\lambda,d_n) \end{pmatrix} \\ = &\begin{pmatrix} A & B \\ C & D \end{pmatrix} \begin{pmatrix} \widehat{T}(\lambda,d_n) \\ \widehat{\phi}(\lambda,d_n) \end{pmatrix} \end{aligned}$$

Once the matrix product involving thermal boundary resistances and hyperbolic coefficients is computed (arbitrarily labelled as (A,B,C,D) above), we need to express $\widehat{T}(\lambda,0)$ as a function of $\widehat{\phi}(\lambda,0)$. We then express $T(x,0)$ taking the inverse Fourier transform of $\widehat{T}(\lambda,0)$, as we did in the previous section. For the general case :

$$\begin{pmatrix} \widehat{T}(\lambda,0) \\ \widehat{\phi}(\lambda,0) \end{pmatrix} = \begin{pmatrix} A & B \\ C & D \end{pmatrix} \begin{pmatrix} \widehat{T}(\lambda,d_n) \\ \widehat{\phi}(\lambda,d_n) \end{pmatrix}$$

Adiabatic boundary condition at the bottom layer ($\widehat{\phi}(\lambda,d_n)=0$) leads to

$$\begin{pmatrix} \widehat{T}(\lambda,0) \\ \widehat{\phi}(\lambda,0) \end{pmatrix} = \begin{pmatrix} A & B \\ C & D \end{pmatrix} \begin{pmatrix} \widehat{T}(\lambda,d_n) \\ 0 \end{pmatrix}$$

which is equivalent to the system of coupled equations

$$\begin{aligned} \widehat{T}(\lambda,0) &= A\widehat{T}(\lambda,d_n) \\ \widehat{\phi}(\lambda,0) &= C\widehat{T}(\lambda,d_n) \end{aligned}$$

which is readily solved, leading to

$$\widehat{T}(\lambda,0) = \frac{A}{C}\widehat{\phi}(\lambda,0) \tag{3.22}$$

Similarly, for isothermal boundary conditions at the bottom layer ($\widehat{T}(\lambda,d_n)=0$), we obtain

$$\widehat{T}(\lambda,0) = \frac{B}{D}\widehat{\phi}(\lambda,0)$$

The Fourier Transform of the heat flux has been computed in the previous section (Eq. (3.6)), it is expressed as $\widehat{\phi}(\lambda,0) = 2\phi_0 \sin(\lambda b)/\lambda$.

Taking the inverse Fourier transform of $\widehat{T}(\lambda,0)$ to recover $T(x,0)$, then averaging over $-b<x<b$ (we define r as either A/C or B/D depending on the boundary condition) :

$$\langle T(x,0)\rangle_{\text{avg}} = \frac{1}{2b}\int_{-b}^{b}\left\{\frac{1}{2\pi}\int_{-\infty}^{\infty}\frac{2\phi_0\sin(\lambda b)}{\lambda}re^{i\lambda x}d\lambda\right\}dx$$

leading to

$$\text{isothermal b.c.} : \langle T\rangle = \frac{P_l}{\pi}\int_0^\infty \frac{B}{D}\frac{\sin^2(\lambda b)}{(\lambda b)^2}d\lambda \tag{3.23a}$$

$$\text{adiabatic b.c.} : \langle T\rangle = \frac{P_l}{\pi}\int_0^\infty \frac{A}{C}\frac{\sin^2(\lambda b)}{(\lambda b)^2}d\lambda \tag{3.23b}$$

where A, B, C and D are computed from

$$\begin{pmatrix} A & B \\ C & D\end{pmatrix} = \prod_{j=1}^{n}\begin{pmatrix}1 & R_{(j-1)j}\\ 0 & 1\end{pmatrix}\begin{pmatrix}\cosh(\gamma_j d_j) & \frac{1}{k_{j_y}\gamma_j}\sinh(\gamma_j d_j)\\ k_{j_y}\gamma_j\sinh(\gamma_j d_j) & \cosh(\gamma_j d_j)\end{pmatrix} \tag{3.23c}$$

$$\gamma_j = \sqrt{k_{j_{xy}}\lambda^2 + i\omega\frac{(\rho Cp)_j}{k_{j_y}}} \tag{3.23d}$$

where the product in Eq. (3.23c) starts from the first layer ($j=1$) beneath the transducer, following the notation of Figure 3.4.

We compare this result to the one derived in the previous section for the case of a heater on substrate, without thermal boundary resistance between the transducer and the substrate ($R_{01}=0$), with adiabatic boundary condition applied at the substrate's bottom. Looking for the coefficients in Eq. (3.23c) using $n=1$, we have $A=\cosh(\gamma d_s)$ and $C = k_y\gamma\sinh(\gamma d_s)$. This leads to :

$$\begin{aligned}\langle T\rangle &= \frac{P_l}{\pi}\int_0^\infty \frac{\cosh(\gamma d_s)}{k_y\gamma\sinh(\gamma d_s)}\frac{\sin^2(\lambda b)}{(\lambda b)^2}d\lambda\\ &= \frac{P_l}{\pi k_y}\int_0^\infty \frac{1}{\gamma\tanh(\gamma d_s)}\frac{\sin^2(\lambda b)}{(\lambda b)^2}d\lambda\\ \text{where } \gamma &= \sqrt{k_{xy}\lambda^2 + i\omega\frac{\rho Cp}{k_y}}\end{aligned}$$

which is consistent with our previous result (Eq. (3.8)). In a similar manner, the temperature oscillation sensed by the transducer can be evaluated for any system of n layers : we look for the coefficients using Eq. (3.23c) and then numerically integrate (3.23a) or (3.23b). This result is equivalent to that derived in Ref. 123, with thermal boundary resistances between layers

included.

The general formalism to infer temperature oscillations sensed by a transducer on a complex structure is now established, and we wish to express a general expression for the specific case of a thin film deposited onto a substrate. This is straightforward using Eq. (3.23), and it will lead to another widely used expression for inferring the thermal conductivity of a thin film.

3.2.1 Extracting a thin film's thermal conductivity

In the following, subscripts "f", "s" and "tr" under relevant parameters will refer to film, substrate and transducer, respectively. Subscripts in italic refer to coordinates. For example, k_{s_y} refers to the cross-plane component of the substrate's thermal conductivity.

The rigorous method to derive the expression of the temperature oscillation sensed by the transducer for a film-on-substrate system is to compute Eq. (3.23) using $n = 2$. This leads to

$$\langle T \rangle = \frac{P_l}{\pi} \int_0^\infty \frac{\sin^2(\lambda b)}{(\lambda b)^2} \frac{1}{k_{f_y} \gamma_f \tanh(\gamma_f d_f)} \frac{\left(1 + \tanh(\gamma_s d_s) \gamma_s k_{s_y} (R_{f/s} + \frac{\tanh(\gamma_f d_f)}{k_{f_y} \gamma_f})\right)}{\left(1 + \tanh(\gamma_s d_s) \gamma_s k_{s_y} (R_{f/s} + \frac{\coth(\gamma_f d_f)}{k_{f_y} \gamma_f})\right)} d\lambda + \frac{P_l}{2b} R_{tr/f} \tag{3.24a}$$

$$\gamma_j = \sqrt{k_{j_{xy}} \lambda^2 + i\omega \frac{(\rho C_p)_j}{k_{j_y}}} \tag{3.24b}$$

This expression is rather complicated and does not seem very intuitive. In particular, it is not straightforward to estimate how the film will affect the temperature oscillation across the heater/thermometer, depending on its thickness or thermal conductivity – though a sensitivity analysis can prove effective ! (see Appendix B)

In this section, we will see that treating the film as a simple thermal *boundary* resistance between the heater and the substrate gives interesting results. Solving Eq. (3.23) for $n = 1$ with a thermal boundary resistance R_{int} at the heater/substrate interface, we have $A = \cosh(\gamma d_s) + R_{int} k_{s_y} \gamma \sinh(\gamma d_s)$ and $C = k_{s_y} \gamma \sinh(\gamma d_s)$, leading to

$$\begin{aligned}
\langle T \rangle &= \frac{P}{\pi l} \int_0^\infty \frac{(\cosh(\gamma d_s) + R_{int} k_{s_y} \gamma \sinh(\gamma d_s))}{k_{s_y} \gamma \sinh(\gamma d_s)} \frac{\sin^2(\lambda b)}{(\lambda b)^2} d\lambda \\
&= \frac{P_l}{\pi} \int_0^\infty \frac{1}{k_{s_y} \gamma \tanh(\gamma d_s)} \frac{\sin^2(\lambda b)}{(\lambda b)^2} d\lambda + \frac{P_l R_{int}}{\pi} \int_0^\infty \frac{\sin^2(\lambda b)}{(\lambda b)^2} d\lambda \\
&= \frac{P_l}{\pi} \int_0^\infty \frac{1}{k_{s_y} \gamma \tanh(\gamma d_s)} \frac{\sin^2(\lambda b)}{(\lambda b)^2} d\lambda + \frac{P_l R_{int}}{\pi} \frac{\pi}{2b}
\end{aligned}$$

$$\langle T \rangle = \frac{P_l}{\pi k_{s_y}} \int_0^\infty \frac{1}{\gamma \tanh(\gamma d_s)} \frac{\sin^2(\lambda b)}{(\lambda b)^2} d\lambda + \frac{P_l}{2b} \times R_{int} \tag{3.25}$$

We notice from Eq. (3.25) that the contribution of thermal boundary resistance between the heater and the substrate only adds a frequency-independent term to the total temperature oscillation. Besides, we recognize the previously defined expression of the heat flux $\phi_0 = P_l/(2b)$ and the integrated form of Fourier's law relating temperature difference to heat flux and thermal resistance : $\langle T \rangle = \phi_0 \times R_{int}$. Albeit we defined R_{int} as the thermal *boundary* resistance

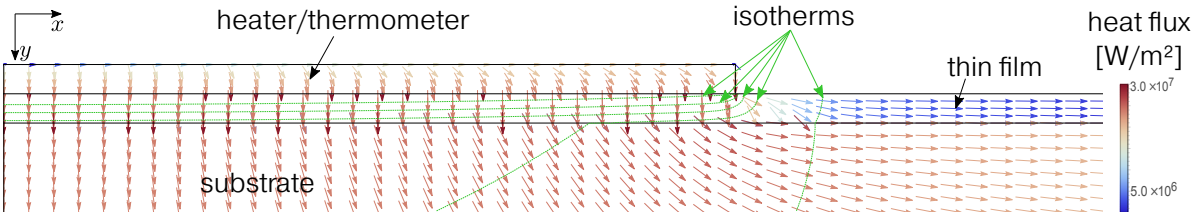

Figure 3.5: Heat flux distribution for a film-on-substrate system, calculated using FEM (see Appendix D). From this plot, we understand that the heat flux is majorly one-directional below the heater/thermometer, since the heater half-width is very large in comparison to the film thickness. The same conclusion can be drawn by looking at the isotherms, displayed as green dashed lines, which are almost parallel across the thickness of the film. Besides, heat flow in the x direction inside the film is very small due to the small thermal conductivity of the film in comparison to that of the substrate (a ratio of 1/25 was taken in this case).

between the heater and substrate, this notation is widely used in the literature[123,145,156–165] to approximate a *thin film* thermal resistance deposited on top of its substrate, using $R_{\text{int}} = R_{\text{film}} = d_{\text{f}}/k_{\text{f}}$, with units of $\text{m}^2.\text{K}.\text{W}^{-1}$. In this case, the thin film is seen as a "heat capacity-less" material[166], and is hence modelled as a simple thermal resistance in series with the heater. It looks very attractive, since we can relatively easily subtract the significant thermal contribution of the substrate (first part of the right-hand side of Eq.(3.25)) from the total temperature oscillation by performing two experiments, one with the film and another one without the film (a reference sample), and hence deduce the thermal contribution of the film only, allowing to infer its thermal conductivity. The resulting temperature difference would lead to :

$$\langle T \rangle_{\text{film}} = \langle T \rangle_{\text{substrate + film}} - \langle T \rangle_{\text{substrate}} = \frac{P_l}{2b} \frac{d_{\text{f}}}{k_{\text{f}_y,\text{1D}}} \tag{3.26}$$

which is a very convenient formula that contains well-known quantities. Extracting a film's thermal conductivity in this way is often referred to as the "differential 3ω method" in the literature. Naturally, it comes along with certain conditions to be satisfied. Looking at Eq. (3.26), the film's anisotropy and heat capacity do not appear, which provides some hints on the conditions to satisfy in order to use this simple model.

First, the absence of anisotropy in Eq.(3.26) means that when using this approximation, we assume the heat flux from the transducer to be completely one-directional (1D) through the film thickness (cross-plane direction, y in Figure 3.5), therefore neglecting heat spreading perpendicularly to the film thickness (in-plane direction) – hence "1D" added to the subscript $k_{\text{f}_y,\text{1D}}$. For the heat flux to be 1D across the film thickness, the heater width should be much larger than the film thickness ($2b \gg d_{\text{f}}$), such that any thermal spreading in the in-plane direction can be neglected when compared to that of the cross-plane. This is exemplified in Figure 3.5.

Second, when thermal circuits are modelled in terms of thermal impedances, in a similar way to the modelling of electrical circuits, the heat capacity has the electrical equivalent of a self capacitance.[167] It means that the temperature response of any material with a given heat capacity changes as a function of excitation frequency, which is precisely what we have shown in the previous part. This is in contradiction with Eq. (3.26) which is frequency-independent, leading to another condition for this approximation to be used : the frequency must be low

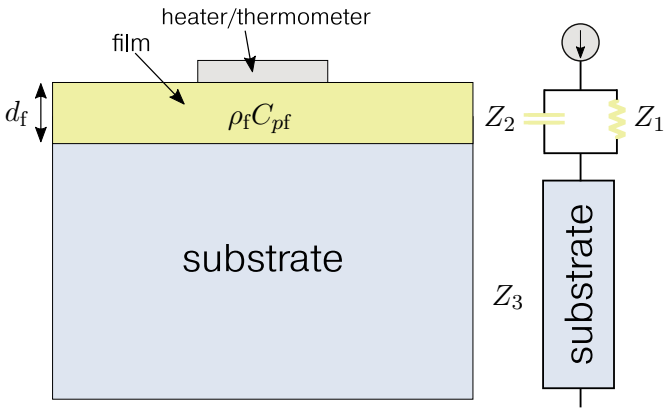

$$
\begin{aligned}
Z_{tot} &= Z_3 + \frac{1}{\frac{1}{Z_1} + \frac{1}{Z_2}} \\
&= Z_3 + \frac{Z_1}{1 + Z_1/Z_2} \\
&= Z_3 + \frac{\frac{d_f}{k_{f_y}}}{1 + \frac{d_f}{k_{f_y}} i\omega\rho_f C_{pf} d_f} \\
&\approx Z_3 + \frac{d_f}{k_{f_y}} \text{ if} \\
\frac{d_f}{k_{f_y}} i\omega\rho_f C_{pf} d_f \ll 1 &\Leftrightarrow \left|\frac{1}{q_f}\right| \gg d_f
\end{aligned}
$$

Figure 3.6: Simplified *thermal* circuit of a film-on-substrate system, emphasizing on the film's heat capacity and the conditions to satisfy in order to neglect it in the thermal model. When the thermal penetration depth becomes much larger than the thickness of the film, the film is considered as a thermal resistance in series with the heater and its heat capacity can be neglected. The temperature rise is readily obtained by multiplying the thermal impedance with the heat flux $P_l/2b$.

enough such that the frequency response due to the heat capacity of the film can be neglected – hence the expression "heat capacity-less". It might be easier to understand in terms of thermal penetration depth : the thermal penetration depth should be much larger than the film thickness ($|1/q_f| \gg d_f$) such that we can consider it as a simple thermal resistance in series with the heater. This condition can be understood using a thermal circuit description of the film-on-substrate system, as depicted in Figure 3.6.

The remaining condition to fulfil in order to use Eq. (3.26) is that the thermal conductivity contrast between the substrate and the film should be large enough ($k_f/k_s \ll 1$), such that the resulting temperature difference can be measured with sufficient accuracy. Indeed, if both the film and substrate have equal thermal conductivities, the system (substrate+film) could be seen as a simple thicker substrate and therefore there would be no temperature difference to be measured. This last condition always hold. Indeed, the 3ω method is not well suited for films whose thermal conductivity is close to that of the substrate onto which they are deposited.

More quantitative criteria of the above arguments have been derived by Borca-Tasciuc *et al.*[123], who compared the simplified expression Eq. (3.25) to the exact one Eq. (3.24). In order to easily compare both exact and approximate (1D) expressions, we follow their notation, and we write

$$
\begin{aligned}
\langle T\rangle_{\text{film, [approx]}} &= \langle T\rangle_{\text{(substrate + film),[approx]}} - \langle T\rangle_{\text{substrate,[exact]}} \\
&= \frac{P_l}{2b}\frac{d_f}{k_{f_y,\text{1D}}}
\end{aligned}
$$

and

$$
\begin{aligned}
\langle T\rangle_{\text{film, [exact]}} &= \langle T\rangle_{\text{(substrate + film),[exact]}} - \langle T\rangle_{\text{substrate,[exact]}} \\
&= \frac{P_l}{2b}\frac{d_f}{k_{f_y,\text{exact}}} Re\left\{\int_0^\infty \frac{2}{\pi}\frac{\sin^2(\lambda)}{\lambda^2} K(\lambda, \beta_f, z_f, z_s, k_f, k_s) d\lambda\right\}
\end{aligned}
$$

where, for a semi-infinite substrate,

$$K(\lambda,\beta_\mathrm{f},z_\mathrm{f},z_\mathrm{s},k_\mathrm{f},k_\mathrm{s}) = \frac{\tanh\left(\beta_\mathrm{f}\sqrt{\lambda^2+z_\mathrm{f}^2}\right)\left(1-\frac{k_{\mathrm{f}_x}k_{\mathrm{f}_y}}{k_\mathrm{s}^2}\left(\frac{\lambda^2+z_\mathrm{f}^2}{\lambda^2+z_\mathrm{s}^2}\right)\right)}{\beta_\mathrm{f}\sqrt{\lambda^2+z_\mathrm{f}^2}\left(1+\frac{\sqrt{k_{\mathrm{f}_x}k_{\mathrm{f}_y}}}{k_\mathrm{s}}\left(\frac{\lambda^2+z_\mathrm{f}^2}{\lambda^2+z_\mathrm{s}^2}\right)^{1/2}\tanh\left(\beta_\mathrm{f}\sqrt{\lambda^2+z_\mathrm{f}^2}\right)\right)} \tag{3.27}$$

with

$$\beta_\mathrm{f} = \sqrt{k_{\mathrm{f}_{xy}}}\left(\frac{d_\mathrm{f}}{b}\right) \quad \text{and} \quad z_\mathrm{i} = q_\mathrm{i}\frac{b}{\sqrt{k_{\mathrm{i}_{xy}}}}$$

In the limit where $f \to 0$ (and therefore $z_i \to 0$), the thermal penetration depth is much larger than the film thickness and heater half-width : $\lambda_\mathrm{tpd} \gg b \gg d_\mathrm{f}$. In this case, the thermal penetration depth, as a length-scale, is disregarded from the analysis. This has the benefit of simplifying the analysis, and to focus only on parameters unrelated to the frequency driving the experiment.[4] Thus, we can simplify the expression for $K(\lambda,\beta_\mathrm{f},z_\mathrm{f},z_\mathrm{s},k_\mathrm{f},k_\mathrm{s})$, which in turn allows to quantify the error coming from using the approximate solution Eq. (3.26) as a function of two important parameters, as what was done for the slope method. Letting $z_i \to 0$ in Eq.(3.27) :

$$K(\lambda,\beta_\mathrm{f},k_\mathrm{f},k_\mathrm{s}) = \frac{\tanh\left(\beta_\mathrm{f}\lambda\right)\left(1-\frac{k_{\mathrm{f}_x}k_{\mathrm{f}_y}}{k_\mathrm{s}^2}\right)}{\beta_\mathrm{f}\lambda\left(1+\frac{\sqrt{k_{\mathrm{f}_x}k_{\mathrm{f}_y}}}{k_\mathrm{s}}\tanh\left(\beta_\mathrm{f}\lambda\right)\right)}$$

and therefore

$$\langle T\rangle_{\text{film, [exact]}} = \frac{P_l}{2b}\frac{d_\mathrm{f}}{k_{\mathrm{f}_y,\mathrm{exact}}}Re\left\{\int_0^\infty \frac{2}{\pi}\frac{\sin^2(\lambda)}{\lambda^3}\frac{\tanh\left(\beta_\mathrm{f}\lambda\right)\left(1-\frac{k_{\mathrm{f}_x}k_{\mathrm{f}_y}}{k_\mathrm{s}^2}\right)}{\beta_\mathrm{f}\left(1+\sqrt{k_{\mathrm{f}_x}k_{\mathrm{f}_y}}/k_\mathrm{s}\tanh\left(\beta_\mathrm{f}\lambda\right)\right)}d\lambda\right\} \tag{3.28}$$

which corresponds to Equation (17) in Ref. 123. We can now quantify the relative error on the cross-plane component of the film thermal conductivity k_{f_y}, made when using Eq. (3.26) instead of Eq. (3.28), as a function of the thermal conductivity contrast between the substrate and the film, and as a function of the film thickness to heater half-width ratio. The relative error is defined as

$$\text{error}(\%) = 100\times\frac{\left|k_{\mathrm{f}_y,\mathrm{exact}}-k_{\mathrm{f}_y,\mathrm{1D}}\right|}{k_{\mathrm{f}_y,\mathrm{exact}}} = \mathrm{f}\left(\frac{\sqrt{k_{\mathrm{f}_x}k_{\mathrm{f}_y}}}{k_\mathrm{s}},\sqrt{k_{\mathrm{f}_{xy}}}\left(\frac{d_\mathrm{f}}{b}\right)\right) \tag{3.29}$$

Its magnitude is plotted in Figure 3.7 as a function of both the thermal conductivity contrast between the substrate and the film, and as a function of the film thickness to heater half-width ratio. From Figure 3.7, it can be read that Eq. (3.26) can be used under the following conditions, with the corresponding error :

[4] Of course, one should try to stay in an appropriate frequency range such that the thermal penetration depth is still less than the substrate's thickness – though one can extend the frequency range to lower frequencies if the film's thermal conductivity is inferred from a "differential 3ω method".

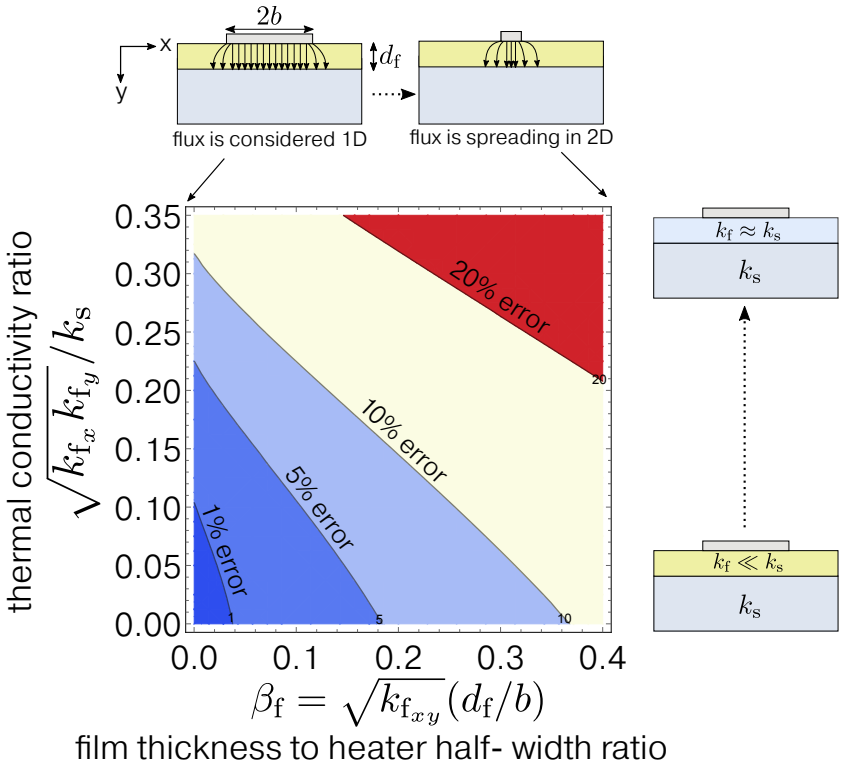

Figure 3.7: Relative error on the film's thermal conductivity if the simple 1D model (Eq. (3.26)) is used instead of the exact expression (Eq. (3.24)). The error is plotted as a function of two important parameters : the film thickness to heater half-width ratio and the thermal conductivity contrast between the film and the substrate.

$$\begin{aligned} &<1\%\text{ error if } && \sqrt{k_{f_{xy}}}d_f/b < 0.038 && \text{and} && \sqrt{k_{f_x}k_{f_y}}/k_s < 0.1 \\ &<5\%\text{ error if } && \sqrt{k_{f_{xy}}}d_f/b < 0.184 && \text{and} && \sqrt{k_{f_x}k_{f_y}}/k_s < 0.23 \\ &<10\%\text{ error if } && \sqrt{k_{f_{xy}}}d_f/b < 0.370 && \text{and} && \sqrt{k_{f_x}k_{f_y}}/k_s < 0.32 \end{aligned} \tag{3.30}$$

These conditions allow to adapt the transducer's dimensions and/or the type of substrate that is used in order to use the very convenient formula Eq. (3.26) for determining the cross-plane component of the film's thermal conductivity, k_{f_y}. Furthermore, we point out that since a smaller transducer width is more sensitive to anisotropic heat flux inside the film, it is possible to perform several experiments using transducer of different widths (one very broad, another one very narrow when compared to the thickness of the film) to infer the thermal anisotropy of the film.[123,146]

We underline that when using the "differential 3ω method", i.e. removing the thermal contribution of the substrate using a reference sample without a film, the contribution of TBR is neglected. Indeed, the (substrate+film+transducer) system will not have the same interfaces as the reference (substrate+transducer) system and therefore the contribution of TBR is *not* removed. Therefore, it should be used only if the contribution of TBR is negligible when compared to the thermal resistance of the film. If that is not the case, another strategy is preferred, as we will discuss now.

3.2.2 Measuring the contribution of thermal boundary resistances

We began our discussion by stating that the thermal resistance of a film could be seen as a thermal *boundary* resistance in series with the heater/thermometer. This is indeed true provided that certain conditions are respected, as we have explained above. In the following, we shall take into account "true" thermal boundary resistances in the thermal model, which are always present in film-on-substrate systems : one at the heater/film interface, the other one at the film/substrate interface, as shown in Figure 3.8(a). Therefore, provided that the aforementioned conditions are met such that the film can be considered 1D, the total temperature rise sensed by the transducer can be written as

$$\langle T\rangle_{\text{total}} = \underbrace{\frac{P_l}{\pi k_{s_y}}\int_0^\infty \frac{\tanh^a\left(\sqrt{k_{s_{xy}}\lambda^2 + i\omega\frac{(\rho_s C_{p_s})}{k_{s_y}}}\,d_s\right)}{\sqrt{k_{s_{xy}}\lambda^2 + i\omega\frac{(\rho_s C_{p_s})}{k_{s_y}}}}\frac{\sin^2(b\lambda)}{(b\lambda)^2}d\lambda}_{\text{substrate}} + \underbrace{\frac{P_l}{2b}\times R_{\text{th}}}_{\text{film + interfaces}} \tag{3.31a}$$

where

$$\begin{aligned} R_{\text{th}} &= R_{\text{film}} + R_{\text{transducer/film}} + R_{\text{film/substrate}} \\ &= \frac{d_f}{k_{f_y}} + R_{\text{tr/f}} + R_{\text{f/s}} \end{aligned} \tag{3.31b}$$

where $a = \pm 1$ in Eq.(3.31) for isothermal or adiabatic boundary condition at the bottom of the substrate. Using Eqs.(3.31a)-(3.31b), it is possible to separate the thermal contribution of the film from that of the interfaces. Indeed, with the cost of performing multiple experiments using films of increasing thicknesses, plotting the thermal resistance R_{th} as a function of the film's thickness d_f permits to extract the cross-plane component of the intrinsic thermal conductivity of the film k_{f_y} and *the sum* of thermal boundary resistances $(R_{\text{tr/f}} + R_{\text{f/s}})$, as explained in Figure 3.8(a)-(c). As thermal boundary resistances usually lie within the range of $10^{-9} - 10^{-7}$ m^2.K.W^{-1} (see Figure 1.10), it is important to measure their contribution (or estimate them if a measurement is not possible). Indeed, for a 50 nm thick film with thermal conductivity $k_f = 1$ W.m^{-1}.K^{-1}, its thermal resistance is $R_{\text{film}} = d_f/k_f = 5.10^{-8}$ m^2.K.W^{-1}, the same order of magnitude as TBRs, which, if discarded, could lead to very large errors on the determination of the film's thermal conductivity.

To summarize, for extracting the thermal conductivity of the substrate, film and the sum of thermal boundary resistances, one may follow the steps described in Figure 3.8(a)-(c). We primarily fit the measured temperature oscillation $\langle T\rangle_{\text{total}}$ to Eq. (3.31a) to obtain $\sqrt{k_{s_x}k_{s_y}}$ and R_{th}. $\sqrt{k_{s_x}k_{s_y}}$ can be uniquely determined using the frequency dependence of $\langle T\rangle_{\text{total}}$ and therefore, once it is known, R_{th} is the remaining free parameter. We then fit each R_{th} for each thin film thickness according to Eq. (3.31b). From the slope of $R_{\text{th}} = f(d_f)$, we extract the intrinsic thermal conductivity of the film. $R_{\text{interfaces}}$ is inferred from its intercept.

This method is valid as long as the film's intrinsic thermal conductivity is not thickness-dependent in the thickness-range where measurements are carried out. This holds true for most amorphous materials which have MFPs of the order of the nanometer[168], but caution must be taken for crystalline materials with long MFP, whose thermal conductivities might be thickness-dependent, in particular at low temperature.

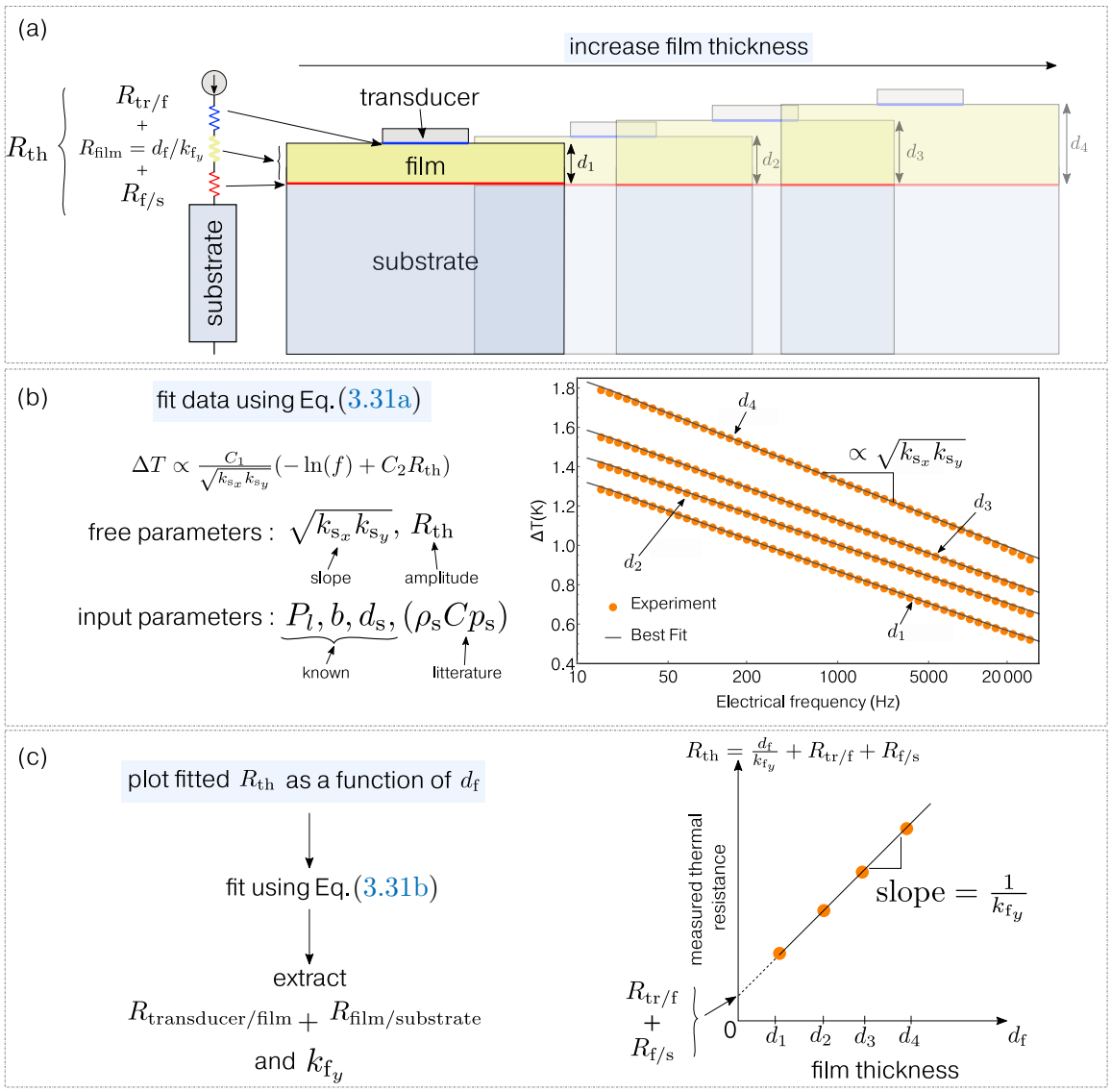

Figure 3.8: Method for extracting the intrinsic thermal conductivity of the film : measuring the thermal resistance of films of increasing thicknesses allows to separate the contribution of interfaces from the contribution of the film alone. This method implies that the film can be treated as a simple thermal resistance in series with the transducer, and therefore fulfil the conditions stated in Eq.(3.30).

The other implicit assumption of Eq. (3.31b) is that TBRs are constant through all films thicknesses, i.e. the TBR for a film with thickness d_1 is the same as that of thickness d_2. This assumption can be wrong for very thin films which have different surface properties (as compared to the same, thicker, material), depending on the deposition technique. For example, the stoichiometry of a film deposited by Atomic Layer Deposition depends on the number of cycles that is needed to grow the film, and thus on the thickness of the film.[169] During the first cycles of the deposition process, the stoichiometry of the film changes and therefore its surface (thus interface) might change as well, making the use of Eq. (3.31b) not valid. Therefore, one would need to characterize films thick enough such that their surface structure is the same among all films. This sets a restriction on the thinnest films that can be measured with sufficient accuracy.

We point out that, when fitting Eq. (3.31a), we must input the substrate's heat capacity ($\rho_s C_{p_s}$) and thermal conductivity anisotropy $k_{s_{xy}}$ in the thermal model. The heat capacity can

usually be found in the literature as opposed to anisotropy. It is therefore preferred to perform experiments onto isotropic substrates. However, from the way we extract the film's thermal conductivity, an error made on either the substrate's heat capacity or anisotropy would not lead to an error on the film's thermal conductivity. This can be seen more clearly by expressing Eq. (3.31a) in the case of a semi-infinite substrate when the thermal penetration depth is much larger than the transducer half-width, $\lambda_{\text{tpd}} \gg b$. In this case, it is written as (using Eq. (3.10))

$$\langle T \rangle = \frac{P_l}{\pi\sqrt{k_{\text{s}_x} k_{\text{s}_y}}} \left[-\frac{1}{2}\ln(\omega) + \frac{1}{2}\ln\left(\frac{k_{\text{s}_y} k_{\text{s}_{xy}}}{\rho_{\text{s}} C_{p_{\text{s}}} b^2}\right) - i\frac{\pi}{4} + \eta \right] + \frac{P_l}{2b}\left[\frac{d_{\text{f}}}{k_{\text{f}_y}} + R_{\text{interfaces}}\right] \tag{3.32}$$

Therefore, if the value of the substrate's heat capacity (or anisotropy) used for the fitting is wrong, it would lead to an extra constant term in Eq. (3.32). Since we used its *slope* with respect to d_{f} (Figure 3.8(c)), this extra constant term would vanish. However, since we use the *intercept* to extract the sum of thermal boundary resistances, an erroneous estimation of the substrate's anisotropy or heat capacity would lead to inaccurate results on the TBR.

Let us examine the effect of the substrate anisotropy on the determined TBR. Re-writing Eq. (3.32) to make the contribution from anisotropy $k_{\text{s}_{xy}}$ more explicit leads to :

$$\begin{aligned}\langle T \rangle = \frac{P_l}{\pi k_{\text{s}_y}\sqrt{k_{\text{s}_{xy}}}} &\left[-\frac{1}{2}\ln(\omega) + \frac{1}{2}\ln\left(\frac{k_{\text{s}_y}\sqrt{k_{\text{s}_{xy}}}}{\rho_{\text{s}} C_{p_{\text{s}}} b^2}\right) + \frac{1}{4}\ln(k_{\text{s}_{xy}}) - i\frac{\pi}{4} + \eta \right] \\ &+ \frac{P_l}{2b}\left[\frac{d_{\text{f}}}{k_{\text{f}_y}} + R_{\text{interfaces}}\right]\end{aligned}$$

Using the "slope method", we infer the quantity $k_{\text{s}_y}\sqrt{k_{\text{s}_{xy}}}$, as explained in Section 3.1.2. Assuming that we know precisely the substrate's heat capacity, the remaining unknown quantities are $k_{\text{s}_{xy}}, k_{\text{f}_y}$ and $R_{\text{interfaces}}$. Re-arranging to distinguish between known and unknown quantities :

$$\begin{aligned}\langle T \rangle = \frac{P_l}{\pi k_{\text{s}_y}\sqrt{k_{\text{s}_{xy}}}} &\left[-\frac{1}{2}\ln(\omega) + \frac{1}{2}\ln\left(\frac{k_{\text{s}_y}\sqrt{k_{\text{s}_{xy}}}}{\rho_{\text{s}} C_{p_{\text{s}}} b^2}\right) - i\frac{\pi}{4} + \eta \right] \\ &+ \frac{P_l}{2b}\underbrace{\left[\frac{d_{\text{f}}}{k_{\text{f}_y}} + R_{\text{interfaces}} + \frac{b}{2\pi k_{\text{s}_y}}\frac{\ln(k_{\text{s}_{xy}})}{\sqrt{k_{\text{s}_{xy}}}}\right]}_{R_{\text{th}'}}\end{aligned}$$

Hence, using the method depicted in Figure 3.8(c), that is, plotting $R_{\text{th}'}$ as a function of d_{f}, we would not only extract the sum of thermal boundary resistances from the intercept, but also a small contribution from the substrate's anisotropy, which scales as $\propto b\ln(k_{\text{s}_{xy}})/(k_{\text{s}_y}(k_{\text{s}_{xy}})^{0.5})$. If the substrate is isotropic, i.e. $k_{\text{s}_{xy}} = 1$, this correction vanishes. As an example, for a transducer half-width of $b = 2.5$ μm, substrate's cross-plane thermal conductivity $k_{\text{s}_y} = 52$ W.m^{-1}.K^{-1} and anisotropy $k_{\text{s}_{xy}} = 1.1$, this quantity would be $\approx 7.10^{-10}$ m^2.K.W^{-1}, which is one to two orders of magnitude smaller than typical values for $R_{\text{interfaces}}$. In most cases it can be neglected, but caution should be taken for large transducer and/or small substrate thermal conductivity, especially if the substrate's thermal anisotropy is not known.

4 Limits of the thermal model

In general, the 2D solution of the temperature oscillation that have been presented in the previous chapter will suffice, and the general solution Eq. (3.23), or the simpler Eq. (3.31) can be used, depending on the geometry and thermal properties of the system. However, in some cases, a more detailed derivation of the thermal model is needed in order to accurately determine the thermal properties of a system. Indeed, the general solution of the temperature oscillation (Eq. (3.23)) sensed by the heater/thermometer, used to determine the thermal properties of the system of interest, have been derived using several assumptions. The first one is, as was shown in Figure 3.1 of Chapter 3, that the heat flux is homogeneous and constant along the width of the heater. This comes from the important approximation that heat conduction within the heater is completely neglected (its thickness is assumed to be zero), which considerably simplifies the thermal model. Besides, the heat that is stored within the transducer is neglected as well, and thus the heater's specific heat is not included in the thermal model. Another assumption is that the model assumes the heater length to be infinitely long in the z direction, allowing to treat the problem in 2D, thus neglecting heat transport in the direction parallel to the heater length. This considerably simplifies the thermal model as well. Eventually, we assumed that the heater dissipates heat only through conduction in the underlying materials, thereby completely neglecting losses by radiation (or convection).

In this chapter, we will therefore discuss these assumptions and their consequences in the determination of thermal properties. We remind the reader that most of these concerns have been discussed in the literature. Cahill discussed the heat loss due to radiation in its seminal paper presenting the 3ω method.[119] A decade later, Borca-Tasciuc *et al.*[123] provided a correction factor to take into account the transducer's heat capacity, while other authors[147,148,170–172] have studied the effect of the transducer's thermal conductivity on the measured temperature

rise. In chronological order, Jacquot *et al.* conducted a 3D FEM analysis to study the temperature oscillation that is measured in the 3ω geometry, including heat conduction within the heater line, and its finite length.[170] Battaglia *et al.*[173] then provided an analytical solution of the 3D problem, including the finite length of the heater line, without considering heat conduction within it. Gurrum *et al.*[147] and Wang *et al.*[148] then provided a semi-analytical solution of the temperature rise measured in 3ω experiments, taking into account heat conduction within the heater, in 2D.

We will first briefly discuss the effect of radiation on the measured temperature rise during a 3ω experiment, as derived by Cahill.[119] Then, the thermal properties of the heater will be included (using FEM or using a simple thermal circuit approach), and their effect on the temperature rise will be discussed. Eventually, an analytical 3D model of the temperature distribution in a multilayer system will be presented, allowing to quantify analytically end effects due to the finite length of the heater/thermometer, which can alter the measurement, in particular when using the slope method for determining the thermal conductivity of a material.

4.1 Heat lost by radiation

If the experiment is carried out under vacuum ($< 10^{-5}$ mbar), as it is the case in this work, the remaining path for heat to be lost is through radiation. The error from blackbody radiation has been quantified by Cahill in his original paper[119] and will be presented here for completeness. The general idea is to quantify the amount of heat that is lost through radiation starting from Stefan-Boltzmann law :

$$P = \sigma \epsilon T^4 \tag{4.1}$$

where $\sigma = 5.67 \times 10^{-8}$ W.m^{-2}.T^{-4} is the Stefan-Boltzmann constant and ϵ is the emissivity of the sample surface. Then, subtract the calculated heat loss from the amount of heat that is produced by joule heating, and then recalculate the temperature oscillation with the correct amount of heat that is actually entering the system through conduction. The resulting temperature oscillation for a semi-infinite isotropic substrate reads[119] :

$$\langle T \rangle = \frac{P_l}{\pi} \int_0^\infty \frac{1}{\left(k_s \sqrt{\lambda^2 + i\omega \frac{(\rho C_p)_s}{k_s}} + 2\epsilon\sigma T_{\text{avg}}^3 \right)} \frac{\sin^2(\lambda b)}{(\lambda b)^2} d\lambda \tag{4.2}$$

where T_{avg} is the average temperature of the heater and surroundings. Qualitatively, for large heater widths, the surface of the heater is large and thus heat lost by radiation is more important. Similarly, for large thermal penetration depth, the heated area is larger and we can therefore expect radiation to be important as well. For thermally insulating materials, the heat flux from the heater is more easily radiated out to the environment, and therefore error from radiation is more important for such materials. The error from radiation is thus expected to scale roughly as $\sim \epsilon T^3 b \lambda_{\text{tpd}} / k_s$.[119,166] We plot the temperature oscillation as a function of frequency for a poorly ($k_s = 0.1$ W/m.K) or conductive ($k_s = 50$ W/m.K) substrate with emissivity $\epsilon = 1$, for several temperatures in Figure 4.1. The effect of radiative heat loss is indeed more pronounced at low frequency (large thermal penetration depth) and at very high temperature, in particular for thermally insulating materials. However, at room temperature and below, it is completely negligible. Since in this work, thermal conductivity measurements are carried out at temperatures below 320 K, the effect of radiation can be safely neglected,

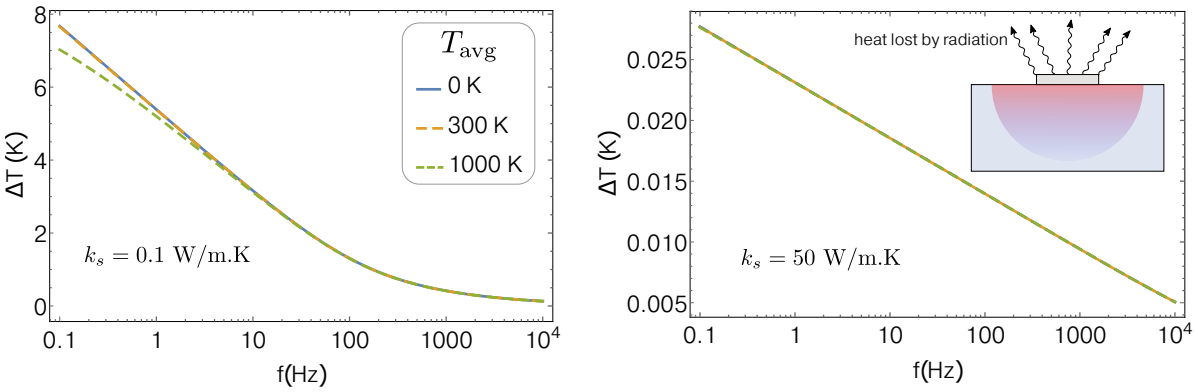

Effect of radiation on the measured temperature oscillation

Figure 4.1: Effect of radiative heat loss on the temperature oscillation as a function of oscillation frequency. The radiative heat loss becomes important only at extremely high temperature, in particular for materials with very low thermal conductivity. The parameters used were $\epsilon = 1$, $b = 15$ μm, $(\rho C_p)_s = 10^6$ J/(K.m^3) and $P_l = 0.625$ W/m.

since the error is below 0.006% at the lowest frequency at 320 K, using $k_s = 50$ W/m.K, $\epsilon = 1$, $b = 15$ μm and $P_l = 0.625$ W/m.

4.2 Including thermal properties of the transducer

4.2.1 Accounting for the transducer's heat capacity

In this part, the effect of the transducer's heat capacity is described using a thermal circuit approach. Although already discussed earlier, thermal boundary resistance between the transducer and the first layer is added to the model for completeness.

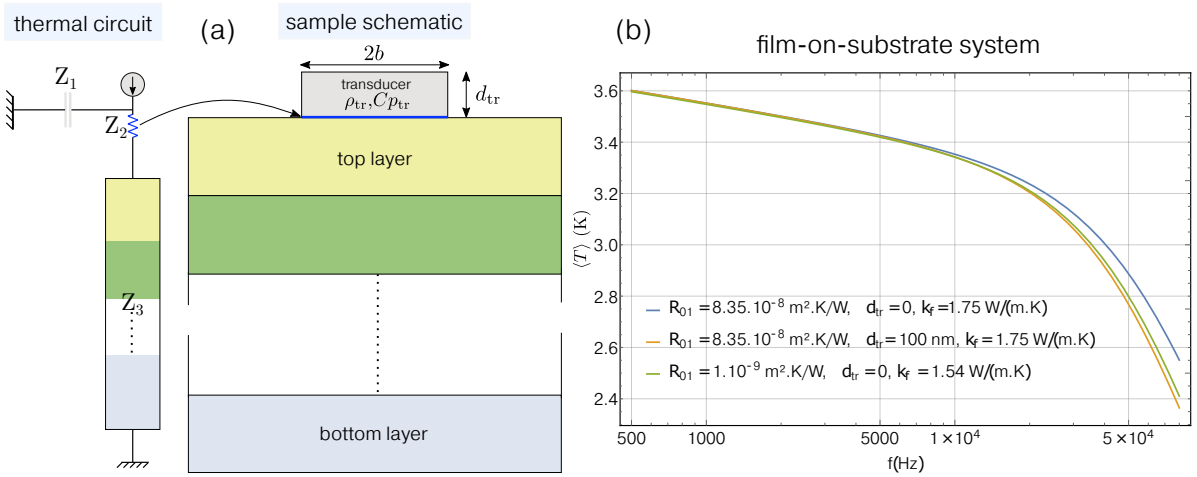

Figure 4.2: (a) Thermal circuit describing the effect of the transducer's heat capacity on the total thermal resistance. The complex impedance Z_3 is derived as described in the main text. (b) Effect of transducer's heat capacity and thermal boundary resistance on the measured temperature oscillation for a film-on-substrate system. Neglecting the heat capacity of the transducer can lead to large errors (12% in this example) on the calculated film thermal conductivity if the heater/top layer TBR is not accurately known.

Figure 4.2(a) is a representation of the "transducer on a multilayer system" in terms of

thermal impedances labelled as Z_1, Z_2 and Z_3. For homogeneity and to provide an easier comparison to what is customary in electrical circuits, Z_1, Z_2 and Z_3 are scaled with unit area and therefore have units of $\mathrm{m}^2.\mathrm{K.W}^{-1}$. We can easily switch to thermal impedance in $\mathrm{K.W}^{-1}$ by dividing these quantities with the transducer area $(2b \times l)$.
The transducer is the heat source, and is the equivalent of a power source in an electrical circuit. The thermal impedance due to the transducer self-capacitance is $Z_1 = 1/(i\omega C_{\mathrm{tr}})$ where $C_{\mathrm{tr}} = (\rho_{\mathrm{tr}} Cp_{\mathrm{tr}}) \times d_{\mathrm{tr}}$. Keeping a similar notation to that of Eq. (3.23), the thermal impedance due to the thermal boundary resistance between the transducer and the first layer is simply $Z_2 = R_{01}$. Then, the total impedance from the layers underneath the transducer is the temperature rise divided by the heat flux, $Z_3 = \langle T \rangle / (P_l/2b)$. From Figure 4.2(a), we can derive the total thermal impedance of the system. Z_2 and Z_3 are together in series while Z_1 is in parallel ; the total impedance Z_{tot} is then :

$$\begin{aligned}
\frac{1}{Z_{\mathrm{tot}}} &= \frac{1}{Z_1} + \frac{1}{Z_2 + Z_3} \\
Z_{\mathrm{tot}} &= \frac{Z_2 + Z_3}{1 + \frac{Z_2 + Z_3}{Z_1}} \\
&= \frac{R_{01} + \langle T \rangle / (P_l/2b)}{1 + (\langle T \rangle / (P_l/2b) + R_{01})(i\omega \rho_{\mathrm{tr}} Cp_{\mathrm{tr}} d_{\mathrm{tr}})}
\end{aligned}$$

Multiplying the total impedance Z_{tot} with the heat flux $(P_l/2b)$ to express the temperature rise, the new temperature rise $\langle T \rangle_{tr}$ accounting for the transducer's heat capacity and thermal boundary resistance is :

$$\langle T \rangle_{tr} = \frac{(P_l/2b) R_{01} + \langle T \rangle}{1 + (\langle T \rangle 2b/P_l + R_{01})(i\omega \rho_{\mathrm{tr}} Cp_{\mathrm{tr}} d_{\mathrm{tr}})} \tag{4.3}$$

a similar result to the one found in Refs. 123,174. Setting $d_{\mathrm{tr}} = 0$, we recover our previous result, i.e. Eq.(3.25). As expected from the thermal circuit shown in Figure 4.2, the heater's heat capacity acts as a low-pass filter and its effect is therefore more pronounced at high frequency. When $\omega = 1/(\langle T \rangle 2b/P_l + R_{01})(\rho_{\mathrm{tr}} Cp_{\mathrm{tr}} d_{\mathrm{tr}}) = 1$, the temperature oscillation is halved. Since $\langle T \rangle$ is as well frequency dependent, a neat expression for a frequency cut-off is not straightforward to derive. This correction will obviously affect thermal conductivity that have been extracted using the slope method. A similar procedure to that carried out in Chapter 3.1.3 can be performed to describe the effects of the transducer's heat capacity and thermal boundary resistance on the validity of the slope method. This is discussed in detail in Ref. 123 for the case of a semi-infinite substrate, and the error is related to the quantity $(\rho_{\mathrm{tr}} Cp_{\mathrm{tr}}/\rho_{\mathrm{s}} Cp_{\mathrm{s}})(d_{\mathrm{tr}}/b)$. The effect of the heater's heat capacity is to reduce the maximum $|q|b$ value for which the approximate slope method is applicable.

Overall, the correction from the heater's heat capacity, Eq. (4.3), is relatively easy to use once $\langle T \rangle$ is derived. The specific heat of metals can easily be found in the literature and therefore its effect on the temperature rise can be readily evaluated. This is important in many practical situations. For example, for a film-on-substrate system, one might want to confine the thermal penetration depth within the film $(\lambda_{\mathrm{tpd}} \ll d_{\mathrm{f}})$ to remove the contribution from both the substrate and the thermal boundary resistance between the film and the substrate in order to infer various thermal properties of the film alone (its heat capacity for instance). In this case, the frequency must be relatively high, which results in a frequency-dependent combined thermal response of both the film and the heater, leading to non-negligible errors

if the thermal mass of the heater is not taken into account. This is exemplified in Figure 4.2(b). The three curves represent the frequency response of the temperature oscillation for a film-on-substrate configuration. The film is chosen to be thick enough (1.2 μm) with low diffusivity such that the thermal wave completely enters the film at high frequency ($\lambda_{\mathrm{tpd}} \ll d_{\mathrm{f}}$, this is seen when the slope is becoming steeper). The substrate has thermal properties of germanium. The blue curve represents the "TBR only" corrected temperature oscillation sensed by the transducer, i.e. Eq. (4.3) with $d_{\mathrm{tr}} = 0$ whereas the yellow one takes into account the heater's heat capacity, using $\rho_{\mathrm{tr}} = 21.45$ g.m^{-3}, $C_{p_{\mathrm{tr}}} = 0.125$ J.g^{-1}.K^{-1} representing platinum with thickness $d_{\mathrm{tr}} = 100$ nm. The correction is increasingly important at high frequency and can lead to a wrong estimation of the measured film's thermal conductivity. This is highlighted by the green curve, which gives a very similar response of the temperature oscillation with respect to frequency, but for wrong values of both the film's thermal conductivity and thermal boundary resistance at the heater/film interface. In other words, one can wrongly fit experimental data if the thermal mass of the heater is not accounted for, because several combinations of film's thermal conductivity/TBR/heater specific heat can produce the same frequency response of the temperature oscillation (the green and yellow curves in Figure 4.2(b) are almost similar while they represent different combinations of thermal properties). Therefore, it is recommended to use the correction Eq. (4.3) whenever one wants to confine the thermal penetration depth within a film of interest, as for example in Ref. 175, 176 or as we will do in Chapter 6.2.2.2.

4.2.2 Heat conduction within the transducer

An important assumption that is almost always assumed to be true in 3ω experiments is that heat conduction within the heater is negligible. This assumption makes the thermal model considerably simpler, but caution must be taken to ensure that it is indeed the case. For a very thick heater deposited onto a sample, a temperature gradient might start to develop within the heater itself, making the assumption of constant heat flux at the top surface of the sample erroneous. Besides, if the heater has a large thermal conductivity and is deposited on top of film with very low thermal conductivity, a non-negligible portion of the heat flux would spread laterally (i.e. in the in-plane direction), within the heater. In this case, the model developed in the previous chapter – which does not take into account heat conduction within the heater – would overestimate the heat flux that is provided to the system, thereby overestimating the calculated temperature rise. This is exemplified in Figure 4.3, where we use FEM to calculate the heat flux distribution within a film-on-substrate system, for two different values of the heater's thermal conductivity (see Appendix D).

Dames[166] provided a simple criterion that must be respected in order for heat conduction within the heater to be safely disregarded. The thermal resistance in the cross-plane direction of the heater should be higher than the cross-plane thermal resistance across the film, such that heat is flowing primarily through the film. This leads to the condition $(d_{\mathrm{tr}} d_{\mathrm{f}}/b^2)(k_{\mathrm{tr}}/k_{\mathrm{f}}) \ll 1$ that should be respected for determining the thermal conductivity k_{f} of a film with thickness d_{f}, using a transducer with thickness d_{tr}, half-width b and thermal conductivity k_{tr}.

Gurrum *et al.*[147] and Wang *et al.*[148] provided a semi-analytical solution for the temperature oscillation sensed in a 3ω experiment, taking into account heat conduction within the heater, in 2D. Their results show that the effect of heat conduction within the heater only adds a frequency-independent offset to the measured temperature oscillation, for $\lambda_{\mathrm{tpd}} > b$ (which

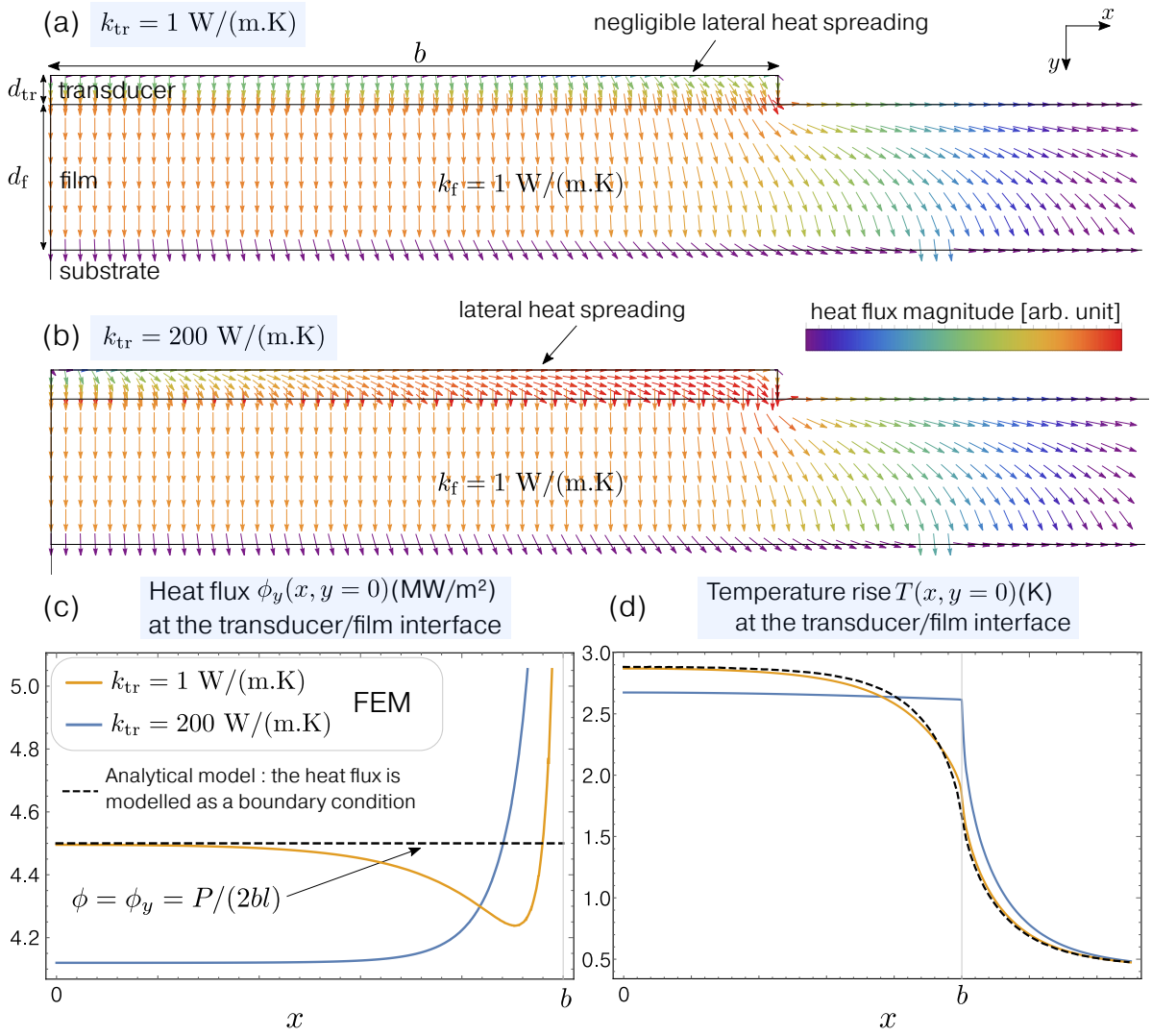

Figure 4.3: Calculated heat flux within the transducer and the film, for different thermal conductivities of the transducer, k_{tr}. For these simulations, we used $d_{tr} = 100$ nm and $d_f = 500$ nm. (a) For a heater with low thermal conductivity on top of a film with low thermal conductivity, heat spreading within the heater is negligible. In this case the assumption of constant, perpendicular heat flux at the heater/film boundary is well respected. (b) In the opposite case of a very conductive heater on top of an insulating film, heat spreads laterally within the transducer. (c) Calculated cross-plane component of the heat flux, ϕ_y, taken at the transducer/film interface, for both configurations, as a function of lateral coordinate x. The heat flux that is assumed in the 2D model, which does not take into account the finite thickness and thermal conductivity of the transducer, is shown for comparison as a dashed line. The heat flux is always somewhat overestimated if the thermal conductivity of the heater is neglected. (d) Temperature oscillation as a function of lateral coordinate x. Because of its large thermal conductivity, the heater redistributes the heat within itself, leading to a smaller average temperature at the film/heater interface.

was shown as well by Jacquot *et al.*[170], using FEM). It is therefore unimportant if the slope method is used, but should be evaluated for any other data reduction procedure that rely on the fitting of the temperature amplitude. Gurrum *et al.* suggested that for this same regime ($\lambda_{\mathrm{tpd}} > b$), and for a fixed $b/\lambda_{\mathrm{tpd,tr}} = 10^{-4}$, representing a heater with high thermal diffusivity, or when the experiment is conducted at low frequency, the quantity $(k_{\mathrm{tr}}/k_{\mathrm{f}})(d_{\mathrm{tr}}/b)$ becomes important. The lower this quantity is, the lower is the contribution from the transducer's thermal properties to the temperature oscillation amplitude.

Both Dames and Gurrum's arguments suggest that the non-dimensional quantities $(k_{\mathrm{tr}}/k_{\mathrm{f}})$ and (d_{tr}/b) should be as small as possible in order for heat conduction within the heater to be negligible.

In this section, we will conduct a 2D FEM analysis to derive the temperature and flux distributions in several film-on-substrate systems, where the heater/thermometer of finite thickness d_{tr} and thermal conductivity k_{tr} is included. We refer the reader to Appendix D for a more detailed description of the FEM implementation of the 3ω method.

The following analysis is based on the arguments presented above. We will focus on the relative error between the temperature oscillation, calculated using the 2D model which does not take into account heat conduction within the heater (i.e. Eq. (3.24) with the correction from the heater's heat capacity, Eq. (4.3)), and the temperature oscillation that we obtain using our FEM implementation of the 3ω method, which includes the heater's thermal properties and finite thickness. The temperature oscillation is obtained for several scenarios, where the half-width b, thermal conductivity k_{tr}, and thickness d_{tr} of the heater are changed.

For example, the temperature oscillation obtained by FEM and that obtained using the analytical expression, Eq. (3.24), is plotted in Figure 4.4 as a function of frequency, for different widths of the heater – every other parameter held constant. In these simulations, the substrate has thermal properties of germanium ($k_{\mathrm{s}} = 52$ W/(m.K)), the film is 100 nm thick with $k_{\mathrm{f}} = 1.7$ W/(m.K) representing amorphous alumina, and the heater is 100 nm thick as well, with $k_{\mathrm{tr}} = 30$ W/(m.K) or 120 W/(m.K). We clearly see that the error decreases for larger b, and smaller k_{tr}. The relatively low thermal conductivity of platinum (about 25-60 W/(m.K) for thin films in the range of 30-100 nm), in comparison to other metals such as gold ($k_{\mathrm{gold}} \approx 150-200$ W/(m.K) for thin films), makes it a good candidate for 3ω measurements if a narrow heater is desired.

The thickness of the heater should be the smallest possible, under the restriction that it is still thick enough such that its temperature coefficient of resistance is appreciable, and therefore can be used as a resistive thermometer. In Figure 4.5, the temperature oscillation is computed for several thicknesses of the heater, with the same parameters as described above, using $b = 2.5$ μm. The error is below 0.4 % on the whole frequency range for $d_{\mathrm{tr}} = 100$ nm, which is the nominal thickness of the thermometers used in this work. The error increases almost linearly with heater thickness. We notice in Figure 4.5(a) that at high frequency, the 2D model taking into account the heater's heat capacity matches the FEM model, since the heater's heat capacity dominates the thermal signal, as explained in the previous section.

The thermal conductivity of the heater, as already introduced in Figure 4.3, will redistribute the heat along the width of the thermometer and will therefore slightly change the shape of the heat flux, leading to a slight decrease of the temperature oscillation - an effect that is more important as the thermal conductivity of the heater increases, all other parameter held constant. This can be seen in Figure 4.6 where we have plotted the temperature oscilla-

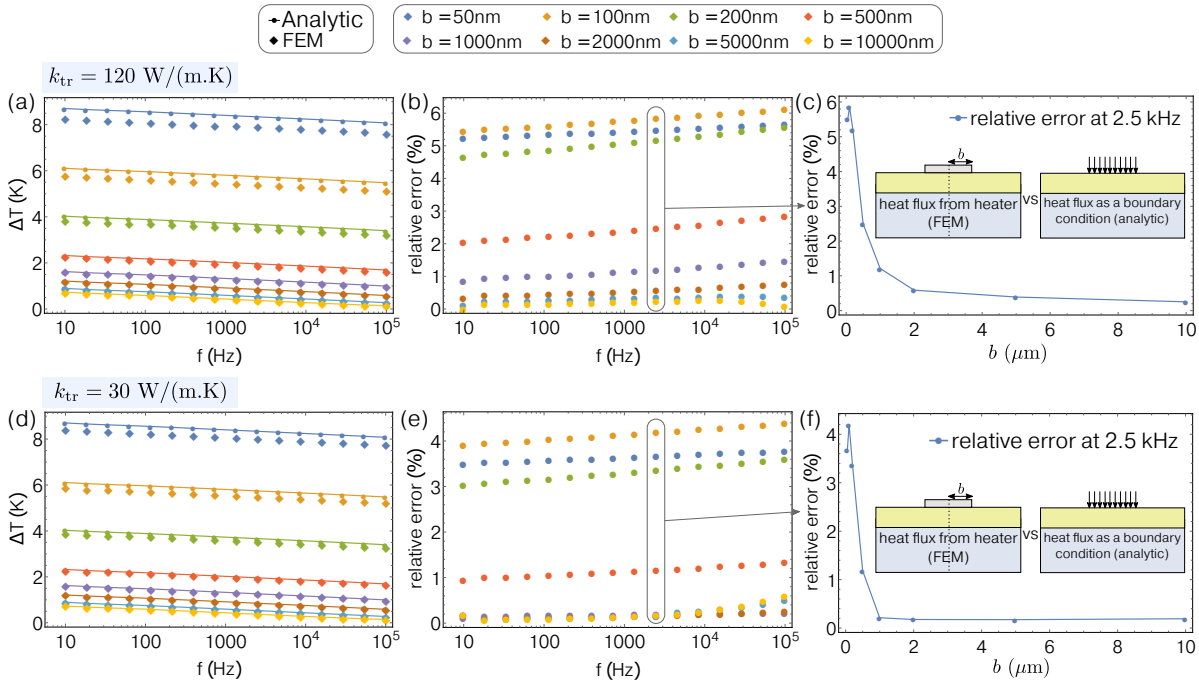

Figure 4.4: Effect of the heater on the measured temperature rise, for several values of the heater half-width, b, and two values of the heater thermal conductivity, k_{tr}. (a) and (d) Temperature oscillation calculated using FEM, taking into account the heater properties, and temperature oscillation calculated using the 2D model, for several b, as a function of electrical frequency. (b) and (e) Relative error between the FEM model and the analytical expression. (c) and (f) Relative error as a function of heater half-width, at a particular electrical frequency, $f = 2.5$ kHz.

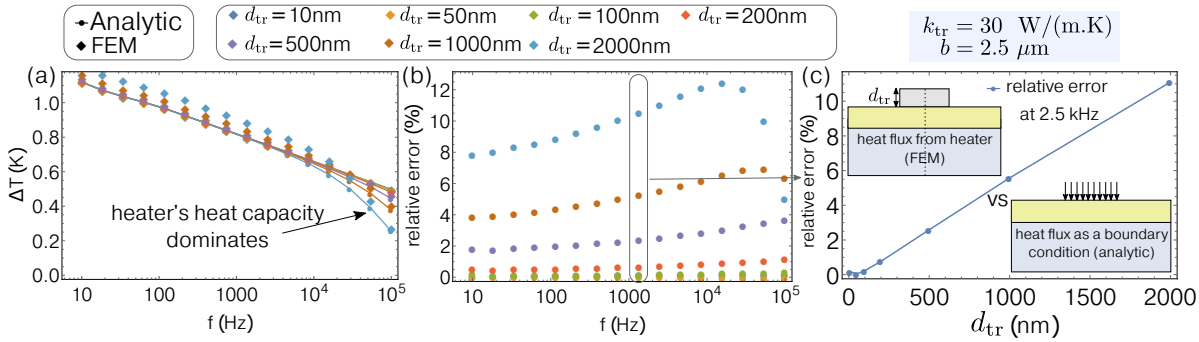

Figure 4.5: Effect of the heater on the measured temperature rise, for several values of the heater thickness, d_{tr}. (a) Temperature oscillation calculated using FEM, taking into account the heater properties, and temperature oscillation calculated using our 2D model, for several d_{tr}, as a function of electrical frequency. (b) Relative error between the FEM model and the analytical expression. (c) Relative error as a function of heater thickness, at a particular electrical frequency, $f = 2.5$ kHz.

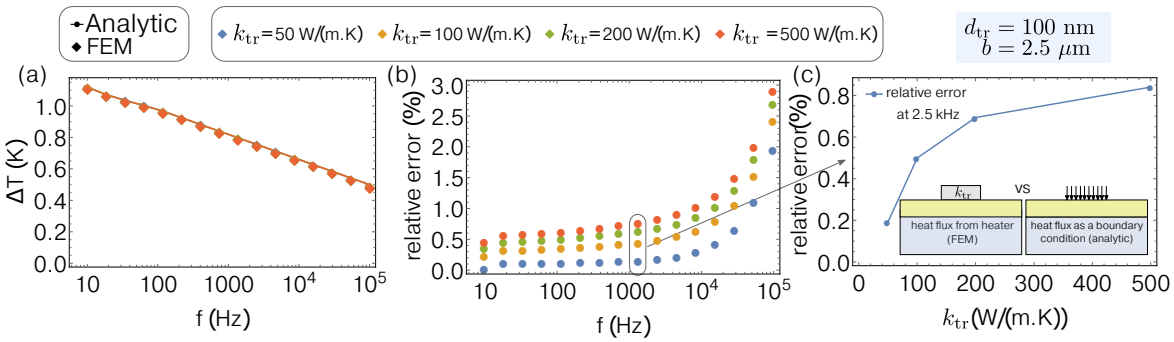

Figure 4.6: Effect of the heater on the measured temperature rise, for several values of the heater thermal conductivity, k_{tr}. (a) Temperature oscillation calculated using FEM, taking into account the heater properties, and temperature oscillation calculated using our 2D model, for several k_{tr}, as a function of electrical frequency. (b) Relative error between the FEM model and the analytical expression. (c) Relative error as a function of heater thermal conductivity, at a particular electrical frequency, $f = 2.5$ kHz.

tion calculated using the constant-heat-flux approximation, and using the FEM model using the aforementioned parameters for the substrate and film, with $b = 2.5$ μm and $d_{tr} = 100$ nm. The relative error between the two models slightly increases for thermally conductive heaters, but remains below 1 % at moderate frequency, even for the most conductive heaters.

We emphasize that these calculations are performed while all the parameters – except one – are held constant. The exact relative error between the two models will depend on the combination of all the thermal and geometric properties of the film, substrate and heater. However, the general trend proposed by Dames[166] and Gurrum[147] is well captured using some specific values of the heater properties in these calculations. Importantly, for all the measurements carried out in this work, we have used a platinum heater with nominal thickness $d_{tr} = 100$ nm and thermal conductivity lying in between 40 and 60 W/(m.K), calculated using the electrical resistivity of the film and Wiedemann-Franz law. It might be lower since the Wiedemann-Franz law is reported not to hold for very thin films[177,178], thus we took the value of $k_{tr} = 30$ W/m.K as a lower bound. The error on the temperature amplitude is calculated to be small, below 0.5%, for most of the measurements carried out using a platinum heater of thickness 100 nm and half-width $b = 2.5\mu$m with an insulating layer with thermal properties of amorphous alumina. Therefore, if not explicitly stated, the measurements have been compared to an analytical 2D expression rather than using a computationally intensive FEM model.

4.3 Finite length of the transducer : 3D end effects

The remaining assumption of the thermal model is related to the geometry of the heat source, which is assumed to be infinitely long. It is obviously never the case in a real experiment, but making this assumption leads to very little error on the calculated temperature rise if the transducer is carefully designed, and the experiment conducted within an adequate frequency range. To quantify the error introduced by the finite length of the transducer, we need to introduce the z direction to our initial 2D problem, and then solve the heat equation in 3D.

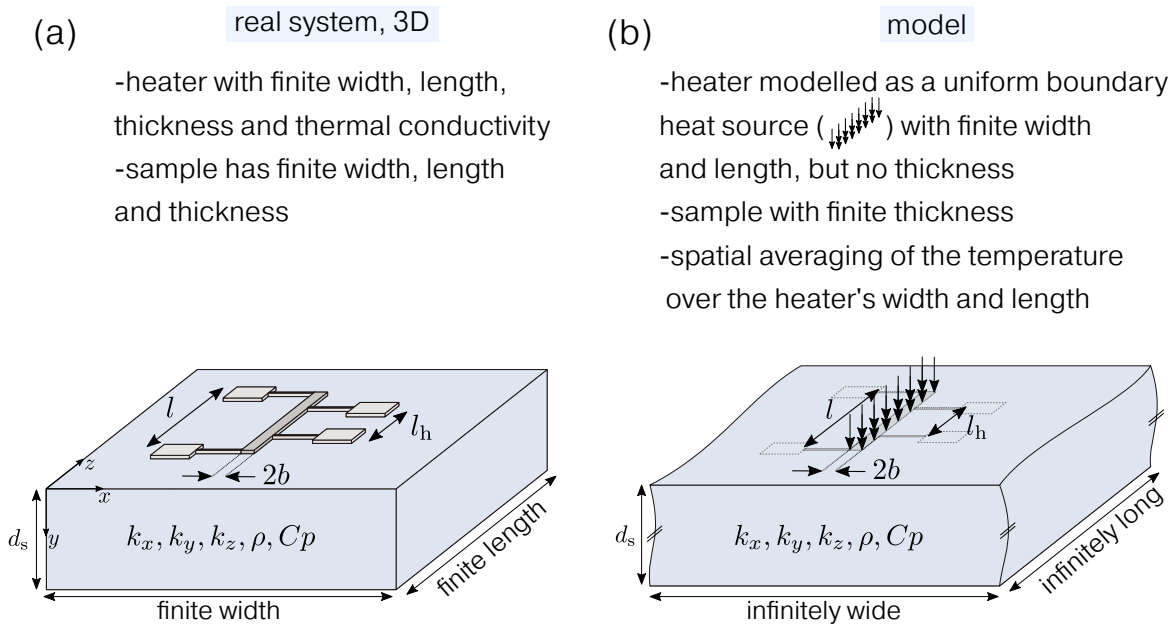

Figure 4.7: (a) System of interest sketched in 3D and (b) the model used to approximate it and calculate the temperature oscillation across the inner leads of the thermometer. As in the 2D model, the heat flux is approximated as a boundary condition, but this time the surface boundary condition is extended in the z direction as well. The thermal conductivity of the system can be anisotropic in all three directions of the cartesian coordinate system (x, y, z).

4.3.1 A 3D model for multilayer systems

The solution of the temperature distribution in 3D is obtained in a very similar way to that that we have used to derive the 2D solution, and is thus deferred to Appendix A. To the best of our knowledge, a 3D model *for multilayer* systems has not been derived previously, and the quantitative analysis that we will provide regarding the applicability of the slope method was performed only using FEM.[170] As we use the method of Fourier Transforms to solve the problem, the sample onto which the heater/thermometer is deposited is assumed to be infinitely large in the x and z directions, but with a finite thickness d_s in the y direction, as shown in Figure 4.7(b). This implies that the finite length of the sample is not taken into account in this study. As we have discussed earlier, this simplification is easily met in real experiments, since samples are about 1×1 cm^2, whereas the length of the transducer is at most a few millimeters, and the thermal penetration depth as well. Therefore, we shall only discuss end effects due to the finite length of the heat source, rather than the finite size (width and length) of the sample.

The geometry of the problem in 3D is displayed in Figure 4.7. l represents the full length of the heater whereas l_h is the quantity that is usually taken to be the length of the heater in a "four-pad" configuration, i.e. the length between the two voltage leads. The general solution of the temperature oscillation for a transducer of finite length l, measured across its inner leads separated by a distance l_h, and assuming a uniform heat source over the width and length of the transducer, as shown in Figure 4.7(b), is given as :

$$\text{isothermal b.c.} : \langle T \rangle_{3D} = \frac{P_l}{\pi^2} \int_{-\infty}^{\infty} \int_{-\infty}^{\infty} \frac{B}{D} \frac{\sin^2(\lambda b)}{(\lambda b)^2} \frac{\sin(\zeta(l/2)) \sin(\zeta(l_h/2))}{l_h \zeta^2} d\lambda d\zeta \tag{4.4a}$$

$$\text{adiabatic b.c.} : \langle T \rangle_{3D} = \frac{P_l}{\pi^2} \int_{-\infty}^{\infty} \int_{-\infty}^{\infty} \frac{A}{C} \frac{\sin^2(\lambda b)}{(\lambda b)^2} \frac{\sin(\zeta(l/2)) \sin(\zeta(l_h/2))}{l_h \zeta^2} d\lambda d\zeta \tag{4.4b}$$

where A, B, C and D are computed from

$$\begin{pmatrix} A & B \\ C & D \end{pmatrix} = \prod_{j=1}^{n} \begin{pmatrix} 1 & R_{(j-1)j} \\ 0 & 1 \end{pmatrix} \begin{pmatrix} \cosh(\xi_j d_j) & \frac{1}{k_{j_y} \xi_j} \sinh(\xi_j d_j) \\ k_{j_y} \xi_j \sinh(\xi_j d_j) & \cosh(\xi_j d_j) \end{pmatrix} \tag{4.4c}$$

$$\xi_j = \sqrt{k_{j_{xy}} \lambda^2 + k_{j_{zy}} \zeta^2 + i\omega \frac{(\rho_j C p_j)}{k_{j_y}}} \tag{4.4d}$$

where $k_{j_{zy}} = k_{j_z}/k_{j_y}$ is the thermal anisotropy in the zy plane. Every other variable have been introduced previously in this manuscript. Importantly, the finite length of the transducer l can be taken to be different from that of the distance between the two inner leads l_h. This allows to study any difference that could arise when using a two-pad configuration rather than a four-pad configuration.

In general, a "four-wire sensing" geometry is used for determining the electrical resistance of a material, eliminating the contribution from leads and contact resistances by using separate pairs of current-carrying and voltage-sensing leads. In a 3ω experiment, this benefits as well in the accurate determination of the transducer's resistance, but most importantly, it plays a role in the thermal model. As we have discussed in Chapter 3.1.1, the temperature along the width of the thermometer is not constant, and we take the spatial average of this temperature variation to compare it to the measurement. The argument is the same for the temperature profile along the length of the transducer. It might not be homogeneous and therefore its spatial average (over its length) can be different from the constant value that is otherwise assumed in the 2D model.

Physically, we expect end effects to be less relevant in several scenarios. One scenario is that the length is indeed very long in comparison to the width ($l \gg 2b$) such that the proportion of end effects that alter the temperature rise are not significant when compared to the total average temperature. The second scenario is when the experiment is designed in such a way that we are only measuring a portion of the heater that is far from the edges of the heating element, thereby less sensitive to end effects. The second scenario represents the well-known four-pad configuration, as displayed in Figure 4.7, where the temperature measurement is performed between the inner (voltage) leads of the thermometer. We emphasize that it is not simply because the experiment is designed in a four-pad geometry that it will be insensitive to end effects of the heater, but rather than the inner leads are "far enough" away from the ends of the heating line. The third scenario, which is of particular interest when performing a 3ω experiment, is when the thermal penetration depth λ_{tpd} is smaller than the length of the heater line. In this case, we expect the temperature oscillation to be unaffected by the finite length of the line, as it can be assumed very large in comparison to the heated area.

To illustrate the effect of the finite length of the heater on the measured temperature rise, we calculate the temperature oscillation amplitude for a substrate-only system, by evaluating Eq. (4.4) using $n = 1$ layer, with no thermal boundary resistance at the heater/substrate interface. This leads to

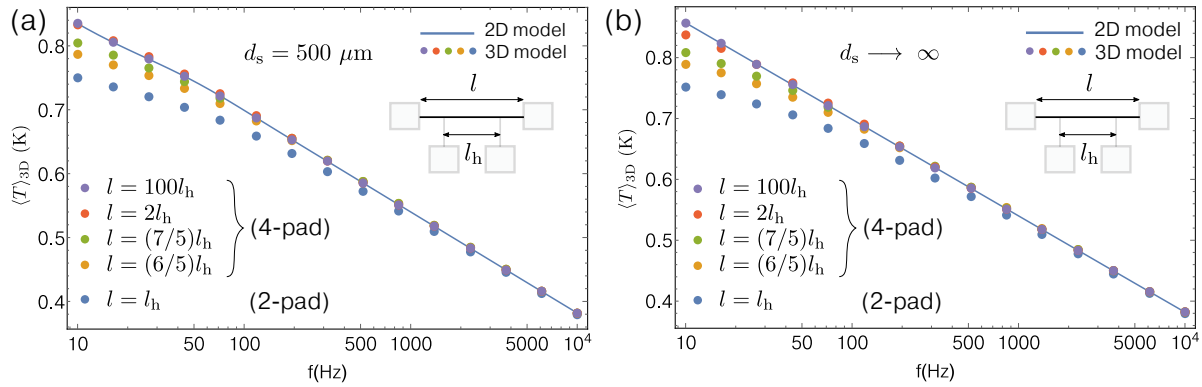

Figure 4.8: Temperature oscillation calculated using a 3D (filled cicrles) or 2D (full line) model. In the 3D model, the temperature measurement is performed across the inner voltage leads separated by a distance l_h, which can be different from the full length of the heating line l, as shown in inset. (a) For a substrate of finite thickness d_s and (b) for a semi-infinite substrate.

$$\langle T \rangle_{3D} = \frac{4P_l}{\pi^2 l_h k_{s_y}} \int_0^\infty \int_0^\infty \frac{\sin^2(\lambda b)}{(\lambda b)^2} \frac{\sin(\zeta(l/2))\sin(\zeta(l_h/2))}{\zeta^2 \xi \tanh(\xi d_s)} d\lambda d\zeta \tag{4.5a}$$

$$\xi = \sqrt{k_{s_{xy}} \lambda^2 + k_{s_{zy}} \zeta^2 + i\omega \frac{(\rho_s C p_s)}{k_{s_y}}} \tag{4.5b}$$

where an adiabatic boundary condition is imposed at the bottom of the substrate, which has finite thickness d_s. In Figure 4.8(a) is plotted the calculated temperature oscillation of a heater dissipating inside a germanium substrate, for different placements of the inner voltage leads. We do not distinguish between the 2D and 3D models at high frequency. More specifically, the effect of the finite length of the heater on the temperature rise is only relevant in the scenario where $\lambda_{tpd} \sim l$. In this case, the length of the heater cannot be assumed infinite, since the thermal penetration depth has the same order of magnitude. However, we remember that the finite thickness of the substrate is also modifying the linear relation $\langle T \rangle = f(\ln(\omega))$ at low frequency (i.e. $\lambda_{tpd} \sim d_s$), and thus in Figure 4.8(a) we do not distinguish the effect of the heater's finite length on the measured temperature oscillation, from that of the substrate's finite thickness.

To circumvent this issue, we have plotted the temperature oscillation in the case of a semi-infinite substrate in Figure 4.8(b). Therefore the low-frequency flattening that is observed in this plot is only due to the effect of the finite length of the heater. One can avoid low-frequency discrepancies by simply placing the two inner leads far enough away from the ends of the heating line, or fitting the measurement at frequencies high enough such that the effect of the heater's finite length is simply discarded. It is clear from Figure 4.8 that a 2-pad configuration is not recommended, as it would require to confine the thermal penetration depth deeply inside the substrate in order to avoid 3D end effects. Experimentally, this can be difficult to reach, since the electrical frequency needed to confine the thermal penetration "deeply" enough inside the substrate becomes very high, especially at low temperature.

4.3.2 Additional criteria for using the slope method

In a similar way to what have been done by Borca-Tasciuc *et al.*[123], who provided several criteria for using the slope method with an error of less than 1%, as a function of the heater

half-width to thermal penetration depth ratio, $(b/(\lambda_{\text{tpd}}\sqrt{k_{s_{xy}}}))$, and substrate's thickness to thermal penetration depth ratio, $(d_s/\lambda_{\text{tpd}})$, (see also Chapter 3.1.2), we would like to provide a similar criterion that would allow one to use the slope method with less than 1% error, as a function of the heater's length to thermal penetration depth ratio, (l/λ_{tpd}).

It was indeed suggested by Jacquot *et al.*[170] that the error depends on the quantity l/λ_{tpd}, and suggested a ratio of $l/\lambda_{\text{tpd}} \approx 4.7$ when using a 4-pad configuration, or $l/\lambda_{\text{tpd}} \approx 15$ for a 2-pad configuration. However, these suggested values were not specific to the error made when using the *slope* method, but rather they represent the *relative* difference between the temperature oscillation *amplitude* calculated using Cahill's formula (Eq.(3.10)), and the temperature oscillation calculated using their 3D FEM model. Besides, their 4-pad geometry only treats the specific case where $l/l_{\text{h}} = 2$.

In the following, we provide a criterion for using the slope method with 1% of accuracy, in the case of a semi-infinite substrate. This criterion indeed depends upon the ratio $(l/(\lambda_{\text{tpd}}\sqrt{k_{s_{zy}}}))$ as well as the ratio (l_{h}/l), i.e. the placement of the voltage leads. The normalized slope is defined as

$$\text{normalized slope} = \frac{\partial Re\{\langle T\rangle_{3\text{D}}\}/\partial \ln(\omega)}{\left(-P_l/2\pi k_{s_y}\sqrt{k_{s_{xy}}}\right)} \tag{4.6}$$

and should be equal to 1 when the slope of the 3D model matches that of the approximate solution Eq.(3.10). The derivation of the normalized slope is deferred to Appendix A. For a semi-infinite substrate and when the thermal penetration depth is much larger than the heater half-width to anisotropy ratio $(\lambda_{\text{tpd}} > 5b/\sqrt{k_{s_{xy}}})$, the normalized slope, as defined in Eq. (4.6), is given by

$$\text{normalized slope} = \int_0^\infty \int_0^\infty \frac{4iq^2\sqrt{k_{s_{xy}}}}{\pi l_{\text{h}}\left(k_{s_{xy}}\lambda^2 + k_{s_{zy}}\zeta^2 + iq^2\right)^{3/2}} \frac{\sin(\zeta(l/2))\sin(\zeta(l_{\text{h}}/2))}{\zeta^2} d\lambda d\zeta \tag{4.7}$$

where $q = \sqrt{\rho_s C p_s \omega/k_{s_y}}$, and we remind that $|1/q| = \lambda_{\text{tpd}}$ is the thermal penetration depth.

We plot the normalized slope as a function of q in Figure 4.9(a), for different values of the full length of the heater l, and several l/l_{h} ratios . From this plot, we observe that the normalized slope of the 3D model is close to that of the approximate solution for large q, i.e. small thermal penetration depth, which is the expected behavior. Besides, the higher the (l/l_{h}) ratio, the smaller the q value required for both 3D model and approximate solution to match – a behavior expected as well since, in this case, the ends of the heating line at $z = \pm l/2$ are farther away from the smaller probed region $(z = \pm l_{\text{h}}/2)$ and therefore the experiment becomes insensitive to ends effects.

In Figure 4.9(b), we plot the relative error made when taking the slope of the approximate solution Eq. (3.10), instead of the slope of the 3D model, for determining the thermal conductivity of a substrate when using the slope method. The relative error is plotted as a function of the heater length to thermal penetration depth ratio (to zy anisotropy ratio).

For a given l/l_{h} ratio, but for different l values, corresponding to symbols having the same color with different shapes in Figure 4.9, the error is similar for any l, *when plotted versus the quantity* $(l/(\lambda_{\text{tpd}}\sqrt{k_{s_{zy}}}))$. This strongly suggests that the error is only a function of $(l/(\lambda_{\text{tpd}}\sqrt{k_{s_{zy}}}))$, as suggested by Jacquot *et al.*[170] (where we have added the anisotropy factor). In order to use the conventional slope method within 1% of accuracy, i.e. determining

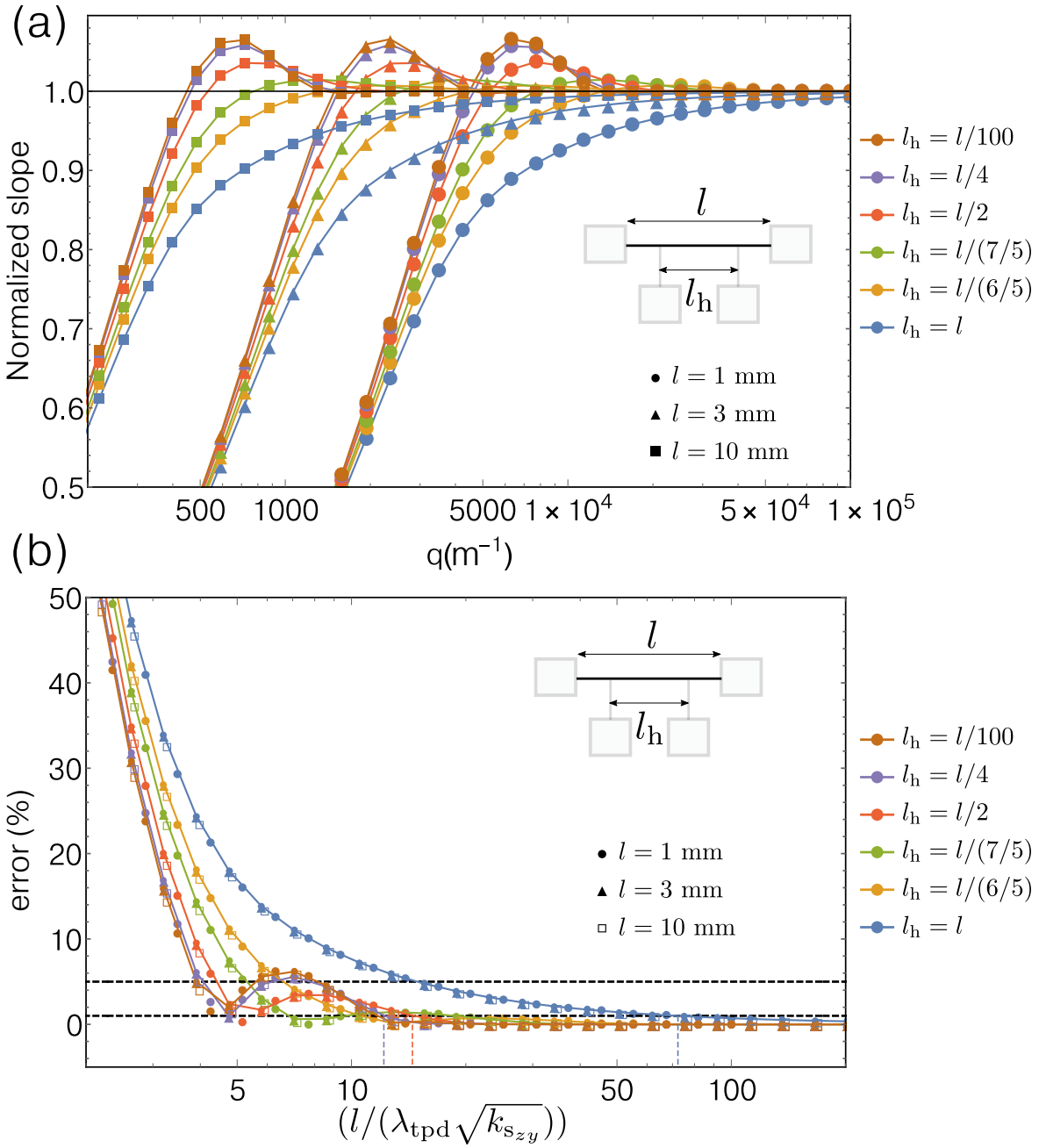

Figure 4.9: (a) Normalized slope computed using Eq.(4.7), as a function of q, for three different values of the length of the heater line (l = 1, 3 and 10 mm), for different values of the length between the voltage leads l_h. (b) Error made when using the approximate solution Eq. (3.10), instead of the 3D model for computing the thermal conductivity of a substrate using the slope method, as a function of heater length to thermal penetration depth ratio (multiplied by zy anisotropy). For a given l/l_h ratio, but for different l_h values, corresponding to symbols having the same color with different shapes in (b), the error overlap when plotted versus the quantity $(l/(\lambda_\mathrm{tpd}\sqrt{k_{\mathrm{s}_{zy}}}))$.

the thermal conductivity of the substrate by taking the slope of $\langle T \rangle = \mathrm{f}(\ln(\omega))$, this analysis suggests to satisfy the following conditions :

$$
\begin{aligned}
l/\left(\lambda_{\mathrm{tpd}}\sqrt{k_{\mathrm{s}_{zy}}}\right) &> 73 \quad \text{if} \quad l_{\mathrm{h}} = l \\
l/\left(\lambda_{\mathrm{tpd}}\sqrt{k_{\mathrm{s}_{zy}}}\right) &> 14.2 \quad \text{if} \quad l_{\mathrm{h}} = l/2 \\
l/\left(\lambda_{\mathrm{tpd}}\sqrt{k_{\mathrm{s}_{zy}}}\right) &> 11.6 \quad \text{if} \quad l_{\mathrm{h}} = l/4
\end{aligned}
$$

If only the amplitude of the temperature oscillation is important, as opposed to the slope versus logarithm of frequency, the following conditions should be respected for the heater/thermometer to be assumed infinitely long in the z direction and thus use a simpler 2D model :

$$
\begin{aligned}
l/\left(\lambda_{\mathrm{tpd}}\sqrt{k_{\mathrm{s}_{zy}}}\right) &> 17.6 \quad \text{if} \quad l_{\mathrm{h}} = l \\
l/\left(\lambda_{\mathrm{tpd}}\sqrt{k_{\mathrm{s}_{zy}}}\right) &> 2.6 \quad \text{if} \quad l_{\mathrm{h}} = l/2 \\
l/\left(\lambda_{\mathrm{tpd}}\sqrt{k_{\mathrm{s}_{zy}}}\right) &> 2.3 \quad \text{if} \quad l_{\mathrm{h}} = l/4
\end{aligned}
$$

In addition to these criteria, the conditions $\lambda_{\mathrm{tpd}} < 5d_{\mathrm{s}}$ and $\lambda_{\mathrm{tpd}} > 5b/\sqrt{k_{\mathrm{s}_{xy}}}$ should be respected as well, following the discussion of Chapter 3.1.3.

Our results, more specifically the condition to satisfy in order to use the slope method with less than 1% of accuracy, are more strict than those suggested by Jacquot *et al.*. This is expected since, as mentioned before, we quantify the error made on the slope of $\langle T \rangle = \mathrm{f}(\ln(\omega))$ rather than the amplitude of $\langle T \rangle$. This is exemplified in Figure 4.10(a), where we use Eq.(4.5) to calculate the temperature oscillation for two semi-infinite substrates, glass and silicon, using the same parameters used by Jacquot *et al.* We numerically find that the relative error on the temperature amplitude is less than 1% for $l/\lambda_{\mathrm{tpd}} = 2.6$ for both substrates in a 4-pad configuration using $l_{\mathrm{h}} = l/2$, as shown in Figure 4.10(b), which is somewhat less than their suggested values of 4.7 (though the error approaches 1% at $l/\lambda_{\mathrm{tpd}} = 4.7$ as can bee seen in Figure 4.10). In a 2-pad configuration ($l = l_{\mathrm{h}}$), the relative error on the temperature amplitude is less than 1% for $l/\lambda_{\mathrm{tpd}} = 17.6$, in reasonable agreement with their suggested value of 15. We note that the error on the amplitude of the temperature oscillation is exactly the same for the two substrates, which have a large contrast in terms of thermal conductivities, for similar $l/(\lambda_{\mathrm{tpd}}\sqrt{k_{zy}})$ and l/l_{h} ratios. A similar conclusion is drawn for the error on the slope of the temperature oscillation versus logarithm of frequency.

The present study and the resulting conditions to be satisfied in order to use the slope method with less than 1% error are useful when designing the transducer's dimensions prior to start its fabrication. Importantly, these conditions provide guidelines to follow in the data treatment if the slope method is used to determine the substrate's thermal conductivity.

4.3.3 Example of application : highly conductive substrate

As a practical example, we provide experimental data from measurements carried out on a sapphire substrate at 100 K. For crystalline materials, when temperature decreases, the thermal conductivity k increases while the heat capacity C_p decreases, following Debye's model of heat capacity. Since the thermal penetration depth is defined as $\lambda_{\mathrm{tpd}} = \sqrt{k/(\rho C_p \omega)}$, it increases

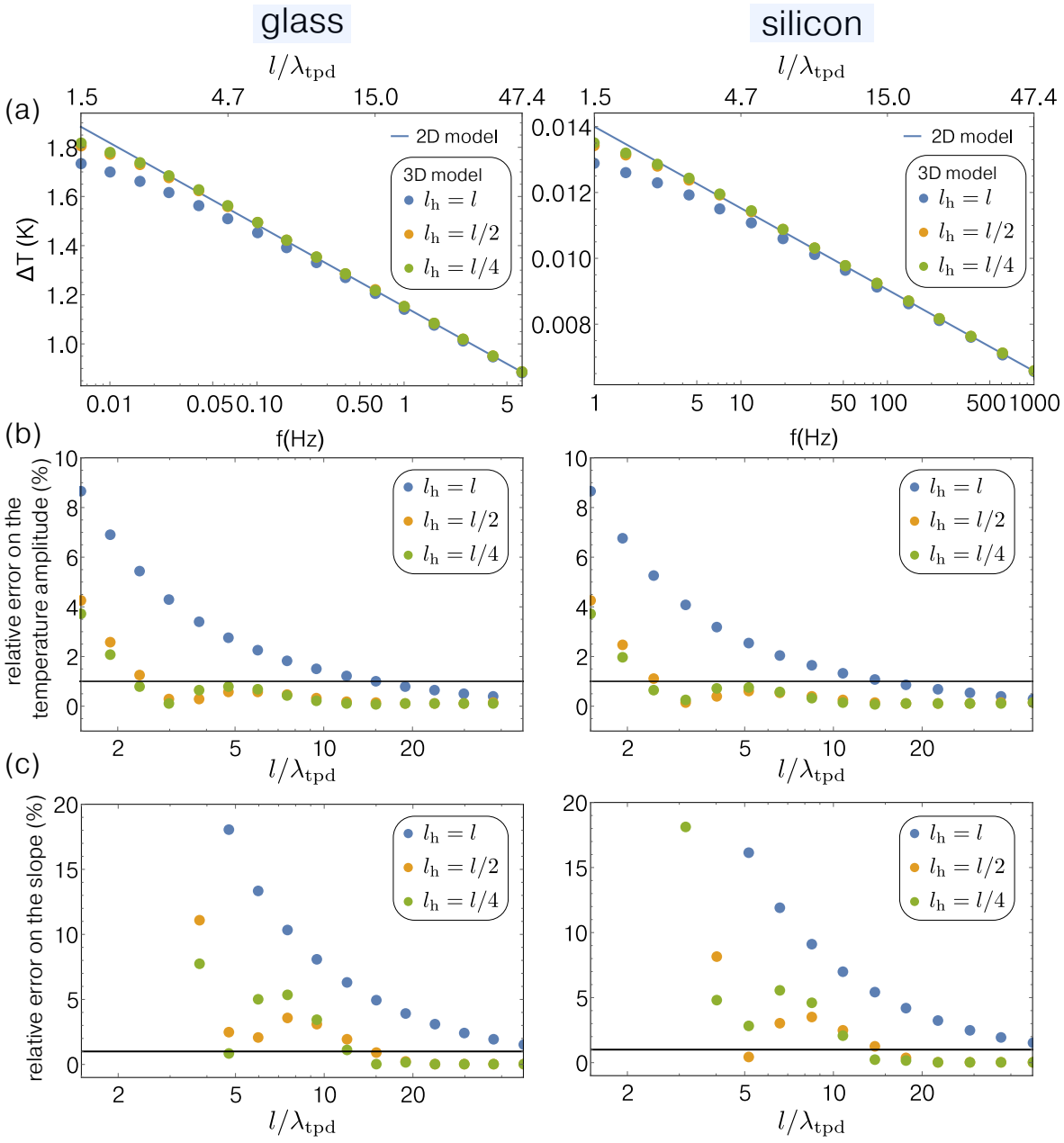

Figure 4.10: Temperature oscillation versus frequency in 2D and 3D, using several placements of the voltage leads, for glass and silicon. Note the difference in the frequency range that is spanned for both materials. Comparison of (b) the relative error between the calculated amplitude of the 3D model and the 2D model, and (c) the relative error of the slope of $\langle T \rangle$ versus $\ln(\omega)$ for the 2D and 3D models. This is the same comparison that was done by Jacquot *et al.*[170] using silicon and glass. We emphasize in this figure that the amplitude of the temperature oscillation can be very similar between the 2D and 3D models for low ratio of l/λ_{tpd} (less than 1% error for l/λ_{tpd}=2.3, 2.6 or 17.6 if l_h/l=1/4, 1/2 or 1). However, the *slope* versus $\ln(\omega)$ of the 2D and 3D models are similar for *higher* l/λ_{tpd} ratios (less than 1% error for l/λ_{tpd}=11.6, 14.2 or 73 if l_h/l=1/4, 1/2 or 1). For simplicity we have set $k_{s_{zy}} = 1$.

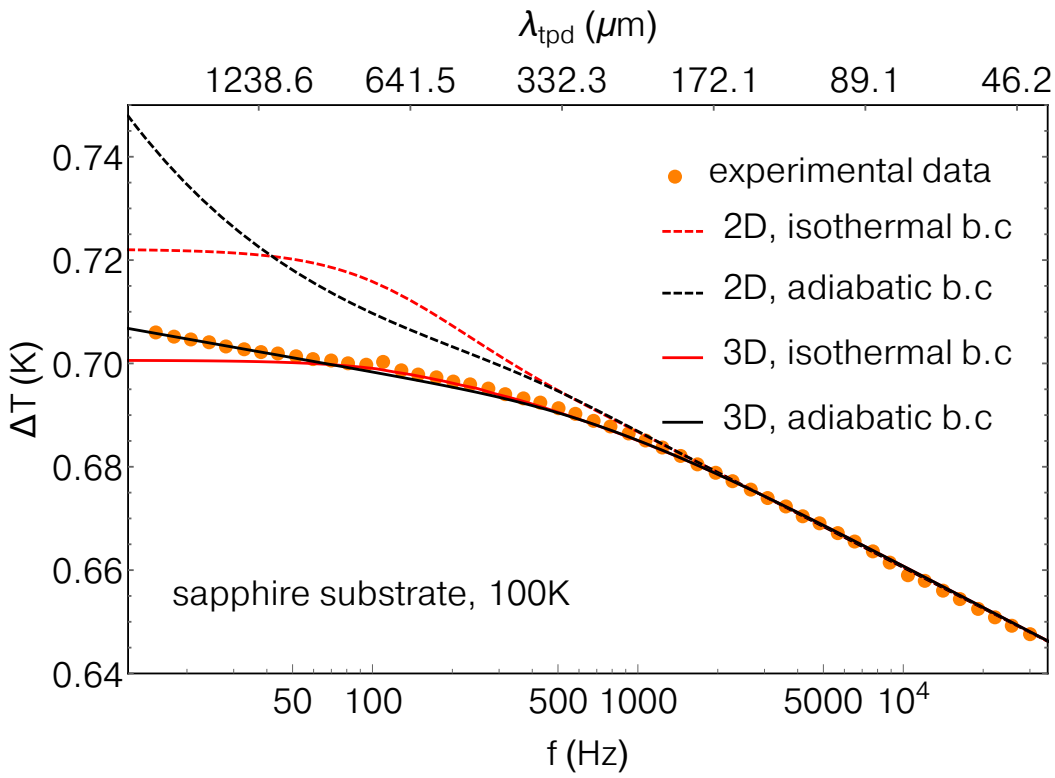

Figure 4.11: Temperature oscillation versus frequency measured on a sapphire substrate at 100 K, with 2D (Eq.(3.23a) and Eq.(3.23b)) and 3D calculations (Eq. (4.5)) using different boundary conditions (b.c) at the substrate/sample holder interface. At low frequency, the finite thickness of the substrate alone cannot explain the discrepancy between the measurement and the 2D model. In this case, one should use a 3D model to take into account the heater's finite length to better fit experimental data at low frequency.

substantially when temperature decreases because of the temperature dependence of k and C_p. For example, at 100 K, sapphire has a thermal conductivity of around 350 W.m^{-1}.K^{-1} and $\rho Cp = 4.73 \times 10^5$J.g^{-1}.m^{-3}, leading to $\lambda_{\text{tpd}} \approx 1.4$ mm at $f = 30$ Hz, which can be of the same order of magnitude as the length of the thermometer, or even higher. In Figure 4.11, we plot the measured temperature rise as a function of electrical frequency, and compare it to the 2D and 3D models, for different boundary conditions at the bottom of the substrate. At low frequency, and given the relatively small heater length ($l = 700$ μm and $l_{\text{h}} = 500$ μm), the 3D model is more appropriate. Importantly, the finite thickness of the substrate (about 700 μm) cannot on its own explain the low-frequency behavior of the measured temperature oscillation. The 2D model using adiabatic boundary condition at the bottom of the substrate is very different from the measurement at low frequency and is thus disregarded in this case. The 2D model using isothermal boundary condition is equivalent to a perfect heat sink beneath the substrate, i.e. a sample holder with very high thermal conductivity. Even though this is the case in this situation, where the sample holder made of copper has a very large thermal conductivity at 100 K (>500 W.m^{-1}.K^{-1}), the 2D model does not fit well at low frequency, suggesting that 3D end effects are indeed responsible for the low-frequency behavior of the temperature oscillation.

5 Using separate lines for heating and sensing : the 2ω method

5.1 The 2ω method : principle and implementation

The previous chapters have been focused on the 3ω method and its range of applicability, according to the simplicity of the model one wants to use to infer a material's thermal properties. The method has been shown to be powerful for easily determining the thermal conductivity of thick substrates, while the thermal conductivity of thin films and the amplitudes of TBRs can be obtained as well by performing several experiments along with careful data analysis. In this section, we will present a measurement technique that is very close to the original 3ω method, the only difference being that the heater and thermometer are distinct lines. It was proposed by Ramu and Bowers[1] and is referred to as the 2ω method. Its major advantages are an enhanced sensitivity to thermal anisotropy, reduced sensitivity to thermal boundary resistances, and under certain conditions enhanced sensitivity to thermally conductive films (when compared to the 3ω method). Besides, the measurement setup does not require a differential bridge, an therefore can be easier to implement.

Exactly as in the 3ω method, an ac current at electrical angular frequency $\omega_e = 2\pi f$ passes through a metallic line which serves as a heater, dissipating heat via Joule heating, leading to a temperature oscillation at $2\omega_e$. This temperature oscillation propagates through the sample, and is measured *using a nearby sensor*, as shown in Figure 5.2. A DC current I_{DC} passes through the thermometer of electrical resistance :

$$R_{\mathrm{e,th}} = R_{\mathrm{e,0,th}}(1 + \beta \Delta T_{\mathrm{tot}})$$

to sense the temperature oscillation at $2\omega_e$, such that a voltage $V_{2\omega_e}$ proportional to the temperature oscillation is read across the thermometer :

$$\begin{aligned} V &= R_{\mathrm{e},0,\mathrm{th}}(1+\beta(\Delta T_{\mathrm{DC}}+\Delta T_{2\omega_e}))\times I_{\mathrm{DC}} \\ &= R_{\mathrm{e},0,\mathrm{th}}I_{\mathrm{DC}}+R_{\mathrm{e},0,\mathrm{th}}I_{\mathrm{DC}}\beta\Delta T_{\mathrm{DC}}+R_{\mathrm{e},0,\mathrm{th}}I_{\mathrm{DC}}\beta\Delta T_{2\omega_e} \\ &= V_{\mathrm{DC}}+V_{2\omega_e} \end{aligned}$$

and thus

$$\Delta T_{2\omega_e}=\frac{V_{2\omega_e}}{R_{\mathrm{e},0,\mathrm{th}}I_{\mathrm{DC}}\beta} \qquad \text{with} \qquad \beta=\frac{1}{R_{\mathrm{e},0,\mathrm{th}}}\frac{dR_{\mathrm{e,th}}}{dT} \tag{5.1}$$

The in-phase and out-of-phase components of the temperature oscillation are read using the in-phase and out-of-phase components of the voltage, as read by the lock-in amplifier. The voltage across the thermometer has a DC component and a component at $2\omega_e$, the latter being proportional to the temperature oscillation generated by the heater, whose amplitude and phase are related to the material's thermal properties. The DC component is several orders of magnitude larger than the $2\omega_e$ component, typically $V_{\mathrm{DC}}/V_{2\omega_e}=(\beta\Delta T_{2\omega_e})^{-1}$, and thus should be attenuated or removed for achieving better sensitivity. This is readily achieved by using a high-pass filter, which is implemented in most commercial lock-in amplifiers as the "input coupling mode". When set to "AC", any voltage below a few tens of mHz is removed by a series-capacitor, thereby removing the DC voltage. The general setup needed to perform the measurement is shown in Figure 5.1. The ac current source can be a true current source,

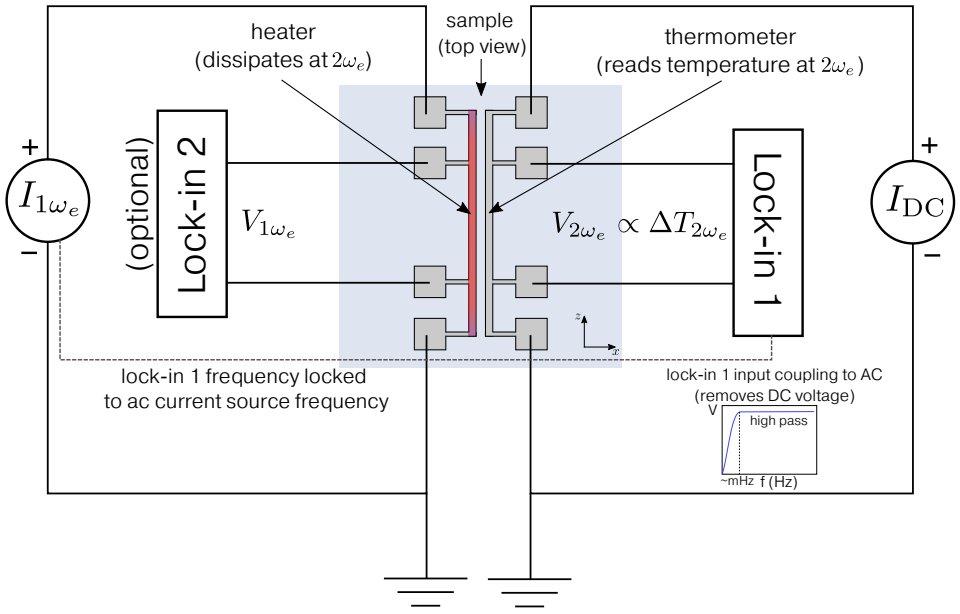

Figure 5.1: General setup for measuring the temperature oscillation generated by the heater, using a nearby temperature sensor.

the voltage output from lock-in 1 followed by a voltage-to-current (V-to-I) converter, or only the voltage output of lock-in 1, under the condition that the resulting current is properly read/calculated. For the DC current source, there is a DC voltage source on the back-panel of most lock-in amplifiers, which can be used to provide a DC current (with a V-to-I converter or large ballast resistor in series). Lock-in 2 in Figure 5.1 is optional as the resistance of the heater can be measured separately before the experiment, instead of measuring it during the experiment. Overall, it depends on the instruments that are available, see for instance Refs.

1 and 179 for some examples of different setups. The temperature coefficient of resistance of the thermometer is measured as usual by measuring the resistance of the metallic element in a four-probe configuration as a function of temperature, under vacuum. The next step consists in comparing the measured temperature oscillation to a thermal model, which we describe now.

5.2 Heat transfer model for the 2ω method

In the scenario where the heater and thermometer are two distinct lines separated by a distance d_{ht}, as illustrated in Figure 5.2, the temperature oscillation measured by the thermometer can be derived in a straightforward manner, using the previously determined results obtained for the 3ω geometry. Going back to Eq. (3.23) for the general case of a multilayer system heated with a metallic line of width $2b_1$, the only difference with the foregoing derivation is that since we are measuring the temperature oscillation at a distance d_{ht} from the heater, we perform the temperature spatial averaging from $-b_2 + d_{\text{ht}}$ to $b_2 + d_{\text{ht}}$, where b_2 refers to the thermometer half-width.[1] The temperature oscillation measured across the thermometer is then

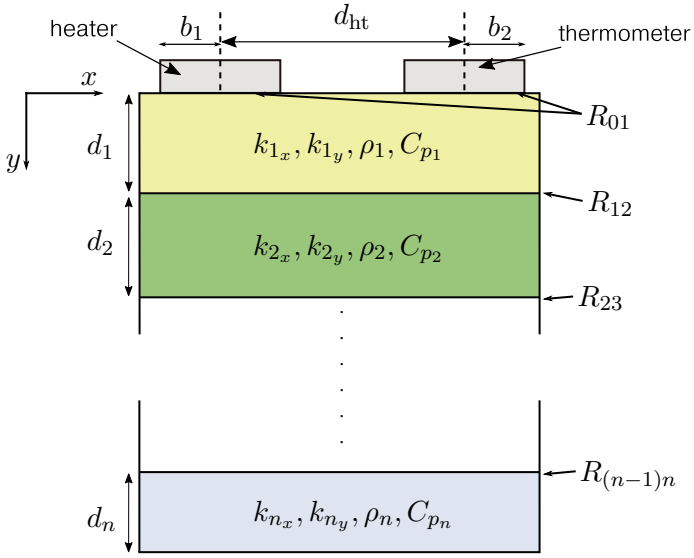

Figure 5.2: Schematic representation of a multilayer system with two metallic lines deposited on top of the first layer, separated by a distance d_{ht}. One is used as a heater while the other one is used as a temperature sensor. This configuration can be used to be more sensitive to in-plane heat conduction, and less sensitive to thermal boundary resistances.

$$\langle T(x,0)\rangle_{2\text{ lines}} = \frac{1}{2b_2}\int_{d_{\text{ht}}-b_2}^{d_{\text{ht}}+b_2}\left\{\frac{1}{2\pi}\int_{-\infty}^{\infty}\frac{2P_l\sin(\lambda b_1)}{(2b_1)\lambda}re^{i\lambda x}d\lambda\right\}dx$$

where r is a ratio which depends on the boundary condition at the bottom surface. It leads to

$$\text{isothermal b.c} : \langle T\rangle_{2\text{ lines}} = \frac{P_l}{2b_1b_2\pi}\int_{-\infty}^{\infty}\frac{\sin(\lambda b_1)\sin(\lambda b_2)}{\lambda^2}\frac{B}{D}e^{i\lambda d_{\text{ht}}}d\lambda \tag{5.2a}$$

$$\text{adiabatic b.c} : \langle T\rangle_{2\text{ lines}} = \frac{P_l}{2b_1b_2\pi}\int_{-\infty}^{\infty}\frac{\sin(\lambda b_1)\sin(\lambda b_2)}{\lambda^2}\frac{A}{C}e^{i\lambda d_{\text{ht}}}d\lambda \tag{5.2b}$$

[1] We could also take the Fourier transform of the heat flux from $d_{\text{ht}} - b_1$ to $d_{\text{ht}} + b_1$ and then perform the spatial averaging from $-b_2$ to b_2

where A, B, C and D are computed from

$$\begin{pmatrix} A & B \\ C & D \end{pmatrix} = \prod_{j=1}^{n} \begin{pmatrix} 1 & R_{(j-1)j} \\ 0 & 1 \end{pmatrix} \begin{pmatrix} \cosh(\gamma_j d_j) & \frac{1}{k_{jy}\gamma_j}\sinh(\gamma_j d_j) \\ k_{jy}\gamma_j \sinh(\gamma_j d_j) & \cosh(\gamma_j d_j) \end{pmatrix} \tag{5.2c}$$

$$\gamma_j = \sqrt{k_{j_{xy}}\lambda^2 + i\omega\frac{(\rho C_p)_j}{k_{j_y}}} \tag{5.2d}$$

In 3D, for a *heater* of finite length l, dissipating heat power per unit length P_l, the temperature oscillation that is measured across the inner leads of the *thermometer*, which are separated by a distance l_h is given as :

$$\text{isothermal b.c} : \langle T\rangle_{\text{2 lines, 3D}} = \frac{P_l}{\pi^2}\int_{-\infty}^{\infty}\int_{-\infty}^{\infty}\frac{B}{D}\frac{\sin^2(\lambda b)}{(\lambda b)^2}\frac{\sin(\zeta(l/2))\sin(\zeta(l_\mathrm{h}/2))e^{i\lambda d_\mathrm{ht}}}{l_\mathrm{h}\zeta^2}d\lambda d\zeta \tag{5.3a}$$

$$\text{adiabatic b.c} : \langle T\rangle_{\text{2 lines, 3D}} = \frac{P_l}{\pi^2}\int_{-\infty}^{\infty}\int_{-\infty}^{\infty}\frac{A}{C}\frac{\sin^2(\lambda b)}{(\lambda b)^2}\frac{\sin(\zeta(l/2))\sin(\zeta(l_\mathrm{h}/2))e^{i\lambda d_\mathrm{ht}}}{l_\mathrm{h}\zeta^2}d\lambda d\zeta \tag{5.3b}$$

where A, B, C and D are computed from

$$\begin{pmatrix} A & B \\ C & D \end{pmatrix} = \prod_{j=1}^{n} \begin{pmatrix} 1 & R_{(j-1)j} \\ 0 & 1 \end{pmatrix} \begin{pmatrix} \cosh(\xi_j d_j) & \frac{1}{k_{j_y}\xi_j}\sinh(\xi_j d_j) \\ k_{j_y}\xi_j \sinh(\xi_j d_j) & \cosh(\xi_j d_j) \end{pmatrix} \tag{5.3c}$$

$$\xi_j = \sqrt{k_{j_{xy}}\lambda^2 + k_{j_{zy}}\zeta^2 + i\omega\frac{(\rho_j C_{p_j})}{k_{j_y}}} \tag{5.3d}$$

5.2.1 Temperature oscillation for a semi-infinite substrate

For a semi-infinite substrate without films and TBRs, in the case where the heater and thermometer have identical widths ($b_1 = b_2 \equiv b$), application of Eq. (5.2) with $d_1 = d_\mathrm{s} \to \infty$ leads to

$$\langle T\rangle_{\text{2 lines, semi-inf}} = \frac{P_l}{2\pi k_y}\int_{-\infty}^{\infty}\frac{\sin^2(\lambda b)}{(\lambda b)^2}\frac{e^{i\lambda d_\mathrm{ht}}}{\sqrt{k_{xy}\lambda^2 + i\omega\frac{(\rho C_p)}{k_y}}}d\lambda$$

Taking advantage of the parity of the integrand combined with the symmetry of the integration interval, it further reduces to

$$\langle T\rangle_{\text{2 lines, semi-inf}} = \frac{P_l}{\pi k_y}\int_{0}^{\infty}\frac{\sin^2(\lambda b)}{(\lambda b)^2}\frac{\cos(\lambda d_\mathrm{ht})}{\sqrt{k_{xy}\lambda^2 + i\omega\frac{(\rho C_p)}{k_y}}}d\lambda \tag{5.4}$$

This is to be compared to Eq. (5.5), provided by Ramu and Bowers[1], who derived the temperature oscillation sensed by the thermometer for a similar geometry to that of Figure 5.2, in the case of a semi-infinite substrate. They used the result of the temperature oscillation sensed by an infinitely narrow heater line, convolved it across the width of the heater, and then performed the spatial average over the thermometer width. This lead to[150]

$$\langle T\rangle_{\text{Ramu}} = \frac{P_l}{\pi\sqrt{k_x k_y}(2b_1)(2b_2)}\int_{x=-b_1}^{x=b1}\int_{\tau=-b_2}^{\tau=b_2} K_0\left(\sqrt{\frac{i\omega\rho C_p}{k_x}}(d_\mathrm{ht}+\tau-x)\right)d\tau dx \tag{5.5}$$

They astutely used cylindrical coordinates because of the geometry of the problem, therefore their analytical solution is expressed using a Bessel function (K_0 is the zeroth-order modified Bessel function of the second kind), which is a general solution of the heat equation in cylindrical coordinates for a narrow heater strip.[137] Both solutions are based on the same assumptions and therefore are equivalent, as shown in Figure (5.3), where we plot Ramu and Bower's expression and the expression we have derived. Eq. (5.2) have several assets. First, it inherently

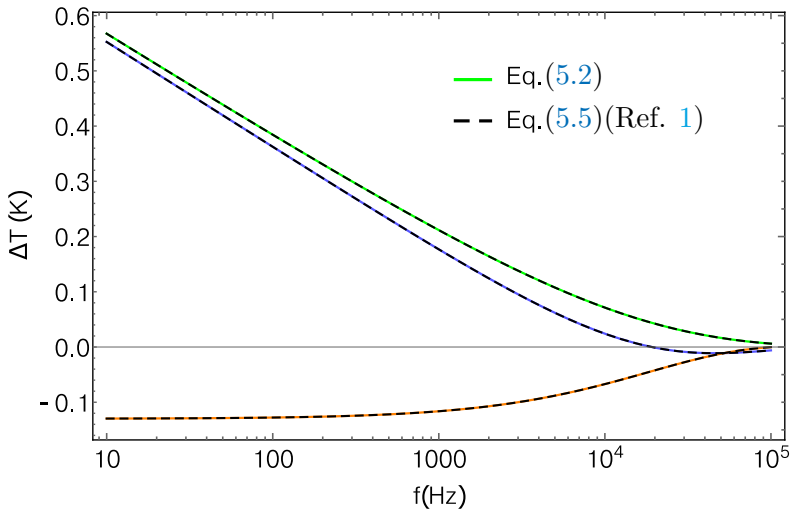

Figure 5.3: Calculated temperature oscillation as a function of electrical frequency for a geometry where the heater and thermometer are two distinct metallic lines. Dashed lines are the solutions from Ref. 1 whereas solid lines are Eq. (5.2). The three lines refer to the absolute value (green), real (purple) and imaginary (orange) parts of the temperature oscillation. Parameters used for the simulation are $P_l = 27$ W/m, $\rho C_p = 1.65$ MJ/m^3.K, $k_{xy} = 1$, $k_y = 52$ W/m.K, $d = 20$ μm, $b_1 = b_2 = 2.5\mu$m.

takes into account the thickness of the specimen studied, and therefore low frequency discrepancies that are measured due to the finite thickness of the substrate can be quantified. Then, and most importantly, its generalization to n layers provides a useful tool to study multilayer systems, without the need of implementing a Finite Element Method scheme, which can be computationally intensive.

Approximations of the solution for a semi-infinite substrate

The main drawback is the integral form of the solution, leading to little physical intuition about which parameters are important. It is possible to express Eq. (5.4) in another form using Parseval's theorem (sometimes called the Parseval–Plancherel identity). This theorem allows to compute the indefinite integral of a product of two functions as the integral of the product of their Fourier transforms. It is therefore useful when the Fourier Transforms of the functions to integrate are known, and in particular if their integral leads to a simple form (in the best scenario, it would lead to a closed-form expression rather than an integral expression).

To simplify Eq. (5.4), we use Parseval's theorem and we choose the two functions to be transformed :

$$f(\lambda) = \frac{\sin^2(\lambda b)}{(\lambda b)^2} \quad \text{and } g(\lambda) = \frac{\cos(\lambda d_{\text{ht}})}{\sqrt{k_{xy}\lambda^2 + q_y^2}} \tag{5.6}$$

The Fourier transform $\widehat{f(k)}$ of $f(\lambda)$ is the triangle function :

$$\widehat{f(k)} = \begin{cases} \frac{\pi}{b}\left(1 - \frac{|k|}{2b}\right), & -2b < k < 2b \\ 0 & \text{otherwise} \end{cases}$$

and the Fourier transform $\widehat{g(k)}$ of $g(\lambda)$ is

$$\widehat{g(k)} = \frac{1}{\sqrt{k_{xy}}}\left(K_0(q_x|d_{\text{ht}} - k|) + K_0(q_x|d_{\text{ht}} + k|)\right) \tag{5.7}$$

Using Parserval's theorem, the integral can therefore be expressed as

$$\begin{aligned} &\int_{-\infty}^{\infty} \frac{\sin^2(\lambda b)}{(\lambda b)^2} \frac{\cos(\lambda d_{\text{ht}})}{\sqrt{k_{xy}\lambda^2 + q_y^2}} d\lambda \\ &= \frac{1}{2\pi}\int_{-2b}^{2b} \frac{\pi}{b}\left(1 - \frac{|k|}{2b}\right) \frac{1}{\sqrt{k_{xy}}}\left(K_0(q_x|d_{\text{ht}} - k|) + K_0(q_x|d_{\text{ht}} + k|)\right) dk \end{aligned}$$

where the new limits of integration are set according to the definition of $\widehat{f(k)}$. In the 2ω geometry, as displayed in Figure 5.2, the inequality $d_{\text{ht}} > (b_1 + b_2)$ always holds (in this example $d_{\text{ht}} > 2b$ since $b_1 = b_2$). Indeed, the distance between the heater and thermometer is always larger than their width, otherwise they would overlap. We can therefore remove the absolute value in the argument of the Bessel functions since $k < 2b$ and therefore $d \pm k > 0$. Furthermore, using the parity of the integrand, the temperature oscillation sensed by the thermometer can eventually be written as

$$\langle T \rangle_{\text{2 lines, semi-inf}} = \frac{P_l}{2\pi b\sqrt{k_x k_y}} \int_0^{2b} \left(1 - \frac{k}{2b}\right)\left(K_0(q_x(d_{\text{ht}} - k)) + K_0(q_x(d_{\text{ht}} + k))\right) dk \tag{5.8}$$

Note that Eq. (5.8) can be solved, leading to a combination of Struve and Bessel functions. Here we will examine specific cases that are of interest during an experiment, leading to solutions that are easy to manipulate, starting from Eq.(5.8). In the scenario where the heater-to-thermometer distance is much larger than their width, i.e. $d_{\text{ht}} \gg 2b$, since the integration variable has the maximum value of $k = 2b$, this implies $k \ll d_{\text{ht}}$, and we can set $K_0(q_x(d_{\text{ht}} \pm k)) \approx K_0(q_x d_{\text{ht}})$. This leads to

$$\langle T \rangle_{d_{\text{ht}} \gg 2b} = \frac{P_l}{\pi\sqrt{k_x k_y}} K_0\left(q_x d_{\text{ht}}\right) \tag{5.9}$$

We notice that this simply corresponds to the temperature oscillation

$$\frac{P_l}{\pi\sqrt{k_x k_y}} K_0\left(q_x r\right)$$

measured at a distance $r = d_{\text{ht}}$, for an infinitely long and narrow heater, as derived by Carslaw and Jaeger.[137] In this configuration (as depicted in Figure 5.2), we notice that the characteristic length is the thermal penetration depth "in-plane", $\lambda_{\text{tpd},x} = |1/q_x|$. We put emphasis on "in-plane" since the thermal penetration depth was expressed using the cross-plane component of the thermal conductivity k_y hitherto. For large $q_x d_{\text{ht}}$, i.e. when the thermal penetration depth in plane is much smaller than the heater-to-thermometer distance, the Bessel function can be written as[137]

$$K_0(q_x d_{\text{ht}}) \underset{q_x d_{\text{ht}} \gg 1}{\approx} \sqrt{\frac{\pi}{2 q_x d_{\text{ht}}}} e^{-q_x d_{\text{ht}}}$$

leading to

$$\langle T \rangle_{d_{\mathrm{ht}} \gg \lambda_{\mathrm{tpd},x} \gg 2b} = \frac{P_l}{\sqrt{2\pi}\sqrt{k_x k_y}} \sqrt{\frac{1}{q_x d_{\mathrm{ht}}}} e^{-q_x d_{\mathrm{ht}}} \tag{5.10}$$

In the opposite case where the thermal penetration depth is much larger than the heater-to-thermometer distance, i.e. $q_x d_{\mathrm{ht}} \ll 1$ we have[137] a result that resembles that of the original 3ω method :

$$\langle T \rangle_{\lambda_{\mathrm{tpd},x} \gg d_{\mathrm{ht}} \gg 2b} = \frac{P_l}{\pi\sqrt{k_x k_y}} \left(-\ln\left(\frac{1}{2} q_x d_{\mathrm{ht}}\right) + \gamma \right) \tag{5.11}$$

where γ is the Euler-Mascheroni constant. It is indeed close to the expression derived for the 3ω geometry, since the thermal penetration depth is much larger than the heater-to-thermometer distance, and hence we can approximate the heater and thermometer as one single element in this limit. However, it does not offer many advantages when compared to the original 3ω method using a single line for both heating and sensing, since taking the slope of the temperature oscillation with respect to logarithm frequency also gives access to the quantity $\sqrt{k_x k_y}$.

The major advantage of using two separate lines relies on the very weak (or zero) sensitivity of the temperature oscillation measured across the thermometer to interfacial thermal resistances, as will be shown shortly. When combined with a classical 3ω method, it permits the measurement of the in-plane component of the thermal conductivity of the material that is studied. If the material is isotropic, then the method can be used to measure the volumetric heat capacity of the substrate, since every other parameters in the thermal model are known.

The sensitivity of the method to the in-plane component of the thermal conductivity can be enhanced for very large heater-to-thermometer distance, with the counterpart of a smaller temperature oscillation to measure.[150] To prove these statements, we will first perform a sensitivity analysis on our model Eq. (5.9) of the measured temperature oscillation for a semi-infinite substrate, and then calculate the contribution of the heater/substrate thermal boundary resistance to the temperature oscillation that is measured by the thermometer.

5.3 Sensitivity analysis

A sensitivity analysis is a powerful tool to quantify how important one specific parameter of a model is, and how does it change quantitatively the output of the model, when the parameter is changed by a small amount. In particular, it is useful to use this tool when an intuitive evaluation of the model is difficult. We will use this tool in the following for determining how important each parameter of the model is, in a 2ω configuration. The sensitivity $S^y_{x_i}$ of model y to parameter x_i is defined as :

$$S^y_{x_i} = \left(\frac{\partial y}{\partial x_i}\right)\left(\frac{x_i}{y}\right)$$

For more informations about how this formula is derived, the reader is referred to Appendix B. It reflects how a relative change of a parameter x_i will affect the model y. For example, a value of $S^y_{x_i} = -1$ means that a 5 % increase in x_i will result in a 5 % decrease in y. In our situation, the model that we want to study is the temperature oscillation that is measured by the thermometer ($\langle T \rangle$) while the parameters can be the width of the metallic line, the specific heat of the substrate, the thermal boundary resistance at one interface, or any other parameter that enters into the thermal model.

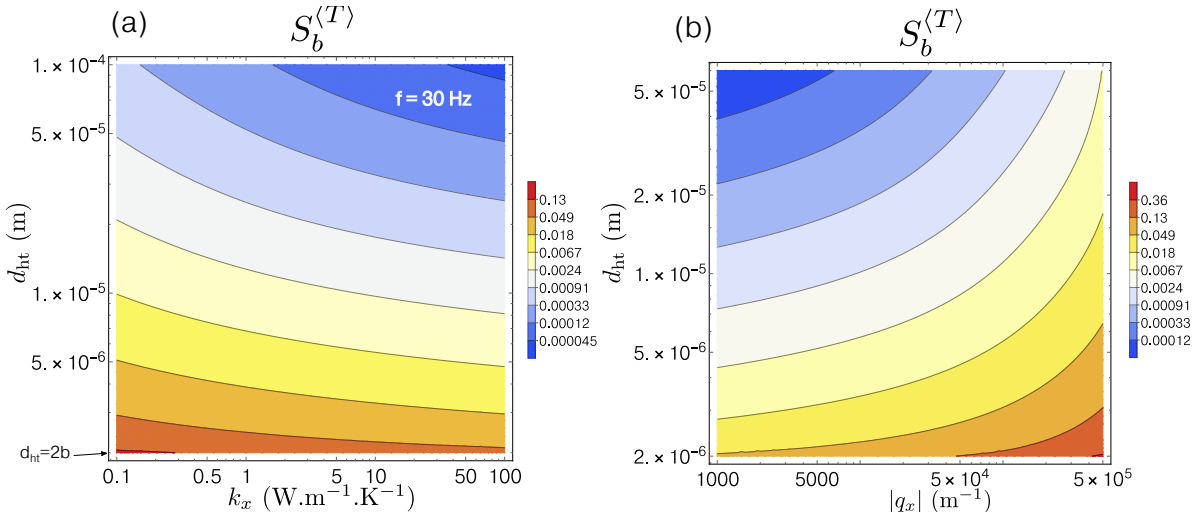

Figure 5.4: Sensitivity of the real part of the temperature oscillation across the thermometer $\langle T\rangle$ (calculated using Eq. (5.8)) to the thermometer half-width b, as a function of different parameters. (a) As a function of k_x and $d_{\rm ht}$ using $b = 1$ μm, $\rho C_p = 1.65$ MJ.m^{-3}.K^{-1} and $f = 30$ Hz. (b) As a function of $|q_x|$ and $d_{\rm ht}$ using $b = 1$ μm. In graph (b), $d_{\rm ht}$ is allowed to vary until 60 μm because higher values (at high $|q_x|$) physically describes infinitely small value of the temperature oscillation (under reasonable heating power), leading to sensitivity with less physical meaning.

5.3.1 Sensitivity to the heater and thermometer widths

Firstly, we plot the sensitivity of the temperature oscillation to the heater and thermometer width, $S_b^{\langle T\rangle}$, using the temperature oscillation derived for a semi-infinite substrate model, Eq. (5.8), as a function of both the heater-to-thermometer distance $d_{\rm ht}$ and the in-plane thermal conductivity k_x, for a fixed $b = 1$ μm. This could give us some hints about whether Eq. (5.8) is sensitive to b, and lead to directions to follow for eventually finding the conditions to satisfy in order to use its simpler form, Eq. (5.9). Figure 5.4(a) reveals that the measured temperature oscillation is weakly sensitive ($S_b^{\langle T\rangle} < 0.05$ at 30 Hz and $d_{\rm ht} = 4b$) to the heater and thermometer widths (which in this case, are taken to be equal). This is expected from the derived approximation Eq. (5.9), which does not depend upon b at all for $d_{\rm ht} \gg 2b$. We also observe that it is inversely proportional to k_x. It actually depends on a combination of $d_{\rm ht}$ and q_x values, as can be seen in Figure 5.4(b), where we fixed $b = 1\mu$m and spanned $|q_x|$ from 10^3 to 10^6, corresponding to thermal penetration depth decreasing from 1 mm to 2 μm, typical values spanned during an experiment. At higher $|q_x|d_{\rm ht}$, which translates to large heater-to-thermometer ratio compared to thermal penetration depth ($d_{\rm ht} \gg \lambda_{{\rm tpd},x}$), the temperature oscillation measured across the thermometer becomes infinitely small (as can be seen at high frequency in Figure 5.3) and physically impossible to measure. Consequently, even though the sensitivity to b increases in this regime, it would not be possible experimentally to measure such small temperature variations resulting from small changes in b, using reasonable heating power per unit length. Overall, Figure 5.4 tells us that the precise knowledge of the heater or thermometer width are not as important as it is for the traditional 3ω method. Figure 5.4 also tells us that combinations of $d_{\rm ht}$ and q_x lead to almost no dependence of the temperature oscillation to b, suggesting that Eq. (5.9) can be used instead of Eq. (5.8) for these $d_{\rm ht}$ and q_x.

To further support this suggestion, we calculate the relative error, defined as

$$\text{error } (\%) = 100 \times \frac{|\langle T\rangle_{\rm exact} - \langle T\rangle_{\rm approx}|}{\langle T\rangle_{\rm exact}} \tag{5.12}$$

where $\langle T\rangle_{\text{exact}}$ refers to Eq. (5.8) while $\langle T\rangle_{\text{approx}}$ to Eq. (5.9). The error is plotted in Figure 5.5(a) as a function of d_{ht} and electrical frequency f, for fixed values $k_x = 100$ W.m^{-1}.K^{-1}, $\rho C_p = 1.65$ MJ.m^{-3}.K^{-1} and $b = 1$ μm. In this scenario, the error is the largest for small d_{ht} but also depends on the frequency. If $d_{\text{ht}} > 4b$, the error is less than 1% over the frequency range spanned (10-5000 Hz). Therefore the condition $d_{\text{ht}} \gg 2b$ is easily achievable.

In Figure 5.5(b) is plotted the error as a function of q_x and d_{ht}, using, $b = 1$ μm. This highlights that the error is dependent on $|q_x|$, not only k_x, which we expected according to our previous sensitivity calculation. Once again, large relative error for large $|q_x|$ are to be put into perspective, since the temperature oscillations are very small and large *relative* errors are still small enough to be beyond the resolution of our instrumentation. This is shown in Figure 5.5(c), where the relative error is infinitely large, but corresponds to a temperature difference of less than 1 mK (Figure 5.5(d)), in the conservative case of $k_x = 1$ W.m^{-1}.K^{-1} and $P_l = 22.5$ W.m^{-1}. Moreover, for large k_x, high value of $|q_x|$ translates to very large value of the electrical frequency that are not reached during an experiment. For example, $|q_x| = 2.10^5$ translates to $f = 200$ kHz for $k_x = 100$ W.m^{-1}.K^{-1}.

Therefore, for low k_x ($\approx$1 W.m^{-1}.K^{-1}), in order to use Eq. (5.9), we suggest to have $d_{\text{ht}} > 10b$. Eq. (5.8) is preferred otherwise. For larger k_x, the criteria is less severe. For example Eq. (5.9) matches with Eq. (5.8) with less than 1% error for $d_{\text{ht}} = 4b$ and $k_x = 100$ W.m^{-1}.K^{-1}.

5.3.2 Sensitivity to other parameters

In the following, we will express the sensitivity of the measured temperature oscillation to several parameters of interest, other than the heater and thermometers half-widths. To do so, we use the definition of the sensitivity coefficient, as we did above, and apply it to Eq. (5.9) :

$$S_{k_x}^{\langle T\rangle} = \frac{k_x}{\langle T\rangle}\frac{\partial\langle T\rangle}{\partial k_x} = \left(-\frac{1}{2} + \frac{1}{2}\frac{K_1(q_x d_{\text{ht}})}{K_0(q_x d_{\text{ht}})} q_x d_{\text{ht}}\right) \tag{5.13}$$

$$S_{k_y}^{\langle T\rangle} = \frac{k_y}{\langle T\rangle}\frac{\partial\langle T\rangle}{\partial k_y} = -\frac{1}{2} \tag{5.14}$$

$$S_{(\rho C_p)}^{\langle T\rangle} = \frac{(\rho C_p)}{\langle T\rangle}\frac{\partial\langle T\rangle}{\partial(\rho C_p)} = \left(-\frac{1}{2}\frac{K_1(q_x d_{\text{ht}})}{K_0(q_x d_{\text{ht}})} q_x d_{\text{ht}}\right) \tag{5.15}$$

$$S_{d_{\text{ht}}}^{\langle T\rangle} = \frac{d_{\text{ht}}}{\langle T\rangle}\frac{\partial\langle T\rangle}{\partial d_{\text{ht}}} = \left(-\frac{K_1(q_x d_{\text{ht}})}{K_0(q_x d_{\text{ht}})} q_x d_{\text{ht}}\right) \tag{5.16}$$

The measured temperature oscillation's sensitivity to k_y does not depend upon any parameters, meaning that whatever the configuration (frequency, heater-to-thermometer distance, substrate's heat capacity,...), the *relative* change of the temperature oscillation with respect to a change in k_y is constant. Therefore there is no knob to play with in order to be more sensitive to k_y. This can be useful if our goal is precisely to be insensitive to k_y and sensitive to another parameter, such as k_x. Since the sensitivity to k_y is constant with respect to every other parameter, we can try to find a combination of parameters (frequency range, heater-to-thermometer distance) that would be very sensitive to k_x while weakly sensitive to k_y.

In Figure 5.6 are plotted the sensitivity of the temperature oscillation to the parameters defined in Eqs. (5.13)-(5.16), as a function of electrical frequency (Figure 5.6(a)-(b)), and heater-to-thermometer distance (Figure 5.6(c)-(d)). Even though the heater-to-thermometer distance is not a quantity that we want to measure, $S_{d_{\text{ht}}}^{\langle T\rangle}$ is displayed to underline that d_{ht} is

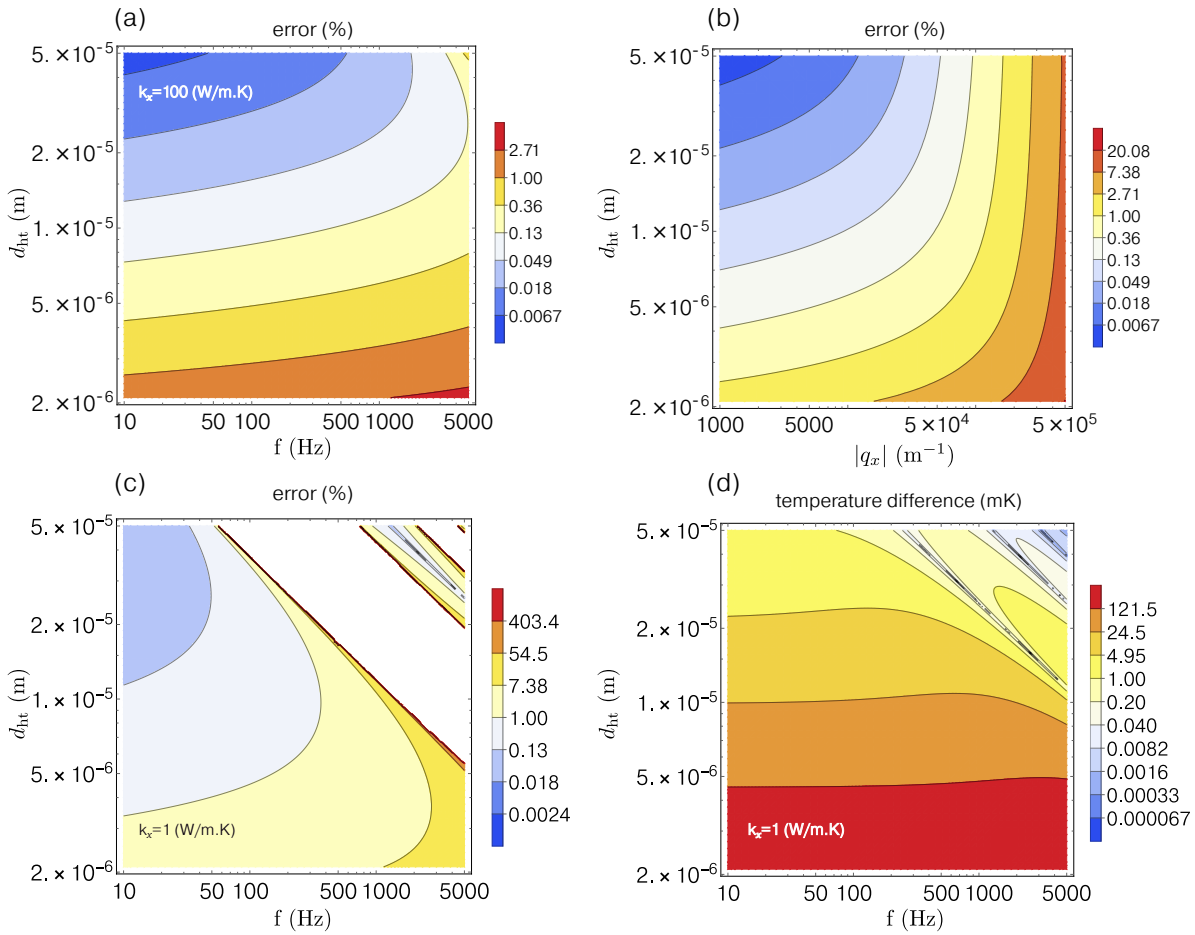

Figure 5.5: Relative error of the real part of the measured temperature oscillation when Eq. (5.9) is used instead of Eq. (5.8), plotted as a function of different parameters. (a) As a function of f and d_{ht} using $k_x = 100$ W.m^{-1}.K^{-1}, $\rho C_p = 1.65$ MJ.m^{-3}.K^{-1}, $b = 1$ μm. (b) As a function of $|q_x|$ and d_{ht}, using, $b = 1$ μm. (c) As a function of f and d_{ht} using $k_x = 1$ W.m^{-1}.K^{-1}, $\rho C_p = 1.65$ MJ.m^{-3}.K^{-1}, $b = 1$ μm. For this value of k_x, the relative error is extremely high (the white areas reflect error above 500%), but it is to be compared to the actual temperature difference between Eq. (5.9) and Eq. (5.8). (d) The temperature difference (in mK) between Eq. (5.9) and Eq. (5.8) is plotted to show that a very high *relative* error arises only for extremely small temperature difference, below 1 mK, which we do not detect experimentally.

a parameter that needs to be carefully measured, since the temperature oscillation is strongly dependent upon this parameter, especially for low k_x at high frequency, as can be seen in Figure 5.6(a)-(b). It is increasingly important as its value increases (Figure 5.6(c)-(d)). Thus, the first conclusion is that the heater-to-thermometer distance must be accurately known for the experiment to be sensitive to other parameters with minimal error.

Sensitivity to k_x is relatively weak when compared to that of k_y in a typical frequency range spanned during an experiment, as can be seen in Figure 5.6(a)-(b) for $d_{\mathrm{ht}} = 10$ μm. The sensitivity to k_x can be increased to be far greater than that to k_y, when the heater-to-thermometer distance is very large and the frequency relatively high, as shown in Figure 5.6(c)-(d). This of course comes with a detrimental lower temperature oscillation to measure, as discussed in the foregoing sensitivity analysis, and mentioned by Ramu and Bowers.[1]

We notice in Figure 5.6(a)-(b) that the sensitivity to the in-plane component of the thermal conductivity, k_x, is negative and then becomes positive as frequency increases. When plotted versus the quantity $\lambda_{\mathrm{tpd},x}/d_{\mathrm{ht}}$, it appears that the sensitivity to k_x is positive when $\lambda_{\mathrm{tpd},x} > d_{\mathrm{ht}}$.

In the case of a large thermal penetration depth in comparison to the heater-to-thermometer distance, the experiment can be seen in a similar way as the 3ω method : the heater and thermometer are close enough, in comparison to $\lambda_{\mathrm{tpd},x}$, such that it is seen as a single element, hence any increase in the thermal conductivity of the material decreases the temperature oscillation sensed by the thermometer, and therefore both $S_{k_x}^{\langle T\rangle}$ and $S_{k_y}^{\langle T\rangle}$ are negative. In the opposite case of $\lambda_{\mathrm{tpd},x} < d_{\mathrm{ht}}$, an increase in the cross-plane component of the thermal conductivity, k_y, still leads to a lower temperature oscillation sensed by the thermometer, but an increase of k_x would in turn increase the temperature sensed across the thermometer. This is because lateral heat spreading would only benefit to a nearby thermometer that is also placed in the lateral direction, as it is the case in this geometry. Obviously, since we are in the limit $\lambda_{\mathrm{tpd},x} < d_{\mathrm{ht}}$, the temperature oscillation sensed by the thermometer would be the smallest, and thus difficult to measure.

One possible way to be more sensitive to k_x than k_y would be to first estimate the amplitude of the temperature oscillation according to our knowledge of the substrate's thermal properties to simulate $\langle T\rangle$ such that it is possible to measure it with sufficient accuracy, choose the largest d_{ht} possible, and perform a measurement at a frequency high enough such that $S_{k_x}^{\langle T\rangle} > S_{k_y}^{\langle T\rangle}$. The experiment can be performed again for several d_{ht}, and fitted using Eq.(5.10).

In practice, since the temperature oscillation is sensitive to both k_x and k_y, the best way to determine k_x is by using a combination of 2ω and 3ω experiments, as suggested in Ref. 1. A standard 3ω experiment would yield a measurement of $\sqrt{k_x k_y}$ using the slope method, while the present 2ω method (using two distinct lines for heating and sensing) would be used subsequently to fit a pair of (k_x, k_y) under the condition that the quantity $\sqrt{k_x k_y}$ must equal what has been measured using the 3ω method. Since the frequency behavior of the temperature oscillation is different in both methods, k_x can be uniquely determined using these two separate experiments.[1]

It was proposed and evidenced experimentally by Borca-Tasciuc *et al.*[123] that the 3ω method alone could be used to probe anisotropic heat conduction using transducers of different widths. The argument is that a large heater dissipates heat mostly in the cross-plane direction if the material is very thin compared to the heater width, while in the opposite case of a narrow heater, the heat flux also spreads laterally in the in-plane direction, leading to the measured temperature oscillation being sensitive to both the in-plane and cross-plane components of the thermal conductivity of the material (this can be seen in Figure 3.7). One would therefore question if using two separate lines for heating and sensing is better to probe anisotropic thermal properties than using two heater/thermometer of different width in a 3ω configuration. The best asset in using distinct lines for heating and sensing relies on the insensitivity of the measured temperature oscillation to the thermal boundary resistance (TBR) between the thermometer and the substrate, or more generally, to the TBR between the heater and the first layer of the multilayer system. Measurements of TBRs are subtle and their amplitude depend on various parameters, such as the nature of the deposition of the materials building the interface, the surface roughness, the contrast in the phonon density of states, speed of sound, and mass density between both materials, to name a few[105], as introduced in he first chapter of this manuscript. Its contribution to the overall thermal resistance in a standard 3ω experiment can be significant and alter the accuracy of extracted thermal properties if its amplitude is poorly known, especially for films with low thermal resistances in comparison to

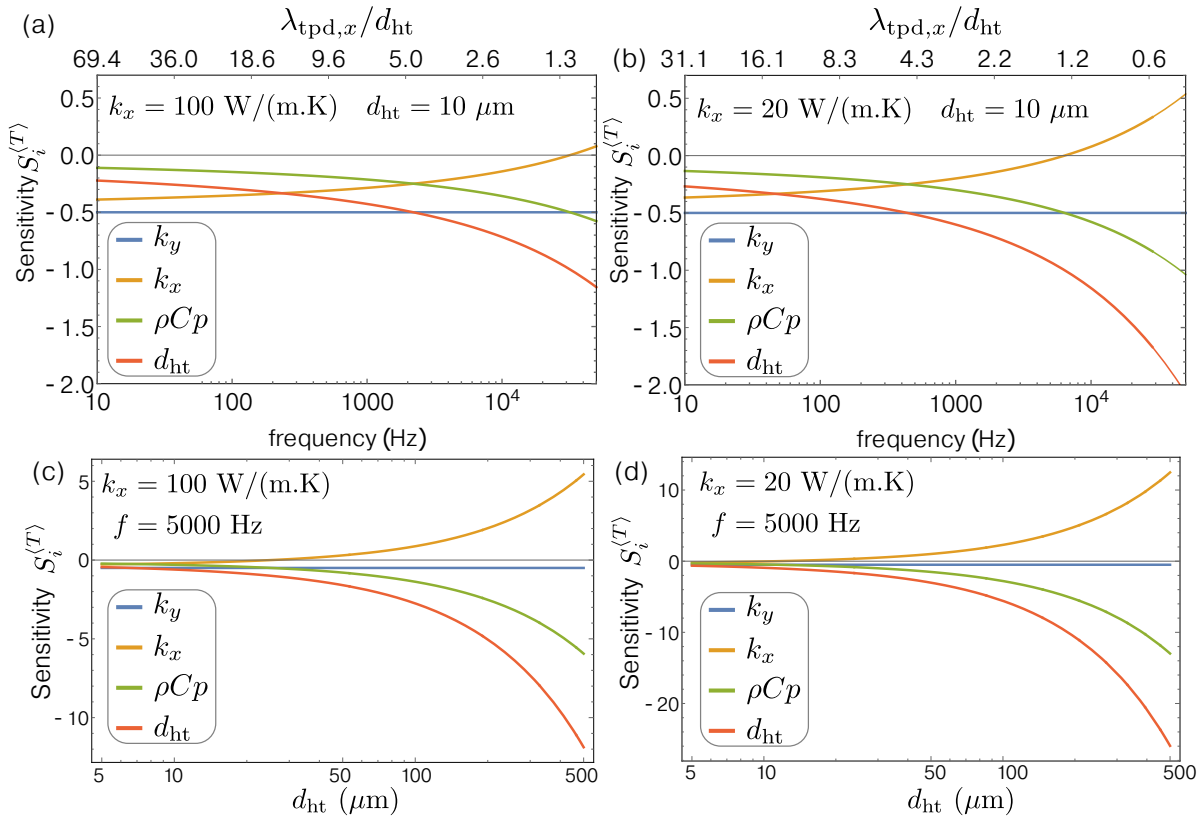

Figure 5.6: Sensitivity $S_i^{\langle T\rangle}$ of the temperature oscillation to parameter i, for several parameters combinations, for a semi-infinite substrate. As a function of electrical frequency using : (a) $k_x = 100$ W.m^{-1}.K^{-1} and $d_{\mathrm{ht}} = 10$ μm, (b) $k_x = 20$ W.m^{-1}.K^{-1} and $d_{\mathrm{ht}} = 10$ μm. As a function of heater to thermometer distance d_{ht} using : (a) $k_x = 100$ W.m^{-1}.K^{-1} and $f = 5000$ Hz, (b) $k_x = 20$ W.m^{-1}.K^{-1} and $f = 5000$ Hz.

TBRs. This is also true when using transducers of different width, since the TBR is always in series with the heater/thermometer. We will show in the next part that the contribution of the heater/first layer's TBR to the temperature oscillation is null when using separate lines for heating and sensing.

5.3.3 Insensitivity to thermal boundary resistance between the thermometer and the first layer

The effect of TBR on the measured temperature oscillation across the thermometer in a 2ω experiment was studied by Ramu and Bowers[150] using FEM, where the interface was modelled as a thin layer with thermal properties of silicon dioxide. They showed that the temperature oscillation across the thermometer was almost completely insensitive to such an interface, for substrates with thermal conductivities varying between 1 and 10 W.m^{-1}.K^{-1}. In this part, we analytically show that this is always true when using separate lines for heating and sensing, whatever the thermal properties of the substrate.

To do so, we use Eq. (5.2), for a substrate with thermal boundary resistance R_{01} at the heater/substrate and thermometer/substrate interfaces, as depicted in Figure 5.2. For simplicity, the heater and the thermometer have the same width, $b_1 = b_2 \equiv b$, the result being similar if their width is different. From Eq. (5.2), the temperature measured across the thermometer

is expressed as

$$\langle T\rangle_{2\text{ lines}} = \frac{P_l}{2\pi}\int_{-\infty}^{\infty}\frac{\sin^2(\lambda b)}{(\lambda b)^2}\frac{A}{C}e^{i\lambda d_{\mathrm{ht}}}d\lambda$$

Using $A = \cosh(\gamma_{\mathrm{s}}d_{\mathrm{s}})+R_{01}k_{\mathrm{s}_y}\gamma_{\mathrm{s}}\sinh(\gamma_{\mathrm{s}}d_{\mathrm{s}})$ and $C = k_{\mathrm{s}_y}\gamma_{\mathrm{s}}\sinh(\gamma_{\mathrm{s}}d_{\mathrm{s}})$, where $\gamma_{\mathrm{s}} = \sqrt{k_{\mathrm{s}_{xy}}\lambda^2 + i(\rho C_{\mathrm{s}})/k_{\mathrm{s}_y}}$, it leads to :

$$\begin{aligned}
\langle T\rangle_{2\text{ lines, TBR}} &= \frac{P_l}{2\pi}\int_{-\infty}^{\infty}\frac{\sin^2(\lambda b)}{(\lambda b)^2}\left(\frac{\cosh(\gamma_{\mathrm{s}}d_{\mathrm{s}}) + R_{01}k_{\mathrm{s}_y}\gamma_{\mathrm{s}}\sinh(\gamma_{\mathrm{s}}d_{\mathrm{s}})}{k_{\mathrm{s}_y}\gamma_{\mathrm{s}}\sinh(\gamma_{\mathrm{s}}d_{\mathrm{s}})}\right)e^{i\lambda d_{\mathrm{ht}}}d\lambda \\
&= \frac{P_l}{2\pi}\int_{-\infty}^{\infty}\frac{\sin^2(\lambda b)}{(\lambda b)^2}\frac{\cosh(\gamma_{\mathrm{s}}d_{\mathrm{s}})}{k_{\mathrm{s}_y}\gamma_{\mathrm{s}}\sinh(\gamma_{\mathrm{s}}d_{\mathrm{s}})}e^{i\lambda d_{\mathrm{ht}}}d\lambda \\
&+ \frac{P_l}{2\pi}\int_{-\infty}^{\infty}\frac{\sin^2(\lambda b)}{(\lambda b)^2}\frac{R_{01}k_{\mathrm{s}_y}\gamma_{\mathrm{s}}\sinh(\gamma_{\mathrm{s}}d_{\mathrm{s}})}{k_{\mathrm{s}_y}\gamma_{\mathrm{s}}\sinh(\gamma_{\mathrm{s}}d_{\mathrm{s}})}e^{i\lambda d_{\mathrm{ht}}}d\lambda \\
&= \frac{P_l}{2\pi}\int_{-\infty}^{\infty}\frac{\sin^2(\lambda b)}{(\lambda b)^2}\frac{e^{i\lambda d_{\mathrm{ht}}}}{k_{\mathrm{s}_y}\gamma_{\mathrm{s}}\tanh(\gamma_{\mathrm{s}}d_{\mathrm{s}})}d\lambda + \frac{P_l R_{01}}{2\pi}\int_{-\infty}^{\infty}\frac{\sin^2(\lambda b)}{(\lambda b)^2}e^{i\lambda d_{\mathrm{ht}}}d\lambda
\end{aligned} \tag{5.17}$$

The first term of the right hand side in Eq. (5.17) represents the contribution of the substrate (with thickness d_{s}) to the temperature oscillation across the thermometer, which, in the limit $d_{\mathrm{s}} \to \infty$, corresponds to Eq.(5.4). Hence the contribution of the TBR to the temperature oscillation is quantified by analysing the second term of the right hand side in Eq. (5.17). In particular, we need to evaluate the quantity

$$\int_{-\infty}^{\infty}\frac{\sin^2(\lambda b)}{(\lambda b)^2}e^{i\lambda d_{\mathrm{ht}}}d\lambda$$

which, using the symmetry of the integration interval and the parity of the integrand, is equivalent to

$$\int_{-\infty}^{\infty}\frac{\sin^2(\lambda b)}{(\lambda b)^2}\cos(\lambda d_{\mathrm{ht}})d\lambda \tag{5.18}$$

We compute this integral using, again, Parseval's theorem, and we choose the two following functions

$$f(\lambda) = \frac{\sin^2(\lambda b)}{(\lambda b)^2} \quad \text{and } g(\lambda) = \cos(\lambda d_{\mathrm{ht}}) \tag{5.19}$$

that will be Fourier Transformed in order to evaluate the integral Eq. (5.18). The Fourier transform $\widehat{f(k)}$ of $f(\lambda)$ is the triangle function[180], defined as :

$$\widehat{f(k)} = \begin{cases} \frac{\pi}{b}\left(1 - \frac{|k|}{2b}\right), & -2b < k < 2b \\ 0 & \text{otherwise} \end{cases}$$

The Fourier Transform $\widehat{g(k)}$ of $g(\lambda)$ is[180]

$$\widehat{g(k)} = \pi\left(\delta(k + d_{\mathrm{ht}}) + \delta(k - d_{\mathrm{ht}})\right) \tag{5.20}$$

where $\delta(k)$ is the Dirac delta function. These two functions are plotted in Figure 5.7. From this graph, the condition for their product to be non-zero is more evident, which is $d_{\mathrm{ht}} < 2b$. Using Parserval's theorem, for $d_{\mathrm{ht}} < 2b$, the integral can therefore be expressed as

$$\begin{aligned}
&\int_{-\infty}^{\infty}\frac{\sin^2(\lambda b)}{(\lambda b)^2}\cos(\lambda d_{\mathrm{ht}})d\lambda \\
&= \frac{1}{2\pi}\int_{-2b}^{2b}\frac{\pi^2}{b}\left(1 - \frac{|k|}{2b}\right)\left(\delta(k + d_{\mathrm{ht}}) + \delta(k - d_{\mathrm{ht}})\right)dk
\end{aligned}$$

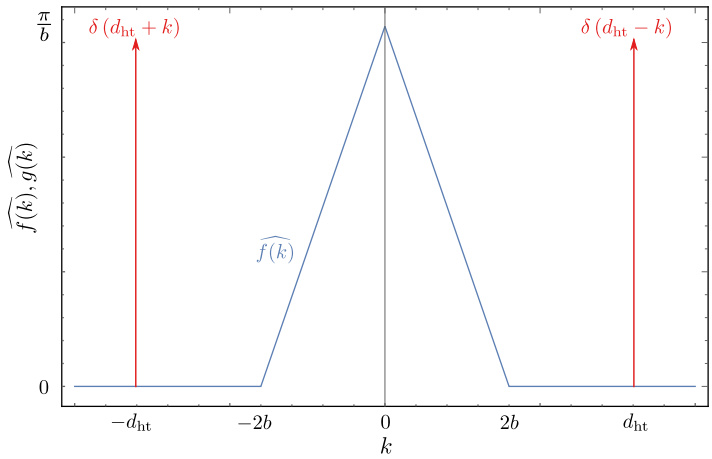

Figure 5.7: Representations of $\widehat{f(k)}$ and $\widehat{g(k)}$ as a function of k. It appears more clearly that their product is zero as long as $d_{\mathrm{ht}} > 2b$.

leading to

$$\int_{-\infty}^{\infty} \frac{\sin^2(\lambda b)}{(\lambda b)^2} \cos(\lambda d_{\mathrm{ht}}) d\lambda = \begin{cases} \frac{\pi}{b}\left(1 - \frac{|d_{\mathrm{ht}}|}{2b}\right) & d_{\mathrm{ht}} < 2b \\ 0 & d_{\mathrm{ht}} \geq 2b \end{cases}$$

The condition $d_{\mathrm{ht}} > 2b$ is always implicitly satisfied when using two distinct lines, since it means that the heater and thermometer do not overlap. If different widths for the heater (b_1) and thermometer (b_2) are used, the condition for the integral to be zero is $d_{\mathrm{ht}} > (b_1 + b_2)$, which is also always satisfied. Therefore the contribution of the heater/substrate's TBR to the measured temperature oscillation is null when using distinct lines for heating and sensing.

We note that when setting $d_{\mathrm{ht}} = 0$, which describes the standard 3ω configuration, the contribution of the TBR to the temperature oscillation is $\Delta T = P_l/(2b) \times R_{01}$, which corresponds to the result derived in Chapter 3.

The insensitivity of the temperature oscillation to the TBR can be expected because the interface is, by definition, a plane with no thickness, and since the heater and thermometer are on this same plane, the thermometer does not feel any cross-plane component, ϕ_y, of the total heat flux, ϕ, coming from the heater that would lead to a temperature rise. Indeed, the temperature drop across an interface is maximum when the heat flux is perpendicular to the interface while it is null if it is parallel to it. The former case represents the standard 3ω geometry while the latter describes the aforementioned 2ω geometry. There is nonetheless a temperature rise across the thermometer/substrate interface which is due to the DC heat flux ϕ_y coming from the (usually small) thermometer Joule heating, arising from the current flowing through the thermometer for sensing the temperature. However, since a DC current is used to sense the temperature response at 2ω, the temperature drop due to this TBR is DC as well and thus barely affects the reading at 2ω.

5.3.4 Sensitivity to the film/substrate's thermal boundary resistance

For a film-on-substrate system, there will be an additional thermal boundary resistance between the film and substrate ($\mathrm{R_{f/s}}$), which will undoubtedly affect the temperature oscillation measured across the thermometer, since it is not placed on the same plane onto which the heater is deposited. However, we can surmise that its effect will be, in most cases, weaker

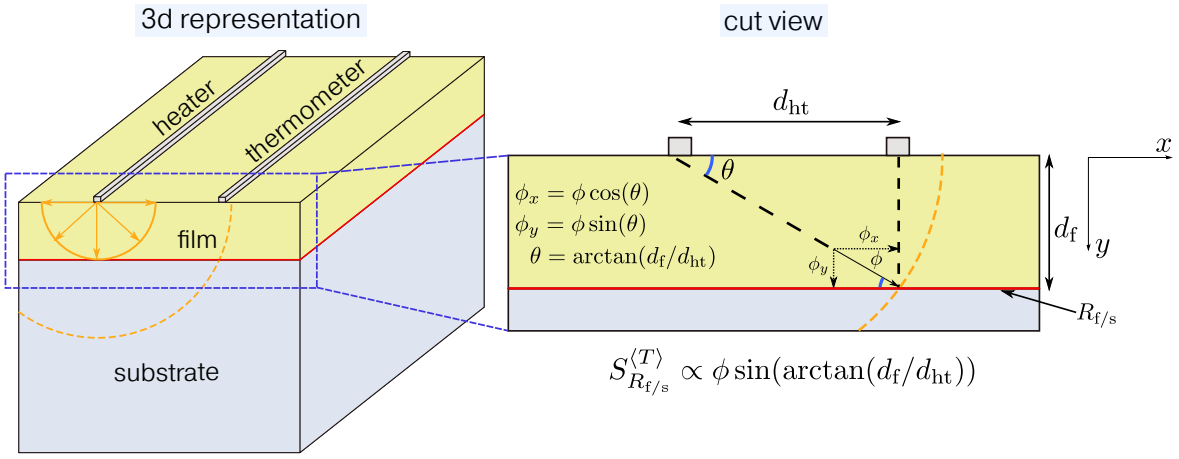

Figure 5.8: Schematic representation of a 2ω experiment, with emphasis on characteristic dimensions that play a role on the sensitivity of the temperature oscillation to the film/substrate TBR, $R_{f/s}$. Isotherms are displayed in orange color. Only the heat flux component that is normal to the interface, ϕ_y, will produce a temperature jump at the interface, and therefore we expect $S^{\langle T\rangle}_{R_{f/s}} \propto \phi_y$.

than that in the 3ω geometry, since the cross-plane component ϕ_y of the total heat flux ϕ crossing the interface in a 2ω geometry is less than that in a 3ω geometry, and the resulting temperature rise consequently smaller as well. To study the sensitivity of the temperature oscillation to the film/substrate's TBR, we use the result of the temperature oscillation measured across the thermometer for a system of two layers, including TBRs, following Eq. (5.2). The average temperature that is sensed by the thermometer is written as :

$$\langle T\rangle = \frac{P_l}{\pi}\int_0^\infty \frac{\sin^2(\lambda b)}{(\lambda b)^2}\frac{\cos(\lambda d_{ht})}{k_{f_y}\gamma_f\tanh(\gamma_f d_f)}\frac{\left(1+\tanh(\gamma_s d_s)\gamma_s k_{s_y}(R_{f/s}+\frac{\tanh(\gamma_f d_f)}{k_{f_y}\gamma_f})\right)}{\left(1+\tanh(\gamma_s d_s)\gamma_s k_{s_y}(R_{f/s}+\frac{\coth(\gamma_f d_f)}{k_{f_y}\gamma_f})\right)}d\lambda \tag{5.21a}$$

$$\gamma_j = \sqrt{k_{j_{xy}}\lambda^2 + i\omega\frac{(\rho C_p)_j}{k_{j_y}}} \tag{5.21b}$$

We can first roughly estimate how does $R_{f/s}$ affect the temperature rise measured across the thermometer, as a function of characteristic dimensions of the system, such as the heater-to-thermometer distance, d_{ht}, and the film thickness, d_f. In order to capture how these characteristic dimensions affect the sensitivity of the temperature oscillation to $R_{f/s}$, we provide a very simple analysis in the limiting case of vanishing width for both the heater and thermometer ($b \to 0$), as shown in Figure 5.8. This simple analysis suggests that $S^{\langle T\rangle}_{R_{f/s}} \propto \phi\sin(\arctan(d_f/d_{ht}))$. As can be seen in Figure 5.9, where $S^{\langle T\rangle}_{R_{f/s}}$ is calculated using the definition of the sensitivity coefficient, applied to Eq. (5.21), it captures relatively well the proposed behavior of the sensitivity as a function of d_f/d_{ht} for two k_f/k_s ratios. Solid lines represent fitting of the calculated sensitivity using an equation of the form $S^{\langle T\rangle}_{R_{f/s}} = A\sin(\arctan(Bd_f/d_{ht}))$, letting A and B as free parameters. The thermal conductivity contrast between the film and the substrate, in addition to the relative amplitude of $R_{f/s}$ as compared to the the film's thermal resistance, surely matter as well in the determination of the sensitivity of the temperature oscillation. Yet, a simple but important conclusion that can be drawn from Figures 5.8 and 5.9, is that the sensitivity to the film/substrate's TBR can be tuned, and therefore be chosen to be small, by playing with the heater-to-thermometer distance. Besides, since in the standard

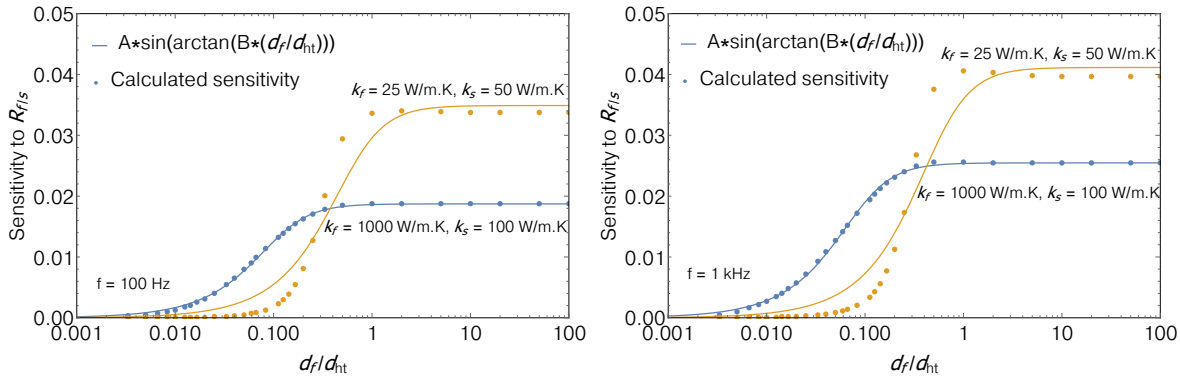

Figure 5.9: Calculated sensitivity of the temperature oscillation to $R_{\mathrm{f/s}}$, for several ratios $d_{\mathrm{f}}/d_{\mathrm{ht}}$, using $d_{\mathrm{f}} = 1$ μm, $R_{\mathrm{f/s}} = 10^{-8}\mathrm{m}^2.\mathrm{K}.\mathrm{W}^{-1}$. To calculate several $d_{\mathrm{f}}/d_{\mathrm{ht}}$ ratios, d_{f} is set to 1 μm while d_{ht} is allowed to vary.

3ω configuration, the experiment is sensitive to the sum of TBRs, i.e. $R_{\mathrm{tr/f}}$+$R_{\mathrm{f/s}}$, while the 2ω method can be arranged to be sensitive to $R_{\mathrm{f/s}}$, $R_{\mathrm{tr/f}}$ could be inferred from a combination of 2ω and 3ω measurements.

Frequency-dependent heat spreader method

We can go further in the sensitivity analysis, and study the effect of the *amplitude* of $R_{\mathrm{f/s}}$, on the sensitivity of the temperature oscillation to several parameters of interest. Up to this point, it would be reasonable to suppose that an increase in TBRs always leads to the degradation of the sensitivity of the experiment to the thermal conductivity of the film, since the TBR would eventually dominate the total thermal resistance of the system. However, motivated by the work of Asheghi *et al.*[2] and later Jang *et al.*[3], we know that a large thermal resistance below the film can be helpful in the determination of its thermal conductivity, in the geometry presented in Figure 5.8, if the substrate underneath efficiently dissipates heat (i.e. $k_{\mathrm{s}} \to \infty$).

This is shown in Figure 5.10(a), where the calculated sensitivity of the temperature oscillation to the in-plane and out-of-plane components of the thermal conductivity of the film and the substrate are plotted as a function of the film/substrate's thermal boundary resistance $R_{\mathrm{f/s}}$. The sensitivity to k_{f_x} is enhanced when the substrate approaches a perfectly isothermal behavior ($k_{\mathrm{s}} \to \infty$), and if the film's thermal resistance is low in comparison to $R_{\mathrm{f/s}}$, such that heat leaks preferably in the in-plane direction rather than in the cross-plane direction. In this case, it leads to an enhanced sensitivity of the temperature oscillation measured using a nearby temperature sensor. In Figure 5.10(b), a similar sensitivity plot is shown, but for the 3ω geometry, i.e. using $d_{\mathrm{ht}} = 0$. In this case, the sensitivity of the temperature oscillation to k_{f_x} is negative and decreases as the film/substrate's TBR decreases, since the heat flux spreads along the in-plane direction of the film, thereby reducing the temperature oscillation that is read across the thermometer.

In practice, a large TBR between the film and substrate is difficult to control, and it is replaced by an insulating thin film, whose thermal resistance $R_{\mathrm{film}} = d_{\mathrm{f}}/k_{\mathrm{f}_y}$ can be tuned by choosing its thickness if its thermal conductivity is well known.[2,3,166] One potential advantage of using this frequency-dependent heat-spreader method, as opposed to the heat spreader method in DC mode, is shown in Figure 5.11. The sensitivity of the temperature oscillation to the in-plane component of the thermal conductivity k_{f_x} is enhanced at higher frequency,

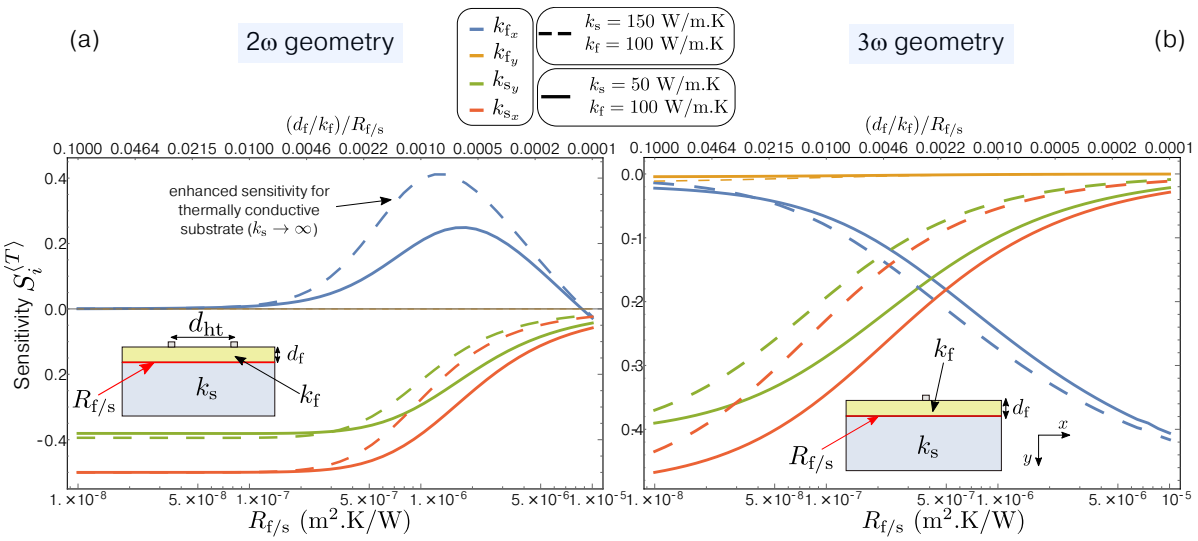

Figure 5.10: Calculated sensitivity of the measured temperature oscillation to the in-plane and out-of-plane components of the thermal conductivity of the film and the substrate, as a function of $R_{f/s}$, in a (a) 2ω or (b) 3ω geometry. As the thermal conductivity of the substrate increases, the sensitivity to the in-plane component of the thermal conductivity of the film can dominate over the sensitivity to other parameters. The heater-to-thermometer distance is set to 10 μm, and the frequency to 10 Hz.

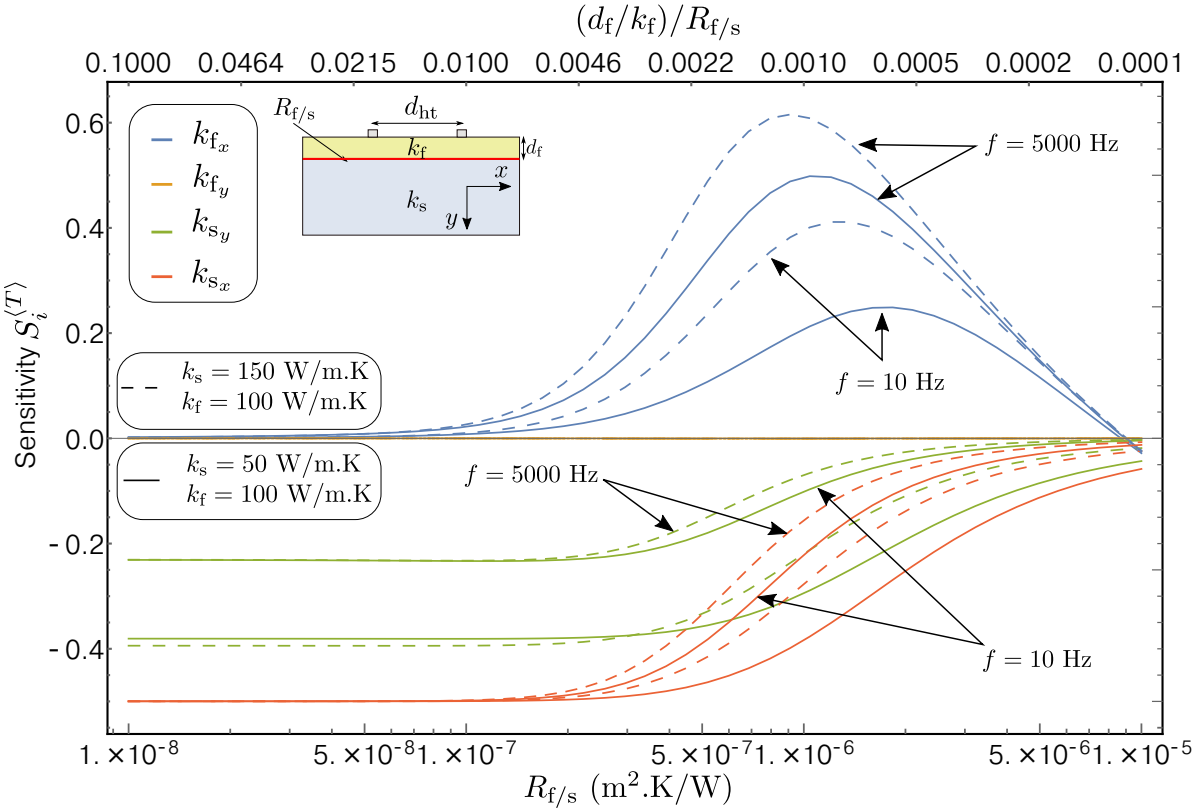

Figure 5.11: Calculated sensitivity of the measured temperature oscillation to the in-plane and out-of-plane components of the thermal conductivity of the film and the substrate, as a function of $R_{f/s}$. The sensitivity to the in-plane component of the thermal conductivity can be enhanced by increasing the excitation frequency. The heater-to-thermometer distance is set to 10 μm.

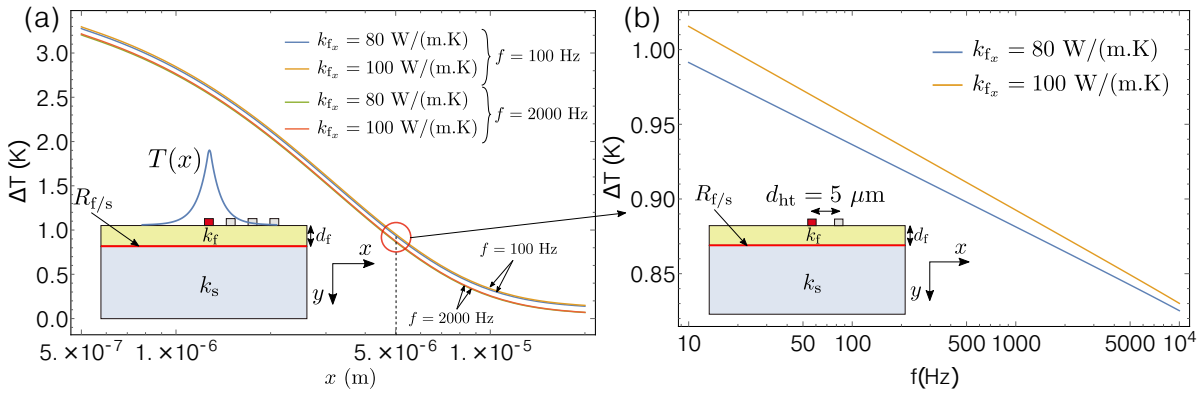

Figure 5.12: (a) Temperature oscillation versus position x (semi-log plot), for two frequencies and two k_{f_x} values. Changing the in-plane component of the thermal conductivity of the film by 20 % does not change substantially the shape of the temperature decay, or the amplitude of the temperature oscillation at one particular frequency. (b) When plotted versus frequency, the temperature oscillation (at one specific position of the thermometer) gives substantially different results if the in-plane component of the thermal conductivity of the film is changed by 20%. In these simulation, we used $R_{\mathrm{f/s}} = 10^{-6}$ m^2.K/W, $d_{\mathrm{f}} = 100$ nm, $b = 0.5$ μm, $P_l = 22.5$ W/m, $(\rho C_p)_{\mathrm{s}} = (\rho C_p)_{\mathrm{f}} = 1.65$ MJ.m^{-3}.K^{-1} and $k_{\mathrm{s}_x} = k_{\mathrm{s}_y} = 150$ W/(m.K).

since the thermal penetration depth is lower and thus the thermal weight of the substrate becomes, relatively, less important. Therefore, in addition to measuring the temperature oscillation as a function of thermometer position and fitting for the spatial temperature decay, one can also perform the measurement at one position *at several frequencies* for a potentially higher sensitivity to the in-plane component of the thermal conductivity of the film. This is exemplified in Figure 5.12(a), where the temperature oscillation is plotted as a function of lateral coordinate x at several frequencies and two k_{f_x} values. We observe that for a 20% change in k_{f_x} (from 100 to 80 W/(m.K)), the shape of the temperature decay, i.e. the temperature plotted versus x, or the amplitude of the temperature oscillation at one specific lateral position, do not change drastically. However, when plotted versus frequency, the temperature oscillation shows an appreciable difference for the two k_{f_x} values, in particular the slope of $\Delta T = \mathrm{f}(\omega)$, as can be seen in Figure 5.12(b). Therefore, fitting the temperature as a function of position *and* frequency could potentially improve the accuracy of the experiment in determining k_{f_x}.

This last example of application of the 2ω method closes this chapter. The 2ω method possesses several advantages as compared to the original 3ω method, such as its insensitivity to the heater/first layer's thermal boundary resistance, and can be adapted such that the thermal conductivity of thin conductive films can be measured with potentially greater accuracy, by using a frequency-dependent heat spreader method, taking advantage of the original heat spreader method combined with the 2ω measurement technique. The calculated temperature oscillation for a *multilayer* system in the 2ω geometry can be useful in designing experiments, without the need of using a FEM model – though it might be needed for complex asymmetric 3D geometries, and if the heater's thermal conductivity becomes important.[3,166]

6 Thermal conductivity measurements

The last chapter of this manuscript is devoted to the application of the 3ω method for measuring the thermal conductivity of thin films, which differ in their structure (crystalline versus amorphous), nanostructuration and thus thermal properties. We then use the 2ω method[1] for measuring the thermal anisotropy of a thick sapphire substrate. In order to perform the measurements efficiently, a non negligible amount of time was dedicated to the automatisation of the measurement setup using the LabView programming software, which is shown in Appendix E. Similarly, data modelling was an important part of the thesis project. In the following, the comparison between the measurements and thermal models have been performed using the programming language Mathematica.

6.1 Amorphous thin films

The motivation behind studying thermal properties of amorphous thin films is three-fold. First, amorphous thin films often serve as coating layers in transistor technology or as low electron leakage dielectrics for magnetic read/write heads, and their ability to spread heat is often coterminous with the efficiency of the device. Second, as the periodic atomic arrangement present in crystalline materials is lost in amorphous structures, the mechanisms responsible for their ability to store and conduct heat are not easily described, and still pose fundamental questions.[181–183] Third, since in this work we use amorphous dielectric thin films for electrically insulating conductive layers that we wish to measure (for preventing shortcuts between the heater and the film of interest), we need to accurately measure their thermal properties.

6.1.1 Amorphous Al_2O_3 on germanium and sapphire

Atomic Layer Deposition-grown (ALD) metal oxide thin films such as Al_2O_3 have a wide range of applications, from dielectric coating layer in transistor technology[184] to assisting layer in lithography processing.[185,186] The diversity of applications comes from their low temperature deposition, conformal coating, large breakdown electric field and sub-nanometer level thickness accuracy.[187,188] Incorporation of high-k dielectric films to replace silicon dioxide in metal-oxide-semiconductor structures gave further relevance to ALD-oxide films in the last decade, while, in addition, the scope of research has been widened for non-silicon based devices in order to further improve devices performances. This consequently led to studies of a variety of stacked systems, among which Ge/ALD-Al_2O_3 structures were investigated because of the intrinsically high charge carrier mobility of germanium.[169,189,190] Ge/Al_2O_3 interfaces, which did not draw great attention in terms of thermal characterization, are highly relevant in the context of Ge nanowires (NWs) growth using techniques such as Au-assisted vapor liquid solid process[191], or template-assisted NW growth using nanoporous alumina.[192] Furthermore, ALD-Al_2O_3 thin films are often employed as insulating layers to prevent electrical leakage in electro-thermal measurements[176,193], as it is the case in this work, where amorphous Al_2O_3 thin films deposited using ALD have been used as electrically insulating layers for all the samples to be measured that were electrically conductive. Consequently, accurate characterization of ALD-Al_2O_3 thin films' thermal conductivity and thermal interfacial resistances are compulsory for the efficient design of novel multilayered structures and for data extraction in thermal measurements involving ALD-Al_2O_3 thin films. The following results are based on our work that have been published in Ref. 194.

6.1.1.1 Sample preparation

Amorphous Al_2O_3 thin films were deposited onto two different crystalline substrates (sapphire and germanium) by ALD using a Cambridge Nanotech Savannah S100 ALD system. Prior to deposition, each substrate was cleaned using acetone, rinsed using ethanol and then subjected to a soft O_2 plasma for a hundred seconds to remove any residual contamination that could alter the interface quality. Then, each sample was subjected to the same ALD deposition conditions : a four cycles process alternating between flow of precursor (Trimethylaluminum, TMA) and H_2O, using N_2 as a purge gas. Growth temperature was stabilized to 150°C and the number of cycles were 145, 350, 500, 750 and 1000, leading to thicknesses of the Al_2O_3 thin films of 17.0, 41.0, 60.1, 89.7 and 119.4 nm, respectively. X-ray reflectivity (XRR) has

been used to measure all the films thicknesses. Typical XRR curves are displayed in Figure 6.1. Using Rutherford backscattering spectrometry (RBS) along with XRR, the films density was measured to be 2.77 ± 0.14 g.cm^{-3}, in good agreement with other ALD-Al_2O_3 films grown at a similar temperature.[187] The following steps have been followed for the fabrication of the heater/thermometer, which are summarized in Figure 6.2 :

- 1. Surface cleaning using acetone and rinsing using ethanol and then distilled water.
- 2. UV-resist deposition on the sample's surface, spin coating at a speed of 6000 rpm and acceleration of 4000 rpm/s, followed by baking it at 115°C for 1 min.
- 3. Laser lithography for patterning the design of the heater/thermometer on the resist.
- 4. Development using a 1:1 ratio of Microposit developer:distilled water for 1 min. The resist is positive such that the exposed area is then removed by the developer.
- 5. Exposition to a soft O_2 plasma for a hundred seconds to remove any excess of resist that was not removed during the previous step.
- 6. Platinum sputtering on the sample using magnetron sputtering, with a nominal thickness of 100 nm.
- 7. Resist removal via lift-off process, using acetone. The sample is then directly rinsed using ethanol.

We note that no adhesion layer has been used prior to the metallic sputtering. The transducers are about 5 μm wide and span 500 μm between the two voltage leads ; dimensions that have been measured using scanning electron microscopy for each sample. Representative SEM images of several thermometers are shown in Figure 6.3. The uncertainty on the length between the inner voltage leads is calculated using their minimum and maximum length, as shown on the top panel of Figure 6.3. In practice, the width of the thermometers are somewhat smaller than their nominal value of 5 μm, therefore it is an important step to accurately measure their width, especially if they are small, as is the case here. We note the presence of silver paste on the four pads in Figure 6.3, which is used for connecting the transducer pads to the sample holder pads, using aluminium wires.

6.1.1.2 Thermal conductivity measurements

Transducer calibration

The calibration of the transducers is performed in a four-probe configuration and under vacuum ($<10^{-5}$ mbar), as explained in Section 2.2. Each transducer's resistance has been measured separately, for each film thickness deposited on two different substrates. We could not reliably measure the thinnest (17 nm) film deposited on germanium, since we have observed a short-circuit between the transducer and the substrate. Therefore, for the alumina films deposited on the germanium substrate, only four transducers have been calibrated, as shown in Figure 6.4. In general, for a given thickness of the transducer, the temperature coefficient of resistance remains unchanged, as can be seen in inset of Figure 6.4 where the four transducers share the same TCR. Experimentally, we have found that the simultaneous measurement of the transducers' resistance versus temperature always leads to better agreement between the

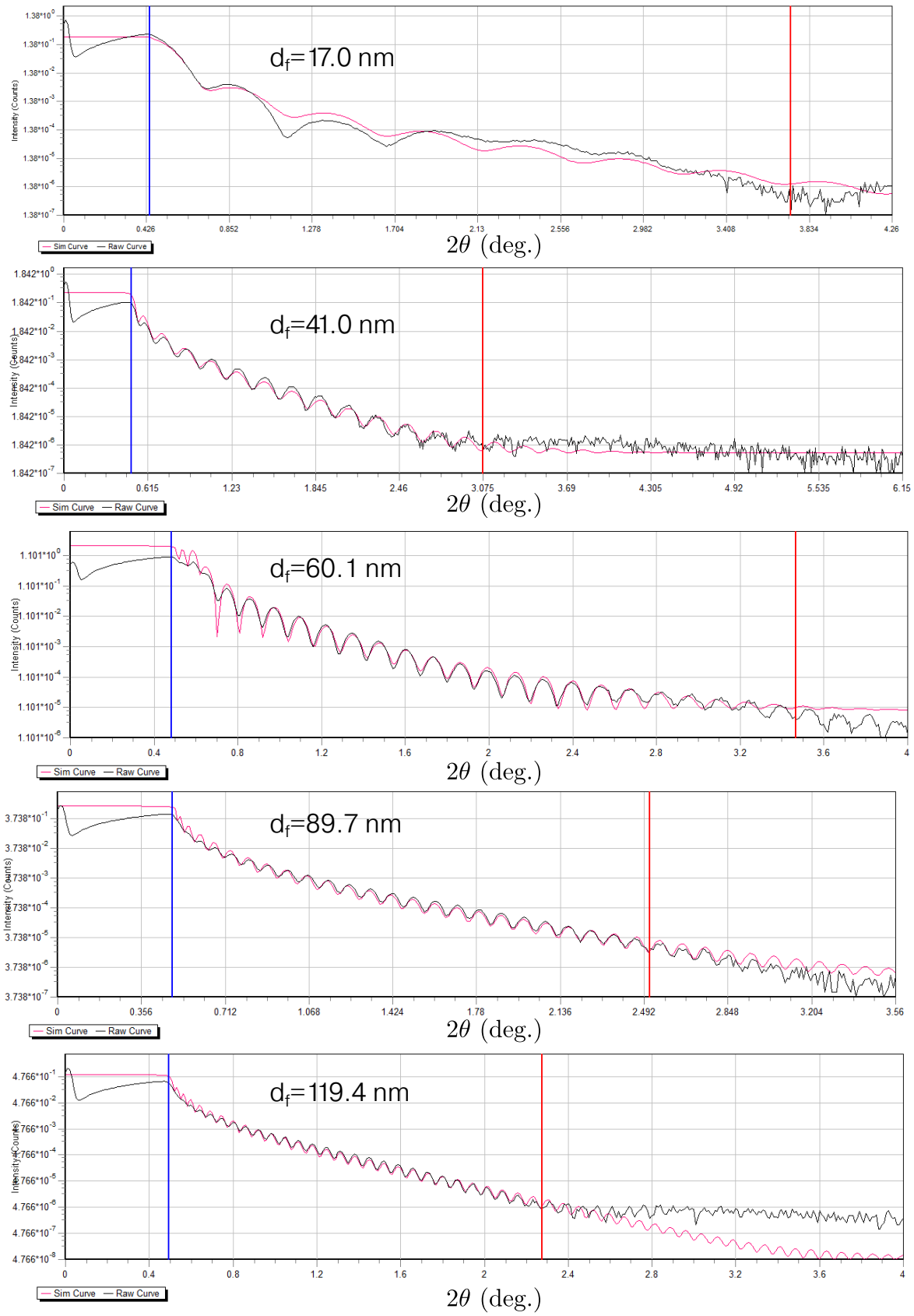

Figure 6.1: Measured beam intensity on the detector as a function of grazing incidence of the X-ray beam, for five thicknesses of the ALD-Al_2O_3 thin films. The period of oscillation of the curves is related to the thickness of the layer. We thankfully acknowledge Eric Mossang from Institut Néel for having carried out the measurements.

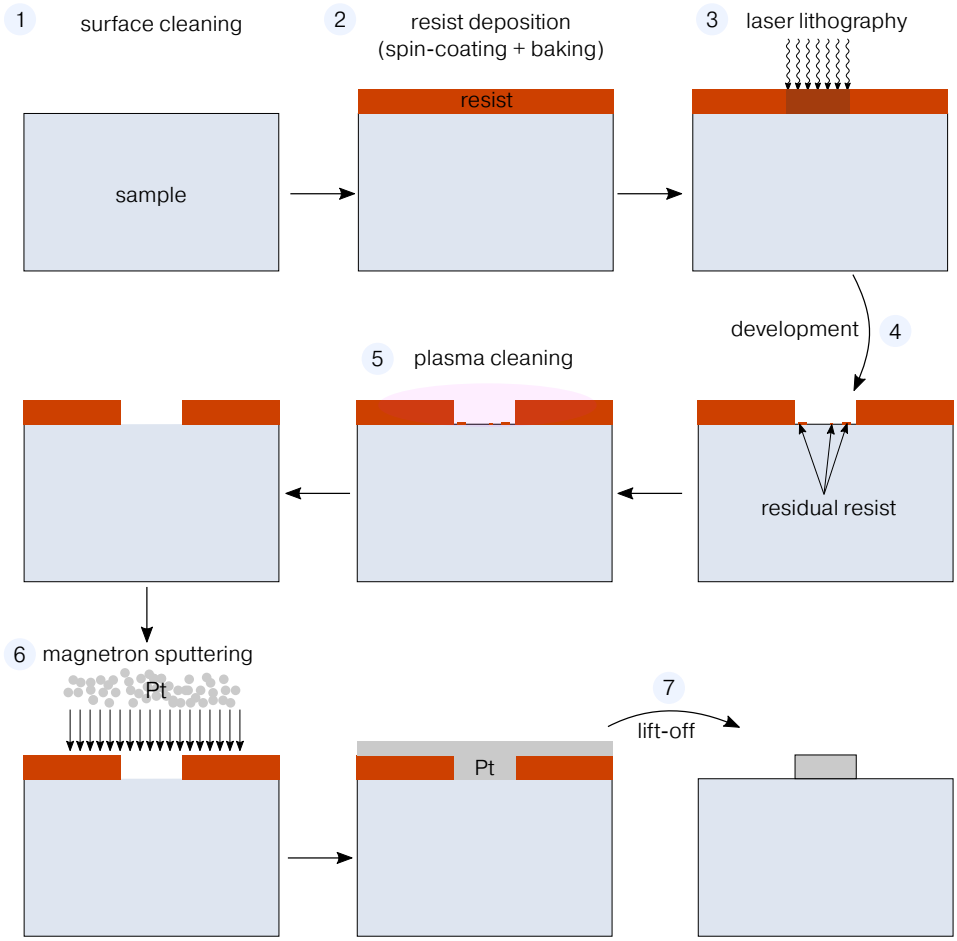

Figure 6.2: Illustration of the steps that we followed for fabricating the transducers on all the experiments carried out in this work. More details are available in the main text.

calculated TCRs of the different transducers. For transducers deposited during the same run, with the same thickness, a discrepancy between their measured TCR is probably caused by the measurement itself.

3ω measurements

A representation of the film-on-substrate systems that are studied is provided in Figure 6.5. Given the expected high thermal conductivity ratio between the thin film and its substrate ($k_s \gg k_f$) (germanium or sapphire) in addition to the high contrast between the heater half-width (2.5 μm) and film thickness (≈17-120 nm), a one dimensional model is relevant to describe the thermal resistance of the film on top of its substrate[123], as detailed in Section 3.2.1. The measured thermal conductivity of the ALD-Al_2O_3 thin films are therefore cross-plane (parallel to growth direction, y-axis in Figure 6.5). The temperature oscillation at $2\omega_e$ sensed by the transducer is then written as[123]:

$$\Delta T_{2\omega_e} = \frac{P_l}{\pi k_{s_y}} \int_0^\infty \frac{1}{\sqrt{k_{s_{xy}}\lambda^2 + i\omega\frac{\rho_s C_{p_s}}{k_{s_y}}}\tanh\left(\sqrt{k_{s_{xy}}\lambda^2 + i\omega\frac{\rho_s C_{p_s}}{k_{s_y}}}d_s\right)} \frac{\sin^2(b\lambda)}{(b\lambda)^2} d\lambda + \frac{P_l}{2b}R_{\text{th}} \quad (6.1)$$

We remind that P_l refers to the electrical power per unit length produced by Joule heating, b is the heater half-width and ω is the angular modulation of the thermal frequency, i.e.

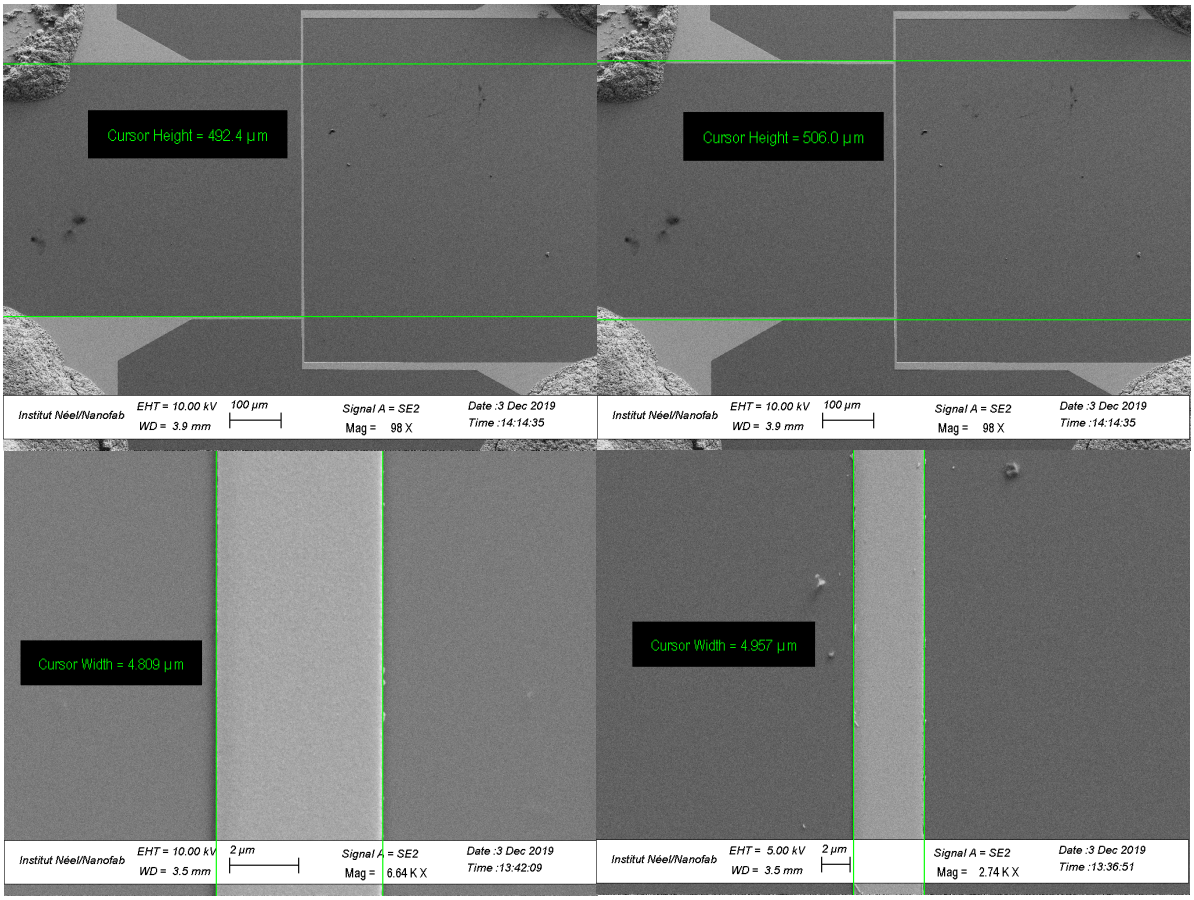

Figure 6.3: SEM pictures of the platinum transducers designed using laser lithography. Top panels : the full thermometer is shown, and the distance between the inner voltage leads is measured, we can see some silver paste on the pads. Bottom panels : the width $2b$ of the thermometer is measured.

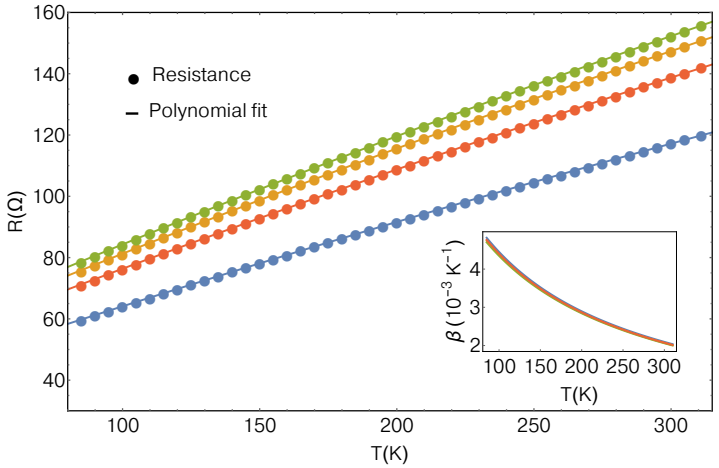

Figure 6.4: Measured electrical resistance R_e as a function of temperature for the four transducers deposited on the germanium+Al_2O_3 systems, i.e. germanium substrates with either 41.0, 60.1, 89.7 or 119.4 nm thick Al_2O_3 thin films. Filled circles represent data whereas solid lines are second order polynomial fits. In inset is displayed the temperature coefficient of resistance $\beta = (1/R_{e,0})dR_e/dT$, calculated from the best fit to the data.

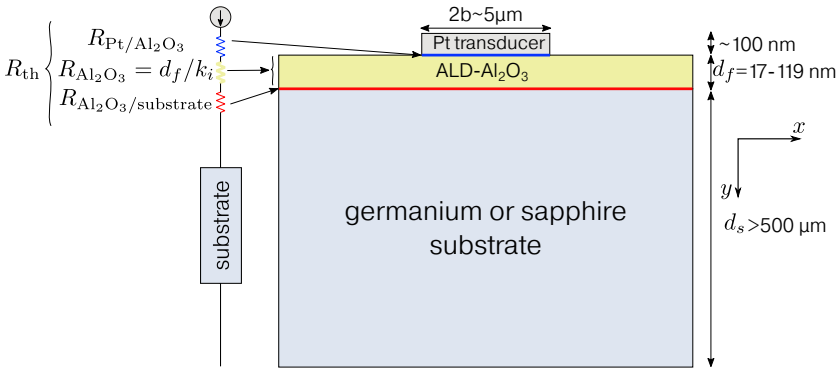

Figure 6.5: Schematic representation of the system measured in this work, either onto a sapphire or germanium substrate. On the left is displayed a simplified thermal circuit in terms of thermal resistances in series with the heat source. The two TBRs R_{Pt/Al_2O_3} and $R_{Al_2O_3/substrate}$ are highlighted in blue and red.

$\omega = 2 \times \omega_e = 4 \times \pi f$ where f is the electrical frequency. k_{s_y}, ρ_s, C_{p_s}, $k_{s_{xy}}$ and d_s stand for the substrate's cross-plane component of the thermal conductivity, density, heat capacity, thermal anisotropy and thickness, respectively. R_{th} is the thermal contribution of the film and interfaces[156], as can be understood from Figure 6.5, and discussed in Section 3.2.1. It is written as :

$$R_{th} = \frac{d_f}{k_{eff}} = R_{int} + \frac{d_f}{k_i} \tag{6.2}$$

where d_f refers to the film thickness, k_{eff} its effective thermal conductivity, R_{int} to the sum of TBRs (heater/film + film/substrate) and k_i stands for the intrinsic thermal conductivity of the film, i.e. independent of its thickness. The latter assumption is expected to hold true given the small mean free path of the heat carriers in amorphous solids (≈ 1 nm)[168] in comparison to the films thicknesses ($17 - 119$ nm), and have been experimentally verified[195,196] for ALD-Al_2O_3 films with smaller thicknesses than that used in the present work. The simple form of Eq. (6.2) also implicitly assumes a constant value of R_{int} among films of increasing thickness. XRR measurements of the alumina films indicate that their top surface rms roughness vary little as a function of film thickness (< 0.15 nm rms), consistent with an other report quantifying the surface roughness of ALD-deposited films as a function of their thickness.[197] Furthermore, since our films are at least 17nm thick, their stoichiometry is expected to be similar among all films[169], and therefore we assume that R_{int} is a constant for all samples (for a given substrate). Possible changes in the stoichiometric composition of the films that could potentially lead to dissimilar surfaces for films of increasing thicknesses are reported to appear during the first cycles (≈ 60) of the deposition process.[169] Since the present films are least 17 nm thick (145 cycles), we assume that the films top surfaces do not exhibit large structural and stoichiometric changes as a function of their thickness.

For extracting the thermal conductivity of the film, substrate and the sum of TBRs, we primarily fit the amplitude[1] of the measured $\Delta T_{2\omega}$ to the amplitude of Eq. (6.1) to obtain k_s and R_{th}. In Eq. (6.1), every parameter is known/measured (heater width, power per unit length, film and sample thickness), except for the substrates' heat capacities and thermal anisotropy. The heat capacity of both substrates have been measured separately using a

[1]We have found that fitting the amplitude of the temperature oscillation rather than the real part leads to better results since phase errors are minimized by reading the amplitude of the temperature oscillation (rather than the in-phase component of the temperature oscillation).

commercially available Physical Property Measurement System from Quantum Design, and are plotted in Figure 6.6 for both substrates. Concerning the thermal anisotropy, for the

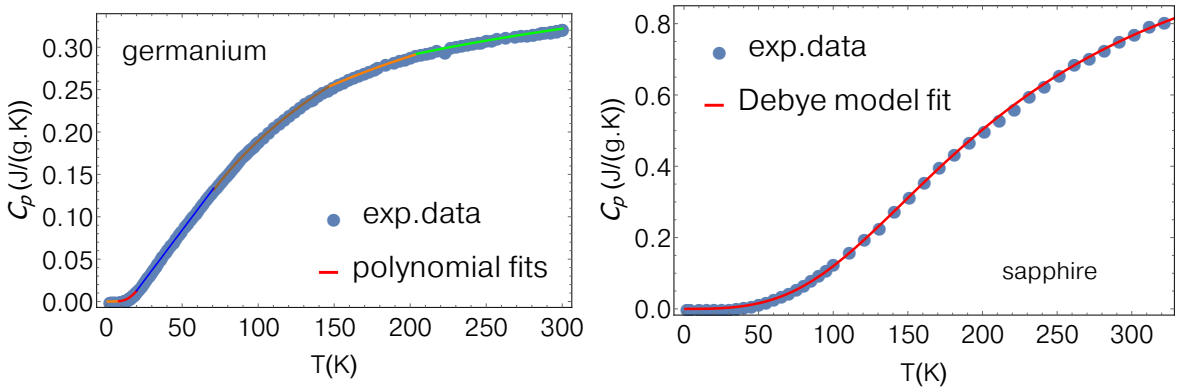

Figure 6.6: Specific heat of the two substrates (sapphire and germanium) onto which the amorphous alumina layers were grown. We emphasize that they have not been measured using the 3ω method, but using a commercially available Physical Property Measurement System from Quantum Design. The substrate's specific heat is used in the modelling of the temperature oscillation to subsequently infer the thermal conductivity of the film.

germanium substrate, we use $k_{s_{xy}} = k_{s_x}/k_{s_y} = 1$ for the fitting of Eq. (6.1), which we assume is a safe assumption given its crystal structure. For the sapphire substrate, it might not be the case and we use $1 < k_{s_{xy}} < 1.3$, from a separate measurement (see Section 6.3). The error introduced from the substrate's thermal anisotropy is included in the Monte Carlo uncertainty analysis that is described in detail in Appendix C.

Once R_{th} has been fitted for each thickness of the films, we plot $R_{\text{th}} = \text{f}(d_{\text{f}})$ as expressed in Eq. (6.2). From the slope of Eq. (6.2), we extract the intrinsic thermal conductivity of the Al_2O_3 film. R_{int} is inferred from the intercept extrapolated to zero thickness.

In practice, the step we systematically conduct after the transducer calibration is to plot the measured third harmonic of the voltage $V_{3\omega}$ as a function of the current's third power. Indeed, we expect a linear relationship of the form $V_{3\omega} \propto I^3$, because $V_{3\omega} \propto R_e I \Delta T$ with $\Delta T \propto I^2$ (see Eq.(2.8)). Such measurements are shown in Figure 6.7. The linearity between the $V_{3\omega}$ voltage and the current's third power ensures the thermal signature of the measured voltage, for several frequencies. In general, if this linear behavior is not observed, there might be a problem somewhere in the electrical setup, or there might be a short-circuit between the transducer and the substrate (i.e. the insulating layer is damaged or too thin). The temperature oscillation is then measured as a function of electrical frequency for each sample. In Figure 6.8, we show such a measurement performed at 300 K, for four different samples, consisting of four thicknesses of the Al_2O_3 films, deposited onto different sapphire substrates (the fifth sample (41 nm) is not shown for clarity). We notice that the curves are almost all parallel. Remembering the discussion about the slope method (Eq.(3.11)), the slope of the temperature oscillation, when plotted versus $\ln(\omega)$, is directly proportional to the thermal conductivity of the substrate. Therefore, for films deposited on substrates made of the same material, sapphire in this case, all the curves should be parallel. The offset comes from the different thermal resistance of each film – the thicker the film is, the greater is its thermal resistance and therefore the higher is the temperature oscillation, for a given applied power P_l. This is what is observed in Figure 6.8, where the sapphire+film system gives a higher ΔT for the thickest (119.4 nm) film. From the $\Delta T = \text{f(frequency)}$ curves, as shown in Figure 6.8, we

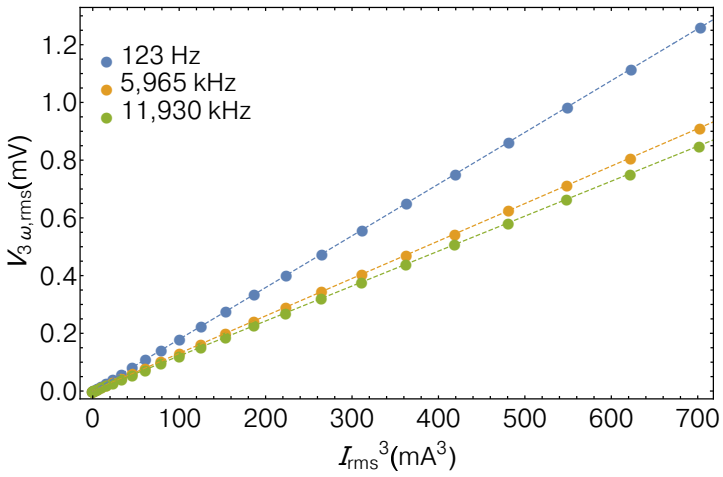

Figure 6.7: Measured 3ω voltage as a function of the third power of the electrical current for several frequencies at 300 K. Dashed lines are linear fits to the data.

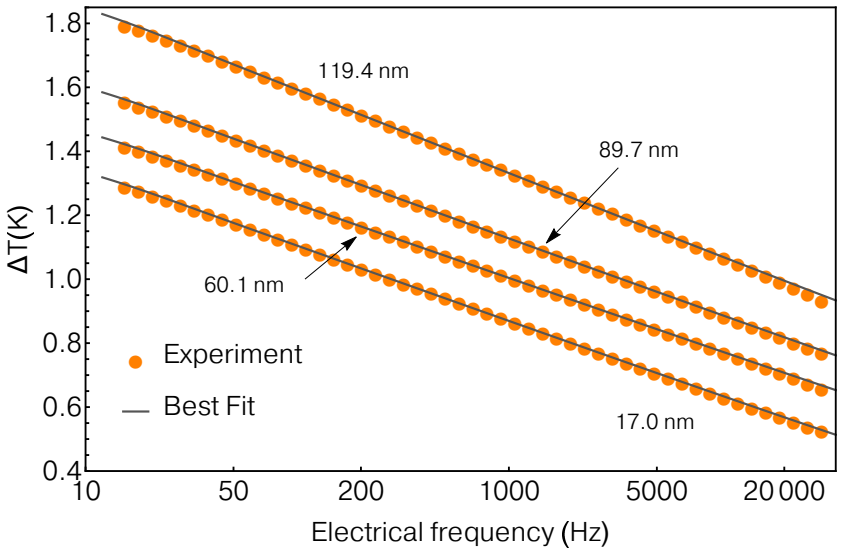

Figure 6.8: Measured $\Delta T_{2\omega_e}$ versus electrical frequency for four thicknesses of the Al_2O_3 films deposited onto the sapphire substrate at 300 K (41.0 nm not shown for clarity). Filled circles are data and solid lines are the best fit to Eq. (6.1). Peak power dissipated lies between 11 and 12 mW for the four transducers.

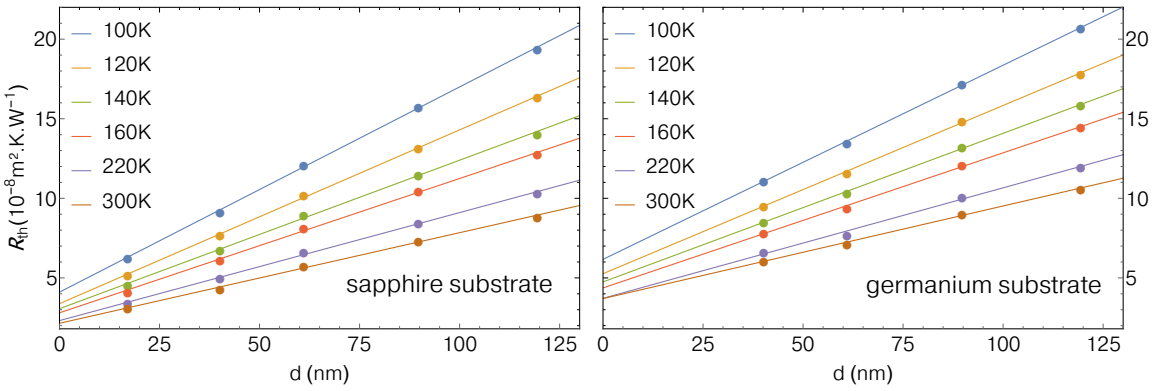

Figure 6.9: Measured thermal resistances of the films as a function of their thickness, for several temperatures. Solid lines are linear fits to the data. Thermal boundary resistances are inferred from the intercepts of the fits extrapolated to zero thickness whereas the intrinsic thermal conductivity of the films is derived from their slope.

extract k_s and R_{th}. We then plot $R_{\text{th}} = \text{f}(d_{\text{f}})$ to extract the intrinsic thermal conductivity of the Al_2O_3 films, and the sum of thermal boundary resistances, $\text{R}_{\text{Pt/Al}_2\text{O}_3} + \text{R}_{\text{Al}_2\text{O}_3\text{/substrate}}$, as shown in Figure 6.9 for the germanium and sapphire substrates at several temperatures.

6.1.1.3 Results and discussion

Intrinsic thermal conductivity of ALD-Al_2O_3 thin films

The intrinsic thermal conductivity of the ALD-Al_2O_3 thin films is plotted versus temperature in Figure 6.10. The values extracted from either substrate are consistent with each other, within the accuracy of the measurements, represented as tinted bands. The error on the measured thermal conductivity of the films and thermal boundary resistances is calculated using a Monte Carlo method, which is described in detail in Appendix C.

Tinted bands in Figure 6.10 and 6.11 represent 68% confidence intervals (CI) derived using the Monte Carlo method, representing values falling within one standard deviation of the mean for a normal distribution. No substrate dependence of the films' thermal conductivity is observed in the temperature range explored, within experimental accuracy – in agreement with other reports.[196,199] The thermal conductivity of the amorphous Al_2O_3 films ranges from 0.80 W.m^{-1}.K^{-1} at 100 K to 1.73 W.m^{-1}.K^{-1} at 300 K (see Table 6.1). The value at 300 K is as well in very good agreement with other values reported for Al_2O_3 films grown in similar conditions. Indeed, literature values lie between 1.3-2.4 W.m^{-1}.K^{-1}, depending on the growth technique and conditions.[121,195,198,199,201–204]

Since the thermal conductivity of amorphous ALD-Al_2O_3 is known to be significantly density dependent[195], we compare the thermal conductivity of the present measurements to reported values of ALD-Al_2O_3 films with known density. For measured densities[2] of 2.72

[2]Atomic densities of 8.02×10^{28} and 9.29×10^{28} atoms.m^{-3} were converted in units of g.cm^{-3} assuming a Al:O ratio of 2:3.

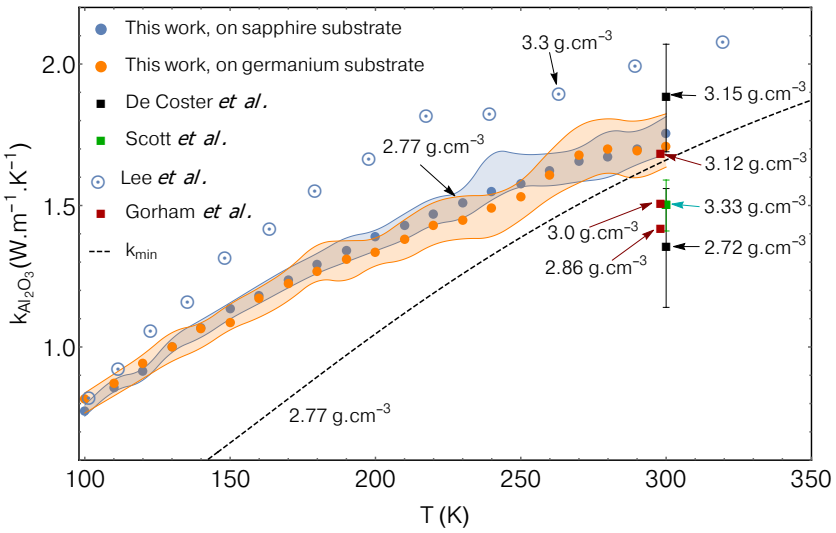

Figure 6.10: Temperature dependence of the intrinsic thermal conductivity of ALD-Al_2O_3 thin films, deposited onto two different substrates. Other data from ALD-Al_2O_3 films with measured density are displayed in comparison, taken from Refs. 195,196,198,199, while k_{min} is calculated from Ref. 200. Data reported using TDTR are shown as squares, whereas other shapes are from 3ω experiments.

g.cm^{-3} and 3.15 g.cm^{-3}, DeCoster *et al.* reported, at room temperature, thermal conductivities of 1.35 ± 0.21 W.m^{-1}.K^{-1} and 1.87 ± 0.26 W.m^{-1}.K^{-1}, respectively, using time-domain thermoreflectance.[196] Lee *et al.* reported 1.99 ± 0.16 W.m^{-1}.K^{-1} for films with density of 3.3±0.1 g.cm^{-3} using a similar 3ω method.[199] Scott *et al.*[198] reported 1.50 ± 0.09 W.m^{-1}.K^{-1} for density of 3.33 ± 0.06 g.cm^{-3}, while Gorham *et al.* reported values from 1.23 to 1.67 W.m^{-1}.K^{-1} for densities ranging from 2.67 to 3.12 g.cm^{-3} (Ref. 195). Our reported averaged value of 1.73 ± 0.08 W.m^{-1}.K^{-1} for a measured density of 2.77 ± 0.14 g.cm^{-3} corroborates reasonably well in terms of density to these reported values. This is in agreement with previously established density dependent thermal conductivity models, such as the lower limit for thermal conductivity[200] and the related differential effective medium approximation[195,205], which serve as reference models to describe the thermal conductivity of amorphous films as a function of their atomic density.

We may notice that, for films with similar densities, our reported value for the thermal conductivity is somewhat higher than other reports, as can be seen from Figure 6.10. For measurements on very thin films (<10 nm), ALD-Al_2O_3 films could be inhomogeneous across the film thickness, due to unstable Al:O ratio during the first cycles of the deposition, before reaching a ratio of 2:3 for large cycle numbers.[169] In this scenario, a measurement performed on very thin films would be more sensitive to the inhomogeneity of the films, and could therefore lead to lower thermal conductivity. This could explain the difference between our data and that reported by Scott *et al.*[198], where the films were between 1 to 10 nm thick with lower thermal conductivity than our films, while having higher density. However, this would not explain our relative difference with data from Gorham *et al.*[195], since they used films with thicknesses comparable to ours. Thus, additional quantitative structural characterizations of the ALD films might prove useful in explaining the relative difference observed in terms of thermal conductivity.

substrate	T (K)	$k_{Al_2O_3}$ (W.m^{-1}.K^{-1})	TBR (10^{-8} m^2.K.W^{-1})	$k_{s,avg}$ (W.m^{-1}.K^{-1})
germanium	100	0.82 [0.77,0.84]	6.1 [5.6,6.4]	148
	200	1.34 [1.29,1.40]	3.8 [3.5,4.0]	77
	300	1.71 [1.66,1.83]	3.7 [3.6,4.0]	52
sapphire	100	0.77 [0.76,0.80]	4.1 [4.0,4.3]	335
	200	1.39 [1.34,1.41]	2.5 [2.3,2.5]	65
	300	1.75 [1.68,1.81]	2.1 [2.0,2.3]	34

Table 6.1: Summary of the measured quantities in this work. $k_{Al_2O_3}$ refers to the intrinsic thermal conductivity of the film, inferred using Eq. (6.2). The thermal conductivity of the substrate $k_{s,avg}$ is calculated from the mean of the four (five for sapphire) samples measured to deduce the thermal conductivity of the film. TBR refers to the sum of thermal boundary resistances in series in the system (Pt/Al_2O_3 + Al_2O_3/substrate). Values in brackets are 68% CI.

Thermal boundary resistances

We see in Figure 6.9 the significance of TBRs, weighting up to two third of the measured total thermal resistance, in the case of the thinnest film (17.0 nm) grown on sapphire, at 300 K. Even for the thickest film (119.4 nm), the contribution from TBRs weights up to 35% of the total thermal resistance, for films deposited onto germanium. These considerations support the need to perform multiple measurements on several film thicknesses for accurate thermal characterization when using the 3ω method[146], even for films having relatively low thermal conductivity. This statement is by all means related to the rather large TBRs measured in this work, when compared to the film thermal resistance.

Figure 6.11 displays the total TBR measured from Al_2O_3 films deposited onto germanium and sapphire substrates. The behavior with temperature is similar for both substrates, and in qualitative agreement with theoretical models predicting an increased TBR between two dissimilar materials as temperature decreases.[104] We clearly observe that the sum of TBRs is larger when the Al_2O_3 film is deposited onto germanium, compared to the same film deposited onto sapphire. Notwithstanding accurate prediction of TBR is an arduous task in this temperature range[105], we can still discuss important key experimental points that could warrant the relatively large TBR measured in this work. Indeed, at 300 K we measure 2.1×10^{-8} and 3.7×10^{-8} m^2.K.W^{-1} for TBR extracted from Al_2O_3 films deposited onto sapphire and germanium, respectively. These values are comparable with others extracted from 3ω experiments[83,165,199,206,207], but generally lie in the higher end of most TBR reported values.[107] Using a similar 3ω method, Lee *et al.*[199], reported that the sum of TBRs is larger from ALD-Al_2O_3 deposited onto silicon ($\approx 2\times10^{-8}$m^2.K.W^{-1}) than that deposited onto sapphire ($\approx 2\times10^{-9}$m^2.K.W^{-1}), though the amplitude is smaller in their study and they used gold as a transducer using a Ti adhesion layer. The large discrepancy – almost a factor of ten – between the reported value for the Au-Ti/ALD-Al_2O_3/sapphire interface compared to our Pt/ALD-Al_2O_3/sapphire interface suggests that Pt/ALD-Al_2O_3 be the prevalent TBR in this case, as will be discussed later. Besides, in sandwiched structures such as ours containing ALD-Al_2O_3 films, other authors have reported TBRs that are at least two times smaller than our results, using TDTR. Indeed, for Al/Al_2O_3/Si, Monachon *et al.* measured $5.2\pm0.5\times10^{-9}$ m^2.K.W^{-1}, while Scott *et al.* reported $6.92\pm0.50\times10^{-9}$ m^2.K.W^{-1}, where the Al layer serving as their opto-thermal transducer was DC sputtered or electron-beam evaporated, respectively.[198,203]

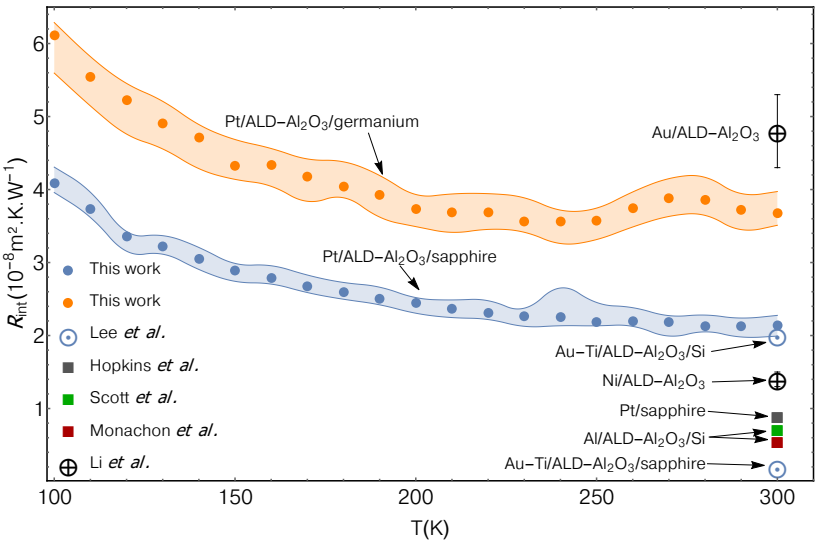

Figure 6.11: Temperature dependence of the sum of thermal boundary resistances measured in two different systems, colored bands represent 68% confidence intervals. TBRs from sapphire have lower error bars due to the fact that five thicknesses were used to extract them, as opposed to the four samples used for the germanium substrate. Other TBRs with related materials are taken from Refs. 198,199,203,207,211. Data reported using TDTR are shown as squares, whereas other shapes are from 3ω experiments.

The variation between these results and our measurements leads us to discuss two particular points. First, the relative difference between TBRs measured from the sapphire and germanium substrates, and second, the overall large sum of TBRs measured for both substrates. For the first aspect, one possible reason is the presence of a native oxide layer on the substrate, that has not been removed prior to the films deposition. On the germanium substrate, this native oxide could substantially impede thermal transfer across the interface, hence increasing the measured TBR.[208] It has been shown in Refs. 169,209 that, even after removing the native oxide from the germanium substrate prior to ALD, a germanium oxide would eventually reform at the interface during the deposition process, with thickness $\approx 0.2 - 0.5$ nm. This would partly explain the difference observed between both substrates, in addition to the greater contrast that exists in terms of mass density and speed of sound between the germanium/ALD-Al_2O_3 interface compared to the sapphire/ALD-Al_2O_3 interface. This would lead to a higher TBR for the germanium/ALD-Al_2O_3 interface, as predicted by the Diffuse Mismatch Model (DMM).[100,104,210]

Since our measurement provide *the sum* of TBRs of two interfaces, we turn to a qualitative discussion, rather than a quantitative one, to explain the contrast observed in terms of TBRs for the same films deposited on different substrates. To have an estimation of how the contrast in thermal properties between two materials might lead to significant change on their thermal boundary resistance, we use a gray approximation of the DMM[32] and estimate the thermal boundary resistance as

$$\mathrm{TBR} \approx \left(\frac{C_i v_i}{4} \frac{C_j v_j}{C_i v_i + C_j v_j} \right)^{-1} \tag{6.3}$$

where C_i and v_i stand for the volumetric heat capacity (in $\mathrm{J.m^{-3}.K^{-1}}$) and phonon group velocity (in $\mathrm{m.s^{-1}}$) of material i, respectively – an approach that have been used in Ref. 198. For the ALD-Al_2O_3 films and sapphire substrate, we assume $v = 8800$ $\mathrm{m.s^{-1}}$ for their

longitudinal speed of sound[212], while for the germanium substrate we use $v = 6240$ m.s^{-1}(Ref. 213). For the volumetric heat capacity, we use our measured value of the heat capacity for the sapphire and germanium substrates, combined with the mass density taken from the literature.[214] For the ALD-Al_2O_3 films, we use the measured heat capacity of the sapphire substrate, combined with the films density that has been measured using RBS. These lead to volumetric heat capacity of $C_{\text{sapphire}} = 3.05$ MJ.m^{-3}.K^{-1}, $C_{\text{germanium}} = 1.72$ MJ.m^{-3}.K^{-1} and $C_{\text{ALD-Al}_2\text{O}_3} = 2.15$ MJ.m^{-3}.K^{-1}.

Using the aforementioned thermal and structural properties, we arrive at

$$\text{R}_{\text{ALD-Al}_2\text{O}_3/\text{germanium}} = 1.6 \times \text{R}_{\text{ALD-Al}_2\text{O}_3/\text{sapphire}} \tag{6.4}$$

which is in reasonable agreement with what is observed experimentally in this work. Using GeO_2 instead of Ge, with volumetric heat capacity and longitudinal speed of sound taken from Ref. 168, we obtain $R_{\text{ALD-Al}_2\text{O}_3/\text{GeO}_2} \approx 3\times\ R_{\text{ALD-Al}_2\text{O}_3/\text{sapphire}}$. We emphasize that this calculation is only qualitative, but agrees relatively well with the trend that is observed here. Thus, the higher TBRs for the germanium substrate can be understood using the aforementioned arguments.

For the second aspect – the relatively high TBR measured for both substrates – we remind that the platinum transducer was DC-sputtered, without any adhesion layer. A recent work from Suk *et al.*[215] suggests that DC magnetron sputtered films have more imperfections at the film/substrate interface – when compared to other metal deposition techniques such as e-gun evaporation – due to its energetic deposition process, hence increasing the TBR. Most importantly, the use of a metallic adhesion layer is reported to enhance thermal interfacial conductance. Indeed, Li *et al.*[207] have reported a 70% reduction of the TBR between amorphous ALD-Al_2O_3 and gold after introducing a nickel layer, thereby reducing it from 4.8×10^{-8}m^2.K.W^{-1} to 1.4×10^{-8}m^2.K.W^{-1}, while Jeong *et al.* succeeded in reducing metal/sapphire TBR by a factor from 2 to 4 by inserting a thin metallic adhesion layer[216], a result reproduced by Blank *et al.*.[217] These arguments go in favor of a higher TBR for DC-sputtered films, in particular when no adhesion layer is used.

The 3ω measurements, performed in this frequency range, cannot discriminate the contribution from the Pt/ALD-Al_2O_3 interface to that of the ALD-Al_2O_3/substrate interface, as we have mentioned before. We can nonetheless estimate an upper/lower bound for each contribution. Hopkins *et al.* reported TBR of 8.6×10^{-9}m^2.K.W^{-1} for a Pt/sapphire interface, using TDTR.[211] We can reasonably take this value to serve as a lower bound for our Pt/ALD-Al_2O_3 interface, since the contrast in density is higher in the case of Pt/ALD-Al_2O_3 than for the Pt/sapphire interface – all other parameters assumed to remain constant. Therefore the thermal contribution of the Pt/ALD-Al_2O_3 TBR would account for *at least* 40 % of the total Pt/ALD-Al_2O_3/sapphire TBR, while for the germanium substrate, its contribution would be 23 %.

To have a lower bound of the contribution of the ALD-Al_2O_3/germanium TBR only, we take the limit where the Pt/ALD-Al_2O_3 TBR accounts for 100% of the total Pt/ALD-Al_2O_3/sapphire TBR, i.e. the contribution from the ALD-Al_2O_3/sapphire TBR is considered

to be negligible. In this case, $R_{\text{Pt/ALD-Al}_2\text{O}_3} = 2.1 \times 10^{-8}\text{m}^2.\text{K/W}$, and thus

$$\begin{aligned} &R_{\text{ALD-Al}_2\text{O}_3/\text{germanium, lower bound}} \\ &= \left(R_{\text{Pt/ALD-Al}_2\text{O}_3} + R_{\text{ALD-Al}_2\text{O}_3/\text{germanium}}\right) - R_{\text{Pt/ALD-Al}_2\text{O}_3} \\ &= 3.7 \times 10^{-8} - 2.1 \times 10^{-8} \\ &= 1.6 \times 10^{-8}\text{m}^2.\text{K/W} \end{aligned}$$

at 300 K.

While further experiments using other metals as transducers or using a metallic adhesion layer would help to give further insight into the contribution of each interface to the total resistance measured, altogether, the arguments presented above qualitatively justify our findings in terms of relative amplitude of the measured TBRs, for both substrates. Importantly, the Pt/ALD-Al_2O_3/germanium TBR has been measured and can be used in subsequent 3ω experiments where a germanium film is capped with an ALD-Al_2O_3 layer with a platinum heater.

6.1.2 SiN on silicon

The second example of thermal conductivity measurement of amorphous thin films deposited on a thick substrate that we have performed in this work is that of silicon nitride thin films grown on silicon. The samples have been provided by the company ST Microelectronics and CEA-LETI, with whom we have collaborated (Pierre Noe and Marie-Claire Cyrille), and thus the detailed growth of the films will not be described. Amorphous Si_3N_4 thin films are widely used as passivation layers, masking layers to prevent oxidation or diffusion in underlying materials in patterned areas, and as final protection layers to finished devices because of their hardness and radiation resistance.[218] As for alumina films, their thermal properties is crucial as they are used in multilayer systems whose sizes become commensurate to the phonon mean free path, and their thermal weight becomes close to that of thermal boundary resistances.

The thermal conductivity measurements are very much the same as those described in the previous section. We first calibrate the transducers, perform a $V_{3\omega} = \text{f}(I^3)$ swipe, and then perform $\Delta T_{2\omega_e} = \text{f(frequency)}$ measurements, and fit it to the same thermal model (i.e. Eq. (6.1)). We use the same thermal model because the films are 30 and 120 nm thick, while the thermometer is chosen to be 20 μm large. Besides, we expect a large contrast between the thermal conductivity of SiN films (between 1-5 W/(m.K)[219]) and the silicon substrate (about 140 W/(m.K), depending on doping level). These two arguments allow us to treat the thin film as a thermal resistance in series with the heater with negligible error (see Figure 3.7), and thus we fit the measured temperature oscillation as a function of frequency using Eq. (6.1). The silicon substrate's specific heat and density have been taken from literature.[214] Four different kind of SiN films with different Si/N ratios have been measured, each with two thicknesses of 30 and 120 nm. Therefore, eight measurements have been performed, from which the intrinsic thermal conductivity of the films and the sum of thermal boundary resistances are extracted.

In Figure 6.12, we have plotted for each kind of SiN film, referred to as batch numbers, the measured temperature oscillation normalized to the power provided by the transducer, as a function of electrical frequency. The effective thermal conductivity of the films is the thermal conductivity obtained if the thermal contribution of thermal boundary resistances is not removed from the total thermal contribution of the system film + TBRs, as expressed

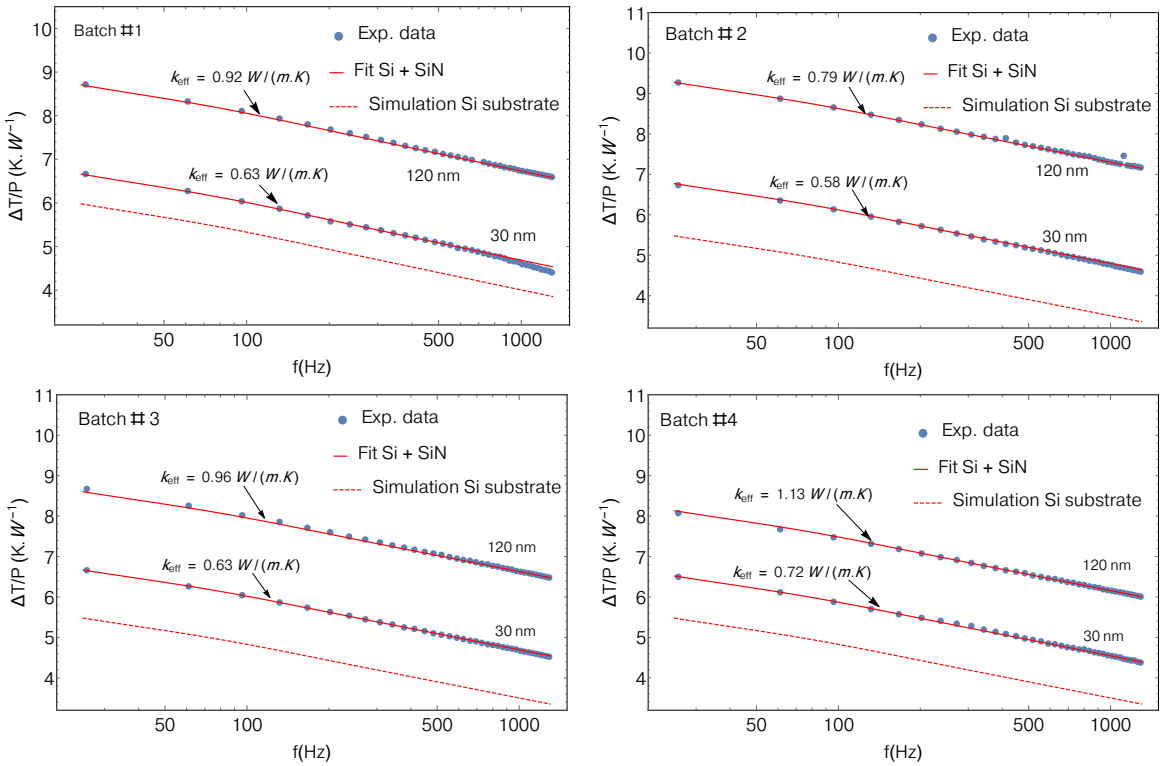

Figure 6.12: Measured temperature oscillations normalized to heating power, as a function of electrical frequency for four different samples of SiN films deposited onto silicon substrates. For each kind of SiN film, we use two thicknesses two remove the contribution of TBRs.

in Eq. (6.2). Therefore, for the thinnest films, their effective thermal conductivity is lower because the contribution of TBRs becomes larger. It is important to understand that the films themselves are not less conductive because of their reduced size, as it is sometimes the case as we have discussed in Chapter 1. It is only by neglecting the contribution from TBRs that they appear to be less conductive. Performing measurements on films of increasing thicknesses, as we have done for the alumina films and the present SiN films, removes this ambiguity. Plotting the effective thermal conductivity as a function of film thickness is an approach that is sometimes used in the literature[156], instead of plotting the thermal resistance of the film as a function of film thickness. We prefer the latter approach because, in our opinion, it is less ambiguous that thermal boundary resistances are responsible for the observed reduced effective thermal conductivity if the thermal resistance is plotted as a function of film thickness. The thermal resistance of each film is plotted versus film thickness in Figure 6.13, for the four samples. The thermal conductivity of the Si_3N_4 films vary from 0.9 to 1.5 W/m.K, while the silicon substrate's thermal conductivity is measured to be 138±5 W/m.K for all samples at 300 K. The TBRs vary from 1.8 to 2.2 $\times 10^{-8}$ m^2.K/W for all samples at 300 K, which is in good agreement with literature.[156] However, it is evident that since we only have measured two thicknesses of each sample, and the films are very thin such that their thermal resistances are comparable to the extracted TBR, more samples should be measured for a better estimation of the TBR.

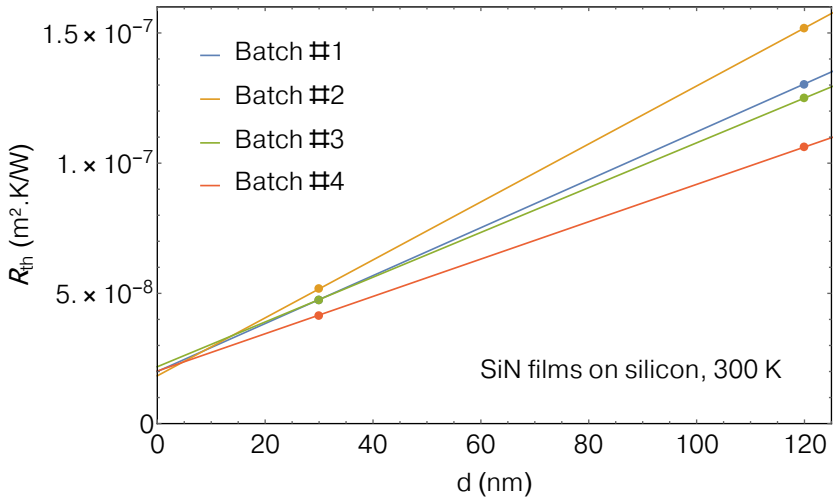

Figure 6.13: Measured thermal resistances for the four different SiN samples grown on silicon, with two thicknesses of the film for each sample. Data are represented as filled circles, whereas solid lines are linear fits. Each TBR is calculated to be around $\sim 2 \times 10^{-8}$ m^2.K/W.

6.2 Nanostructured germanium-based crystalline thin films

6.2.1 Effect of nano-inclusions : GeMn

As we have introduced in the first chapter, it is difficult to think of a device whose efficiency and durability are not limited by its thermal performances. Some devices will work well if heat is efficiently dissipated to the environment, whereas others, such as thermoelectric devices, will work more efficiently if their building blocks are poor heat conductors. Remembering that the efficiency of thermoelectric devices is given by their figure of merit $ZT = \sigma S^2/(k_{\text{el}} + k_{\text{lat}})$, where σ is the electrical conductivity, S is the Seebeck coefficient while $k_{\text{el}} + k_{\text{lat}}$ refers to the sum of the electronic and lattice contribution to the thermal conductivity, materials referred to as "phonon-glass electron-crystal" (PGEC)[74,220,221] are expected to be the most promising candidates for building efficient thermoelectric devices. PGECs refer to materials which are both good electrical conductors and poor heat conductors. It is in this context that crystalline semi-conductors with embedded crystalline nano-inclusions are model materials, since nano-inclusions, depending on their sizes and distribution, are expected to increase phonon scattering and thus reduce the lattice thermal conductivity, whereas the crystalline nature of the material would in principle let the electrical properties unaffected.

In this work, we have studied the thermal properties of an innovative nano-inclusions embedded semi-conductor, which consists of a crystalline germanium matrix with embedded crystalline spherical Ge_3Mn_5 nano-inclusions. We will present the fabrication process of this state-of-the art material, and then turn to the thermal conductivity measurements that have been achieved during this thesis.

6.2.1.1 Fabrication of a nanostructured germanium matrix with embedded spherical Ge_3Mn_5 nano-inclusions

The growth of the GeMn films have been performed in the research group SINAPS/INAC at CEA Grenoble, by Mustapha Boukhari and Dimitri Tainoff. The fabrication process of these films can be divided into several steps, which we describe now. First, the Ge(001) substrate

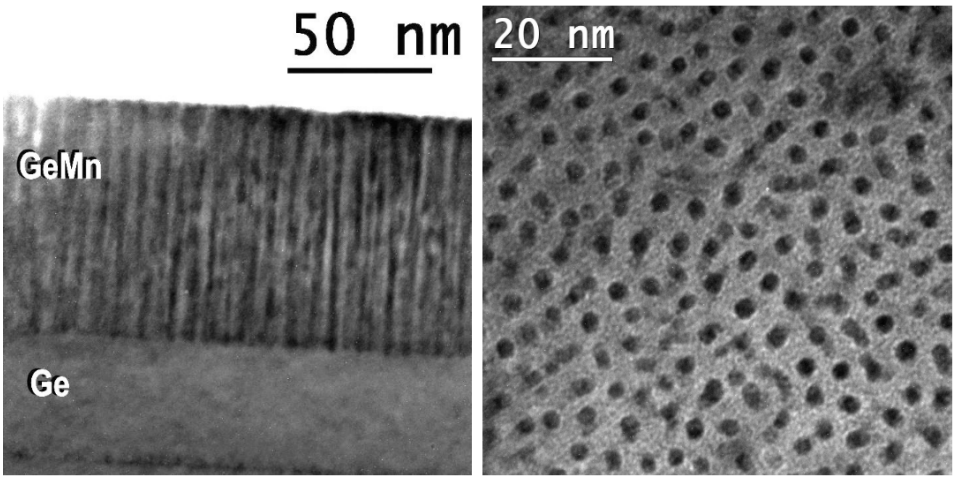

Figure 6.14: (a) Transverse and (b) plane view TEM micrographs of a $Ge_{0.89}Mn_{0.11}$ film on a Ge(001) substrate, which, at this step, consists of auto-organized GeMn nano-columns in a crystalline germanium matrix. Reprinted with permission from Ref. 223.

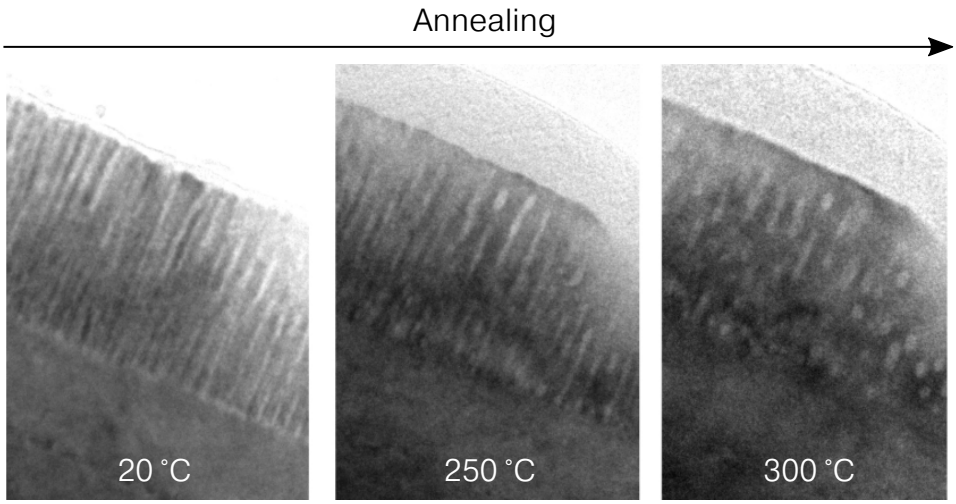

Figure 6.15: A post-growth annealing of the columnar GeMn film leads to the formation of Ge_3Mn_5 nano-clusters within the germanium matrix. Reprinted with permission from Ref. 223.

is etched to remove the oxidation layer that is present on its top surface. The films are then grown by Molecular Beam Epitaxy (MBE) in ultra-high vacuum on a $\sim$ 40 nm buffer Ge layer, deposited on the Ge substrate. Germanium and manganese are co-deposited using standard Ge and Mn effusion cells, at a growth temperature around 100 °C to minimize phase separation owing to the solubility of Mn in Ge.[222] The film thickness is well controlled because of the slow growth rate of 1.3 nm/min. The co-deposition leads to the formation of auto-organized nano-columns, which correspond to the segregation of Mn-rich phase induced by a spinodal decomposition. TEM micrographs of the nano-columns are shown in Figure 6.14.

To obtain GeMn spherical nano-inclusions in the germanium matrix rather than nano-columns, the film is annealed after growth at high temperature (450-500 °C) for about 15 min, leading to the formation of randomly distributed Ge_3Mn_5 nano-inclusions in a Mn doped crystalline germanium matrix. TEM micrographs showing the transition from columnar to nano-clusters in the film are shown in Figure 6.15.

The stoichiometry and crystallinity of the germanium matrix and nano-inclusions have

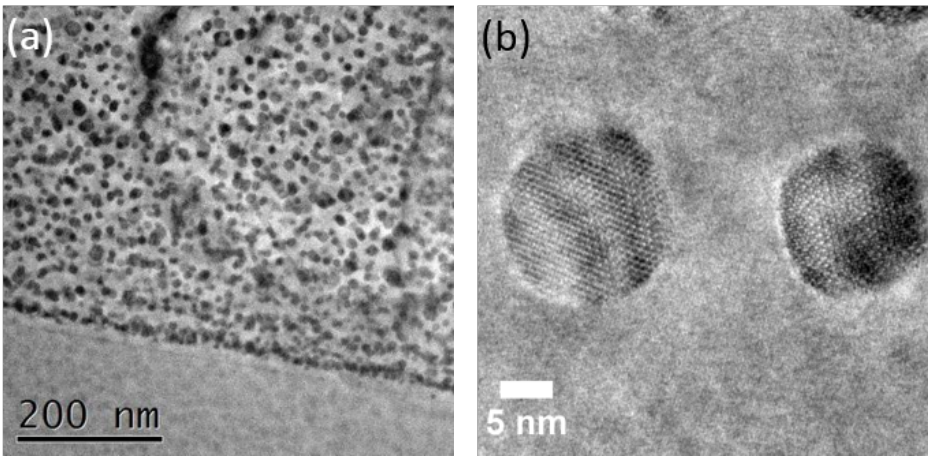

Figure 6.16: TEM images of the nanostructured GeMn films, taken by Eric Prestat from INAC. (a) showing the nano-inclusions distribution across the film and (b) showing the crystalline structure of both the hosting germanium matrix and Ge_3Mn_5 nano-inclusions.

been studied by means of HRTEM and XRD, which can be found in Refs. 224,225. The resulting film that consists of Ge_3Mn_5 nano-inclusions within a germanium matrix is shown in Figure 6.16.

The most interesting feature of the growth process is that the size distribution of the Ge_3Mn_5 nano-inclusions can be tuned by controlling the amount of manganese that is introduced during the growth and the annealing temperature. This is shown in Figure 6.17, where Mn concentrations of 8, 10, 12 and 14%, annealed at the same temperature, lead to different size distributions of the Ge_3Mn_5 nano-inclusions. In the bottom panel of Figure 6.17, the size distribution of the nano-inclusions within each germanium matrix is calculated using a image-processing counting software based on the samples' TEM micrographs.

Following the idea introduced in the first chapter, the nano-inclusion size distribution is an important parameter to play with in order to tune phonon transport and efficiently scatter a broad portion of the entire phonon spectrum. The well-controlled nano-inclusions size distribution of this innovative material as well as the perfect crystallinity of the germanium matrix make it a model material to study phonon transport. To quantify the effect embedded phonon scattering centers may have on phonon transport, we have measured the thermal conductivity of one nanostructured GeMn sample with 8 %Mn, as a function of temperature, using the 3ω method.

6.2.1.2 Thermal conductivity measurements

In the following, the germanium matrix with embedded spherical Ge_3Mn_5 nano-inclusions will be referred to as "GeMn" for simplicity. The thermal conductivity of the GeMn film has been measured using the 3ω method. The measurement of this sample has been very tedious and took a lot of time for several reasons. The surface quality of several samples have been shown to be flawed because of the migration of manganese during the annealing step of the growth process, leading to a very rough surface with Ge_3Mn_5 bubbles appearing at the film's surface, as shown in Figure 6.18. Several samples were therefore unusable because the deposited thermometers were electrically connected to the layer, even with a 60 nm Al_2O_3 insulating layer deposited on their surface. After these observations, we were able to grow

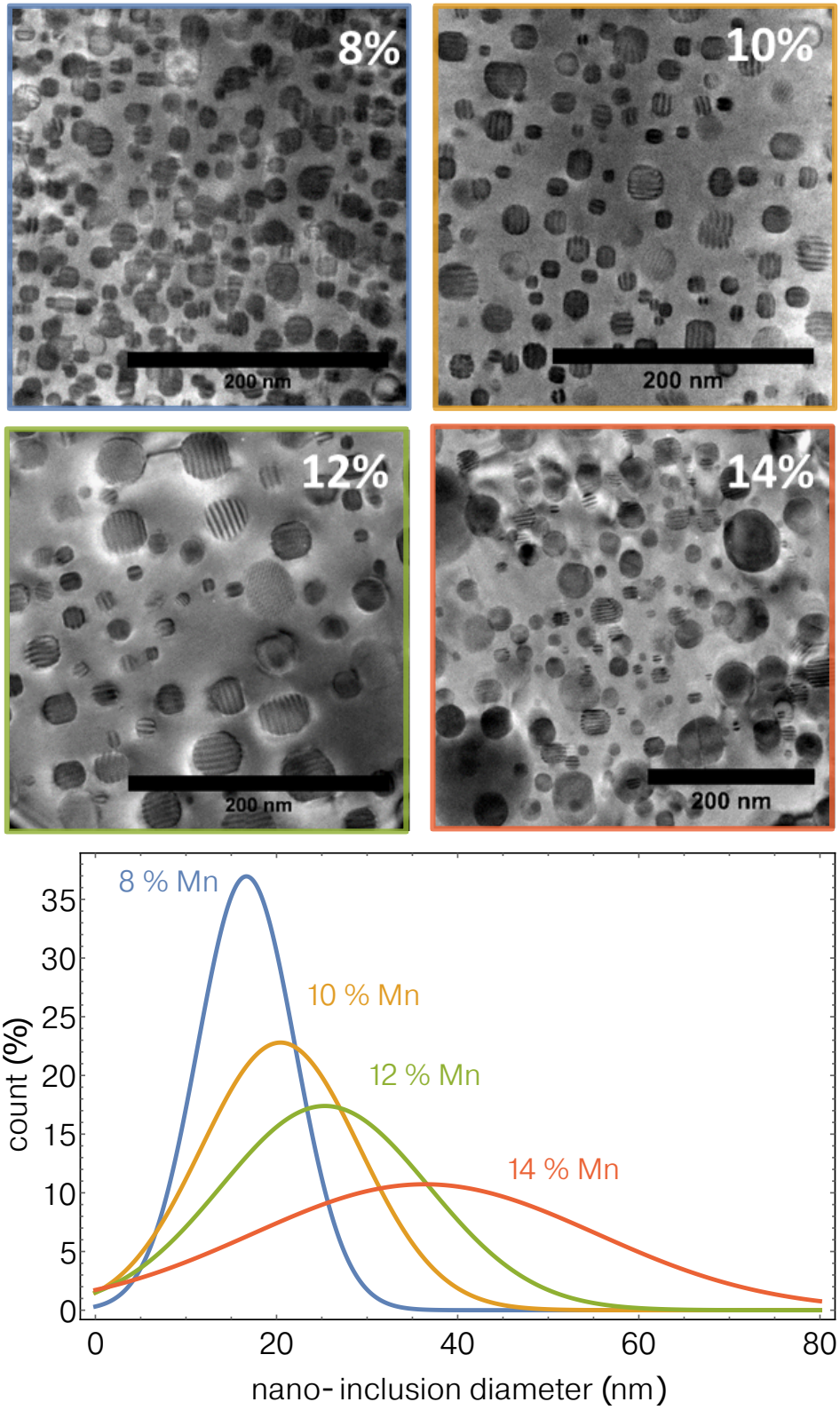

Figure 6.17: Top panels : cross sectional TEM images of the nanostructured GeMn films showing the nano-inclusions size distribution for different %Mn introduced during the growth process. Bottom panel : Gaussian fits of the measured size distributions of the Ge_3Mn_5 nano-inclusions, for different %Mn. The size distributions have been obtained using an image-processing counting software.

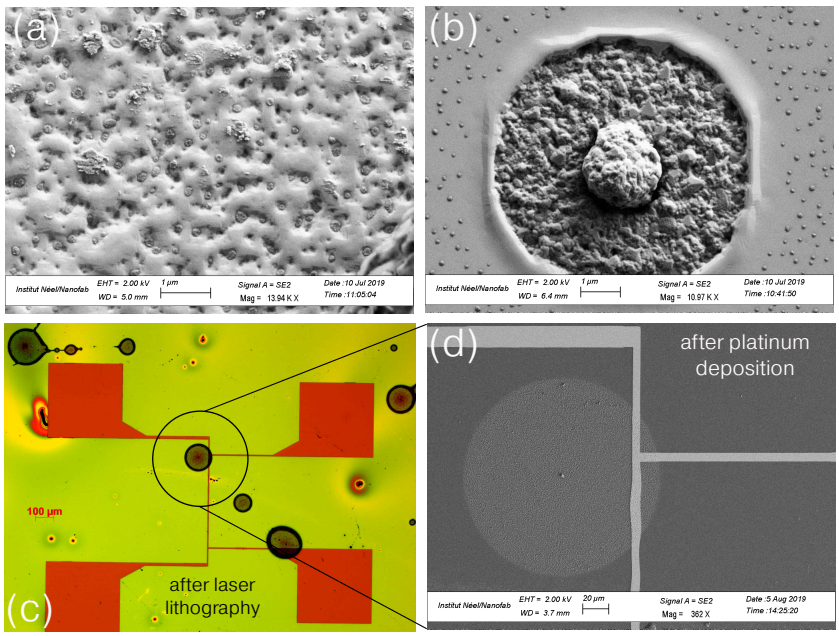

Figure 6.18: (a)-(b) SEM pictures of the surface of unusable GeMn samples, where we see Ge_3Mn_5 clusters that have migrated towards the surface. (c) optical and (d) SEM pictures of a thermometer which is (unfortunately) deposited on top of a Ge_3Mn_5 cluster, making it electrically connected to the substrate and therefore unusable.

several GeMn samples, which were capped in situ with a 80 nm germanium layer prior to the annealing step. This extra thin germanium layer was successful in making the surface smoother, allowing for the deposition of electrically insulated thermometers.

The other difficulty that we have faced, which is not related to the sample's surface quality, is the relatively high thermal conductivity of the film, which was difficult to estimate beforehand. As we have emphasized throughout this manuscript, the contribution of thermal boundary resistances is far from being negligible, in particular for thermally conductive films. The total thermal boundary resistances of the system Pt/ALD-Al_2O_3 + ALD-Al_2O_3/Ge have been measured in the first section of this chapter in order to estimate its contribution for the thermal conductivity measurements of the GeMn samples. The initial samples that were grown and ready to measure were 240 nm thick, and by estimating their thermal conductivity to about 20 W/m.K, leads to a thermal resistance of the film of $R_{\mathrm{GeMn}} = d_{\mathrm{GeMn}}/k_{\mathrm{GeMn}} = 240 \times 10^{-9}/20 = 1.2 \times 10^{-8}\mathrm{m}^2.\mathrm{K/W}$. In comparison, an estimation of the thermal weight of the Pt/ALD-Al_2O_3 + ALD-Al_2O_3/Ge TBRs, in addition to the 60 nm protecting Al_2O_3 layer is, based on our previous measurement :

$$\begin{aligned} &R_{\mathrm{Pt/ALD\text{-}Al_2O_3}} + R_{\mathrm{ALD\text{-}Al_2O_3/Ge}} + d_{\mathrm{Al_2O_3}}/k_{\mathrm{Al_2O_3}} \\ &= 3.7 \times 10^{-8} + 60 \times 10^{-9}/1.73 \\ &= 7.2 \times 10^{-8}\mathrm{m}^2.\mathrm{K/W} \end{aligned}$$

at 300 K and therefore the thermal contribution of the film would only account for 14% of the total thermal resistance. Therefore, thicker films have been grown, with thicknesses of 380 and 720 nm. A schematic of the multilayer system that has been measured is presented in Figure 6.19. Three samples have been used to infer the thermal conductivity of the film. One sample consisting of a germanium substrate with a 60 nm Al_2O_3 layer deposited on top

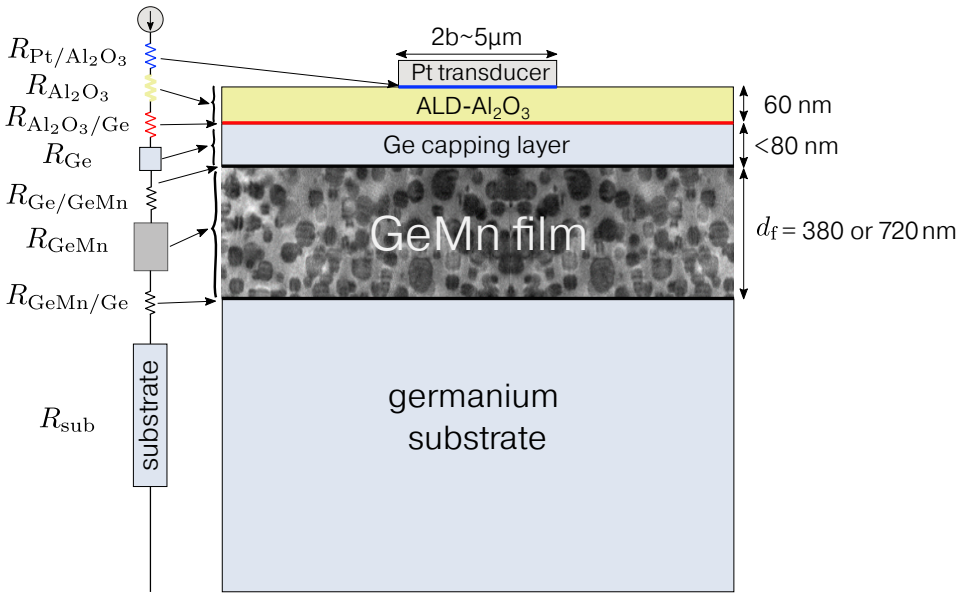

Figure 6.19: Schematic of the multilayer system studied, with an equivalent thermal circuit showing the thermal contribution of the films and interfaces to the total thermal resistance that is measured. The thermal circuit is shown for pedagogical purposes, we did not consider the GeMn film as a simple 1D thermal resistance in the data modelling.

(referred to as a reference sample in the following), and the other two with a GeMn thin film (380 and 720 nm) grown on a similar germanium substrate, covered with the same 60 nm Al_2O_3 layer that was deposited during the same ALD run. The platinum deposition has been performed during the same run for the three samples as well, with the purpose of creating the same interfaces between the film/insulating layer/thermometer for the three samples, to the best of our capability.

After the transducers' calibration and the usual $V_{3\omega} = f(I^3)$ measurements, the temperature oscillation is measured as a function of frequency at several temperatures for the three samples.

Data reduction procedure

The data treatment that we have performed for inferring the thermal conductivity of the GeMn layer is somewhat different from what we did in the past sections. In this particular case, following the recommendations of the jury who are gratefully acknowledged, we have considered the germanium capping layer as an extra layer in the thermal model instead of a simple thermal resistance in series with the heater. The reason for this is that the thermal conductivity of the Ge capping layer is not small and as such it can spread heat laterally, invalidating the approximation of the layer as a simple 1D thermal resistance since it would actually *lower* the temperature oscillation read across the thermometer. Besides, there exists an uncertainty on both the thickness and thermal conductivity of the germanium capping layer that should be accounted for in the fitting of the measurement to a thermal model.

The uncertainty on the thickness of the capping layer comes from the following reason. Several nominal thicknesses of the germanium capping layer have been deposited as trials, and a thickness of 80 nm was found to be a good compromise to keep a thin capping layer while preventing the surface to be affected by the migration of manganese during the annealing

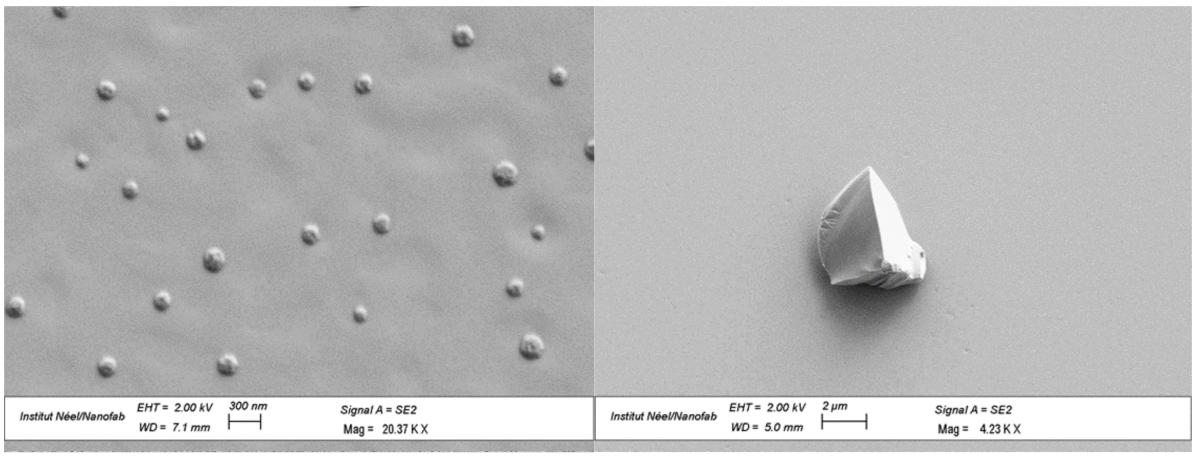

Figure 6.20: Effect of the germanium capping layer on the smoothness of the surface of the sample. Using a 30 nm thick germanium capping layer (left panel), we still observe the migration of Mn at the surface. A 80 nm thick capping germanium layer (right panel, the Ge chunk only serves here as a contrast reference) ensures a smoother surface, allowing for the deposition of a thermometer (after the subsequent deposition of an electrically insulating Al_2O_3 layer).

step, as explained in the beginning of this section. A 30 nm thick capping layer was not successful in making the surface of the GeMn layer smoother, as can be observed in Figure 6.20 where Mn islands can still be distinguished. This means that the thickness of the germanium capping layer is somewhat different from its nominal value since at 30 nm it still contains Mn. Therefore we expect the germanium layer to be around 50 nm thick if not less. Additional TEM characterization are necessary to estimate the true thickness of the germanium layer that is free from manganese. It also raises the question as if we should consider the germanium capping layer to be part of the GeMn film since its thickness is of the order of the inter-inclusion distance, or if it should be considered as an extra layer with different thermal properties from that of the GeMn layer. In the following, we consider the film as an extra layer with thermal properties taken from literature.

The thermal conductivity of the thin capping germanium layer is unknown but it is reasonable to assume that it is smaller than that of bulk germanium ($k_{\text{bulk Ge}} \approx 52$ W/m.K) due to its reduced thickness that is reducing the Ge phonon mean free path. This is confirmed by the measurements of Alvarez-Quintana and co-workers, suggesting that it lies between 15 and 35 W/m.K for these thicknesses.[226]

In order to take into account the effect of this layer on the determination of the thermal conductivity of the GeMn layer, we fit the measured frequency-dependence of the temperature oscillation using

$$\langle T \rangle = \langle T \rangle_{\text{Ge substrate+GeMn+capping Ge}} + \frac{P_l}{2b} R_{\text{TBRs+Al}_2\text{O}_3} \tag{6.5}$$

where

$$\langle T \rangle_{\text{Ge substrate+GeMn+capping Ge}} = \frac{P_l}{\pi} \int_0^\infty \frac{A}{C} \frac{\sin^2(\lambda b)}{(\lambda b)^2} d\lambda \tag{6.6}$$

with A and C are computed from

$$\begin{pmatrix} A & B \\ C & D \end{pmatrix} = \prod_{j=1}^{n} \begin{pmatrix} \cosh(\gamma_j d_j) & \frac{1}{k_{j_y}\gamma_j}\sinh(\gamma_j d_j) \\ k_{j_y}\gamma_j \sinh(\gamma_j d_j) & \cosh(\gamma_j d_j) \end{pmatrix} \tag{6.7a}$$

$$\gamma_j = \sqrt{k_{j_{xy}}\lambda^2 + i\omega\frac{(\rho Cp)_j}{k_{j_y}}} \tag{6.7b}$$

for $n = 3$ layers, following the thermal model derived in Ref. 123 and introduced in Chapter 3. The 3 layers considered here are the germanium substrate, the GeMn layer and the Ge capping layer. The contribution of thermal boundary resistances and of the 60 nm Al_2O_3 layer are accounted for in the second term of the right hand side of Eq.(6.5). The contribution of TBRs at the heater/film and film/substrate interfaces as well as the contribution of the alumina layer are taken from our separate measurement of the reference sample consisting of a 60 nm thick alumina film deposited onto a germanium substrate, from which we infer $R_{\mathrm{TBRs+Al_2O_3}} = R_{\mathrm{Pt/Al_2O_3}} + R_{\mathrm{Al_2O_3}} + R_{\mathrm{Al_2O_3/Ge}}$ (see Figure 6.21) and plug it into Eq.(6.5). Note that considering the contribution of TBRs and of the alumina film as one simple thermal resistance instead of considering the alumina film separately leads to an error of less than 1 mK on the resulting temperature oscillation, which is of the order of several hundred of mK.

We underline that when we proceed in this way, we assume the thermal boundary resistances at the GeMn/capping Ge and GeMn/buffer Ge interfaces to be negligible in comparison to the other thermal resistances : $R_{\mathrm{GeMn/Ge}} \approx R_{\mathrm{Ge/Ge}} \approx 0$. This should be well respected since the GeMn is mostly a germanium matrix.

The thermometers used for carrying out the measurements are about 5.5 μm large, and the distance between the two inner voltage pads is 500 μm – lengths that have been measured using SEM for each thermometer. The heat capacity of the GeMn sample is calculated using the weighted average of the heat capacity of Ge and Mn, which we have measured for germanium, and taken from literature[227] for manganese. The thermal anisotropy of the film is set to 1, which is an assumption based on TEM micrographs showing the homogenous repartition of the nano-inclusions. In any case, the temperature oscillation is not very sensitive to the film's thermal anisotropy since the heater is still relatively large compared to the thickness of the GeMn films.

As a preliminary verification procedure, we compare the thermal resistance measured on the reference sample – consisting of a germanium substrate on which a 60 nm thick layer of Al_2O_3 was deposited *during the same run* in which the alumina layers used to electrically insulate the GeMn samples were deposited – to the thermal conductivity and TBRs measurements obtained in Section 6.1.1 for the same structure, i.e. a 60 nm thick alumina layer deposited on a germanium substrate. This is what is displayed in Figure 6.21, where the thermal resistance measured for the reference sample (i.e. $R_{\mathrm{TBRs+Al_2O_3}}$) falls well within the uncertainty window that we have obtained in our previous measurement, illustrating the repeatability of the measurement.

The temperature oscillation normalized to heating power is plotted as a function of frequency for the three samples along with their best fit to Eq.(6.5) in Figure 6.22, at 300 K (for only one value of the thickness and thermal conductivity of the germanium capping layer in this particular example). We note a remarkable consistency between the three samples, with a fitted value for the germanium substrates of 52.9 W/m.K with a deviation of no more than 0.2 W/m.K, at 300 K. Note that the fitting is performed up to 3300 Hz. At 100 K, we

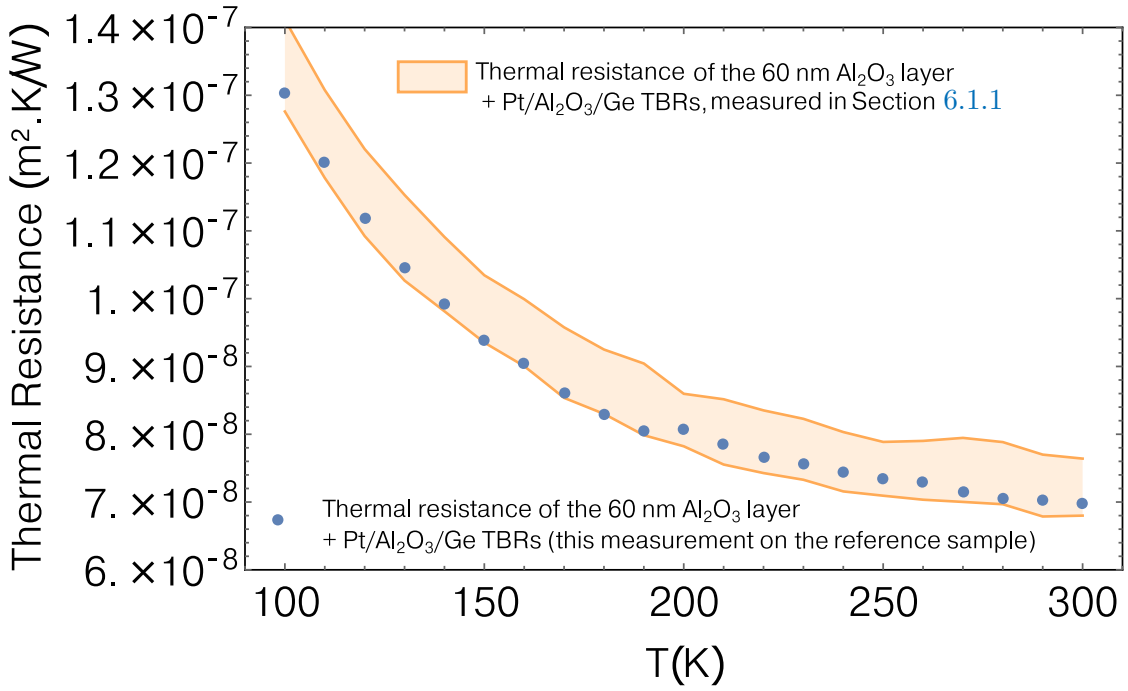

Figure 6.21: Comparison between the thermal resistance from the 60 nm thick Al_2O_3 layer and TBRs measured in Section 6.1.1 and the reference sample of this experiment. The reference sample consists of a germanium substrate on which a 60 nm thick layer of Al_2O_3 was deposited *during the same run* in which the alumina layers used to electrically insulate the GeMn samples were deposited. The fact that the two measurements coincide well underlines the repeatability of the experiment.

observe more discrepancies between the fitted values of the germanium substrate, as can be observed from Figure 6.23 with values ranging from 158 to 164 W/m.K, which is nonetheless very satisfying. At low frequency, we observe a combination of the effects of the finite length of the heater and of the thermal contact between the sample and sample holder on the measured temperature oscillation, making the fitting less accurate. At high frequency, for the temperature oscillation measured for the substrate with alumina only (in blue), the discrepancy is attributed to capacitive effects in the electrical circuit.

In order to quantify the contribution of the germanium capping layer on the measured temperature oscillation, in the fitting procedure, the thermal conductivity of the germanium capping layer is taken to be either 15 or 35 W/m.K, using thicknesses of 50 or 80 nm as lower and upper bounds, and constant from 100 to 300 K.[226]

Since we have measured two thicknesses of the GeMn film (380 and 720 nm), we fit the data for the two thicknesses of the films separately, leading to eight different results for the thermal conductivity of the film according to the thermal conductivity of the germanium capping layer used for the fitting (15 or 35 W/m.K) as well as its thickness (50 or 80 nm). The spread of thermal conductivity values obtained from the fitting of the different measurements leads to a range into which the thermal conductivity of the GeMn layer should fall into. The resulting thermal conductivity of the GeMn layers that is measured using the fitting procedure just described is shown in Figure 6.24.

The effect of the germanium capping layer is relatively weak at room temperature, where the thermal conductivity of the GeMn layer changes between 14 and 16 W/m.K for the 720 nm thick GeMn layer according to the thermal properties and thickness of the germanium capping layer. Similarly, it varies from 14 to 17 W/m.K for the 380 nm thick GeMn layer.

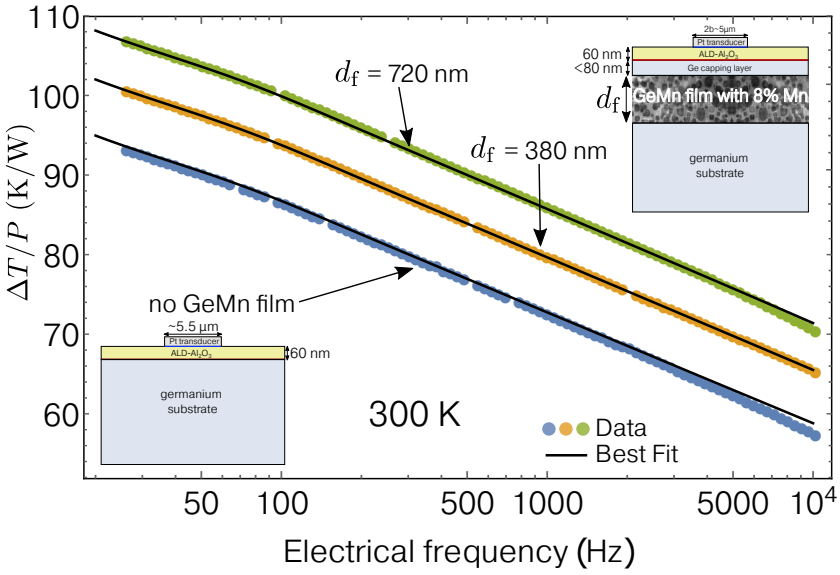

Figure 6.22: Temperature oscillation normalized by heating power versus frequency for the three samples at 300K. The greater thermal resistance of both GeMn samples, in comparison to the same system without the film, allows to infer their thermal conductivity.

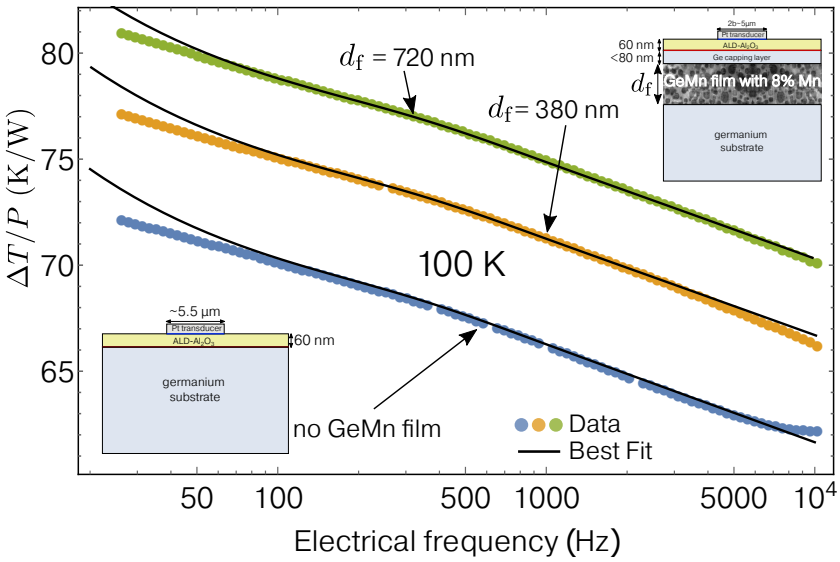

Figure 6.23: Temperature oscillation normalized by heating power versus frequency for the three samples at 100K. The discrepancies at high frequency comes from capacitive coupling effects in the electrical circuit. At low frequency, the discrepancy between the 2D model and the data comes from both the effect of the sample holder/sample contact, and the finite length of the thermometer. In principle, one can try to better fit data using a 3D model as introduced in Chapter 4.3. Here, we simply fit data from around 200 Hz such that the low-frequency effects are disregarded.

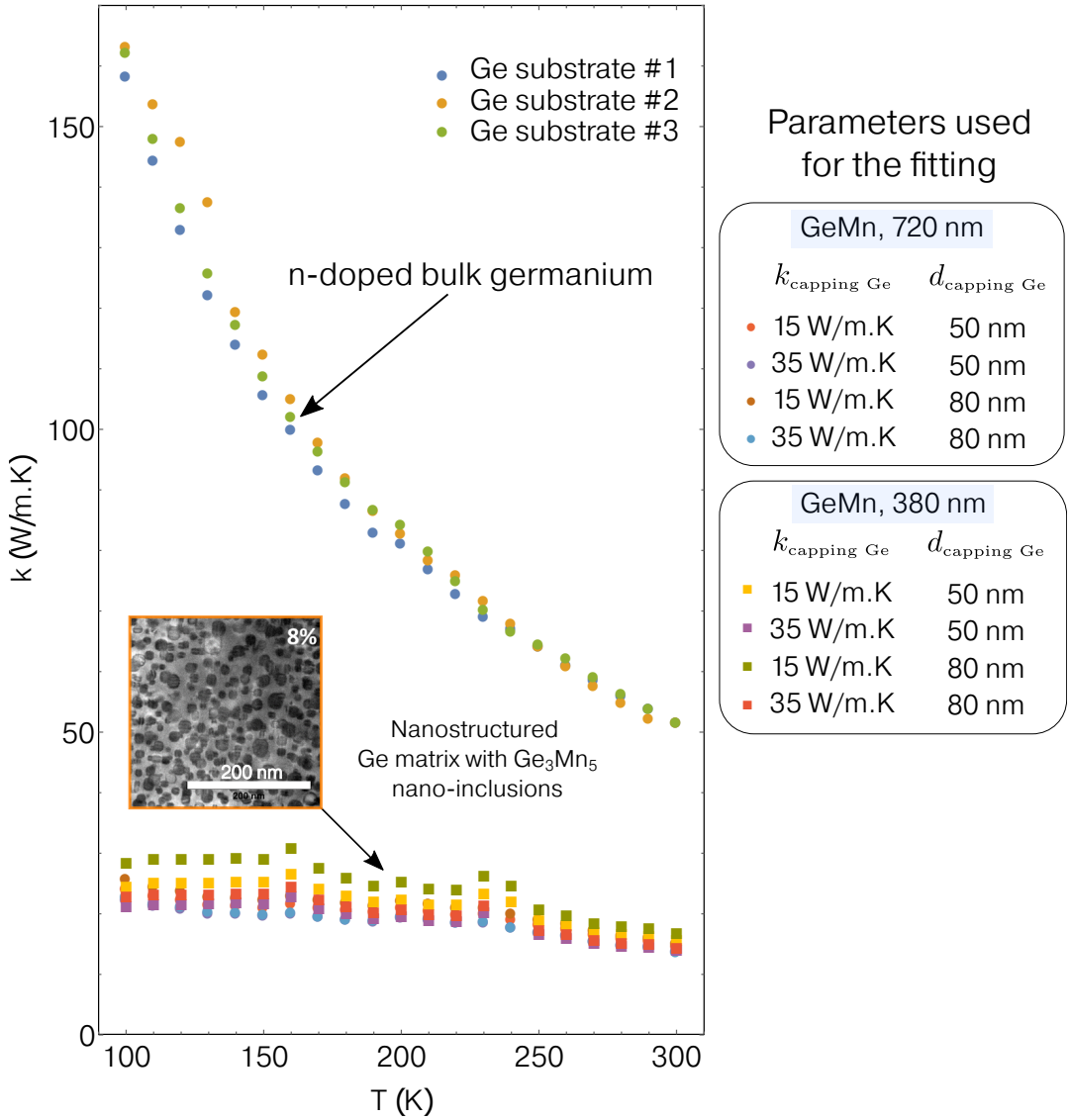

Figure 6.24: Thermal conductivity of the GeMn layer as function of temperature, obtained by changing the value of the thermal conductivity of the germanium capping layer as well as its thickness in the fitting process. The purpose is to quantify how does the germanium capping layer influence the value that we extract for the thermal conductivity of the GeMn film. At room temperature, it does not influence much the extracted thermal conductivity of the GeMn film but it does at 100 K. The thermal conductivity of the three germanium substrates are displayed as well and superpose reasonably well.

It also underlines the repeatability of the experiment since we obtain similar results for two different samples with different thicknesses. We do not expect the thermal conductivity of the GeMn films to be thickness-dependent since we assume the phonon mean free path in GeMn to be less than the phonon mean free path in bulk germanium, which is between 170 and 230 nm at room temperature[228,229] and thus smaller than the thickness of the films (380 and 720 nm).

There is however a more pronounced change at lower temperature (100 K), where the thermal conductivity of the GeMn layer varies between 22 and 28 W/m.K according to the thickness of the GeMn layer as well as the thickness and thermal conductivity of the germanium capping layer that we use for the fitting. We will take the upper and lower bonds of the fitted thermal conductivity as the uncertainty of the measurement in the following part, however we underline that the thickness of the GeMn films as well as that of the capping layer have to be measured using TEM in order to have a more rigorous estimation of the uncertainty of the thermal conductivity of the nanostructured film.

6.2.1.3 Results and discussion

The intrinsic thermal conductivity of the GeMn film, consisting of a Mn-doped crystalline germanium matrix, with embedded spherical nano-inclusions of Ge_3Mn_5 is shown in Figure 6.24. The three thermal conductivities of the three different germanium substrates are shown in comparison, and overlap quite well, with some deviation below 130 K of less than 10%. Most importantly, we observe a slight increase of the thermal conductivity of the nanostructured GeMn sample when temperature decreases, from around 14 W/m.K at 300 K to 28 W/m.K at 100 K. Solely based on the uncertainty of the thickness and thermal conductivity of the germanium capping layer, we estimate the uncertainty on the GeMn thermal conductivity to be around 30% at 100 K and lower as temperature increases.

To discuss the reduction by a factor of ∼3.5 of the thermal conductivity at room temperature, and most importantly its temperature dependence, we compare our results using two approaches.

Modified Effective Medium Approximation

The first approach is the modified Effective Medium Approximation (mEMA) developed by Minnich and Chen[228], which introduces an effective thermal conductivity for a host matrix with spherical nano-inclusions, following the work of Nan *et al.*[230] The mEMA is well adapted in situations where the characteristic length of the inclusion is on the order of or smaller than the phonon mean free path (MFP), which is the case for our system, as the mean inclusion diameter is of the order of 15 nm while the phonon mean free path in germanium is about 170 to 230 nm.[228,229] In the mEMA, it is assumed that the effective thermal conductivity is a function of the bulk MFP and a characteristic length that accounts for the nano-inclusion density – taken to be the *interface* density Φ, i.e. the surface area of a spherical nano-inclusion per unit volume of composite ; it is defined as[228] :

$$\Phi = \eta 4\pi r_{\mathrm{ni}}^2 \tag{6.8}$$

where r_{ni} is the nano-inclusion radius and η the number of nano-inclusions per unit volume (with unit of m^{-3}). The volume fraction of nano-particles φ (in %) is

$$\varphi = \eta \frac{4}{3} \pi r_{\mathrm{ni}}^3 \tag{6.9}$$

and thus $\Phi = \frac{3\varphi}{r_{\mathrm{ni}}}$. Since the effective area of collision for a phonon incident to a spherical inclusion is πr_{ni}^2, it will encounter $\eta \pi r_{\mathrm{ni}}^2 L$ inclusions while travelling a distance L. The phonon mean free path Λ_{coll} is thus written as

$$\Lambda_{\mathrm{coll}} = \frac{L}{\eta \pi r_{\mathrm{ni}}^2 L} = \frac{1}{\eta \pi r_{\mathrm{ni}}^2} = \frac{4}{\Phi} = \frac{4 r_{\mathrm{ni}}}{3\varphi} \tag{6.10}$$

The effective mean free path of the host material (Ge) is derived using Matthiessen's rule :

$$\frac{1}{\Lambda_{\mathrm{eff,Ge}}} = \frac{1}{\Lambda_{\mathrm{bulk,Ge}}} + \frac{1}{\Lambda_{\mathrm{coll}}} = \frac{1}{\Lambda_{\mathrm{bulk,Ge}}} + \frac{\Phi}{4} \tag{6.11}$$

In a "Casimir spirit", the phonon mean free path in the particle phase (Ge_3Mn_5) is set to be the characteristic length of the particle, i.e. its diameter. The effective mean free path in the inclusion's phase is thus

$$\frac{1}{\Lambda_{\mathrm{eff,Ge_3Mn_5}}} = \frac{1}{\Lambda_{\mathrm{bulk,Ge_3Mn_5}}} + \frac{1}{2 r_{\mathrm{ni}}} \tag{6.12}$$

The thermal conductivity k of both the host and particle phases can then be estimated in a first approximation using kinetic theory :

$$k = \frac{1}{3} \int C_p(\omega) v(\omega) \Lambda(\omega) d\omega \approx \frac{1}{3} C_p v \Lambda \tag{6.13}$$

The mEMA then leads to the following expression for the effective thermal conductivity of the germanium matrix with spherical Ge_3Mn_5 nano-inclusions[228,230] :

$$k_{\mathrm{eff}} = \frac{1}{3} C_{p,\mathrm{Ge}} v_{\mathrm{Ge}} \frac{1}{(1/\Lambda_{\mathrm{Ge}}) + \Phi/4} \times \frac{k_{\mathrm{Ge_3Mn_5}}(1+2\delta) + 2k_{\mathrm{Ge}} + 2(\Phi r_{\mathrm{ni}}/3)[k_{\mathrm{Ge_3Mn_5}}(1-\delta) - k_{\mathrm{Ge}}]}{k_{\mathrm{Ge_3Mn_5}}(1+2\delta) + 2k_{\mathrm{Ge}} - (\Phi r_{\mathrm{ni}}/3)[k_{\mathrm{Ge_3Mn_5}}(1-\delta) - k_{\mathrm{Ge}}]} \tag{6.14}$$

where $\delta = R_{\mathrm{TBR}} k_{\mathrm{Ge}} / r_{\mathrm{ni}}$, R_{TBR} being the thermal boundary resistance between the particle and the host material.

We need several thermal properties from both the host and inclusions phases in order to estimate the effective thermal conductivity of the medium. The heat capacity that is measured experimentally takes into account the contribution of acoustic and optical phonons, for all wave-vectors. However, optical phonons do not contribute much to the thermal conductivity since their group velocity is very small. Besides, at room temperature, most phonons are populated at the edge of the Brillouin zone where the phonon group velocity is significantly smaller than the sound velocity.[32] One should thus only account for the acoustic phonons' contribution to the thermal conductivity in the kinetic theory, and similarly, the phonon group velocity should be calculated from approximate dispersion relations (sine-type for instance), as well as the phonon specific heat.[32] For Ge, it leads to a reduction of the phonon group velocity by a factor of ~ 4, compared to Debye's velocity. Therefore, we will use values from Ref. 228 for computing the thermal conductivity of the germanium host matrix in the kinetic model. They are reproduced in Table 6.2. For the Ge_3Mn_5 phase, it is less trivial since little literature exists for the phonon group velocity and mean free path. However, it is noticed that the effective thermal conductivity of the Ge_3Mn_5 phase is only modified from its bulk value by adding

Material	C_p (MJ.m^{-3}.K^{-1})	v (m.s^{-1})	Λ (nm)
Ge	0.87	1042	171

Table 6.2: Parameters taken to estimate the thermal conductivity, *using the kinetic formula*, for the germanium host (Ge). Taken from Ref. 228.

an additional mean free path that is equal to the particle diameter. Therefore it becomes relevant only when the phonon mean free path is larger than the nano-inclusion size. Here, the thermal conductivity of the Ge_3Mn_5 phase is taken to be that derived in Ref. 231 using molecular dynamics, i.e. $k_{Ge_3Mn_5} \approx 3.7$ W/m.K. For thermal conductivities of this order of magnitude, the mean free path can be roughly estimated to be of the order of tens of nm. For instance, the calculated mean free path of GeTe, whose thermal conductivity is of the same order of magnitude as that of Ge_3Mn_5, is calculated to be about 16 nm.[232] Consequently, our calculation will take a fixed value for the thermal conductivity of the particle phase, $k_{Ge_3Mn_5} = 3.7$ W/m.K. In other words, we assume that the thermal conductivity of the particle phase is not drastically reduced because of its diameter. However the interface density, which takes into account the nano-inclusion volumetric fraction and diameter, is accounted for in the calculation of the effective thermal conductivity of the germanium host matrix.

The effective thermal conductivity of the medium is then very dependent on the volume fraction of nano-inclusions. It has been estimated using TEM micrographs but is still difficult to quantify accurately. It was estimated to be around 12 % by Yanqing Liu, the previous PhD student in our group.[233] Using this estimation leads to an effective thermal conductivity of 15 W/m.K at 300 K. Changing the thermal boundary resistance from 10^{-9} to 10^{-8} m^2.K/W does not substantially affect the result. Evidently, given the difference in terms of thermal conductivity between the host matrix and nano-particles, the greater the volume fraction of nano-particles, the more reduced the thermal conductivity. This approach gives very good results in terms of the thermal conductivity reduction that is observed in the GeMn sample, at room temperature, and suggests that the reduction in the thermal conductivity of the effective media is mostly due to the low thermal conductivity of the nano-inclusions, their volumetric fraction along with the interface density.

We will now turn to a more general approach for calculating the thermal conductivity of the material as a function of temperature, which makes no assumption about the thermal conductivity of the phase material, but considers the scattering cross section of the nano-inclusion size distribution, and other relevant scattering mechanisms, as we have introduced in Chapter 1.

Modelling using Boltzmann transport equation

We now use the frequency and temperature dependence of the phonon scattering rates to compute the thermal conductivity of the GeMn films, as a function of temperature. Several expression of increased complexity exist for expressing the thermal conductivity of a material as a function of phonon relaxation time, temperature and frequency.[26,34,45] Here we will use the model and fitting constants provided by Morelli *et al.*[45] in order to compute the thermal conductivity of germanium as a function of temperature, which is one of the most advanced model to describe the lattice thermal conductivity in germanium. Note that their work follows

the formulation of the thermal conductivity of Asen-Palmers and co-workers, based on the Debye-Callaway formalism.[34,44]

In this model, the thermal conductivity is expressed as the sum of the contribution of the longitudinal (L) and transverse (T) components of the thermal conductivity :

$$k = k_L + 2k_T \tag{6.15}$$

where

$$k_L = k_{L1} + k_{L2} \tag{6.16}$$

The partial conductivities k_{L1} and k_{L2} are expressed as :

$$k_{L1} = \frac{1}{3} C_L T^3 \int_0^{\theta_L/T} \frac{\tau_C^L(x) x^4 e^x}{(e^x-1)^2} dx \tag{6.17}$$

$$k_{L2} = \frac{1}{3} C_L T^3 \frac{\left[\int_0^{\theta_L/T} \frac{\tau_C^L(x) x^4 e^x}{\tau_N(x)(e^x-1)^2} dx\right]^2}{\int_0^{\theta_L/T} \frac{\tau_C^L(x) x^4 e^x}{\tau_N^L(x)\tau_R^L(x)(e^x-1)^2} dx} \tag{6.18}$$

for longitudinal phonons, and

$$k_{T1} = \frac{1}{3} C_T T^3 \int_0^{\theta_T/T} \frac{\tau_C^T(x) x^4 e^x}{(e^x-1)^2} dx \tag{6.19}$$

$$k_{T2} = \frac{1}{3} C_T T^3 \frac{\left[\int_0^{\theta_T/T} \frac{\tau_C^T(x) x^4 e^x}{\tau_N(x)(e^x-1)^2} dx\right]^2}{\int_0^{\theta_T/T} \frac{\tau_C^T(x) x^4 e^x}{\tau_N^T(x)\tau_R^T(x)(e^x-1)^2} dx} \tag{6.20}$$

for transverse phonons, where

$$C_{L,T} = \frac{k_B^4}{2\pi^2 \hbar^3 v_{L(T)}} \qquad \text{and} \qquad x = \frac{\hbar\omega}{k_B T} \tag{6.21}$$

A Debye model for the phonon density of states is implied, as explained in Chapter 1. The inverse relaxation times are separated into a resistive (τ_R) and a normal (τ_N) term. The resistive term includes the relaxation times for specific scattering processes using Matthiessen's rule :

$$[\tau_{\mathrm{R}}^L]^{-1} = [\tau_{\mathrm{b}}^L]^{-1} + [\tau_{\mathrm{u}}^L]^{-1} + [\tau_{\mathrm{i}}^L]^{-1} + [\tau_{\mathrm{ni}}^L]^{-1} \tag{6.22}$$

and

$$[\tau_{\mathrm{R}}^T]^{-1} = [\tau_{\mathrm{b}}^T]^{-1} + [\tau_{\mathrm{u}}^T]^{-1} + [\tau_{\mathrm{i}}^T]^{-1} + [\tau_{\mathrm{ni}}^T]^{-1} \tag{6.23}$$

for the longitudinal and transverse phonon branches, respectively.[45] The expressions for the relaxation times considered for computing the thermal conductivity are listed in Table 6.3, adapted from Ref. 45.

In Table 6.3, we use $\theta_L = 333$ K, $\theta_T = 150$ K, $v_T = 3540$ m.s^{-1} and $v_L = 4920$ m.s^{-1}, representing the Debye temperature and phonon group velocity in germanium for both phonon polarizations. Every constant and expression in Table 6.3 is taken from Ref. 45 except for the constant term (A) for impurity scattering that we took from Ref. 34.

Using the expression of the thermal conductivity Eqs.(6.15)-(6.23) as well as the form of the scattering rates and constants as expressed in Table 6.3, we calculate the thermal

Scattering process	Phonon branch	Inverse relaxation time (s^{-1})	Relevant constant
Boundary	L	$[\tau_b^L]^{-1} = v_L/L_e$	Relevant length (m)
	T	$[\tau_b^T]^{-1} = v_T/L_e$	Relevant length (m)
Impurity	L	$[\tau_i^L]^{-1} = Ax^4(k_B/\hbar)^4T^4$	$A = 1.1 \times 10^{-44}(s^{-1})$
	T	$[\tau_i^T]^{-1} = Ax^4(k_B/\hbar)^4T^4$	$A = 1.1 \times 10^{-44}(s^{-1})$
Umklapp	L	$[\tau_u^L]^{-1} = B_U^L(k_B/\hbar)^2x^2T^3e^{-\theta_L/3T}$	$B_U^L = 1.3 \times 10^{-19}(s^{-1}K^{-3})$
	T	$[\tau_u^T]^{-1} = B_U^T(k_B/\hbar)^2x^2T^3e^{-\theta_T/3T}$	$B_U^T = 1.6 \times 10^{-19}(s^{-1}K^{-3})$
Normal	L	$[\tau_n^L]^{-1} = B_N^L(k_B/\hbar)^2x^2T^5$	$B_N^L = 1.9 \times 10^{-23}(s^{-1}K^{-5})$
	T	$[\tau_n^T]^{-1} = B_N^T(k_B/\hbar)xT^5$	$B_N^T = 3.7 \times 10^{-12}(s^{-1}K^{-5})$
Nano-inclusion	L	$[\tau_{ni}^L]^{-1} = \sigma(\chi)\eta v_L$	-
	T	$[\tau_{ni}^T]^{-1} = \sigma(\chi)\eta v_T$	-

Table 6.3: Form of the scattering processes as well as the associated constants used for calculating the thermal conductivity of germanium from 100 to 300 K. We use $\theta_L = 333$ K, $\theta_T = 150$ K, $v_T = 3540$ m.s^{-1} and $v_L = 4920$ m.s^{-1}, for the Debye temperature and phonon group velocity of germanium, taken from Ref. 45.

conductivity of bulk germanium, by setting the length L_e in the boundary scattering term to be the thickness of the germanium substrate, i.e. we set $L_e = 500$ μm. Importantly, the nano-inclusion scattering term is set to zero ($[\tau_{ni}^T]^{-1} = 0$). The resulting thermal conductivity is plotted in Figure 6.26 as a dashed black line, and fits relatively well with the measured thermal conductivity of the three germanium substrates on the temperature range of 100-300 K. Therefore, we will keep the form of the scattering rates as well as their associated constants in the following.

Before calculating the effect of the nano-inclusions, we first quantify the effect of the reduced thickness of the GeMn layer in order to verify that the decreased thermal conductivity of the film is not *only* due to phonon boundary scattering. This is shown in Figure 6.26, where we plot the thermal conductivity of germanium as a function of temperature using Eqs.(6.15)-(6.23) with the parameters of Table 6.3 and setting $L_e = 380$ nm (blue solid line) and $L_e = 720$ nm (dark yellow solid line). From this calculation, we can conclude that the thickness of the layer does reduce the thermal conductivity of germanium, but does not explain the drastic reduction of the thermal conductivity that is observed in our GeMn films.

To try to explain this reduction, we then calculate the thermal conductivity of the GeMn sample, using the same parameters used for fitting the temperature dependence of the substrate's thermal conductivity and adding the nano-inclusions scattering term $[\tau_{ni}^T]^{-1}$ (as well as the boundary constant term L_e which is set to to be the thickness of the GeMn film[3]).

The inverse relaxation time for phonon scattering with nano-inclusions is proportional to the nano-inclusions concentration η, phonon group velocity $v_{L,T}$ and most importantly the scattering cross-section $\sigma(\chi)$. As we have introduced in the first chapter, an expression for the scattering cross-section due to nano-inclusions has been proposed by Kim and Majumdar[77], which introduces the size distribution of the nano-inclusions. The form of the scattering cross-section depends on the size parameter χ that relates the phonon wavevector k to the radius of the nano-inclusion r_{ni} via $\chi = kr_{ni}$. In the limit $\chi \to 0$, we have $\sigma \propto r_{ni}^6/\lambda^4$, representing

[3]Setting the thickness of the GeMn film to 380 nm or 720 nm does not change drastically the thermal conductivity of the GeMn film, when the nano-inclusion scattering term is added. Therefore we use L_e= 720 nm.

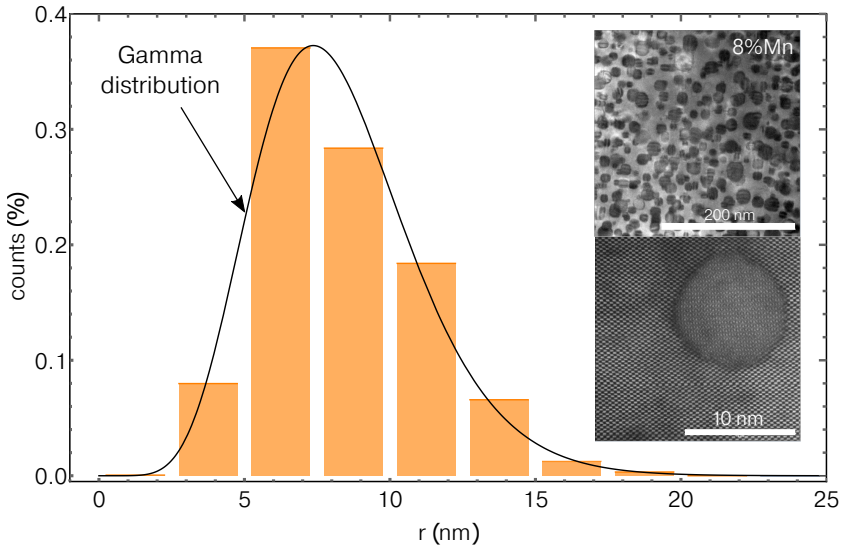

Figure 6.25: Measured size distribution of Ge_3Mn_5 nano-inclusions in the Ge matrix (orange histograms) and Gamma distribution that best fit the data (solid black line). The fitted gamma distribution has the following parameters : $\alpha_g = 8.92$ and $\beta_g = 0.93$ nm (see Eq.(6.25)). In inset are TEM images of the material, showing the distribution of nano-inclusions, as well as one Ge_3Mn_5 nano-inclusion. Images taken by Eric Prestat.

the Rayleigh scattering regime. In the opposite case where $\chi \gg 1$, we have $\sigma = 2\pi r_{\text{ni}}^2$ which is the so-called geometric limit. In the temperature range explored (100-300 K), the dominant phonon wavelength is of the order of the nanometer while the nano-inclusion radius is of the order of 10 nm. Therefore we expect to be in the geometric limit since $\chi \gg 1$, and the scattering cross section for a particular nano-inclusion size is set to $2\pi r^2$. The total scattering cross-section σ_{sct}, accounting for the size distribution of nano-inclusions is written as[77] :

$$\sigma_{\text{sct}} = \int_0^\infty 2\pi r^2 f(r) dr \tag{6.24}$$

where $f(r)$ is the size distribution of nano-inclusions. We have fitted the size distribution estimated from TEM micrographs[233], using a gamma function, which takes into account only positive numbers such that the size of the nano-inclusions cannot be negative. The gamma distribution is expressed as :

$$g(r, \alpha_g, \beta_g) = \frac{r^{\alpha_g - 1} e^{-r/\beta_g}}{\beta_g^{\alpha_g} \Gamma(\alpha_g)} \tag{6.25}$$

where $\Gamma(\alpha_g)$ is the gamma function evaluated at α_g. The mean value of a gamma distribution is given by $\alpha_g \beta_g$ while the variance is $\alpha_g \beta_g^2$. Fitting the measured size distribution of Ge_3Mn_5 nano-inclusions in the germanium matrix to a gamma function leads to $\alpha_g = 8.92$ and $\beta_g = 0.93$ nm, leading to a mean nano-particle radius of 8.3 nm with standard deviation of 2.77 nm. The measured and fitted size distribution are shown in Figure 6.25.

By using the measured value[233] of the nano-inclusion concentration $\eta = 3.91 \times 10^{22}$ m^{-3}, the inverse scattering time can be calculated and the thermal conductivity of the GeMn film computed. The calculated thermal conductivity, computed using Eqs.(6.15)-(6.23), and using the scattering rates as expressed in Table 6.3, is plotted as a function of temperature in Figure 6.26. The green curve takes into account phonon scattering with polydispersed nano-inclusions, whose scattering cross section is computed using Eq.(6.24) using the fitted parameter of the nano-inclusions' size distribution. Using this model, the thermal conductivity of the film is

reduced by a factor of more than 4 at room temperature to reach 12 W/m.K, which is close to our finding of around 15 W/m.K at room temperature. However, the thermal conductivity computed using the form of the relaxation rates presented in Table 6.3 does not reproduce well the amplitude of the measured thermal conductivity at lower temperature. We underline that the computed thermal conductivity is heavily dependent on the nano-inclusions concentration η. A large uncertainty on the nano-inclusions concentration translates to a large uncertainty on the calculated thermal conductivity.

In an attempt to estimate the length scale that is defining heat transport in this nanostructured material on the explored temperature range of 100-300 K, we adjust the boundary scattering rate $\tau_b^{-1} = v/L_e$ by changing the constant L_e such that the calculated thermal conductivity matches experimental data, while setting the nano-inclusion scattering term to zero. By definition, L_e is a characteristic length scale that is closely related to the phonon mean free path. In Figure 6.26, the purple line represents the computed thermal conductivity of a germanium film using a characteristic length of $L_e = 100$ nm, which is the length that best fits our experimental findings. Note that adjusting this boundary scattering term to fit the measured thermal conductivity is only performed here to provide an estimation of the phonon mean free path. However, physically, the length of 100 nm represents neither the thickness of the film nor the average inter-inclusion distance, which is of the order of 30 nm for this sample, and thus should only be understood as an effective length. In other words, using this model, a 720 nm thick nanostructured GeMn film is as efficient in reducing heat transport as a 100 nm thick germanium thin film free of nano-inclusions. The almost flat temperature dependence of the thermal conductivity of the nanostructured GeMn film also tells us that nano-inclusions are the dominant phonon scattering centers and dominates over scattering processes such as umklapp and impurity scattering. These experimental findings are one additional evidence of reduced thermal conductivity using nanostructuration in a fully crystalline material.

Before moving on to the next part, we underline that other approaches have been developed to describe more rigorously heat transport in porous media, with inclusions of different sizes, which can be aligned or randomly distributed. For instance, Jean *et al.*[234] used phonon Monte Carlo Ray Tracing to estimate the phonon mean free path in porous germanium and silicon. Our collaborators from LEMTA (Nancy), supervised by D. Lacroix, have calculated the thermal conductivity of the GeMn sample using a Monte Carlo method, using the porosity and distribution of our sample while considering the nano-inclusions to be filled with air. For a 1 μm thick film, it leads to a thermal conductivity of around 10 W/m.K. We can reasonably take this value as a lower bound for the thermal conductivity of the GeMn material, since the thermal conductivity of the nano-inclusions is expected to be much larger than that of air. This is in good agreement with our measurement of $k \approx 15$ W/m.K.

By analysing the temperature dependence of the simulated thermal conductivity of the GeMn film plotted in Figure 6.26, it is evident that measuring the thermal conductivity of the film at lower temperature would be an important step towards the understanding of scattering processes governing phonon transport in this model material. Indeed, we would expect phonon-scattering to follow a Rayleigh-like description, since the dominant phonon wavelength would eventually become larger than the nano-inclusion size at sub-Kelvin temperatures. Besides, samples with different nano-inclusion size-distributions would prove useful in quantifying the effect of size-distribution on phonon transport – which is a perspective of this work.

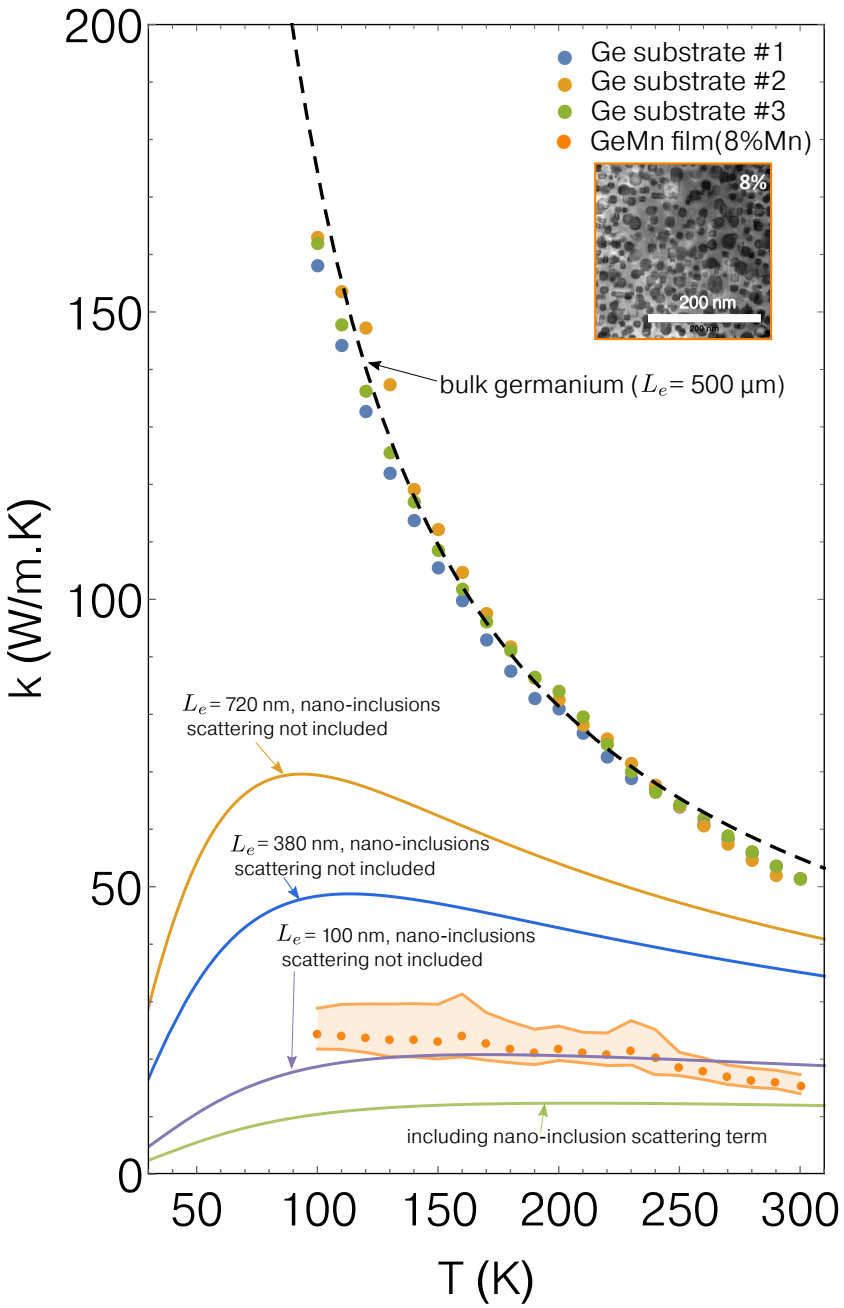

Figure 6.26: Temperature dependence of the measured thermal conductivity for bulk germanium and the nanostructured GeMn film (filled circles), along with calculation using Boltzmann transport equation under the relaxation time approximation, following the model of Ref. 45 (lines). The dashed and solid lines have been computed using Eqs.(6.15)-(6.23) and the parameters displayed in Table 6.3. The thermal conductivity of the GeMn film corresponds to the mean of the 8 values that have been derived when changing the thickness and thermal conductivity of the germanium capping layer (that are displayed in Figure 6.24), as explained in the main text. The upper and lower bounds correspond to the highest and lowest thermal conductivity of the film.

6.2.2 Effect of grains and doping : GeTe and GeTeC

We now turn to a different kind of material, still germanium-based, but which consists of an *alloy* of germanium and telluride. GeTe is a very popular chalcogenide phase change material (PCM), primarily because of its is ability to quickly and reversibly switch between its amorphous and crystalline states. The large contrast of the material's electrical conductivity in both phases allows for a high contrast between logical states, a primary criteria for enhanced performances in phase change memories applications.[235–237] Because of its inherently low thermal conductivity and great electrical conductivity, it is also a very promising material for thermoelectric applications.[238,239] For the two applications, a reduced thermal conductivity is desired for enhanced device performance. In phase change memory applications, switching between the crystalline and amorphous phase of the material requires to pass a current through a metallic layer placed below the material, which will locally heat the material via Joule heating and induce a phase transition. Thus for low thermally conductive materials, heat confinement is much more effective, which allows to use a lower programming current in the metallic heater – hence leading to a better efficiency of the device.

We have performed thermal conductivity measurements on different kind of GeTe-based materials, which have been grown with the intent of reducing the materials' thermal conductivity. We underline that this was part of a collaborating project with Valentina Giordano from Institut Lumière Matière (Lyon), and Pierre Noé from CEA-LETI (Grenoble). In the following, we will introduce how the material is grown, and present our thermal conductivity measurements, performed using the 3ω method.

6.2.2.1 Growth of chalcogenide thin films : GeTe and C-doped GeTe

GeTe and C-doped GeTe thin films were grown in CEA-LETI by Pierre Noe and Rebecca Chahine. GeTe thin films with thicknesses of 500 nm and 1000 nm were grown by DC magnetron sputtering from GeTe mono-targets on Si(001) substrates with a 10 nm SiN or SiO_2 capping layer, under argon atmosphere with a pressure of 0.005 mbar, at room temperature. They were then capped using a 10 nm SiN or SiO_2 layer. A subsequent thermal annealing post growth induces crystallization of the GeTe films.

The C-doped samples have been prepared by co-sputtering of GeTe and C targets, by DC magnetron sputtering as well on Si(001) substrates with a 10 nm capping SiN layer. In this work, two different C-doped GeTe samples have been measured, with 9 % and 16 % of carbon atomic content (%at.). For the sample with 9%at., two thicknesses of the films (100 nm and 1000 nm) have been grown, with a 10 nm SiN capping layer in order to prevent oxidation. Only one thickness (1000 nm) has been grown for the 16 % C-doped GeTe sample. Similarly, they have been annealed post growth to induce crystallization.

6.2.2.2 Thermal conductivity measurements

The thermal conductivity of GeTe and C-doped GeTe thin films have been measured using the 3ω method as well. Since the thickest films are 1 μm thick, the thermometers used for conducting the 3ω measurements have been chosen to be 30 μm large, such that a 1D heat transfer model can be used – for all but the amorphous film – to model the thin films as simple thermal resistances in series with the heater/thermometer. Besides, the thermal conductivity of all films is expected to be much lower (ranging from 0.2 to $\sim$8 W/m.K according

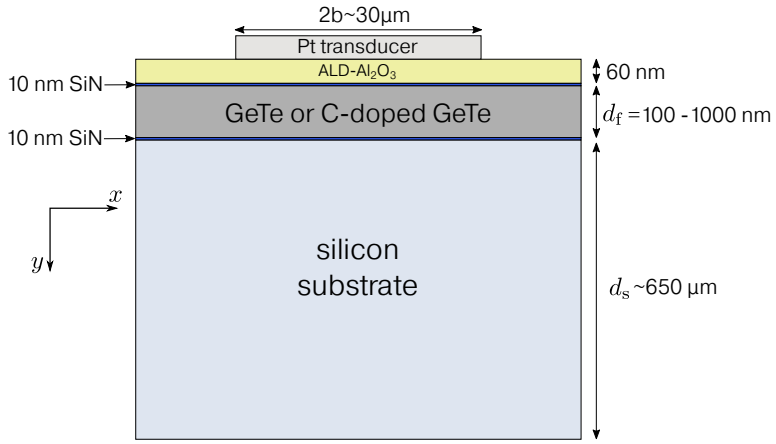

Figure 6.27: Schematic of the sample geometry. The thickness of the film of interest, GeTe or C-doped GeTe, is either 100, 500 or 1000 nm, as explained in the text. Note that there are thermal boundary resistances between each consecutive layer.

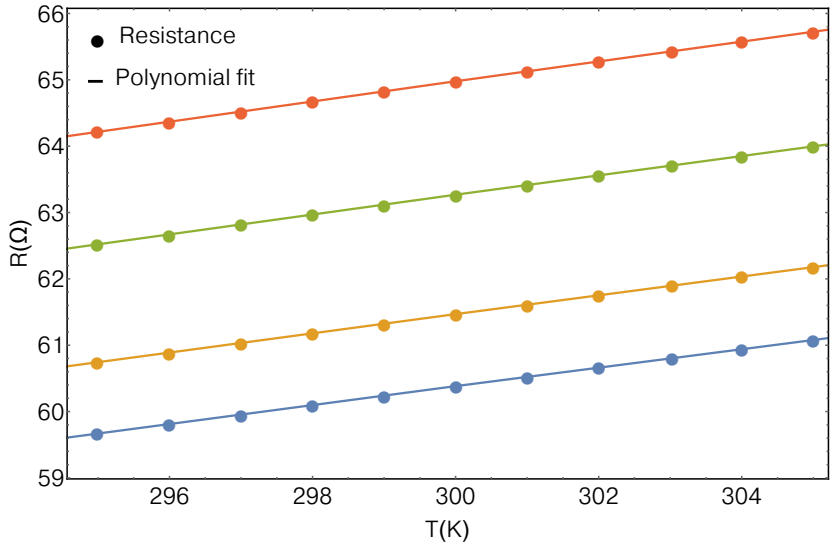

Figure 6.28: Measured electrical resistance as a function of temperature for four transducers that have been deposited on four different samples (two thicknesses of GeTe and two thicknesses of C-doped GeTe with 9% carbon atomic content). The lines represent the best fit to the data using an order two polynomial.

to literature data[240–242]), than that of the silicon substrate (about 140 W/m.K). The platinum heater/thermometers have a nominal thickness of 100 nm, and the distance between the inner voltage leads is 2 mm. All samples have been coated with an electrically insulating 60 nm Al_2O_3 layer deposited by ALD, since the 10 nm SiN capping layer was not successful in electrically insulating the film from the platinum transducer. The width of the thermometers have been measured using an optical microscope. A schematic of the system is depicted in Figure 6.27.

Each transducer deposited on each sample have been calibrated in a temperature range between 295 and 305 K. An example of calibration of the thermometers for four different samples is shown in Figure 6.28, from which we obtain a temperature coefficient of resistance of around 2.1×10^{-3} K^{-1} at 300 K.

We will start by describing the 3ω measurement performed on the amorphous C-doped GeTe sample, which is a very good example of application of the 3ω method for relatively

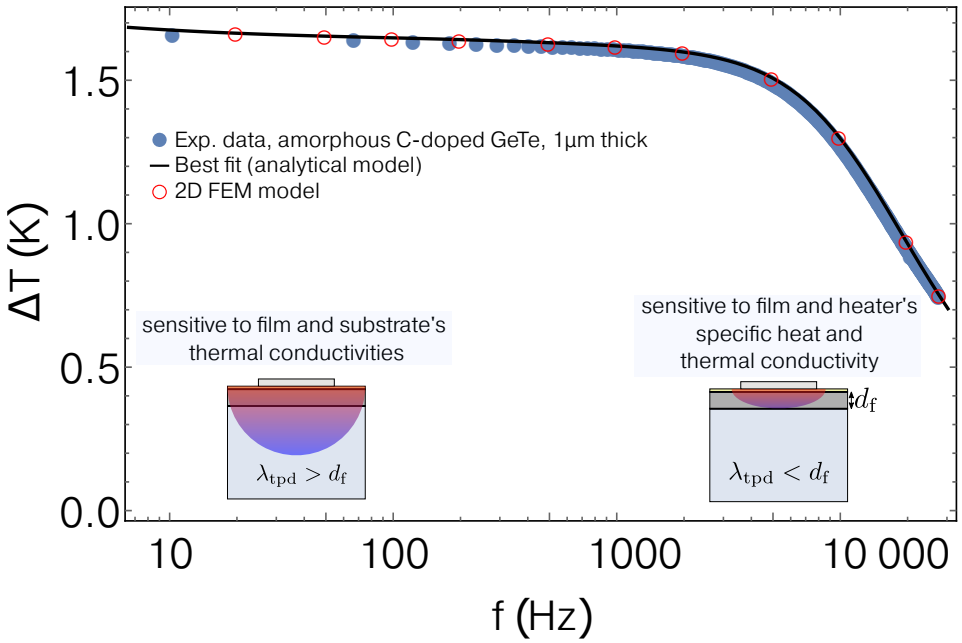

Figure 6.29: Temperature oscillation versus frequency measured for the 1 μm thick, C-GeTe sample with 9%at. carbon content, at 300K. Filled circle are experimental data while the solid line is the best fit to Eq.(6.26). We can extract the film's specific heat at high frequency, when the thermal wave completely dampens within the film, making the experiment insensitive to the substrate's thermal properties. It can be understood using the analogy with electrical circuits where at high frequency, we are sensitive to capacitive effects. We have verified the effect of the heater's thermal conductivity using a 2D FEM model (open red circles), as described in Appendix D.

thick, thermally insulating materials. It is the only sample where we have used the complete expression for the temperature oscillation for a system consisting of two layers, and succeeded in measuring the volumetric specific heat of the film. The film is so thermally resistive that the thermal penetration depth λ_{tpd}, i.e. the length over which the temperature oscillation extends, can be tuned to be of the order or less than the film's thickness, by performing the experiment at high frequency, since $\lambda_{tpd} \propto \sqrt{k/\omega}$. In this case, the experiment becomes insensitive to the thermal contribution of the substrate, and is only sensitive to the thermal properties of the film and the metallic heater (thermal conductivity *and* volumetric specific heat). This is exemplified in the inset of Figure 6.29.

The temperature oscillation has been measured until about 30 kHz, and we observe in Figure 6.29 a sharp decrease in the frequency dependence of the temperature oscillation. Remembering that the slope of temperature oscillation versus frequency is inversely proportional to the thermal conductivity, the transition around 2000 Hz in Figure 6.29 where the slope becomes steeper corresponds to the heat wave going from a material with high thermal conductivity (the silicon substrate) to a material with very low thermal conductivity (the amorphous C-doped GeTe). It is evident that in the situation where $\lambda_{tpd} < d_f$, the film cannot be described as a simple thermal resistance in series with the heater, where the effect of the film's heat capacity is neglected. Besides, if $\lambda_{tpd} < d_f$, the thermal properties of the heater can affect the experiment as well. Therefore, we have fitted the temperature oscillation using the complete solution for a film-on-substrate system, using the correction for the transducer's specific heat, as provided in Chapter 4.2. The modelling was also verified using a 2D FEM model, where the thermal conductivity of the heater is taken into account as well. To summarize, the

measured temperature oscillation was fitted using :

$$\Delta T = \frac{\langle T \rangle}{1 + (\langle T \rangle 2b/P_l)(i\omega \rho_{\mathrm{tr}} C p_{\mathrm{tr}} d_{\mathrm{tr}})} \tag{6.26}$$

where

$$\langle T \rangle = \frac{P_l}{\pi} \int_0^\infty \frac{\sin^2(\lambda b)}{(\lambda b)^2} \frac{1}{k_{\mathrm{f}_y} \gamma_{\mathrm{f}} \tanh(\gamma_{\mathrm{f}} d_{\mathrm{f}})} \frac{\left(1 + \tanh(\gamma_{\mathrm{s}} d_{\mathrm{s}}) \gamma_{\mathrm{s}} k_{\mathrm{s}_y} (\frac{\tanh(\gamma_{\mathrm{f}} d_{\mathrm{f}})}{k_{\mathrm{f}_y} \gamma_{\mathrm{f}}})\right)}{\left(1 + \tanh(\gamma_{\mathrm{s}} d_{\mathrm{s}}) \gamma_{\mathrm{s}} k_{\mathrm{s}_y} (\frac{\coth(\gamma_{\mathrm{f}} d_{\mathrm{f}})}{k_{\mathrm{f}_y} \gamma_{\mathrm{f}}})\right)} d\lambda + \frac{P_l}{2b} R_{\mathrm{Al_2O_3}} \tag{6.27a}$$

$$\gamma_j = \sqrt{k_{j_{xy}} \lambda^2 + i\omega \frac{(\rho C_p)_j}{k_{j_y}}} \tag{6.27b}$$

where the thermal resistance of the alumina film $R_{\mathrm{Al_2O_3}} = d_{\mathrm{Al_2O_3}}/k_{\mathrm{Al_2O_3}}$ is computed using our previous thermal conductivity measurements (see 6.1.1). The density and specific heat of silicon and platinum have been taken from Ref. 214, and the thermal anisotropy of the film is set to 1, which we assume to be a safe assumption due to its amorphous nature. The thermal conductivity of the 1 μm thick amorphous C-doped GeTe is measured to be $k = 0.19 \pm 0.01$ W/m.K, and its volumetric specific heat $\rho C_p = 2 \pm 0.2$ MJ/m^3.K, which is in very good agreement with other experimental literature data.[242,243] The very low thermal conductivity of amorphous GeTe is attributed non propagating or quasistationary phonons, whose mean free path are of the order of 0.1-1 nm.[244] Note that we did not include TBRs, since, in this particular case, the thermal resistance of the film

$$\begin{aligned} R_{\text{C-doped am. GeTe}} &= (d_{\text{C-doped am. GeTe}})/(k_{\text{C-doped am. GeTe}}) \\ &= 10^{-6}/0.19 = 5.26 \times 10^{-6} \mathrm{m}^2.\mathrm{K.W}^{-1} \end{aligned}$$

is a hundred times higher than TBRs we have previously measured ($\sim 2 - 5 \times 10^{-8}$m^2.K/W at 300 K). Using the same arguments, the thermal resistance of the 10 nm SiN films are not included.

Even though this measurement is a very good example to show how to use the 3ω method in this configuration (film-on-substrate) to infer the volumetric specific heat of the film, the thermal conductivity of the *amorphous* C-GeTe film is not of prime interest in this study, since the effect of carbon doping on the thermal conductivity is hidden by the amorphous nature of the GeTe alloy, which is a very poor conductor – regardless of the introduction of carbon.

We now turn to the measurement of the crystalline phases of the GeTe and C-doped GeTe. The temperature oscillation, normalized to heating power is plotted versus frequency in Figure 6.30 for all the samples that have been measured. As already mentioned, since the films are thin in comparison to the heater width ($d_{\mathrm{f}} \ll b$) and the thermal conductivity contrast between the films and the silicon substrate is very large ($k_{\mathrm{s}} \gg k_{\mathrm{f}}$), we consider the films as thermal resistances in series with the heater. Therefore, the temperature oscillation versus frequency is fitted using :

$$\Delta T = \frac{P_l}{\pi k_{\mathrm{s}_y}} \int_0^\infty \frac{1}{\sqrt{k_{\mathrm{s}_{xy}} \lambda^2 + i\omega \frac{\rho_{\mathrm{s}} C_{p_{\mathrm{s}}}}{k_{\mathrm{s}_y}}} \tanh\left(\sqrt{k_{\mathrm{s}_{xy}} \lambda^2 + i\omega \frac{\rho_{\mathrm{s}} C_{p_{\mathrm{s}}}}{k_{\mathrm{s}_y}}} d_{\mathrm{s}}\right)} \frac{\sin^2(b\lambda)}{(b\lambda)^2} d\lambda + \frac{P_l}{2b} R_{\mathrm{th}} \tag{6.28}$$

The thermal conductivity of the substrate can be uniquely determined from the slope of the temperature oscillation versus logarithm of frequency, the density and specific heat of the

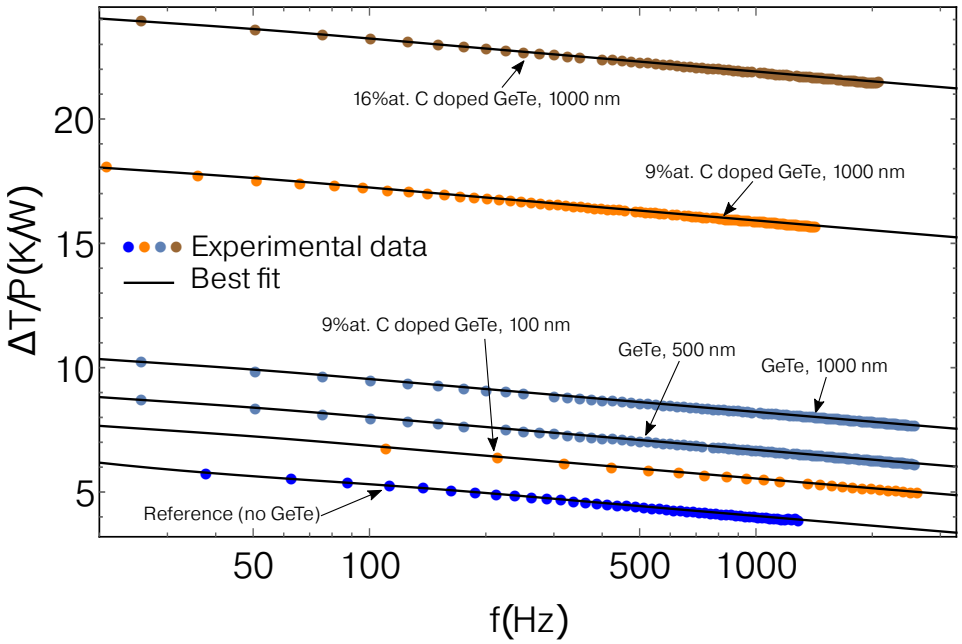

Figure 6.30: Temperature oscillation versus frequency for all the GeTe and C-doped GeTe samples measured in this work, in their *crystalline* phase. A higher temperature oscillation, normalized to heating power, translates to a higher thermal resistance of the film, and thus a lower thermal conductivity. Each thermometer is 30 μm large and the distance between the voltage leads is 2 mm. Note that every fitting gives a thermal conductivity of the silicon substrate of 138 $\pm$3 W/m.K.

silicon substrate are taken from literature[214], while the thermal anisotropy of silicon is set to 1. The only remaining fitting parameter in Eq.(6.28) is then R_{th}, which is expressed as

$$R_{\text{th}} = \frac{d_{\text{f}}}{k_{\text{eff}}} = R_{(\text{TBRs + SiN + Al}_2\text{O}_3)} + \frac{d_{\text{f}}}{k_{i_y}} \tag{6.29}$$

to take into account the contribution of thermal boundary resistances. We remind that d_{f} refers to the thickness of the film of interest (GeTe or C-GeTe), k_{eff} its effective thermal conductivity, and k_i stands for the intrinsic thermal conductivity of the film of interest (GeTe or C-GeTe), i.e. independent of the thickness of the film. In this case, $R_{\text{TBRs + SiN + Al}_2\text{O}_3}$ refers to the sum of TBRs between layers, but also includes the contribution from the 10 nm SiN and 60 nm Al_2O_3 films to the total thermal resistance.

In terms of thermal resistances of the coating layers, R_i, with thickness d_i and thermal conductivity k_i, and thermal boundary resistances between the films, $R_{i/j}$, following the notation of Eq.(6.29), we have (see Figure 6.27) :

$$\begin{aligned} &R_{(\text{TBRs + SiN + Al}_2\text{O}_3)} \\ &= R_{\text{Pt/Al}_2\text{O}_3} + R_{\text{Al}_2\text{O}_3} + R_{\text{Al}_2\text{O}_3/\text{SiN}} + R_{\text{SiN}} + R_{\text{SiN/GeTe}} + R_{\text{GeTe/SiN}} + R_{\text{SiN}} + R_{\text{SiN/Si}} \\ &= R_{\text{Pt/Al}_2\text{O}_3} + \frac{d_{\text{Al}_2\text{O}_3}}{k_{\text{Al}_2\text{O}_3}} + R_{\text{Al}_2\text{O}_3/\text{SiN}} + \frac{d_{\text{SiN}}}{k_{\text{SiN}}} + R_{\text{SiN/GeTe}} + R_{\text{GeTe/SiN}} + \frac{d_{\text{SiN}}}{k_{\text{SiN}}} + R_{\text{SiN/Si}} \end{aligned} \tag{6.30}$$

Note that it is possible to merge all TBRs and the contribution of the coating layers into one single thermal resistance since the driving frequency that we use to conduct the experiment (less than 3.3 kHz in this case), is low enough such that the thermal penetration depth is always much larger than the GeTe films' thicknesses, and therefore we cannot separate the thermal

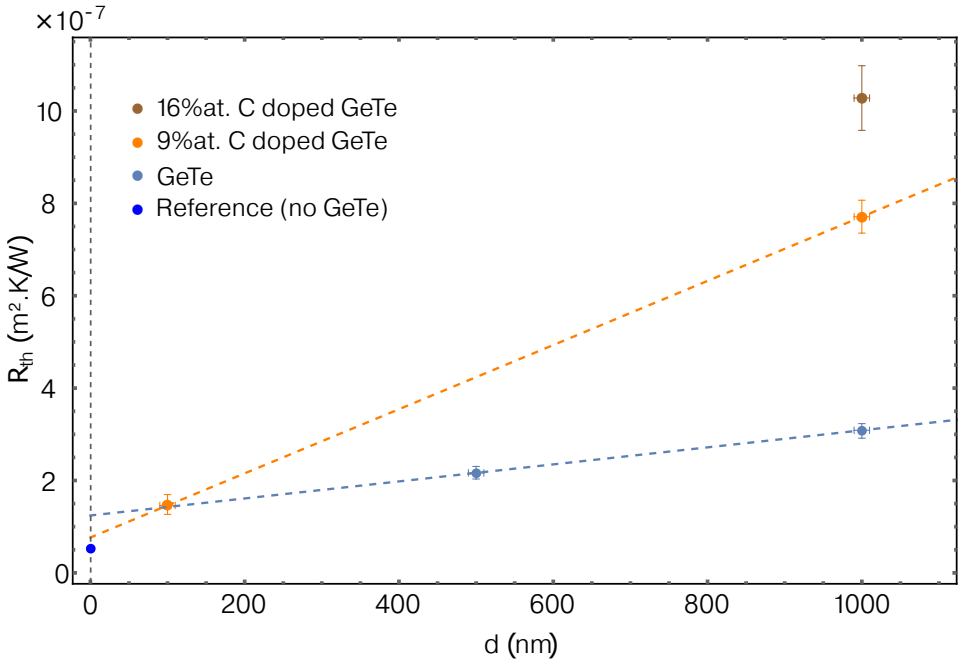

Figure 6.31: Measured thermal resistance versus film thickness for the different GeTe and C-GeTe samples. Filled circles are data while dashed lines are linear fits to the data. The fitting is performed using only two thicknesses of each sample. A reference sample has been measured, without any GeTe film (hence a "thickness" of 0 nm). Note that the thermal resistance is evaluated using Eq.(6.28) and Eq.(6.29), and therefore the intercept at zero thickness includes the contribution from TBRs *and* the SiN and Al_2O_3 layers.

contribution from one particular TBR to that of the thermal resistance of one single coating layer (see the example in Appendix B).

In addition, we have measured the thermal resistance of a reference sample, consisting of the same silicon substrate that have been used to grow all the samples, with the same SiN layers, coated with a 60 nm thick Al_2O_3 layer – without any GeTe layer. The purpose of such a measurement is to estimate the thermal resistance of the coating layers and *some* of the TBRs. Indeed, for the reference sample, the total thermal resistance R_{th} is, removing the contribution of the substrate :

$$\begin{aligned} R_{\text{th}} &= R_{\text{Pt/Al}_2\text{O}_3} + R_{\text{Al}_2\text{O}_3} + R_{\text{Al}_2\text{O}_3/\text{SiN}} + R_{\text{SiN}} + R_{\text{SiN/Si}} \\ &= R_{\text{Pt/Al}_2\text{O}_3} + \frac{d_{\text{Al}_2\text{O}_3}}{k_{\text{Al}_2\text{O}_3}} + R_{\text{Al}_2\text{O}_3/\text{SiN}} + \frac{d_{\text{SiN}}}{k_{\text{SiN}}} + R_{\text{SiN/Si}} \end{aligned}$$

Therefore, by comparing the above expression to Eq.(6.30) there is an additional TBR of amplitude $2 \times R_{\text{GeTe/SiN}}$ on the samples with GeTe, that is absent in the reference sample. For this reason, we did not use the reference sample as a way of extracting the thermal conductivity using a "differential" 3ω method, as the amplitude of $R_{\text{GeTe/SiN}}$ is unknown, and might not be negligible. But we did use this measurement to compare it to our previous findings, since we have measured multilayer systems that are relatively close to this reference sample.

The measured thermal resistances of all films are plotted in Figure 6.31 as a function of their thickness. We have measured two film thicknesses for the 9%at. C-doped GeTe (100 and 1000 nm) and undoped GeTe samples (500 and 1000 nm). We estimate both the thermal conductivity of the films and the contribution from $R_{(\text{TBRs + SiN + Al}_2\text{O}_3)}$ by plotting

Sample	k (W/m.K)	$R_{(\text{TBRs + SiN + Al}_2\text{O}_3)}$ (10^{-8}m^2.K/W)	$R_{(\text{TBRs + SiN})}$ (10^{-8}m^2.K/W)	Comments
GeTe	5.5±1.5	12.4 ±4.0	8.9 ±4.0	unusually high TBRs
C-GeTe (9% at.)	1.44 ± 0.15	7.6 ±2.4	4.1 ±2.4	TBRs comparable to our previous measurements
C-GeTe (16% at.)	0.95± 0.08	-	-	k calculated using the other two TBR measurements
Ref. sample (Si+SiN+Al_2O_3)	-	5.2 ± 0.4	1.7 ± 0.4	no GeTe/SiN or C-GeTe/SiN interface

Table 6.4: Summary of the extracted thermal properties of the GeTe and C-doped GeTe samples. The error bars are estimated by assuming a ±10 nm error on the films' thicknesses, and a ±1 μm error on the thermometer width.

$R_{\text{th}} = \text{f}(d_{\text{f}})$ according to Eq.(6.29). We underline (again) that this method assumes that the thermal conductivity of the films are independent of their thickness, i.e. the phonon mean free path is assumed to be smaller than the thickness of the films. A recent theoretical study by Ghosh *et al.* estimates the phonon mean free path in GeTe to be of the order of ∼15 nm.[232] Since all films are thicker than 100 nm, we therefore do not expect to be sensitive to phonon boundary scattering effects, and thus assume the thermal conductivity of all films to be independent of their thickness.

The 16%at. C-doped GeTe sample has been measured for only one thickness of the film (1000 nm) and therefore we use the estimation of $R_{(\text{TBRs + SiN + Al}_2\text{O}_3)}$, derived from the GeTe and 9%at. C-doped GeTe measurements, to infer its thermal conductivity.

6.2.2.3 Results and discussion

Table 6.4 provides a summary of the thermal properties of all samples, extracted using the 3ω method. The thermal resistance $R_{(\text{TBRs + SiN})}$ is calculated by removing the thermal contribution of the 60 nm thick Al_2O_3 film, using our previous measurement of the alumina film (see Section 6.1.1). Therefore,

$$\begin{aligned} R_{(\text{TBRs + SiN})} &= R_{(\text{TBRs + SiN + Al}_2\text{O}_3)} - R_{\text{Al}_2\text{O}_3} \\ &= R_{\text{Pt/Al}_2\text{O}_3} + R_{\text{Al}_2\text{O}_3/\text{SiN}} + \frac{d_{\text{SiN}}}{k_{\text{SiN}}} + R_{\text{SiN/GeTe}} + R_{\text{GeTe/SiN}} + \frac{d_{\text{SiN}}}{k_{\text{SiN}}} + R_{\text{SiN/Si}} \end{aligned} \tag{6.31}$$

The first important remark concerns the amplitude of TBRs that have been extracted for the two GeTe and 9%at. C-GeTe samples. Even though it is difficult to quantitatively estimate the amplitude of TBRs in a straightforward manner, we can nonetheless observe that there is more than a factor of 2 between the measurements performed on both GeTe and C-GeTe samples. It is difficult to explain why the C-GeTe sample would have a substantially *lower* TBR than a crystalline GeTe. Besides, the large TBRs measured for the GeTe samples are among the largest we have measured in this work, at 300 K. If we remove the contribution from the Pt/Al_2O_3, Al_2O_3/SiN and Si/SiN TBRs using our measurement of the reference sample, we still arrive at $2 \times R_{\text{GeTe/SiN}} \approx 7.2 \times 10^{-8}$m^2.K/W, which, referring to Figure 1.10 from Chapter 1 is in the high end of reported TBRs. We emphasize that such high TBRs have been reported is some experiments[241,243], however the nature of the interfaces was dissimilar (SiO_2

instead of SiN, Au as a transducer compared to our Pt one). It is suggested that an additional experiment should be carried out using a third film with a different thickness in order to further support these findings, since the unusually large TBR observed from our measurement using two thicknesses of the GeTe leads to attributing a large thermal conductivity to the GeTe film. It would be nonetheless of technological interest to have large TBRs in GeTe based interfaces, for enhanced performances in interface phase change memory devices.[236]

The measured thermal conductivity of 5.5±1.5 W/m.K for the crystalline GeTe film is in accordance with several reports showing a room temperature thermal conductivity between 5.9 and 8 W/m.K.[240,245] However, other studies have reported a lower room temperature thermal conductivity of around 3 W/m.K for crystalline GeTe.[241–243]

Since the electronic contribution k_e to the total thermal conductivity $k_{\text{tot}} = k_e + k_{\text{lat}}$ can be different among different samples according to their electrical resistivity, we estimate its contribution using Wiedemann-Franz law. The Wiedemann-Franz law relates the electronic contribution to the thermal conductivity to the electrical resistivity and temperature through the equation : $k_e = LT/\rho_e$. $L = 2.44 \times 10^{-8}$ W.Ω.K^{-2} refers to the Lorenz number, ρ_e (with units of Ω.m) is the electrical resistivity while T refers to the absolute temperature, in K. From electrical resistivity measurements carried out by our collaborators Pierre Noe and Valentina Giordano, we estimate $k_e = (2.44 \times 10^{-8} \times 300)/(4.82 \times 10^{-6}) = 1.5$ W/m.K. The lattice contribution to the thermal conductivity is therefore $k_{\text{lat}} = 4$ W/m.K.

In comparison, Fallica *et al.* reported $k_e = 0.73$ W/m.K using their measured electrical resistivity of $\rho_e = 1.1 \times 10^{-3}$ Ω.cm, leading to $k_{\text{lat}} = 2.35$ W/m.K. Additionally, first principle calculations suggest k_{lat} to lie within 2.14 - 3.2 W/m.K.[232,246] There is no clear understanding for the higher thermal conductivity observed in our crystalline GeTe film – though the Ge vacancy content can play a role in the lattice contribution to the thermal conductivity, which can be different among films according to their growth process.[236] Besides, the unusually large TBR observed from our measurement using two thicknesses of the GeTe film also requires greater attention, as it leads to attributing a large thermal conductivity to the GeTe film.

We note however that the thermal conductivity of both C-doped GeTe films decreases upon increased doping content, a behavior also observed in N-doped GeTe[241], where introducing nitrogen was shown to reduce the thermal conductivity of the film by about 40%, when compared to undoped GeTe. The measured electrical resistivity of the GeTe films is increased as well upon carbon doping, which could be explained by the reduced carrier density that is also decreased upon carbon doping.

However, the mechanisms responsible for the observed reduction in the thermal conductivity for C-doped GeTe samples are not straightforward to decipher. A simple additional scattering process resulting from mass-difference scattering due to the introduction of carbon might not be the only contributing factor to the observed reduced thermal conductivity of the C-GeTe film. Indeed, in Figure 6.32, a TEM micrograph of the 9% at. C-doped GeTe sample, taken by Nicolas Bernier from CEA-LETI, shows crystalline GeTe grains with amorphous carbon at the grain boundaries. The C-GeTe sample is therefore a nanocomposite made of *nano-crystalline* grains and *amorphous* carbon.

It is plausible that the thermal conductivity reduction stems from the crystalline grain size itself (10 to 20 nm in diameter), which, similarly to the GeMn nano-inclusions of the previous section, could effectively scatter mid-wavelength phonons. Besides, it seems reasonable to assume that the amorphous layer at the grain boundaries impedes thermal transfer across the

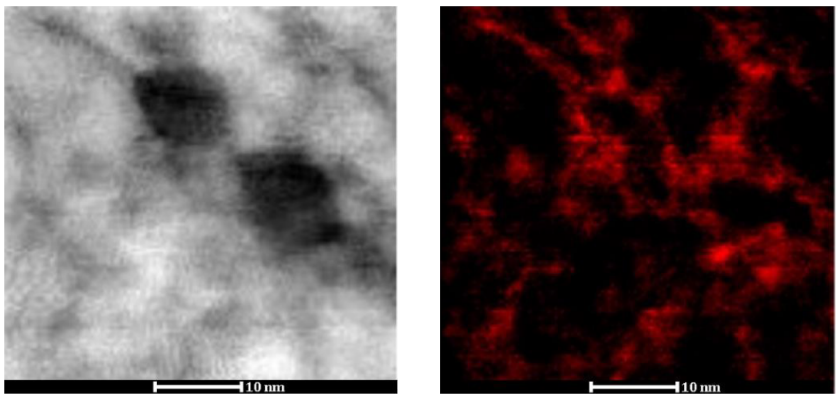

Figure 6.32: Left : TEM image of the 9% at. C-doped GeTe sample. Right : Electron Energy Loss Spectroscopy image of the same region presented in the left panel. Red color indicates carbon, which is observed to concentrate at grain boundaries. TEM images taken by Nicolas Bernier from CEA-LETI, Audrey Jannaud prepared the ultrathin layer for TEM observations.

grains, due to the changes of vibrational features at the crystalline/amorphous interface.[100] Moreover, the possibility of a higher vacancy content in C-doped GeTe would increase impurity (Rayleigh-like) scattering and further reduce the thermal conductivity as well.[239]

To deconvolve the contribution of the aforementioned possible origins of the observed thermal conductivity reduction, several additional experiments are envisaged. The first one is the measurement of a GeTe sample with nano-grains only, i.e. without introducing carbon, such that the effect of the nano-grains alone can be more rigorously quantified. The second one is the measurement of these samples on a larger temperature range, as we have suggested for the GeMn sample, since certain scattering processes are expected to be prevalent according to the temperature range and relevant dominant phonon wavelength (see Chapter 1.3.3). Indeed, it would be of great interest to determine the relevant length scales that ultimately dictate phonon heat transport in this heterogeneous material and to compare it with the nanostructured GeMn presented in the previous section, as they both have grain (or nano-inclusions) sizes of the order of 10 to 20 nm.

6.3 Anisotropic thermal conductivity of a sapphire substrate

The last section of this chapter is devoted to an example of application of the 2ω method[1], that have been implemented during this thesis, to estimate the thermal anisotropy ratio of a thick (700 μm) sapphire substrate. Besides, the method is used to provide an estimation of the Pt/sapphire thermal boundary resistance.

6.3.1 Sample preparation

The sapphire sample has been purchased from a company (Dupond), and is randomly oriented, i.e. it is not a c-axis (0001) oriented sapphire substrate (see Figure 6.33). This has been verified using X-ray diffraction, performed by Jerome Debray and Olivier Leynaud from Institut Néel, who are gratefully acknowledged. Since the surface of the sample – where the heater and thermometers are deposited – is not perpendicular to the c-axis of the sample, we can expect to be sensitive to anisotropic thermal properties of the sapphire sample. Indeed, it has been

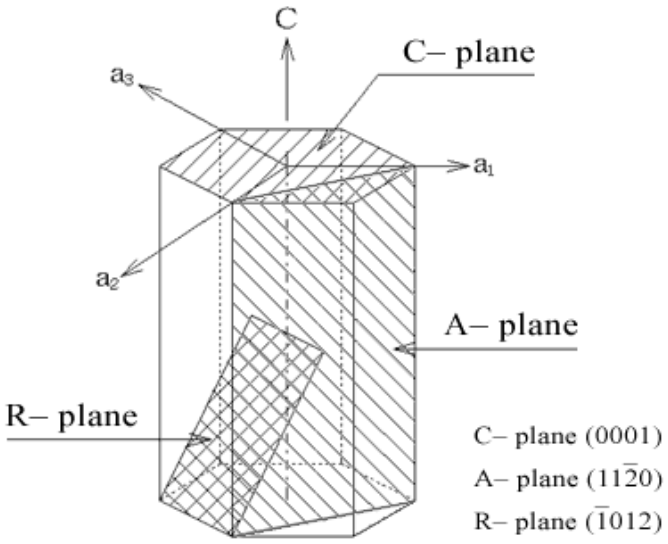

Figure 6.33: Primary planes of a sapphire crystal. Our sample is randomly oriented, i.e. it does not follow the C, A or R planes as described above, as verified using X-ray diffraction. The cut plane of our sample is more tilted than the R-plane shown here. Image reproduced from https://www.sapphire.lt/sapphire/.

reported that any anisotropy in the crystallographic orientation leads to an anisotropy in the material's thermal conductivity.[1,151]

The experiment has been initially designed to be used with a very sensitive thermometer, based on NbN thermometry. This material shows remarkable properties, in particular, its temperature coefficient of resistance can reach about 8×10^{-3} K^{-1} at room temperature[247,248], in comparison to the platinum film that we have used in all our experiments, showing a TCR of about 2×10^{-3} K^{-1}, at room temperature. The only disadvantage of this material is its inherent high electrical resistivity ($\sim$ 4 to 27 mΩ.cm), which makes it difficult to implement in frequency-dependent experiments such as this one, where parasitic capacitive effects greatly affect the measurement. Typically, we need $R_e C\omega \ll 1$ for parasitic capacitive effects to be unimportant. R_e refers to the electrical resistance (in Ω) of the heater or thermometer and C refers to the parasitic capacitance (in F) in the electrical circuit (see for instance Eq.(2.11)).

In an attempt to reduce the electrical resistance of the NbN heater and thermometer, we have reduced their length while keeping their width relatively large. Unfortunately, the electrical resistances of the NbN heater and thermometers were still of the order of a dozen of kΩ, and the 2ω measurements suffered from capacitive effects in the electrical circuit, making us unable to extract reliable thermal properties using this material as a heater/thermometer. However, we had prepared heater and thermometers made of platinum, with the same design, in order to compare our hypothetical results, extracted from the different materials making up the heater/thermometers (i.e. Pt or NbN). In the following, we will therefore present 2ω measurements that have been made using Pt heater and thermometers, which are relatively small in length because of the aforementioned reasons. The distance between the voltage sensing leads is 250 μm, while the full length of the strip is 350 μm. We put emphasis on the geometry of the heater and thermometers because, as we have discussed in Chapter 4.3, a small heater or thermometer is not ideal because of 3D end effects. It is therefore not the optimal design for conducting 2ω or 3ω measurements. Yet, it provides interesting data regarding the

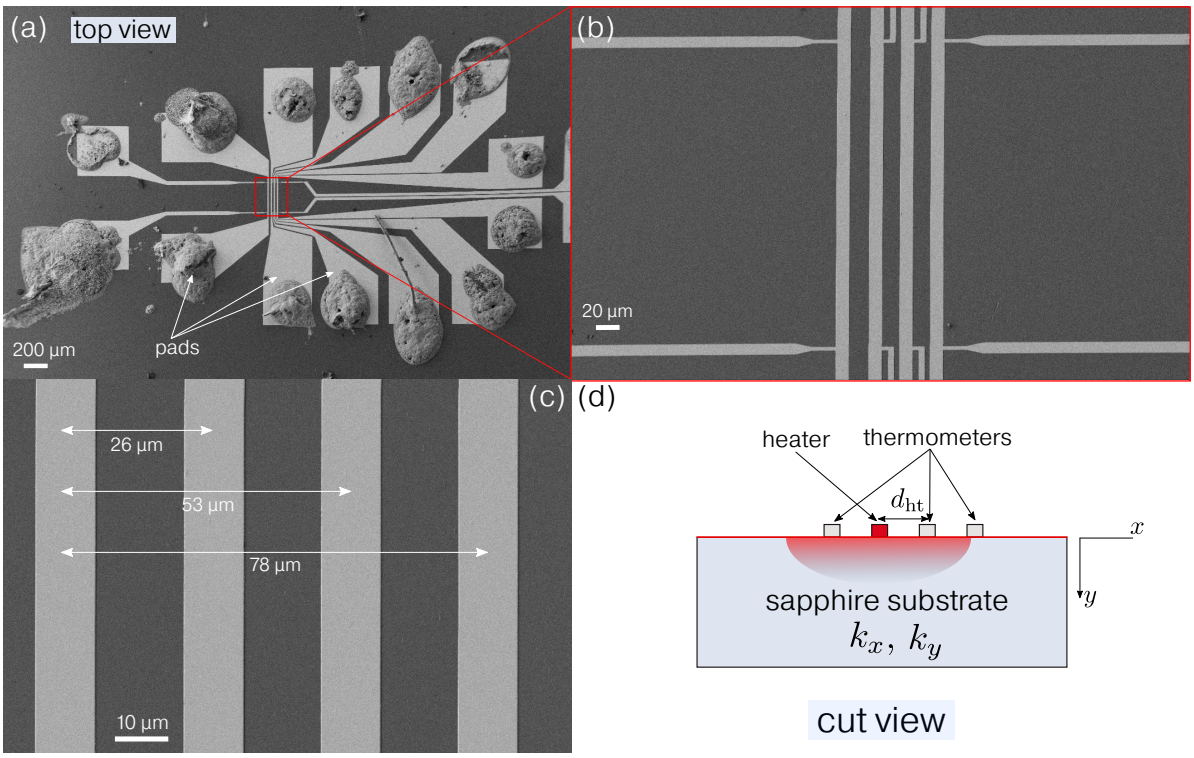

Figure 6.34: (a), (b) and (c) : SEM images (top view) of the platinum heater and thermometers used to conduct the 2ω experiments. (d) Schematic (cut view) of the experiment : one line is used as a heater while we subsequently measure the frequency-dependent temperature oscillation using the other three thermometers.

effects of pads on 2ω and 3ω measurements.

The thermometers have been fabricated using DC magnetron sputtering, in a similar manner to all previous depositions. Note that they have been deposited directly on the sapphire substrate (no adhesion layer, nor oxide removal). In Figure 6.34, we provide SEM pictures of the four platinum lines, used as heater and thermometers, that have been used to conduct 2ω experiments. One line serves as the heater while the other three are used as temperature sensors. Note that the parts connecting the lines to the pads were made intentionally large in order to reduce the electrical resistance. The width of each line is 11 μm, and the three distances between the different pairs are 26, 53 and 78 μm, as shown in Figure 6.34(c). We also observe on each pad, the silver paste that we use to connect the sensors to the sample holder using aluminium wires.

6.3.2 2ω measurements

As introduced in Chapter 5, a 2ω experiment consists in producing an oscillating heat source using a resistive heater, and measuring the resulting temperature oscillation as a function of frequency, using a *nearby* temperature sensor. After the calibration of each thermometer, as shown in Figure 6.35, we have conducted several experiments, using each line as a heater while the other three are used as temperature sensors. This leads in total to twelve possible measurements, which are shown in Figure 6.36(a). As the heater-to-thermometer distance d_{ht} is relatively large, the heat power per unit length provided by the heater that we used was large as well : $P_l = 125$ W/m, compared to typically 20 W/m for our previous 3ω experiments.

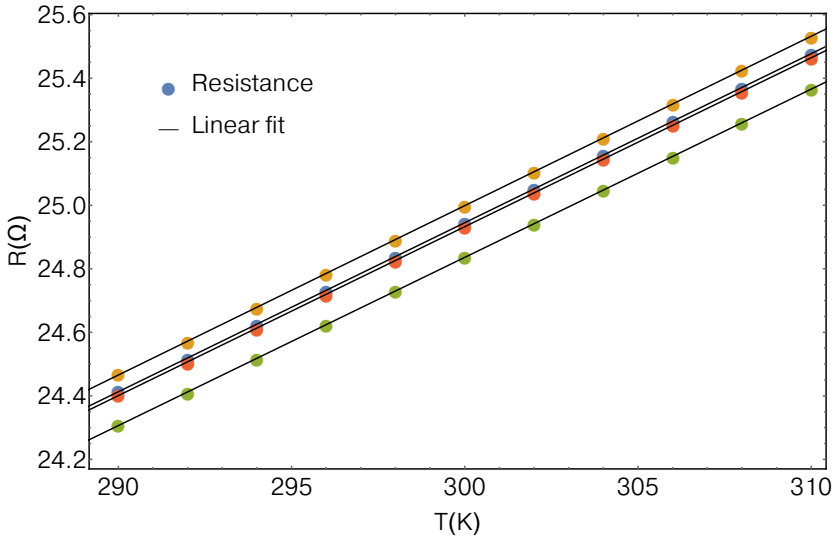

Figure 6.35: Electrical resistance of the four platinum lines measured as a function of temperature. Each color represents a different platinum line. Data are fitted to a linear model of the form $R = aT + b$.

The electrical setup that we have used is the one presented in Figure 5.1 of Chapter 5. Regarding the DC current passing through the thermometers, we have found that $I_{\mathrm{DC}} = 100\ \mu$A is a good compromise for reading the temperature oscillation with sufficient accuracy without substantial self-heating (it leads to a dissipated power per unit length of about 12 mW/m). The AC current is provided by a commercial Keithley 6221 current source, while the DC current comes from the DC voltage source of the lock-in amplifier's rear panel (model 7230 from Ametek), which goes through a home-made voltage-to-current converter. The voltage at 2ω is read across the thermometer using the aforementioned lock-in amplifier, which is locked to the ac current source. For each 2ω measurement, we have performed a standard 3ω sweep as well, as shown in Figure 6.36(b). We observe that the temperature oscillation is higher than our previous measurements (it reaches about 6 K here compared to about 2 K in our previous 3ω measurements), since the power per unit length is higher. In Figure 6.36(a), the agreement between different measurements performed using different heater/thermometer pairs, but where the heater-to-thermometer distance d_{ht} is the same, is satisfying. Typically, in the frequency range where $l > 10\lambda_{\mathrm{tpd}}$ (roughly $f > 700$ Hz), there is a 3 % discrepancy between different measurements performed with the same d_{ht}, for $d_{\mathrm{ht}} = 53$ and 78 μm. For $d_{\mathrm{ht}} = 26\ \mu$m, two measurements give lower temperature oscillations, 10% lower than the other four.

An important feature that is observed in Figure 6.36, is the discrepancy between the measurements at low frequency. However, we are confident that the origin of such discrepancies is the length and shape of the pads used for connecting the thermometers to the sample order using silver paste, which are different for each metallic line, as can be seen in Figure 6.34. As we have discussed in Chapter 4.3, if the thermal penetration depth is commensurate to the length of the heater, the temperature oscillation departs from its ideal behavior (i.e. a straight line when plotted as a function of $\ln(\omega)$). This is what we observe for both 2ω and 3ω experiments at low frequency. Notice in the inset of Figure 6.36(b) how the temperature oscillation measured at low frequency is lower if the pads are very close to the heating line (blue filled circles), while it is relatively unaffected if the pads are more distant from the central

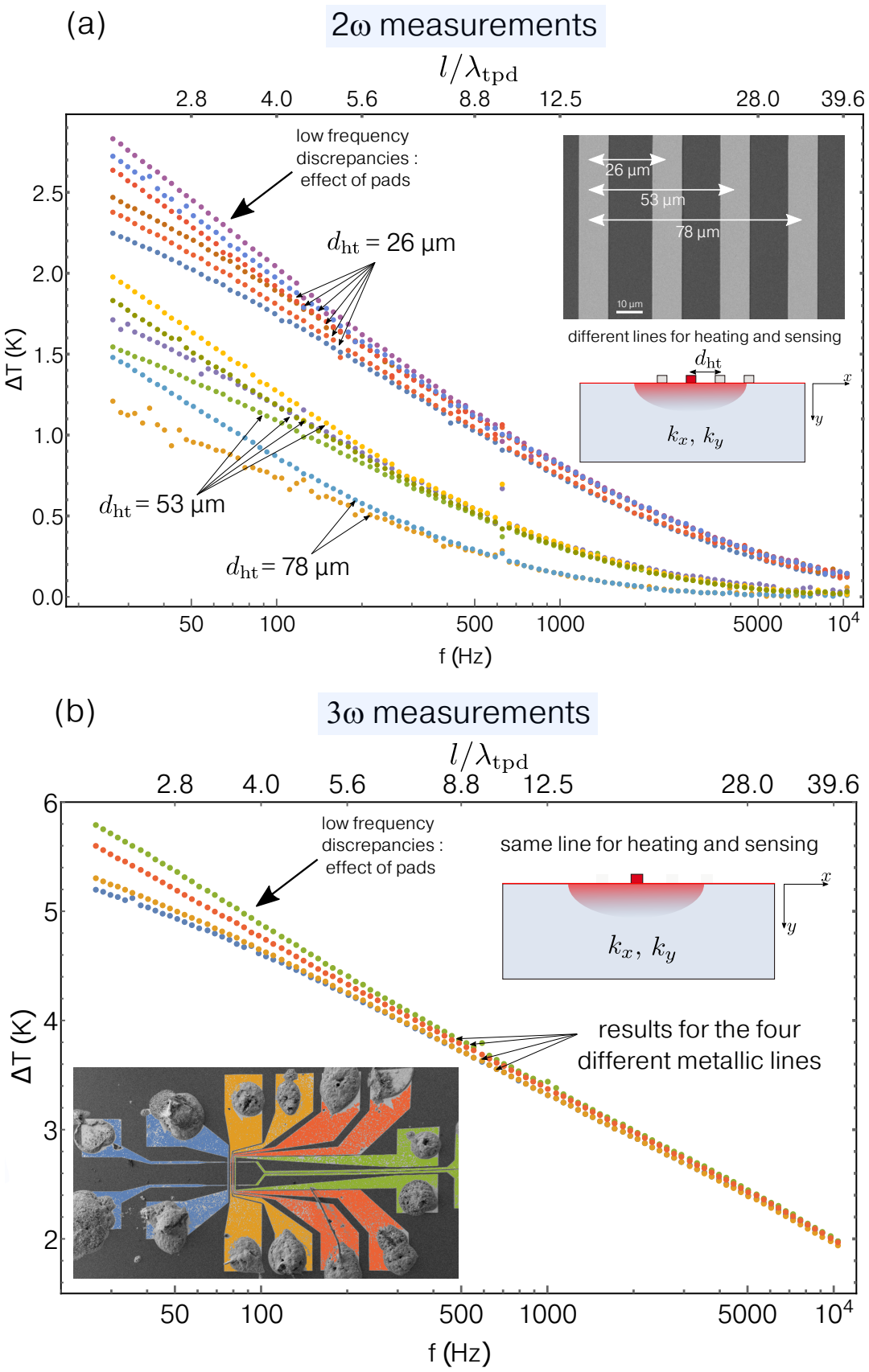

Figure 6.36: (a) Temperature oscillation measured as a function of frequency, in a 2ω configuration. Since there are four different lines, 12 measurements have been performed accounting for every possible heater/thermometer pairs. (b) Temperature oscillation measured as a function of frequency in a standard 3ω configuration, the color of the data match with the color of the transducer with which the measurement was performed (as shown in inset). The measurements have been performed at 300 K.

line (green filled circles). A simple explanation is that the large platinum pads act as heat sinks and therefore reduce the temperature oscillation that is measured by the thermometer.

It could be tempting to try to fit these measurements to the 3D model presented in Chapter 5 (Eq.(5.3b)), however we must underline that the 3D model assumes the heating line to be a perfect rectangle with a finite length and width. The geometry that we have here is different, since the full length of each line is not clearly defined, i.e. they are not perfect rectangles. The distance between the inner voltage leads is, however, well defined, as shown in Figure 6.34(b). We will therefore compare experimental results to a thermal model in an appropriate frequency range, where end effects due to the shape of the heater and thermometers pads become unimportant.

6.3.3 Results and discussion

The procedure to infer the thermal anisotropy ratio of the sapphire substrate, $k_{xy} = k_x/k_y$, consists of two steps, as proposed in Ref. 1. In the first step, we conduct a standard 3ω measurement, which gives a measure of the quantity :

$$\sqrt{k_x k_y} = \frac{-P_l}{2\pi} \frac{1}{\frac{\partial Re\{\langle T \rangle\}}{\partial(\ln(\omega))}} \tag{6.32}$$

using the "slope method" as explained in Chapter 3.1.2. The above expression is correct, provided that we are in the appropriate frequency range, such that the effect of the finite thickness of the substrate and the finite length of the heater do not affect the value of the slope of the temperature oscillation versus logarithm of frequency. Our calculation from Chapter 4.3 (Figure 4.9 in particular) suggests that for the length of our thermometer and the placement of the voltage leads ($l/l_{\mathrm{h}} = ((350\times10^{-6})/(250\times10^{-6}) = 7/5$), the slope method is valid to within 1.5% for $\lambda_{\mathrm{tpd}} > 10$. Using $k_y \approx 34$ W/m.K based on our previous measurement of the sapphire substrate (see Table 6.1), it translates to a minimum frequency of $f = 720$ Hz. Once $\sqrt{k_x k_y}$ is known, we can then perform 2ω measurements and subsequently fit for a single parameter, k_x. Indeed, in a 2ω configuration, since we are insensitive to thermal boundary resistances, only the volumetric specific heat of the substrate needs to be provided in the thermal model. For ease of reading, we re-write below the temperature oscillation sensed by the thermometer, which is located a distance d_{ht} away from the heater, if the substrate is considered semi-infinite :

$$\begin{aligned}\langle T \rangle_{2\text{ lines}} &= \frac{P_l}{\pi k_y} \int_0^\infty \frac{\sin^2(\lambda b)}{(\lambda b)^2} \frac{\cos(\lambda d_{\mathrm{ht}})}{\sqrt{k_{xy}\lambda^2 + i\omega\frac{\rho C_p}{k_y}}} d\lambda \\ &= \frac{P_l}{2\pi b\sqrt{k_x k_y}} \int_0^{2b} \left(1 - \frac{k}{2b}\right) \left(K_0\left(\sqrt{i\omega\frac{\rho C_p}{k_x}}(d_{\mathrm{ht}} - k)\right) + K_0\left(\sqrt{i\omega\frac{\rho C_p}{k_x}}(d_{\mathrm{ht}} + k)\right)\right) dk\end{aligned} \tag{6.33}$$

where K_0 is the zeroth-order modified Bessel function of the second kind. Note that in Eq.(6.33), the form of the expression in the second line is easier to use since it is directly a function of $\sqrt{k_x k_y}$ and k_x, rather than k_y and k_{xy}. Since we measure $\sqrt{k_x k_y}$ in the previous step, we can then simply solve for k_x because every other parameter is known or has been measured.

From the 3ω measurements, as shown in Figure 6.36(b), taking the slope of the temperature oscillation between 720 Hz and 3300 Hz, measured using the four different transducers, we

obtain four values for $\sqrt{k_x k_y}$ ranging from 33.7 to 35 W/m.K – in very good agreement with our previous results (Table 6.1) that we obtained using longer transducers (700 μm long). We will take the average value of the four measurements, $(\sqrt{k_x k_y})_{\text{avg}} = 34.5$ W/m.K, to fit the measured temperature oscillations versus frequency obtained in a 2ω geometry (Figure 6.36(a)), in order to find k_x using Eq.(6.33).

In Figure 6.37, we plot as a function of frequency, the measured *amplitude* of the temperature oscillation, along with the components of the temperature oscillation that are *in-phase* and *out-of-phase* with the heating[4], for the twelve possible different measurements. We remind that these correspond to the *magnitude*, *real* and *imaginary* parts of Eq.(6.33). Black solid lines in Figure 6.37 represent the best fit of the data to Eq.(6.33).

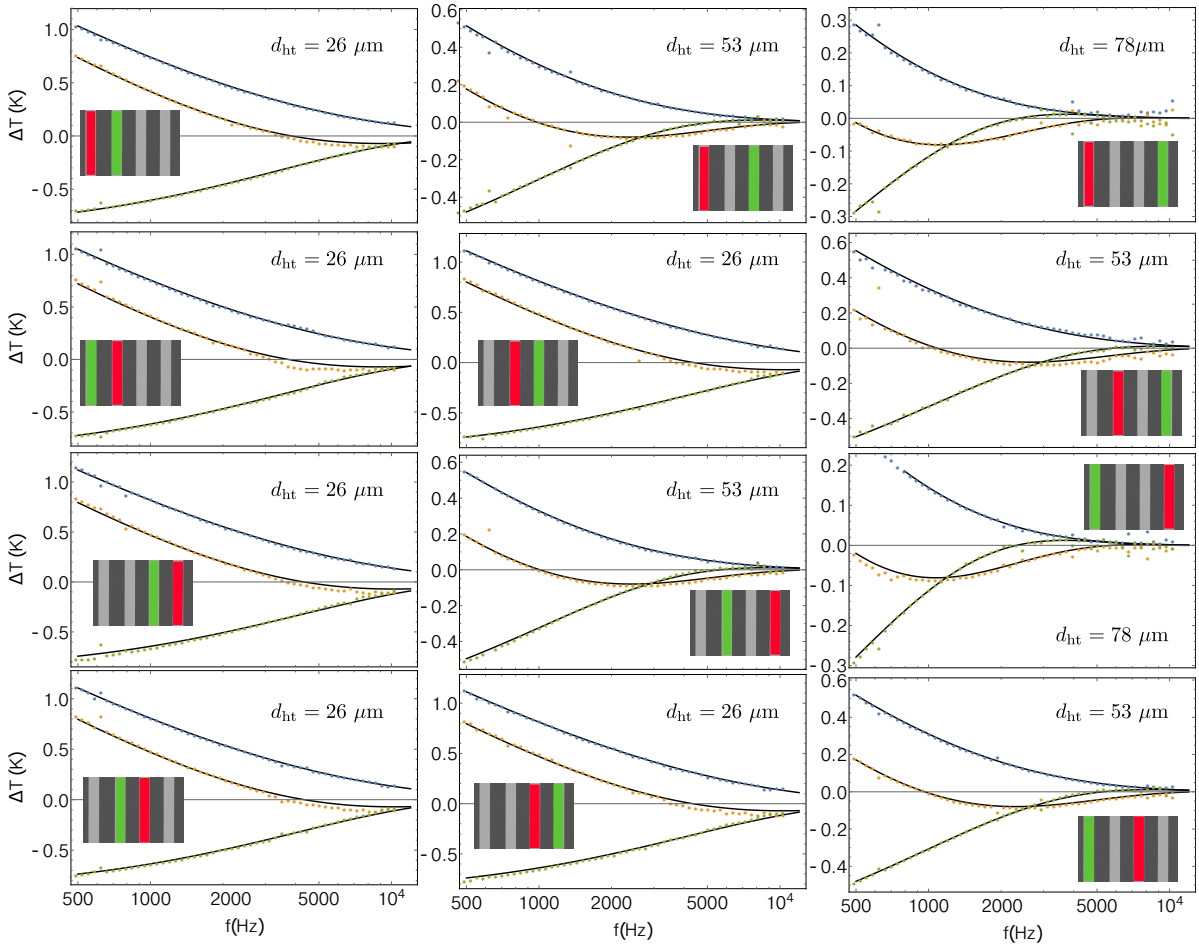

Figure 6.37: Temperature oscillation versus frequency measured while heating with one metallic line (red color in inset), and measuring with the three other lines (green color in inset). For each measurement, we record the amplitude of the temperature oscillation (blue filled circles) as well as the component of the temperature oscillation that is in-phase (orange filled circles) and out-of-phase (green filled circles) with the heating. Solid black lines are the best fit of the data to the magnitude, real and imaginary parts of Eq.(6.33).

During the fitting process, we impose that the amplitude, in-phase and out-of-phase components of the temperature oscillation for each measurement (out of the twelve possible ones) must fit the amplitude, real and imaginary part of Eq.(6.33) *using one and only one value of* k_x. Each measurement is fitted that way, and we obtain twelve k_x values that best fit the

[4]These are measured using the R, X and Y outputs of the lock-in amplifier.

twelve different measurements.

The k_x values obtained using the method just described vary between 35 and 39.3 W/m.K. We note however that two measurements coming from the same heater-thermometer pair (26 μm apart), give $k_x \approx 31$ W/m.K. It is the only heater-thermometer pair that leads to $k_x < \sqrt{k_x k_y} \leftrightarrow k_{xy} < 1$. For the ten other measurements, using $\sqrt{k_x k_y} = 34.5$ and $35 < k_x < 39.3$ leads to a thermal anisotropy of

$$1.0 < k_{xy} < 1.3$$

for the sapphire substrate. It is difficult to compare this finding with literature data because our sample is randomly oriented, but it seems reasonable to assume, for the very same reason, that the thermal conductivity of the sapphire substrate is indeed anisotropic.

Since we have measured the thermal conductivity of the sapphire substrate in both in-plane and out-of-plane directions, and we know its specific heat, we can go back to our 3ω measurement in order to fit for the last unknown of the system : the thermal boundary resistance at the platinum/sapphire interface, $R_{\text{platinum/sapphire}}$. Indeed, in a 3ω geometry, the temperature oscillation as a function of frequency has the form :

$$\Delta T = \frac{P_l}{\pi k_y} \int_0^\infty \frac{1}{\sqrt{k_{xy}\lambda^2 + i\omega\frac{\rho_s C_{ps}}{k_y}}\tanh\left(\sqrt{k_{xy}\lambda^2 + i\omega\frac{\rho_s C_{ps}}{k_y}}d_s\right)} \frac{\sin^2(b\lambda)}{(b\lambda)^2} d\lambda + \frac{P_l}{2b} R_{\text{platinum/sapphire}} \tag{6.34}$$

and the only unknown is thus $R_{\text{platinum/sapphire}}$. Using the measured anisotropy $1.0 < k_{xy} < 1.3$, and quite arbitrarily assigning an uncertainty of $\pm 5\%$ to the substrate's specific heat, fitting our 3ω measurements using Eq.(6.34), we finally obtain

$$5 \times 10^{-9}\text{m}^2.\text{K.W}^{-1} < R_{\text{platinum/sapphire}} < 2 \times 10^{-8}\text{m}^2.\text{K.W}^{-1}$$

This estimation is in good agreement with the reported Pt/sapphire TBR of $8.7 \pm 0.8 \times 10^{-9}$ $\text{m}^2.\text{K.W}^{-1}$ measured by Hopkins.[249]

Overall, the 2ω setup that have been implemented works well and the measurements on an anisotropic sapphire substrate provide additional informations that cannot be obtain with the 3ω method alone. Experimentally, we have found that the in-phase and out-of-phase components of the temperature oscillations measured in a 2ω configuration are in very good agreement with the thermal model, up to $\approx$10 kHz in this case. This is much better than all our 3ω measurements, where the out-of-phase component of the temperature oscillation often departs from its ideal behavior when plotted versus frequency. This undesired effect has been reported as well in literature.[119] Besides, the setup does not need a differential bridge and is thus considerably simpler to implement.

We notice however that the uncertainty on the measured thermal anisotropy and, consequently, on the platinum/sapphire TBR are quite large. Fitting twelve measurements to a thermal model to infer one single parameter with minimum dispersion is difficult to achieve but is statistically more relevant. To improve the accuracy of the measurement, the first step would obviously be to increase the length of the heating lines such that 3D end effects are easily avoided – as in a standard 3ω measurement. Reducing the width of the sensing lines would prove useful as well, as it would be equivalent to reducing the uncertainty on d_{ht}. Thermometers with better temperature coefficient of resistance would undoubtedly improve the

accuracy of the measurement as well, allowing to measure small temperature oscillation for thermometers that are far away from the heater, and thus more sensitive to in-plane conduction.

As a perspective of this work, measuring the thermal anisotropy of sapphire substrates with other orientations will be an important step in order to comparatively quantify the effect of crystallographic orientation on the thermal conductivity of bulk materials, and would allow to rigorously determine the accuracy of the 2ω method for measuring anisotropic thermal properties.

Conclusion

Improvement in the overall performances of nanoscale systems is inevitably correlated with the ability of these systems to efficiently manage the temperature gradients that develop at the smallest scales. Such a reduction in the characteristic sizes of nanoscale devices significantly changes the way heat dissipates within these systems, as well as the techniques needed to measure temperature gradients that develop across short distances. In applications such as thermoelectricity or phase change memories, a reduction in the ability of materials to conduct heat is necessary to significantly improve device working performances. The nano-structuration of materials at scales corresponding to the characteristic length scales defining heat transport, such as the phonon mean free path or phonon dominant wavelength, is an effective means of reducing the phononic contribution to the thermal conductivity.

In this thesis, from a thermal measurement standpoint, a particular effort has been made to describe the measurement method that have been used, the 3ω method, as well as the thermal models used, whose step-by-step derivation might allow a clearer understanding of the models that can be found in the literature, for example by using analogies with electrical circuits. A detailed description of how experimental data are modeled to derive various thermal properties is also provided, for several multilayer systems.

An additional criterion for using the slope method to determine the thermal conductivity of bulk materials with minimal error is proposed, based on a 3D analytical model for multilayer systems. This criterion takes into account the placement of the voltage leads of the thermometer, its length, the thermal penetration depth as well as the anisotropy of the studied material. In addition, this 3D thermal model for multilayer systems is useful when dimensional constraints require the measurement to be performed using small thermometers ($<$300 μm long), where the effects of the finite size of the thermometer affect the accuracy of the measurement. Heat conduction within the thermometer, which is often neglected in most thermal models in order to simplify data processing, has been studied using a FEM method that was implemented during this thesis work. In particular, we have quantified for several types of thermometers the effect of their thermal properties as well as their geometry on the temperature oscillations that are measured in 3ω experiments.

In addition, the 2ω method for measuring the thermal anisotropy of bulk samples, which is less popular than the 3ω method and therefore less documented, has been analysed in detail and an analytical thermal model for multilayer systems has been presented. An important advantage of this technique is its insensitivity to the thermal boundary resistance between the heating element and the substrate, which has been explained by analytical means. This method, combined with the 3ω method, can be used to extract the anisotropic thermal properties of bulk substrates and also estimate the thermal boundary resistance between the heating element and the substrate – if the system consists of a heater and thermometer directly deposited on the substrate. The implementation of this technique has allowed us to estimate the thermal anisotropy of a sapphire substrate (750 μm thick), as well as the thermal boundary resistance at the platinum/sapphire interface. The multilayer model that we have proposed to model the temperature oscillations in situations where the heating element and the ther-

mometer are separated by a finite distance, has allowed us to study a particular multilayer configuration, used in so-called "heat spreader" measurements, in order to adapt it to 2ω measurements. Like the "heat spreader" method, we suggest that the 2ω method can be adapted to measure the thermal conductivity of materials with relatively large thermal conductivities, with a potentially better sensitivity, when compared to the original "heat spreader" method, which is not a frequency-dependent measurement.

Several experimental results have been obtained throughout the study using the 3ω method. A reduction of more than a factor 3 of the thermal conductivity of a single-crystalline germanium matrix with embedded poly-dispersed spherical crystalline Ge_3Mn_5 nano-inclusions, having an average diameter of 16 nm has been reported experimentally. This thermal conductivity reduction from 52 W/m.K in bulk germanium to 15 W/m.K in this nano-structured germanium material is attributed to enhanced phonon scattering by the poly-dispersed spherical nano-inclusions which dominates over other scattering mechanisms. Such a reduction of the phononic transport properties observed in this nano-structured material is not sufficient to consider thermoelectric applications based on this material, but provides additional key elements necessary to understand heat transport in nano-structures from a fundamental perspective. The measurement of the thermal properties of this state-of-the-art material was possible thanks to complementary measurements of thermal boundary resistances that were shown to be the dominant source of thermal resistance in our multilayer system, and as such could not be neglected. We were able to accurately quantify thermal boundary resistance across Pt/Al_2O_3/germanium and Pt/Al_2O_3/sapphire systems, which have highlighted the impact that these interfacial thermal resistances may have on potential devices based on Ge/Al_2O_3 architectures.

In the same way, the chalcogenide GeTe, popular for phase-change memory applications, was studied in its amorphous and crystalline phases, and for different carbon doping levels. The thermal properties of this alloy, which are of crucial importance to reduce programming currents in phase-change memory devices, are significantly impacted by the introduction of carbon. In that case, we report a thermal conductivity of the order of 1 W/m.K, a reduction of more than a factor of 5 when compared to undoped GeTe. The clear origin of the mechanisms responsible for the reduction of the thermal conductivity of carbon-doped GeTe requires further experiments that would help to better quantify the impact of grain size, and the presence of carbon, on the thermal properties of this heterogeneous material. Nevertheless, the clear impact of the introduction of carbon in this alloy on its phononic properties is very encouraging, also for thermoelectricity applications, given the nano-crystalline nature of the grains which moderately affect electronic transport properties.

From a broader perspective, the work carried out during this thesis has allowed us to better understand the various difficulties that can be encountered during thermal conductivity measurements carried out using electro-thermal methods. Beyond the potential applications that could result from the reduced thermal conductivity of some of the measured materials, the variety of materials that have been studied, which differ in their thermal properties (conductive or thermally insulating) and thickness (from bulk substrates to nanometric layers, including interfaces), has allowed an in-depth analysis of the 3ω method and its range of applicability.

From the work that has been presented in this manuscript, it seems natural that several additional measurements would prove useful in providing further insights on the microscopic mechanisms responsible for the reduction of thermal conductivity, especially for germanium-

based nano-structures materials, GeMn and GeTe. For GeMn, measuring the thermal conductivity of this nano-structured material for different size distributions of nano-inclusions will provide further hints on the importance of the inclusion size, dispersion, and inter-inclusion distance on the thermal conductivity. Measurements at lower temperatures would also allow to quantify the effect of inclusions on phononic transport, when the phonon dominant wavelength starts to be comparable to the size of the inclusions – although this would require reaching temperatures below one Kelvin, in which case a new type of thermometer would have to be developed and implemented. For the GeTe material, measurements of the thermal conductivity of the material with nano-sized grains, but without the introduction of carbon, would allow us to quantify more precisely the origin of the thermal reduction in this nano-structured material. Measuring the thermal conductivity of this material as a function of temperature is also a perspective of this work.

Version en langue française

L'amélioration des performances globales des systèmes dimensionnés à l'échelle nanométrique est inévitablement corrélée à la capacité de ces systèmes à gérer de manière efficiente les gradients de températures qui se développent aux plus petites échelles. Une telle réduction des tailles caractéristiques de ces nano-systèmes change de manière conséquente la façon dont la chaleur se dissipe au sein de ces systèmes, ainsi que les techniques à utiliser afin de mesurer ces dissipations de chaleur. Dans des applications telles que la thermoélectricité ou bien les mémoires à changement de phase, une réduction de la capacité des matériaux à conduire la chaleur est nécessaire pour améliorer les performances de ces applications. La nano-structuration des matériaux à des échelles correspondant aux grandeurs caractéristiques définissant le transport de chaleur, comme le libre parcours moyen des phonons ou leur longueur d'onde dominante, est un moyen efficace permettant la réduction de la conductivité thermique de ces matériaux.

Du point de vue de la mesure thermique, un effort particulier a été mené pour décrire la méthode de mesure qui a été utilisée, la méthode 3ω, ainsi que les modèles thermiques utilisés, dont la dérivation étape par étape peut permettre une compréhension plus claire des modèles utilisés dans la littérature, par exemple en utilisant des analogies avec les circuits électriques. Une description détaillée décrivant la manière dont les données expérimentales sont modélisées afin d'en tirer diverses propriétés thermiques, est également fournie. Un critère additionnel permettant d'utiliser la "slope method" pour déterminer la conductivité thermique d'un matériau massif avec une erreur minimale, est proposé, basé sur un modèle analytique en 3D pour un système multicouche. Ce critère prend en compte le placement des lignes de tension du thermomètre utilisé, la longueur du thermomètre, la longueur de pénétration thermique ainsi que l'anisotropie du matériau étudié. De plus, ce modèle thermique 3D pour des systèmes multicouches peut s'avérer utile lorsque des contraintes dimensionnelles imposent d'effectuer la mesure en utilisant des petits thermomètres (<300 μm de long), où les effets de la taille finie du thermomètre peuvent affecter la précision des mesures. La conduction de chaleur dans le thermomètre, qui est souvent négligé dans la plupart des modèles thermiques afin de simplifier le traitement de données, est étudié à l'aide d'une méthode FEM qui a été implémentée au cours de ces travaux de thèse. En particulier, nous avons quantifié, pour plusieurs types de thermomètres, l'effet de leurs propriétés thermiques ainsi que de leur géométrie sur les oscillations de température qui sont mesurées lors des expériences 3ω.

En outre, la méthode dite 2ω permettant de mesurer l'anisotropie thermique d'échantillons massifs, qui est moins populaire que la méthode 3ω et donc moins documentée, est analysée en détail et un modèle thermique analytique permettant l'analyse de système multicouches est présenté. Un avantage important de cette technique est son insensibilité à la résistance d'interface entre l'élément chauffant et le substrat, que nous expliquons par des moyens analytiques. Cette méthode, combinée à la méthode 3ω, peut être utilisée afin d'extraire les propriétés thermiques anisotropes de substrats massifs et également estimer la résistance d'interface entre l'élément chauffant et le substrat. L'implémentation de cette technique nous a permis d'estimer l'anisotropie d'un substrat de saphir massif (750 μm d'épais), ainsi que la résistance d'interface platine/saphir. De plus, le modèle multicouche que nous avons proposé pour modéliser les oscillations de température lorsque l'élément chauffant et le thermomètre sont séparés d'une distance finie nous a permis d'étudier un système multicouche particulier, utilisée lors de mesures dites "heat spreader", afin de l'adapter à des mesures 2ω. A l'instar

de la méthode "heat spreader", nous suggérons que cette méthode peut être adaptée afin de mesurer la conductivité thermique de matériaux conduisant plus fortement la chaleur, avec une potentielle meilleure sensibilité comparée à la méthode "heat spreader" originale, qui elle n'est pas une mesure fréquentielle.

Les travaux effectués lors de cette thèse ont montré expérimentalement une réduction de plus d'un facteur 3 de la conductivité thermique d'une matrice cristalline de germanium possédant des inclusions cristallines sphériques de Ge_3Mn_5 poly-dispersées, ayant pour diamètre moyen 16 nm. Cette réduction de la conductivité thermique passant de 52 W/m.K dans le germanium massif, à 14 W/m.K dans ce matériau nano-structuré, est expliquée par un processus de diffusion des phonons par ces inclusions sphériques, qui s'ajoute aux processus de diffusion présents dans les matériaux massifs. Une telle réduction des propriétés de transport phononique observé dans ce matériau nano-structuré n'est pas suffisante pour envisager des applications en thermoélectricité basées sur ce matériau, mais apporte des éléments clés nécessaires à la compréhension du transport de chaleur dans les nano-structures, d'un point de vue fondamental. La mesure des propriétés thermiques de ce matériau à l'état de l'art a été possible grâce à des mesures complémentaires de résistances thermiques d'interfaces qui ne pouvaient être négligées, et que nous avons pu quantifier pour des systèmes Pt/Al_2O_3/germanium et Pt/Al_2O_3/saphir. Ces mesures ont également pu mettre en avant l'impact que ces résistances thermiques d'interface pouvaient avoir, sur des potentiels dispositifs qui seraient basées sur des architectures de type Ge/Al_2O_3.

De la même manière, un matériau chalcogène, GeTe, populaire dans les applications de type mémoire à changement de phase, a été étudié en fonction de ses phases amorphe et cristalline, et pour différent pourcentages de dopage à base de carbone. Les propriétés thermiques de cet alliage, qui sont d'une importance cruciale afin de réduire les courant de programmation dans des dispositifs de mémoire à changement de phase, sont impactées de manière significative par l'introduction de carbone, où nous mesurons une conductivité thermique de l'ordre de 1 W/m.K, soit une réduction de plus d'un facteur 5 comparé au GeTe non dopé. L'origine claire des mécanismes responsables de la réduction de la conductivité thermique du GeTe dopé au carbone nécessite des expériences complémentaires qui aideraient à mieux quantifier l'impact de la taille des grains, et de la présence de carbone, sur les propriétés thermique de ce matériau hétérogène. Néanmoins, l'impact clair de l'introduction de carbone dans cet alliage sur ses propriétés phononiques est très encourageant, également pour des applications en thermoélectricité, étant donné le caractère nano-cristallin des grains qui impactent de manière modérée le transport électronique.

De manière générale, le travail effectué pendant cette thèse nous a permis de mieux appréhender les diverses difficultés que l'on peut rencontrer lors des mesures de conductivité thermiques effectuées grâce à des méthodes électro-thermiques. Au delà des potentielles applications qui pourraient découler, ou pas, des conductivités thermiques réduites de certains matériaux mesurés, la variété des matériaux qui ont été étudiés, qui diffèrent de par leurs propriétés thermiques (conducteur ou isolant thermique) et leur épaisseur (du substrat massif jusqu'aux couches nanométriques, en passant par les interfaces), a permis une analyse approfondie de la méthode 3ω et de ses domaines d'applicabilité.

A partir des travaux présentés dans ce manuscrit, il semble naturel que plusieurs mesures additionnelles apporteraient davantage d'informations quant aux mécanismes microscopiques responsables de la réduction de la conductivité thermiques, en particulier pour les matériaux

à base de germanium, GeMn et GeTe. Pour le matériau GeMn, il est évident que mesurer la conductivité thermique de ce matériau nano-structuré pour différentes distributions de taille d'inclusions fournirait des éléments essentiels nous renseignant sur l'importance de la taille des inclusions, de leur dispersion, et de la distance inter-inclusions, sur la conduction thermique. Effectuer des mesures à plus basse température (<100 K) permettrait également de quantifier l'effet des inclusions sur le transport phononique, lorsque la longueur d'onde dominante des phonons commence à être comparable à la taille des inclusions – bien que cela nécessiterait d'atteindre des températures inférieures au Kelvin, au quel cas un nouveau type de thermomètre devrait être développé. Pour le matériau GeTe, des mesures de conductivité thermique du matériau présentant des grains de taille nanométrique, mais sans introduction de carbone, nous permettrait de quantifier de manière plus précise l'origine de la réduction thermique dans ce matériau nano-structuré. Mesurer la conductivité thermique de ce matériau en fonction de la température est également une perspective de ce travail.

Appendices

A Derivation of the temperature oscillation in 3D for multilayer systems

A.1 3D solution of the temperature oscillation for the 3ω geometry

In 3 dimensions, the heat equation has the form :

$$\rho C_p \frac{\partial T(x,y,z,t)}{\partial t} = k_x \frac{\partial^2 T(x,y,z,t)}{\partial x^2} + k_y \frac{\partial^2 T(x,y,z,t)}{\partial y^2} + k_z \frac{\partial^2 T(x,y,z,t)}{\partial z^2} \tag{A.1}$$

Dividing Eq. (A.1) by k_y we get

$$\frac{\rho C_p}{k_y} \frac{\partial T(x,y,z,t)}{\partial t} = k_{xy} \frac{\partial^2 T(x,y,z,t)}{\partial x^2} + \frac{\partial^2 T(x,y,z,t)}{\partial y^2} + k_{zy} \frac{\partial^2 T(x,y,z,t)}{\partial z^2} \tag{A.2}$$

Upon writing

$$T(x,y,z,t) = T(x,y,z)e^{i\omega t} \tag{A.3}$$

Plugging Eq.(A.3) in Eq.(A.2), dividing by $e^{i\omega t}$ and then rearranging, it leads to

$$\frac{\rho C_p}{k_y} i\omega T(x,y,z) = k_{xy} \frac{\partial^2}{\partial x^2} T(x,y,z) + \frac{\partial^2}{\partial y^2} T(x,y,z) + k_{zy} \frac{\partial^2}{\partial z^2} T(x,y,z) \tag{A.4}$$

We perform two successive Fourier Transforms (FT) of Eq.(A.4). The first FT is performed with respect to x, in λ-space. It leads to

$$\frac{\rho C_p}{k_y} i\omega \widehat{T}(\lambda,y,z) = -k_{xy}\lambda^2 \widehat{T}(\lambda,y,z) + \frac{\partial^2}{\partial y^2} \widehat{T}(\lambda,y,z) + k_{zy} \frac{\partial^2}{\partial z^2} \widehat{T}(\lambda,y,z)$$

The second one is subsequently performed with respect to z, in ζ-space, leading to

$$\frac{\rho C_p}{k_y} i\omega \widehat{T}(\lambda,y,\zeta) = -k_{xy}\lambda^2 \widehat{T}(\lambda,y,\zeta) + \frac{\partial^2}{\partial y^2} \widehat{T}(\lambda,y,\zeta) - k_{zy}\zeta^2 \widehat{T}(\lambda,y,\zeta)$$

The new equation to solve has now the form :

$$\frac{\partial^2}{\partial y^2} \widehat{T}(\lambda,y,\zeta) - \underbrace{\left(k_{xy}\lambda^2 + k_{zy}\zeta^2 + \frac{\rho C_p}{k_y} i\omega \right)}_{\xi^2} \widehat{T}(\lambda,y,\zeta) = 0$$

whose solution has the form

$$\widehat{T}(\lambda,y,\zeta) = C_1 e^{\xi y} + C_2 e^{-\xi y}$$

From this step, one can follow the quadrupole method as explained in Chapter 3. The difference stems from the heat flux which is now assumed as a surface boundary condition, over the surface of the heater/thermometer. It is defined as

$$\phi(x, y=0, z) = \begin{cases} \phi_0 & \text{if } -b < x < b \text{ and } -l/2 < z < l/2 \\ 0 & \text{otherwise} \end{cases}$$

Its FT is then

$$\widehat{\phi}(\lambda, 0, \zeta) = \phi_0 \int_{-l/2}^{l/2} e^{i\zeta z} dz \int_{-b}^{b} e^{i\lambda x} dx = \frac{4\phi_0 \sin(\lambda b)}{\lambda} \frac{\sin(\zeta(l/2))}{\zeta}$$

As in the 2D case, after completing the quadrupole method, the temperature oscillation at the top surface $y = 0$ is obtained as

$$\widehat{T}(\lambda, 0, \zeta) = \frac{A}{C} \widehat{\phi}(\lambda, 0, \zeta)$$

for adiabatic boundary condition at the bottom surface, or

$$\widehat{T}(\lambda, 0, \zeta) = \frac{B}{D} \widehat{\phi}(\lambda, 0, \zeta)$$

for isothermal boundary conditions. In the 3D case, the coefficients only differ by replacing γ of the 2D case by ξ, which is defined above. The coefficientA, B, C and D are computed by evaluating the following matrix product :

$$\begin{pmatrix} A & B \\ C & D \end{pmatrix} = \prod_{j=1}^{n} \begin{pmatrix} 1 & R_{(j-1)j} \\ 0 & 1 \end{pmatrix} \begin{pmatrix} \cosh(\xi_j d_j) & \frac{1}{k_{j_y}\xi_j} \sinh(\xi_j d_j) \\ k_{j_y}\xi_j \sinh(\xi_j d_j) & \cosh(\xi_j d_j) \end{pmatrix} \tag{A.5a}$$

$$\xi_j = \sqrt{k_{j_{xy}}\lambda^2 + k_{j_{zy}}\zeta^2 + i\omega\frac{(\rho_j C p_j)}{k_{j_y}}} \tag{A.5b}$$

To retrieve the temperature oscillation in real space, we take its inverse FT twice, and perform a spatial averaging over both the width $2b$ and the distance between the voltage leads of the thermometer, l_h. Note that the length l_h where the spatial averaging is performed can be different from the full length of the heater l. It leads to :

$$\langle T(x,0,z)\rangle_\mathrm{avg} = \frac{1}{2b}\frac{1}{l_\mathrm{h}} \int_{-b}^{b}\int_{-l_\mathrm{h}/2}^{l_\mathrm{h}/2} \left\{ \frac{1}{(2\pi)^2} \int_{-\infty}^{\infty}\int_{-\infty}^{\infty} 4\phi_0 \frac{\sin(\lambda b)}{\lambda} \frac{\sin(\zeta(l/2))}{\zeta} r e^{i\lambda x} e^{i\zeta z} d\lambda \right\} dx dz$$

where r is the ratio A/C or B/D, depending on the boundary condition at the bottom surface. This can be reduced to

$$\begin{aligned}
\langle T(x,0,z)\rangle_\mathrm{avg} &= \frac{1}{2b}\frac{1}{l_\mathrm{h}} \int_{-b}^{b}\int_{-l_\mathrm{h}/2}^{l_\mathrm{h}/2} \left\{ \frac{1}{(2\pi)^2} \int_{-\infty}^{\infty}\int_{-\infty}^{\infty} 4\phi_0 \frac{\sin(\lambda b)}{\lambda} \frac{\sin(\zeta(l/2))}{\zeta} r e^{i\lambda x} e^{i\zeta z} d\lambda d\zeta \right\} dx dz \\
&= \frac{1}{2b}\frac{1}{l_\mathrm{h}} \left\{ \frac{1}{(2\pi)^2} \int_{-\infty}^{\infty}\int_{-\infty}^{\infty} 4\phi_0 \frac{\sin(\lambda b)}{\lambda} \frac{\sin(\zeta(l/2))}{\zeta} r d\lambda d\zeta \right\} \int_{-b}^{b}\int_{-l_\mathrm{h}/2}^{l_\mathrm{h}/2} e^{i\lambda x} e^{i\zeta z} dx dz \\
&= \frac{1}{2b}\frac{1}{l_\mathrm{h}} \left\{ \frac{1}{(2\pi)^2} \int_{-\infty}^{\infty}\int_{-\infty}^{\infty} \frac{4P}{2bl} \frac{\sin(\lambda b)}{\lambda} \frac{\sin(\zeta(l/2))}{\zeta} r d\lambda d\zeta \right\} \frac{4\sin(\lambda b)}{\lambda} \frac{\sin(\zeta(l_\mathrm{h}/2))}{\zeta} \\
&= \frac{P_l}{\pi^2} \int_{-\infty}^{\infty}\int_{-\infty}^{\infty} \frac{\sin^2(\lambda b)}{(\lambda b)^2} \frac{\sin(\zeta(l/2))\sin(\zeta(l_\mathrm{h}/2))}{\zeta^2 l_\mathrm{h}} r d\lambda d\zeta
\end{aligned}$$

A.2 Normalized slope accounting for the heater's finite length

For a substrate-only system of thickness d_s, with adiabatic boundary conditions applied at the bottom, the complex temperature oscillation read across the thermometer is given by

$$\langle T\rangle_{3\mathrm{D}} = \frac{4P_l}{\pi^2 l_\mathrm{h} k_{\mathrm{s}_y}} \int_0^\infty \int_0^\infty \frac{\sin^2(\lambda b)}{(\lambda b)^2} \frac{\sin(\zeta(l/2))\sin(\zeta(l_\mathrm{h}/2))}{\zeta^2 \xi \tanh(\xi d_\mathrm{s})} d\lambda d\zeta \tag{A.6a}$$

$$\xi = \sqrt{k_{\mathrm{s}_{xy}}\lambda^2 + k_{\mathrm{s}_{zy}}\zeta^2 + i\omega\frac{(\rho_\mathrm{s} C p_\mathrm{s})}{k_{\mathrm{s}_y}}} \tag{A.6b}$$

The normalized slope (NS), defined as

$$\mathrm{NS} = \frac{\partial Re\{\langle T\rangle_{3\mathrm{D}}\}/\partial \ln(\omega)}{\left(-P_l/2\pi k_{\mathrm{s}_y}\sqrt{k_{\mathrm{s}_{xy}}}\right)} \tag{A.7}$$

which, applied to Eq. (A.6), leads to

$$\mathrm{NS} = \int_0^\infty \int_0^\infty \frac{4iq^2\sqrt{k_{\mathrm{s}_{xy}}}}{\pi l_\mathrm{h}\xi^3 \tanh(d_\mathrm{s}\xi)} \left(1 + \frac{4d_\mathrm{s}\sqrt{k_{\mathrm{s}_{xy}}}\xi}{e^{2d_\mathrm{s}\xi} - e^{-2d_\mathrm{s}\xi}}\right) \frac{\sin(\zeta(l/2))\sin(\zeta(l_\mathrm{h}/2))}{\zeta^2} \frac{\sin^2(\lambda b)}{(\lambda b)^2} d\lambda d\zeta \tag{A.8}$$

where $q = \sqrt{\rho_s C p_s \omega / k_{\mathrm{s}_y}}$. For a semi-infinite substrate, $d_\mathrm{s} \to \infty$, it simplifies to

$$\mathrm{NS} = \int_0^\infty \int_0^\infty \frac{4iq^2\sqrt{k_{\mathrm{s}_{xy}}}}{\pi l_\mathrm{h}\xi^3} \frac{\sin(\zeta(l/2))\sin(\zeta(l_\mathrm{h}/2))}{\zeta^2} \frac{\sin^2(\lambda b)}{(\lambda b)^2} d\lambda d\zeta \tag{A.9}$$

Motivated by the assumption that the *slope* of the temperature oscillation versus logarithm of frequency should only depends on the heater half-width at high frequency where $\lambda_\mathrm{tpd} \approx b$, in the opposite regime $\lambda_\mathrm{tpd} \gg b$, the normalized slope does not depend on b, and the above expression can be well approximated by

$$\underset{\lambda_\mathrm{tpd}\gg b}{\mathrm{NS}} = \int_0^\infty \int_0^\infty \frac{4iq^2\sqrt{k_{\mathrm{s}_{xy}}}}{\pi l_\mathrm{h}\xi^3} \frac{\sin(\zeta(l/2))\sin(\zeta(l_\mathrm{h}/2))}{\zeta^2} d\lambda d\zeta \tag{A.10}$$

B Sensitivity analysis

Several times in this manuscript, we have performed what is called a "sensitivity analysis", which is becoming prominent in the heat-transfer community, in particular for experimentalists who ask themselves "Which parameter should I adjust to make my experiment more sensitive to this particular quantity?" or "Should I know this particular quantity very accurately when fitting my data to my model, or a rough estimate is sufficient ?". A sensitivity analysis aims to describe how much model output values are affected by changes in model input values.[250] We refer the reader to Ref. 251 for an exhaustive description of all the tools that are available for conducting a sensitivity analysis.

Since many models used in this thesis for describing the temperature oscillation in 2ω and 3ω experiments are analytic, a convenient way of performing a sensitivity analysis is by means of partial differentiation.

For a function $y = f(x_1, ..., x_i, ...x_n)$, that does not vary too rapidly as a function of parameter x_i, keeping all parameters – except for x_i – constant, Taylor expansion of y around $x_{i,0}$ is written (to leading order) as

$$y(x_1, ..., x_i, ...x_n) \approx y(x_1, ..., x_{i,0}, ...x_n) + (x_i - x_{i,0}) \left.\frac{\partial y}{\partial x_i}\right|_{x_i = x_{i,0}}$$

The change $\Delta y = y(x_1, ..., x_i, ...x_n) - y(x_1, ..., x_{i,0}, ...x_n)$ resulting from a small change $\Delta x_i = (x_i - x_{i,0})$ is therefore written as

$$\Delta y = \Delta x_i \left.\frac{\partial y}{\partial x_i}\right|_{x = x_{i,0}}$$

which has the same units as y. The *relative* change of y resulting from a change Δx_i is written (in %) as

$$\frac{\Delta y}{y} = \frac{\Delta x_i}{y} \left.\frac{\partial y}{\partial x_i}\right|_{x = x_{i,0}} = \frac{\Delta x_i}{x_i} \frac{x_i}{y} \left.\frac{\partial y}{\partial x_i}\right|_{x = x_{i,0}}$$

which we write as

$$\frac{\Delta y}{y} = \frac{\Delta x_i}{x_i} \times S^y_{x_i} \tag{B.1}$$

Therefore, assuming no correlation between input parameters and for small perturbations of parameter x_i, the sensitivity $S^y_{x_i}$ of model $y = f(x_1, ..., x_i, ..., x_n)$ to parameter x_i is defined as[250]

$$S^y_{x_i} = \left(\frac{\partial y}{\partial x_i}\right)\left(\frac{x_i}{y}\right) \tag{B.2}$$

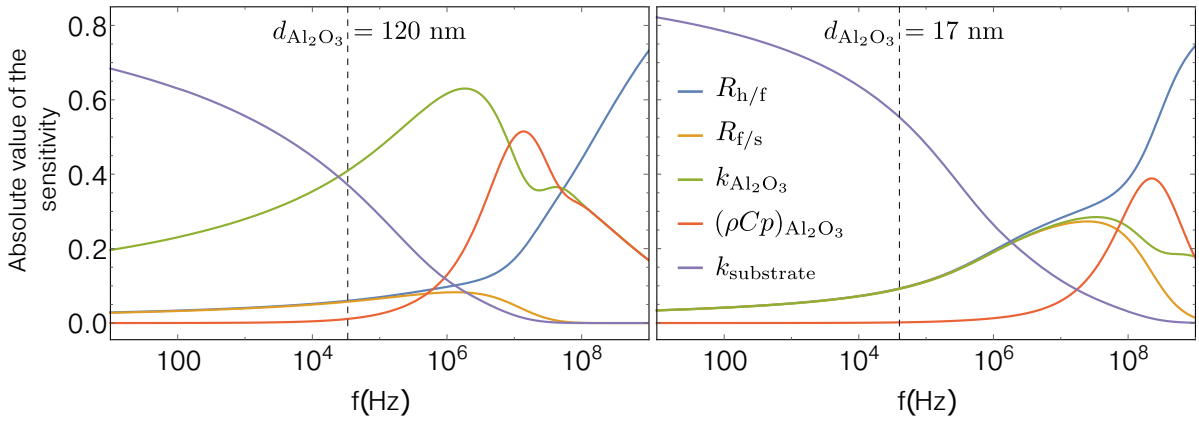

Figure B.1: Absolute value of the sensitivity of the temperature oscillation to several parameters, for a film-on-substrate system. The parameters used are as follow : $b = 2.5$ μm, $k_s = 35$ W/(m.K), $(\rho C_p)_s = 3.03$ MJ/(m^3.K), $k_{Al_2O_3} = 1.7$ W/(m.K), $(\rho C_p)_{Al_2O_3} = 2.17$ MJ/(m^3.K), $R_{tr/f} = R_{f/s} = 10^{-8}$ m^2.K/W. The dashed vertical line indicates the usual maximum frequency that is reached during a 3ω experiment.

The sensitivity of y to parameter x_i is evaluated around its typical value $x_{i,0}$, while all other parameters are held constant. It is clear from Eq. (B.1) that it is the *relative* change of y that is proportional to the relative change of x_i through the defined sensitivity $S^y_{x_i}$. Therefore, a sensitivity of $S^y_{x_i} = -5$ means that a 1% increase in x_i results in a 5% decrease in y.

A sensitivity analysis is therefore useful for comparing the relative contribution of each input parameter to the resulting output. To better understand how useful it is in practice, we provide an example of its use, adapted from our work published in Ref. 194.

The expression of the temperature oscillation amplitude for a film-on-substrate system in a 3ω geometry, including thermal boundary resistances, is derived by solving the 2D heat equation using Fourier Transforms and subsequent spatial averaging over the transducer width, as explained in Chapter 3. It leads to :

$$\Delta T_{2\omega} = \frac{P_l}{2\pi}\int_{-\infty}^{\infty}\frac{\sin^2(\lambda b)}{(\lambda b)^2}\frac{1}{k_f\gamma_f\tanh(\gamma_f d_f)}\frac{\left(1+\tanh(\gamma_s d_s)\gamma_s k_s(R_{f/s}+\frac{\tanh(\gamma_f d_f)}{k_f\gamma_f})\right)}{\left(1+\tanh(\gamma_s d_s)\gamma_s k_s(R_{f/s}+\frac{\coth(\gamma_f d_f)}{k_f\gamma_f})\right)}d\lambda + \frac{P_l}{2b}R_{tr/f} \tag{B.3a}$$

$$\gamma_i = \sqrt{k_{xy,i}\lambda^2 + i2\omega_e\frac{\rho_i C_{p_i}}{k_i}} \tag{B.3b}$$

It looks rather difficult, and not straightforward to deduce how a change in one parameter will affect the temperature oscillation. Therefore, a sensitivity analysis of this particular expression seems adequate. The absolute value of the sensitivity to the Temperature Oscillation (TO), $S_p^{\Delta T_{2\omega}}$, is plotted in Figure B.1, for two different thicknesses of the film, and for various parameters (p) of interest. The substrate has thermal properties of sapphire, and the film represents amorphous Al_2O_3.

As explained above, the sensitivity analysis is useful for comparing the relative contribution of each parameter to the temperature oscillation, at a particular frequency. Plotting its absolute value provides a quick way of doing such a comparison. Moreover, we find it particularly useful for pedagogical purposes. For example, in Figure B.1, the absolute value of the sensitivity is plotted over an intentionally extremely wide frequency range, to illustrate that

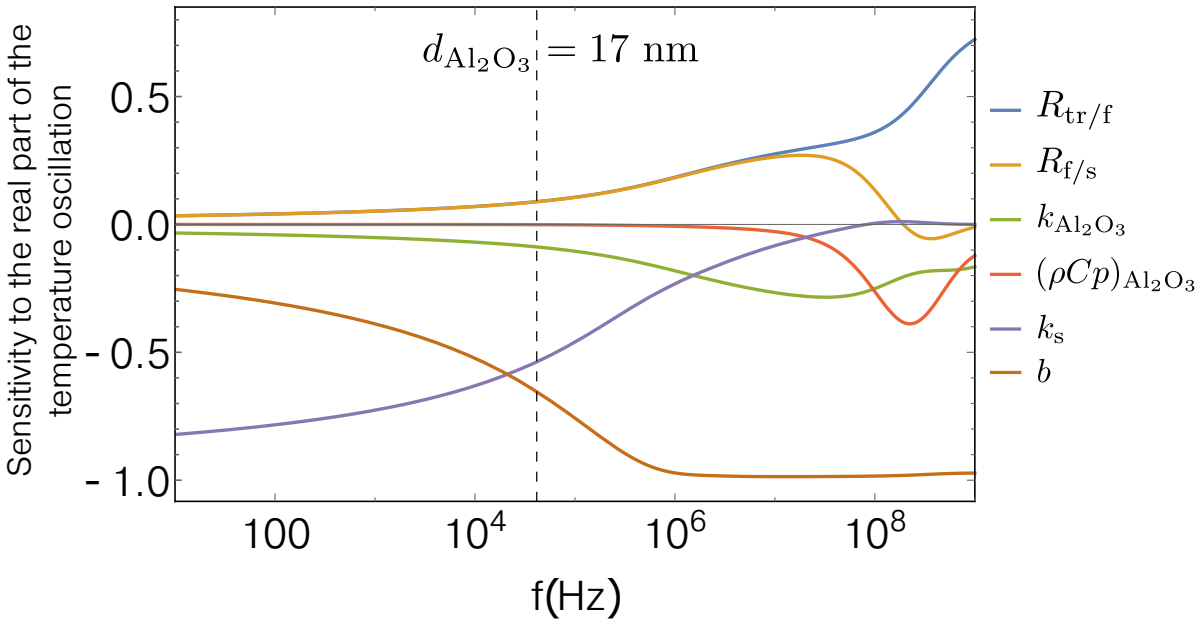

Figure B.2: Real part of the sensitivity of the temperature oscillation to several parameters, for a film-on-substrate system. The parameters used are as follow : $b = 2.5$ μm, $k_s = 35$ W/(m.K), $(\rho C_p)_s = 3.03$ MJ/(m^3.K), $k_{Al_2O_3} = 1.7$ W/(m.K), $(\rho C_p)_{Al_2O_3} = 2.17$ MJ/(m^3.K), $R_{tr/f} = R_{f/s} = 10^{-8}$ m^2.K/W. The dashed vertical bar indicates the usual maximum frequency that is reached during a 3ω experiment.

we cannot distinguish between the film/substrate and transducer/film thermal boundary resistances, $R_{f/s}$ and $R_{tr/f}$, on the usual frequency range that is spanned during a 3ω experiment, if the film is too thin. By increasing the film's thickness from 17 to 120 nm, the minimum frequency to reach in order to separate the contribution from $R_{f/s}$ to that of $R_{tr/f}$ is still beyond the maximum frequency we reach in our experiments – though it provides some hints on how to do it.

Figure B.1 also tells us that the thermal conductivity of the substrate, k_s, is a very important parameter in this experiment, and if it is not the quantity that we are mainly interested about, then it should be measured carefully such that the other parameters, which we are interested in measuring (typically the thermal conductivity of the film, $k_{Al_2O_3}$), are accurately extracted from fitting the measured temperature oscillation to the data. The sensitivity to k_s goes to zero when frequency increases, illustrating the concept of thermal penetration depth. The comparison of the sensitivity to $k_{Al_2O_3}$ for two thicknesses is a clear indication that it is easier to measure a thick film than a thin one, as the sensitivity for the thicker film is always larger than that of the thin film, over the entire frequency range. Eventually, we also understand that the film's heat capacity, $(\rho C_p)_{Al_2O_3}$, is not important in the usual frequency range, as the sensitivity of the TO to the film's heat capacity is zero.

Now, if we plot the real part (since it is complex in this particular case) of the sensitivity of the TO to the parameters, as opposed to its absolute value, we obtain additional informations about the way changes in parameters influence the TO. This is plotted in Figure B.2. From this plot, looking at the sign of the sensitivity, we directly understand if a change in a parameter will decrease or increase the temperature oscillation. For example, by increasing the substrate or film's thermal conductivity, we decrease the temperature oscillation sensed by the thermometer. Similarly, to obtain a higher temperature oscillation, reducing the width of the thermometer can prove useful.

It is clear from this example that the sensitivity analysis is a very powerful tool for both designing an experiment, and for the comparing data to a model after the measurement is performed.

C Uncertainty analysis

In the process of measuring a variable, we must remember that we are only seeing a particular state of this variable through a (hopefully!) tiny window, whose size reflects the finite precision of our measuring apparatus. The measurement is subsequently compared to a model which, supposedly, is the best description of the underlying processes experienced by the variable. It is therefore as important to determine an unknown's variable quantity through a carefully designed experiment that it is to provide the range into which the unknown variable is believed to fall within if the experiment is conducted a large number of times.

In Chapter 6.1.1, the so-called Monte Carlo method has been used to compute the uncertainty of the parameters that were obtained by comparing experimental data to a model. There are several pros and cons for using this method, which we will discuss hereafter. The pros and cons of the method are best described when compared to the other alternative that exists to perform an uncertainty analysis, which is the conventional method of "partial derivatives".

C.1 The method of partial derivatives

In this method, a function

$$y = f(x_1, ..., x_i, ...x_n)$$

is Taylor expanded, and its standard deviation is given by

$$\sigma(y) \approxeq \sqrt{\sum_{i=1}^{N} \left(\frac{\partial f}{\partial x_i}\right)^2 \sigma(x_i)^2 + 2 \sum_{i=1}^{N-1} \sum_{j=i+1}^{N} \frac{\partial f}{\partial x_i} \frac{\partial f}{\partial x_j} \sigma(x_i x_j)}$$

where higher-order derivative terms are usually neglected. The standard deviation of each input parameter x_i is written as $\sigma(x_i)$, and the second term under the square root reflects the correlation (if any) between input parameters. From this standard deviation $\sigma(y)$, one can infer intervals within which there is a probability P that the mean of repeated measurement values will fall within the interval $y \pm \alpha_P \sigma$, where α_P is defined as the coverage factor, which depends upon the probability P. It is best practice to specify so-called Confidence Intervals (CIs) that relate α_P to the probability P, as a percentage of data that will fall within the interval $y \pm \alpha_P \sigma$, if measurements are repeated a large number of times.

Any % CI can be computed, but only a few are customary in the scientific community. The CI, often regarded as the "uncertainty" of the measurement, corresponds to a specific value of α_P. For example, there is about 68% confidence that y lies between $y \pm 1\sigma$ (CI of 68%),

whereas there is a 95% confidence that y lies within $y \pm 2\sigma$ (CI of 95%). These specific α_P values and percentages arise from the Normal distribution, for which values less than one (two) standard deviation away from the mean account for 68.27% (95.45%) of the dataset building the distribution.[1]

By construction, this method only allows to compute the uncertainty of a model whose input parameters are "small" (the Taylor expansion is truncated at first order), and symmetrically distributed around their mean. Besides, the standard deviation obtained using the above-mentioned method is related to a specified CI, only if the resulting error on y is normally distributed. However, it is perfectly plausible for the resulting error distribution of y to be non-gaussian, even if all of its parameters $(x_1, ...x_n)$ have a gaussian distribution, if the model is non-linear.[252] Therefore, it is usually preferred not to use the method of partial derivatives when the error of the input parameters are large and their probability distribution asymmetric.

C.2 The Monte Carlo method

The Monte Carlo method finds it relevance in cases where these two conditions are not met, since it works for both small and large uncertainty, with any shape of the distribution function. Besides, the computation of partial derivative is not necessary and the correlation between input parameters is automatically taken into account. However, this comes with a higher computational cost. The method is promptly described by Anderson[253], and we will simply quote him in the following :

> *The method is based on repeated calculations of a result, each time having each input datum changed by a random selection from its error probability distribution. The element of randomness or chance results in the name of the technique. The accumulated answers define a distribution which can be used as an uncertainty distribution. Note that, unlike regression analysis, the 'best value' of the result is not in question. It is given by using the best or mean values of the input data. It is only the uncertainty of the result which is needed.*

A schematic explanation of the method that we have implemented for this work is provided in Figure C.1. In this example, we apply the Monte-Carlo method to obtain the uncertainty distribution of the thermal conductivity of the substrate and the thermal resistance of the films and interfaces, when fitting the measured temperature oscillation (dependent variable) as a function of excitation frequency (independent variable). Input parameters have all been measured. The model corresponds to the temperature oscillation sensed in a 3ω experiment as a function of the transducer's excitation frequency, for a film-on-substrate system, including thermal boundary resistances. The unknown fitting parameters are the cross-plane component of the substrate's thermal conductivity, k_{s_y}, and the thermal resistance of the film and interfaces, R_{th}. The method is described in Ref. 254 p.807, and we followed the thorough tutorial given in Ref. 152. We also highly recommend the very detailed tutorial on Will Clarkson's personal webpage.[255]

In the following, we describe the steps that we followed to conduct our uncertainty analysis, as sketched in Figure C.1.

[1] $\int_{-\sigma}^{\sigma} (1/\sqrt{2\pi\sigma^2}) e^{-x^2/(2\sigma)^2} dx \approx 0.68$, or 0.95 for integration between $\pm 2\sigma$.

- Step (1) : the best fit parameters $k_{s_y}^{\text{fit}}$ and $R_{\text{th}}^{\text{fit}}$ are obtained by fitting the model using our best guess/measured value of each input parameter $(P, b, l, \rho, C_p, k_{s_{xy}})$, in the standard way (least squares). We use Mathematica's NonlinearModelFitting function, using a "LevenbergMarquardt" method to perform the fitting, which works well and rapidly.

- – Step (2)(a) : we build a new set of data using $k_{s_y}^{\text{fit}}$ and $R_{\text{th}}^{\text{fit}}$, and perturbed values of the input parameters. These perturbed values of the input parameters are randomly drawn from the probability distribution function of each parameter. We use Mathematica's RandomVariate[_Distribution] to perform random draws ('_Distribution' can be any distribution with finite standard deviation). The probability distribution function can have a large standard deviation and be non Gaussian. For example, if the measured values of the input parameters are as follow : $(P = 20\text{ mW}, b = 5\ \mu\text{m}, l = 500\ \mu\text{m}, \rho = 5.323\text{ g.cm}^{-3}, C_p = 0.32\text{ J.g}^{-1}\text{.K}^{-1}, k_{s_{xy}} = 1)$, a random draw might lead to $(P_i = 19.5\text{ mW}, b_i = 5.15\ \mu\text{m}, l_i = 494\ \mu\text{m}, \rho_i = 5.326\text{ g.cm}^{-3}, C_{p,i} = 0.31\text{ J.g}^{-1}\text{.K}^{-1}, k_{s_{xy},i} = 1.02)$.
  Using these perturbed value $(P_i, b_i, l_i, \rho_i, C_{p,i}, k_{s_{xy},i})$, and $k_{s_y}^{\text{fit}}$ and $R_{\text{th}}^{\text{fit}}$, we build a new {f, $\langle T\rangle$} dataset, using the same number of points of the independent variable (in this example, the frequency f).
  – Step (2)(b) : similarly, we perturb each point of this new set, according to the probability distribution function *of the temperature oscillation* $\langle T\rangle$. For example, the perturbed value of the previous step (2)(a) might lead to $\langle T\rangle = 0.95$ K (at a particular frequency), and a random draw – from the temperature oscillation's probability distribution function – might give $\langle T\rangle_i = 0.98$ K. A new set is built this way : $\{f, \langle T\rangle\}_i$.
  – Step (2)(c) : we perform a fitting of the synthetic dataset $\{f, \langle T\rangle\}_i$, using our best guess/measured value of each input parameter $(P, b, l, \rho, C_p, k_{s_{xy}})$, to obtain a new set of fitted parameters $\{k_{s_y,i}, R_{\text{th},i}\}$.

- Step (3) : after repeating Step (2) N times (which should be as large as possible), we have a distribution of $\{k_{s_y,i=1}, ..., k_{s_y,i=N}\}$ and $\{R_{\text{th},i=1}, ..., R_{\text{th},i=N}\}$, from which we can extract statistical indicators, such as confidence intervals.

The method is relatively easy to implement, using pre-built functions available in many free (python for example) or paid (Mathematica that is used in this work, Matlab, etc.) softwares/programming languages.

After Step (3), we possess a distribution of k_{s_y}'s, from which we extract the confidence interval of the substrate's thermal conductivity, presented along its best-fit value. Additionally, and importantly, we have built the distribution of R_{th}'s, that will be used subsequently in order to extract the thermal conductivity of the *film*. After performing several experiments on systems with films of increasing thicknesses (see Section 3.2.1), the new model to fit is the following :

$$R_{\text{th}} = \frac{d_f}{k_i} + R_{\text{int}} \tag{C.1}$$

where R_{th} is measured and its probability distribution function has been built. In this model, d_f is the independent variable while k_i and R_{int} are sought-parameters. By following exactly the same steps as described above, we infer the best-fit parameters, along with their probability distribution function, of the sought-parameters.

There is an important assumption which is made when using this method in order to infer statistical indicators about the best fit parameters. Since it is impossible to know the 'truth-value', $k_{s_y}^{\text{truth}}$ and $R_{\text{th}}^{\text{truth}}$, of the unknown parameters – it would require error-free measurements acquired using infinite-precision apparatus –, we assume that the shape of the probability distribution $k_{s_y,i} - k_{s_y}^{\text{fit}}$ in our synthetic experiment is nearly the same as the shape of the 'true' probability distribution $k_{s_y,i} - k_{s_y}^{\text{truth}}$ (and similarly for the probability distribution of $R_{\text{th},i} - R_{\text{th}}^{\text{fit}}$).[254] It is equivalent to say that *"the way in which random errors enter the experiment and data analysis does not vary rapidly as a function of $k_{s_y}^{truth}$, so that $k_{s_y}^{fit}$ can serve as a reasonable surrogate."* Therefore we use and $k_{s_y}^{\text{fit}}$ and $R_{\text{th}}^{\text{fit}}$ for producing each synthetic dataset in Step (2)(a), instead of using $k_{s_y}^{\text{truth}}$ and $R_{\text{th}}^{\text{truth}}$ (which would be impossible).

This way of obtaining an uncertainty estimation of the fitted parameters is particularly useful in this example, because we do not believe the anisotropy ratio of the thermal conductivity, $k_{s_{xy}}$, to follow a normal distribution, in the case where the substrate is made of sapphire. This assumption stems from the specific crystal orientation of the material, in addition to separate experiments that we carried out, which were specifically designed to measure the thermal anisotropy ratio of sapphire. These two aspects suggest that the anisotropy is always greater than 1, but is very unlikely to be lower than 1. If we assume the anisotropy to be likely within the range of $1 < k_{s_{xy}} < 1.3$, with an expected value of 1.05, an asymmetric probability distribution function is needed, thus discarding the normal distribution. Importantly, varying the anisotropy in the proposed range of $1 < k_{s_{xy}} < 1.3$ is not considered a "small perturbation" (it is about 30% !), and therefore violates the fundamental assumptions of the method of partial derivatives. Among various asymmetric distribution functions, the Lognormal or Pareto distribution functions can be used in such a scenario.

The model has the following form, with unkown fitting parameters, and known input parameters :

$$\langle T \rangle = \frac{P}{\pi l k_{s_y}} \int_0^\infty \frac{1}{\sqrt{k_{s_{xy}}\lambda^2 + i4\pi f \rho C_p / k_{s_y}}} \frac{\sin^2(\lambda b)}{(\lambda b)^2} d\lambda + \frac{P}{2bl} \times R_{\text{th}}$$

Step (1)

Get $k_{s_y}^{\text{fit}}$ and $R_{\text{th}}^{\text{fit}}$ by fitting the experimental dataset $\{f, \langle T \rangle\}_{\text{exp}}$ to the model, using the measured/best guess values of the input parameters, $P, b, l, \rho, Cp, k_{s_{xy}}$.

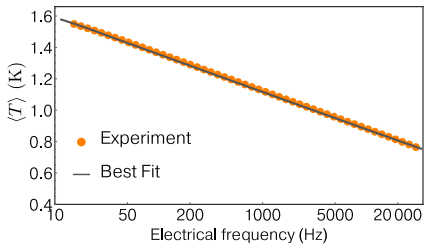

Step (2)

repeat N times

random draw from distribution

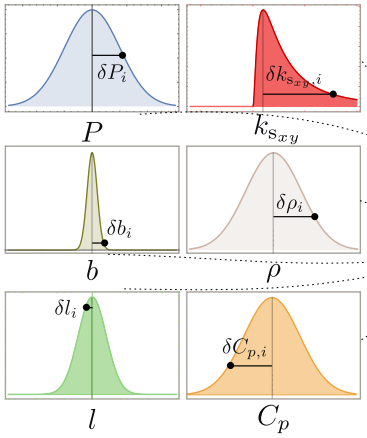

(a) Build new dataset $\{f, \langle T \rangle\}$ using perturbed values of the input parameters, randomly drawn from their distribution.

$$\langle T \rangle = f(f, k_{s_y}^{\text{fit}}, R_{\text{th}}^{\text{fit}}, P_i, b_i, l_i, \rho_i, Cp_i, k_{s_{xy},i})$$

(b) Build 'synthetic' dataset $\{f, \langle T \rangle_i\}_i$ by perturbing the values of the dependent variable $\langle T \rangle$ built in the previous step (a), using a random draw from its probability distribution function :

$$\langle T \rangle \rightarrow \langle T \rangle + \delta \langle T \rangle_i$$

random draw from distribution

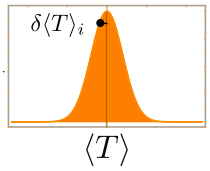

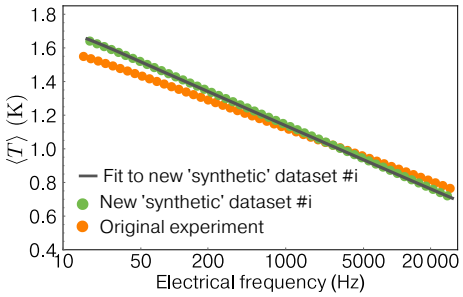

(c) Get new $k_{s_y,i}$ and $R_{\text{th},i}$ by fitting the 'synthetic' dataset $\{f, \langle T \rangle_i\}_i$, using $P, b, l, \rho, Cp, k_{s_{xy}}$ as input parameters, in the same manner as Step (1).

Step (3)

Extract statistical parameters by repeating Step (2) N times

"k_{s_y} = ... with 68% Confidence Interval of [... , ...]"

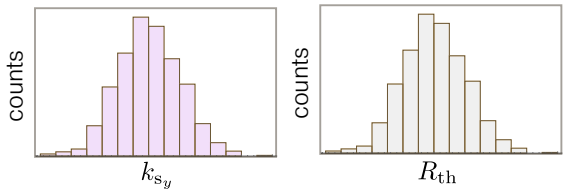

Figure C.1: Explanation of the general Monte Carlo method used for determining the uncertainty of the fitted parameters k_{s_y} and R_{th}, when fitting the measured temperature oscillation as a function of frequency in a 3ω experiment.

D Finite Element Method implementation of the 3ω method

If possible, we always try to compare our measurements to analytical descriptions of the physics and geometry that best represent our model, for extracting unknown parameters. Besides its satisfying and appealing form, an analytical description of a model allows a fast and computer-efficient analysis of experimental data. However, when the geometry and/or the physics underlying a process is complex, its analytical description can be cumbersome and other tools exist to make our life easier. The finite element method (FEM) is a widespread numerical technique useful for solving partial differential equations that describe a process, especially for complex geometries. There is a large amount of documentation about the FEM method that can be found in the literature, such as Refs. 256,257, to which the reader is referred to for a detailed explanation of the technique.

In a finite element analysis, the geometry of the problem is divided into smaller, simpler parts that are called finite elements, built in the process of meshing. Each finite-sized element has its own set of locally approximate equations, which are subsequently recombined into a global system of equations, whose solution is numerically inferred. Once the geometry, governing equations of the underlying physics, and boundary conditions of the problem are set, it is therefore possible to numerically extract a quantity of interest and compare it to experimental data.

In this work, we have used Mathematica's FEM framework to run all FEM analysis, which we will describe hereafter. A detailed tutorial on how to use Mathematica to run a FEM analysis can be found in Ref. 258, which we followed to implement the heat transfer FEM analysis for the 3ω geometry.

Similarly to the work of Ramu and Bowers[150], who implemented a frequency-domain FEM formulation of the 3ω method problem, we chose to directly work in the frequency domain rather than in the time domain for solving the heat equation. We made this choice because, even though the transient informations about the temperature rise in a 3ω experiment are rich of informations about the thermal properties of the system, they are never used : experimentally we are only measuring the "steady-periodic" behavior of the temperature oscillation when measuring the third harmonic of the voltage, as shown in Figure D.1.

We are therefore only interested in the frequency response of the temperature across the transducer, when a periodically oscillating heat source is produced within it. Therefore, because the response in the thermal domain is linear[138], periodic Joule heating at frequency ω

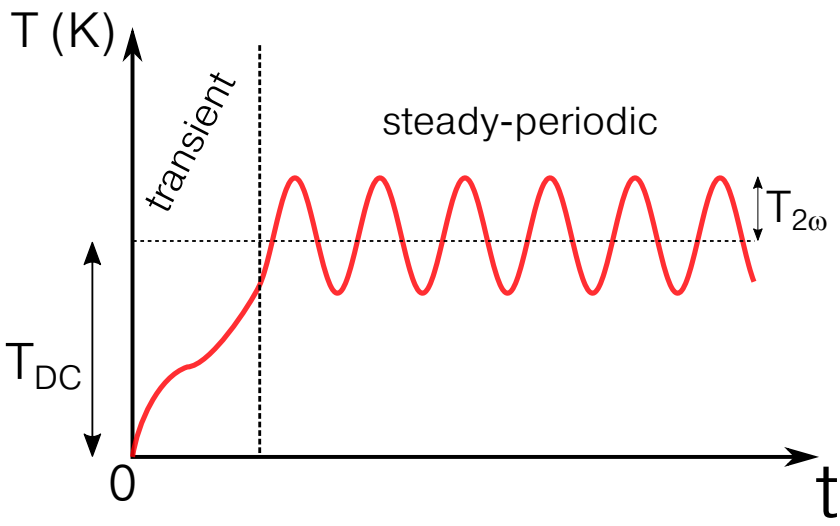

Figure D.1: Sketch of the temperature behavior as a function of time, with the transient and steady-periodic states. When using the 3ω method, we are interested in the steady-periodic behavior of the temperature, which is the part that we model using FEM. The transient is discarded.

induces temperature oscillation at the same frequency, and we write

$$T(x,y,z,t) = T(x,y,z)e^{i\omega t}$$

which, when plugged into the time-dependent heat equation with volumetric heat source Q_0 (in W.m^{-3}),

$$\rho C_p \frac{\partial T(x,y,z,t)}{\partial t} = k_x \frac{\partial^2 T(x,y,z,t)}{\partial x^2} + k_y \frac{\partial^2 T(x,y,z,t)}{\partial y^2} + k_z \frac{\partial^2 T(x,y,z,t)}{\partial z^2} + Q_0$$

leads to the heat equation in the frequency-domain

$$k_x \frac{\partial^2}{\partial x^2} T(x,y,z) + k_y \frac{\partial^2}{\partial y^2} T(x,y,z) + k_z \frac{\partial^2}{\partial z^2} T(x,y,z) + Q_0 - \rho C_p i\omega T(x,y,z) = 0 \qquad \text{(D.1)}$$

that is numerically solved. Since the temperature oscillation is complex, it has a real and imaginary part (oscillations that are in-phase and out-of-phase with the periodic heating, respectively), leading to the notation $T(x,y,z) = T(x,y,z)_{\text{Re}} + iT(x,y,z)_{\text{Im}}$. When plugged into Eq.(D.1), and upon separating the real and imaginary parts of the temperature oscillation, it leads to the following system of coupled equations

$$k_x \frac{\partial^2}{\partial x^2} T(x,y,z)_{\text{Re}} + k_y \frac{\partial^2}{\partial y^2} T(x,y,z)_{\text{Re}} + k_z \frac{\partial^2}{\partial z^2} T(x,y,z)_{\text{Re}} = -Q_0 - \rho C_p \omega T(x,y,z)_{\text{Im}} \qquad \text{(D.2a)}$$

$$k_x \frac{\partial^2}{\partial x^2} T(x,y,z)_{\text{Im}} + k_y \frac{\partial^2}{\partial y^2} T(x,y,z)_{\text{Im}} + k_z \frac{\partial^2}{\partial z^2} T(x,y,z)_{\text{Im}} = \rho C_p \omega T(x,y,z)_{\text{Re}} \qquad \text{(D.2b)}$$

which is equivalent to Eqs. (22a) and (22b) in Ref. 150. In Mathematica, we numerically solve Eq.(D.1), which is implicitly separated into a real and imaginary part. We can then manipulate the numerically-determined quantity $T(x,y,z) = T(x,y,z)_{\text{Re}} + iT(x,y,z)_{\text{Im}}$, and compare it to existing models of the temperature rise for the 3ω geometry.

The FEM can handle both 2D and 3D geometries, though the latter requires greater computational resources. As the geometry is symmetric about the y-axis (in 2D), we only model half of the domain for computational efficiency. Since the quantity that we eventually

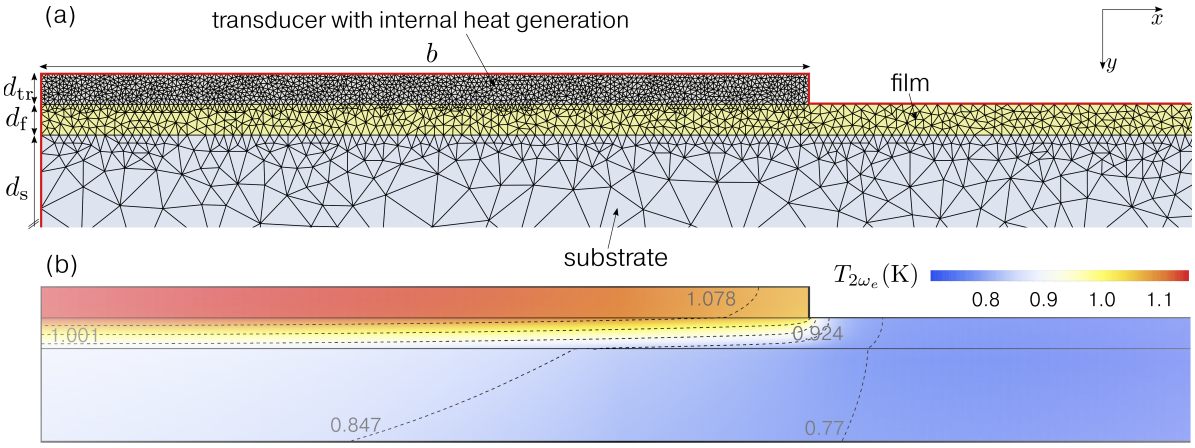

Figure D.2: (a) Zoomed-in view of the meshing performed for a film-on-substrate system, with a finite-sized heater/thermometer with volumetric heat generation. On the red boundaries, zero-flux (Neumann) boundary conditions are applied. (b) Resulting density plot of the real part of the temperature oscillation at frequency $\omega = 2\omega_e$, with isotherms displayed as dashed lines. The heating frequency is 20 Hz. The heater has thermal properties of platinum, the film that of amorphous alumina, and the substrate represents germanium.

compare with our experimental data is the temperature across the heater/thermometer, the meshing is particularly refined in this area, as can be seen in Figure D.2(a). In real systems, the width of the domain is very large in comparison to both the heater width and to the thermal penetration depth. In practice, we increase the width (x-axis in Figure D.2) of the geometry until the temperature oscillation does not vary more than about 0.1% of its previously determined value. The depth (y-axis in Figure D.2) of the larger domain, which is the substrate in all cases, is adapted to the sample that is modelled, but is not truncated. The reason is that the finite thickness of the substrate plays an important role when measuring the temperature oscillation at low frequency. However, the meshing is adapted, as can be seen in Figure D.2(a). Each layer has its own set of thermal properties that are tuned at will, and importantly, the volumetric heat source

$$Q_0 = \frac{P}{2bld_{\mathrm{tr}}}$$

is only non-zero within the heater. The result will then depend on the boundary conditions applied on the outer surfaces of the domain. We either specify the temperature at a boundary/surface, or the flux across it. We apply adiabatic (Neumann) boundary conditions over all outer surfaces of the domain, representing a perfectly thermally insulated sample, except at the bottom of the sample, where we apply either isothermal or adiabatic boundary conditions to compare the resulting temperature with analytical models that treat both boundary conditions. A thermally insulated boundary has no heat flux across it, it is written as :

$$\vec{n} \cdot (k\nabla T(x,y,z)) = 0 \tag{D.3}$$

where $\vec{n}$ is the normal vector (perpendicular to the given surface/boundary). An isothermal boundary condition at the bottom of the substrate consists in specifying its temperature :

$$T(x,y,z)|_{\mathrm{bottom}} = T_0 \tag{D.4}$$

We remind that we are only studying the oscillating part of the temperature oscillation, not the actual DC temperature of the sample. An isothermal boundary condition with $T_0 = 0$

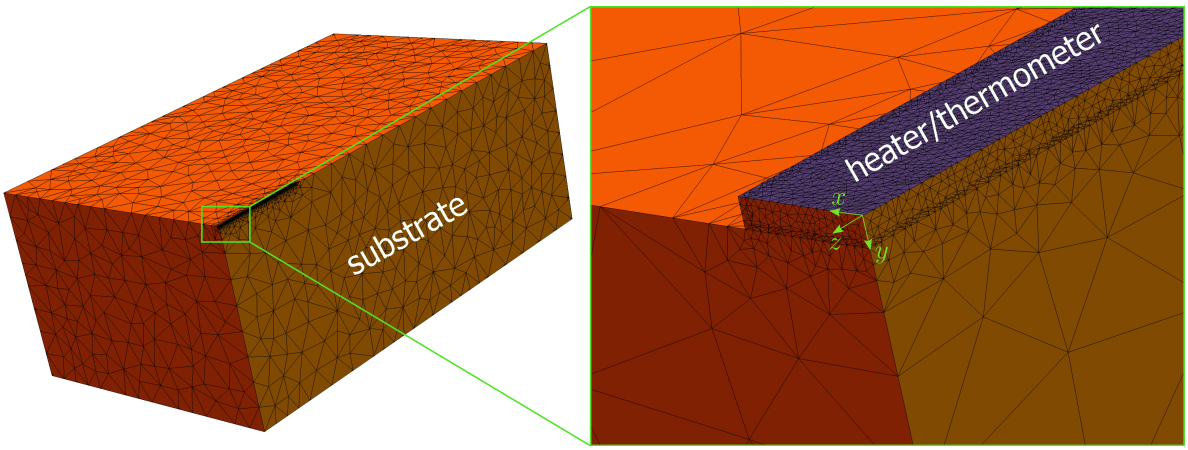

Figure D.3: Visualization of the 3D meshing of a substrate, with a heater/thermometer on top. Only one fourth of the symmetric domain is built for computational efficiency.

represents a heat sink that is perfectly coupled the substrate. It does not mean that the actual absolute temperature is 0 K.

A 2D density plot, as displayed in Figure D.2(b), is useful for pedagogical purposes, but, as mentioned above, the only quantity that we can actually compare to experimental measurements is the temperature oscillation across the heater/thermometer, which we calculate as the spatial average of the temperature oscillation across both the width and thickness of the thermometer :

$$\langle T \rangle_{2D} = \frac{1}{d_{tr}} \frac{1}{b} \int_0^b \int_0^{d_{tr}} T(x,y) dx dy \tag{D.5}$$

The double integration is performed numerically, and the real and imaginary part of the temperature oscillation obtained in this way are then compared to analytical models.

A 3D model of the 3ω geometry has been built as well, for comparing the analytical expression of the temperature oscillation that we have obtained analytically in 3D. Similarly to the 2D model, we increase the length of the model until convergence is reached. A 3D meshing of the substrate-only system is shown in Figure D.3. Because the domain and temperature response are symmetric around both x and z axis, only one fourth of the domain is built. The complex temperature oscillation numerically obtained is then averaged across the width, length and thickness of the thermometer :

$$\langle T \rangle_{3D} = \frac{1}{(l/2)} \frac{1}{d_{tr}} \frac{1}{b} \int_0^{(l/2)} \int_0^b \int_0^{d_{tr}} T(x,y,z) dx dy dz \tag{D.6}$$

Note that the averaging can be performed as well between the inner voltage leads (l_h) instead of the full length of the heater/thermometer l.

E LabView program for automatic 3ω experiments run as a function of temperature

A non-negligible part of this thesis was spent setting-up the experiment, and making it run automatically. A program has been written using LabView, allowing to automatically record diverse informations (voltage, phase, temperature, etc.), adjust the differential bridge at each temperature to run 3ω experiments, and estimate the temperature oscillation amplitude using MATLAB within one interface. The front panel of the program is shown below.

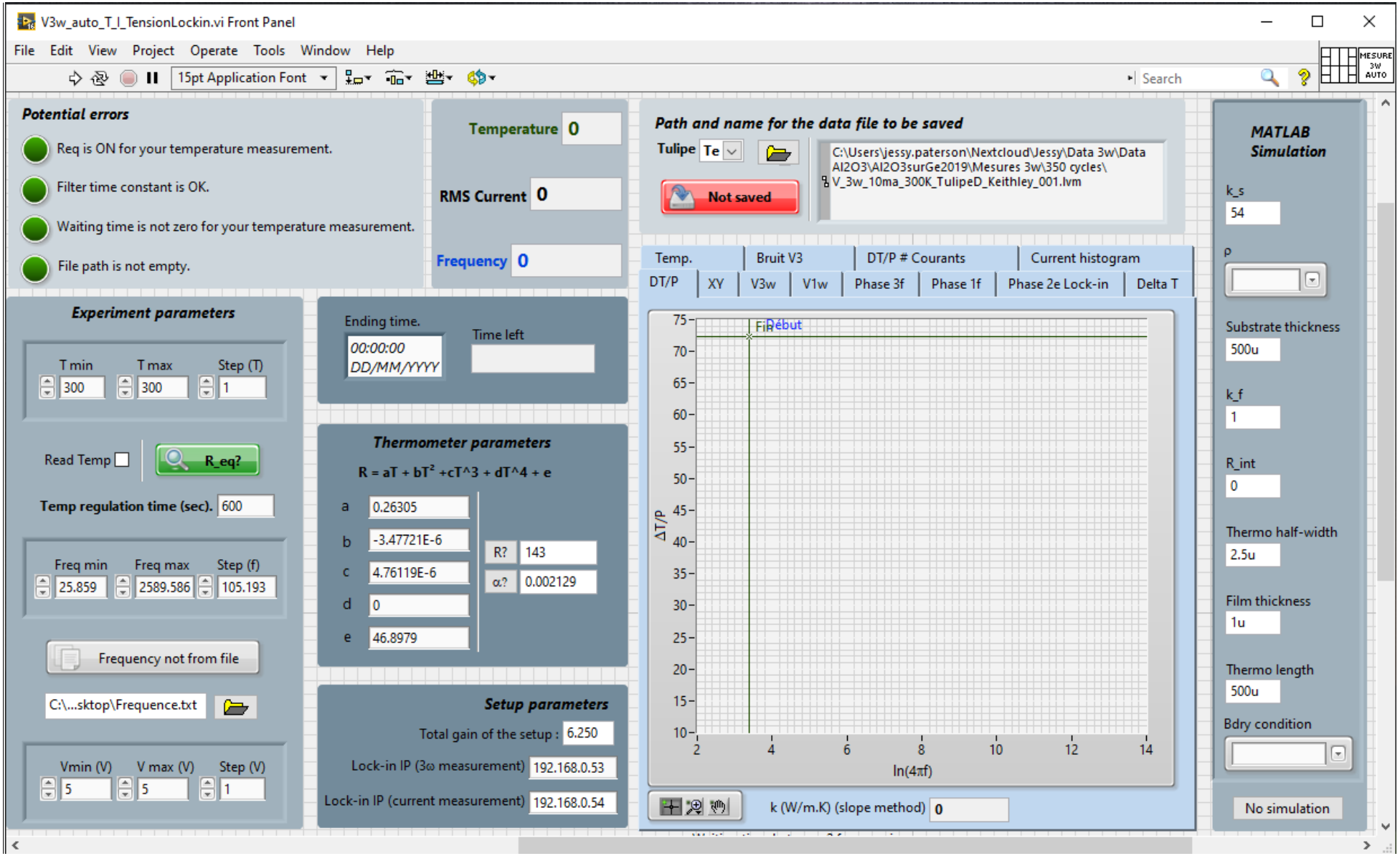
V3w_auto_T_I_TensionLockin.vi Front Panel
File Edit View Project Operate Tools Window Help
15pt Application Font
Search
MESURE 3W AUTO
Potential errors
Req is ON for your temperature measurement.
Filter time constant is OK.
Waiting time is not zero for your temperature measurement.
File path is not empty.
Temperature 0
RMS Current 0
Frequency 0
Path and name for the data file to be saved
Tulipe Te
Not saved
C:\Users\jessy.paterson\Nextcloud\Jessy\Data 3w\Data Al2O3\Al2O3surGe2019\Mesures 3w\350 cycles\V_3w_10ma_300K_TulipeD_Keithley_001.lvm
MATLAB Simulation
k_s
54
ρ
Substrate thickness
500u
k_f
1
R_int
0
Thermo half-width
2.5u
Film thickness
1u
Thermo length
500u
Bdry condition
No simulation
Experiment parameters
T min
T max
Step (T)
300
300
1
Read Temp
R_eq?
Temp regulation time (sec). 600
Freq min
Freq max
Step (f)
25.859
2589.586
105.193
Frequency not from file
C:\...sktop\Frequence.txt
Vmin (V)
V max (V)
Step (V)
5
5
1
Ending time.
00:00:00
DD/MM/YYYY
Time left
Thermometer parameters
R = aT + bT² +cT^3 + dT^4 + e
a 0.26305
b -3.47721E-6
c 4.76119E-6
d 0
e 46.8979
R? 143
α? 0.002129
Setup parameters
Total gain of the setup : 6.250
Lock-in IP (3ω measurement) 192.168.0.53
Lock-in IP (current measurement) 192.168.0.54
Temp.
Bruit V3
DT/P # Courants
Current histogram
DT/P
XY
V3w
V1w
Phase 3f
Phase 1f
Phase 2e Lock-in
Delta T
Début
Fin
ΔT/P
ln(4πf)
k (W/m.K) (slope method) 0

Bibliography

[1] A. T. Ramu and J. E. Bowers, Review of Scientific Instruments **83**, 124903 (2012).

[2] M. Asheghi, M. N. Touzelbaev, K. E. Goodson, Y. K. Leung, and S. S. Wong, Journal of Heat Transfer **120**, 30 (1998).

[3] W. Jang, Z. Chen, W. Bao, C. N. Lau, and C. Dames, Nano Letters **10**, 3909 (2010).

[4] T. N. Narasimhan, Physics Today **63**, 36 (2010).

[5] J. B. J. Fourier, *Théorie analytique de la chaleur* (1822).

[6] P. Debye, Annalen der Physik (1912).

[7] R. Peierls, Annalen der Physik **395**, 1055 (1929).

[8] O. Bourgeois, D. Tainoff, A. Tavakoli, Y. Liu, C. Blanc, M. Boukhari, A. Barski, and E. Hadji, Comptes Rendus Physique **17**, 1154 (2016).

[9] W. Kim, R. Wang, and A. Majumdar, Nano Today **2**, 40 (2007).

[10] M. Beekman, D. T. Morelli, and G. S. Nolas, Nature Materials **14**, 1182 (2015).

[11] N. Ashcroft and N. Mermin, *Solid State Physics*, hrw intern ed. (Holt, Rinehart and Winston, 1976).

[12] G. Chen, *Nanoscale energy transport and conversion: a parallel treatment of electrons, molecules, phonons, and photons* (Oxford University Press, 2005).

[13] K. E. Termentzidis, *Nanostructured Semiconductors: Amorphization and Thermal Properties* (CRC Press, 2017).

[14] T. L. Bergman, A. S. Lavine, F. P. Incropera, and D. P. DeWitt, *Wiley* (2018).

[15] C. Monachon, *Thermal boundary conductance between metals and dielectrics*, Ph.D. thesis, EPFL (2013).

[16] R. B. Wilson and D. G. Cahill, Nature Communications **5**, 5075 (2014).

[17] R. B. Wilson and D. G. Cahill, Applied Physics Letters **107**, 203112 (2015).

[18] A. T. Ramu, N. I. Halaszynski, J. D. Peters, C. D. Meinhart, and J. E. Bowers, Scientific Reports **6**, 33571 (2016).

[19] Y. K. Koh and D. G. Cahill, Physical Review B **76**, 075207 (2007).

[20] Y. R. Koh, M. Shirazi-HD, B. Vermeersch, A. M. S. Mohammed, J. Shao, G. Pernot, J.-H. Bahk, M. J. Manfra, and A. Shakouri, Applied Physics Letters **109**, 243107 (2016).

[21] A. A. Maznev, J. A. Johnson, and K. A. Nelson, Physical Review B **84**, 195206 (2011).

[22] A. T. Ramu and J. E. Bowers, Journal of Heat Transfer **139**, 10.1115/1.4034796 (2017).

[23] F. X. Alvarez and D. Jou, Applied Physics Letters **90**, 2005 (2007).

[24] A. Beardo, M. Calvo-Schwarzwälder, J. Camacho, T. Myers, P. Torres, L. Sendra, F. Alvarez, and J. Bafaluy, Physical Review Applied **11**, 034003 (2019).

[25] M. Maldovan, Nature **503**, 209 (2013).

[26] M. G. Holland, Physical Review **132**, 2461 (1963).

[27] A. Balandin and K. L. Wang, Physical Review B **58**, 1544 (1998).

[28] C. Marchbanks and Z. Wu, Journal of Applied Physics **117**, 084305 (2015).

[29] O. Delaire, J. Ma, K. Marty, A. F. May, M. A. McGuire, M.-H. Du, D. J. Singh, A. Podlesnyak, G. Ehlers, M. D. Lumsden, and B. C. Sales, Nature Materials **10**, 614 (2011), arXiv:1103.2564 .

[30] D. M. Rowe and V. S. Shukla, Journal of Applied Physics **52**, 7421 (1981).

[31] P. G. Klemens, International Journal of Thermophysics **15**, 1345 (1994).

[32] G. Chen, Physical Review B **57**, 14958 (1998).

[33] J. J. Hopfield, Physical Review **182**, 945 (1969).

[34] M. Asen-Palmer, K. Bartkowski, E. Gmelin, M. Cardona, A. P. Zhernov, A. V. Inyushkin, A. Taldenkov, V. I. Ozhogin, K. M. Itoh, and E. E. Haller, Physical Review B **56**, 9431 (1997).

[35] J. Ziman, *Electrons and Phonons* (Oxford University Press, 2001).

[36] H. Casimir, Physica **5**, 495 (1938).

[37] P. G. Klemens, Proceedings of the Royal Society of London. Series A. Mathematical and Physical Sciences **208**, 108 (1951).

[38] C. Herring, Physical Review **95**, 954 (1954).

[39] P. G. Klemens, Proceedings of the Physical Society. Section A **68**, 1113 (1955).

[40] I. Pomeranchuk, J. Phys. USSR **4** (1941).

[41] D. J. Ecsedy and P. G. Klemens, Physical Review B **15**, 5957 (1977).

[42] G. A. Slack and S. Galginaitis, Physical Review **133**, A253 (1964).

[43] Z. Wang, J. E. Alaniz, W. Jang, J. E. Garay, and C. Dames, Nano Letters **11**, 2206 (2011).

[44] J. Callaway, Physical Review **113**, 1046 (1959), arXiv:1308.3269 .

[45] D. T. Morelli, J. P. Heremans, and G. A. Slack, Physical Review B **66**, 195304 (2002).

[46] P. Al-Alam, G. Pernot, M. Isaiev, D. Lacroix, M. De Vos, N. Stein, D. Osenberg, and L. Philippe, Physical Review B **100**, 115304 (2019).

[47] Z.-G. Chen, G. Han, L. Yang, L. Cheng, and J. Zou, Progress in Natural Science: Materials International **22**, 535 (2012).

[48] J.-S. Heron, C. Bera, T. Fournier, N. Mingo, and O. Bourgeois, Physical Review B **82**, 155458 (2010).

[49] R. Yanagisawa, J. Maire, A. Ramiere, R. Anufriev, and M. Nomura, Applied Physics Letters **110**, 133108 (2017).

[50] J.-K. Yu, S. Mitrovic, D. Tham, J. Varghese, and J. R. Heath, Nature Nanotechnology **5**, 718 (2010).

[51] P. E. Hopkins, C. M. Reinke, M. F. Su, R. H. Olsson, E. A. Shaner, Z. C. Leseman, J. R. Serrano, L. M. Phinney, and I. El-Kady, Nano Letters **11**, 107 (2011).

[52] D. Li, Y. Wu, P. Kim, L. Shi, P. Yang, and A. Majumdar, Applied Physics Letters **83**, 2934 (2003).

[53] W. Kim, Materials Research Innovations **15**, 375 (2011).

[54] O. Bourgeois, T. Fournier, and J. Chaussy, Journal of Applied Physics **101**, 016104 (2007).

[55] M. Y. Swinkels, M. R. van Delft, D. S. Oliveira, A. Cavalli, I. Zardo, R. W. van der Heijden, and E. P. A. M. Bakkers, Nanotechnology **26**, 385401 (2015).

[56] P. N. Martin, Z. Aksamija, E. Pop, and U. Ravaioli, Nano Letters **10**, 1120 (2010).

[57] M. Verdier, D. Lacroix, S. Didenko, J.-F. Robillard, E. Lampin, T.-M. Bah, and K. Termentzidis, Physical Review B **97**, 115435 (2018).

[58] A. I. Hochbaum, R. Chen, R. D. Delgado, W. Liang, E. C. Garnett, M. Najarian, A. Majumdar, and P. Yang, Nature **451**, 163 (2008).

[59] C. Blanc, A. Rajabpour, S. Volz, T. Fournier, and O. Bourgeois, Applied Physics Letters **103**, 043109 (2013).

[60] S. Lee, H. Yoo, W.-Y. Won, H. Cho, M. Seo, B. D. Kong, M. Meyyappan, and C.-K. Baek, Applied Physics Letters **116**, 203901 (2020).

[61] S. Mukherjee, U. Givan, S. Senz, M. de la Mata, J. Arbiol, and O. Moutanabbir, Nano Letters **18**, 3066 (2018).

[62] Z. Wang and N. Mingo, Applied Physics Letters **99**, 101903 (2011).

[63] J. Tang, H.-T. Wang, D. H. Lee, M. Fardy, Z. Huo, T. P. Russell, and P. Yang, Nano Letters **10**, 4279 (2010).

[64] N. Zen, T. A. Puurtinen, T. J. Isotalo, S. Chaudhuri, and I. J. Maasilta, Nature Communications **5**, 3435 (2014).

[65] J. Maire, R. Anufriev, and M. Nomura, Scientific Reports **7**, 41794 (2017).

[66] R. Anufriev, R. Yanagisawa, and M. Nomura, Nanoscale **9**, 15083 (2017).

[67] Z. Yu, Z. Ren, and J. Lee, Scientific Reports **9**, 1805 (2019).

[68] M. Sledzinska, B. Graczykowski, J. Maire, E. Chavez-Angel, C. M. Sotomayor-Torres, and F. Alzina, Advanced Functional Materials **30**, 1904434 (2020).

[69] L. Yang, N. Yang, and B. Li, Nano Letters **14**, 1734 (2014).

[70] S. Sakane, T. Ishibe, T. Hinakawa, N. Naruse, Y. Mera, M. Mahfuz Alam, K. Sawano, and Y. Nakamura, Applied Physics Letters **115**, 182104 (2019).

[71] J. R. Scotsman, R. J. Pcionek, H. Kong, C. Uher, and M. G. Kanatzidis, Chemistry of Materials **18**, 4993 (2006).

[72] W. Kim, J. Zide, A. Gossard, D. Klenov, S. Stemmer, A. Shakouri, and A. Majumdar, Physical Review Letters **96**, 045901 (2006).

[73] A. M. S. Mohammed, Y. R. Koh, B. Vermeersch, H. Lu, P. G. Burke, A. C. Gossard, and A. Shakouri, Nano Letters **15**, 4269 (2015).

[74] N. Mingo, D. Hauser, N. P. Kobayashi, M. Plissonnier, and A. Shakouri, Nano Letters **9**, 711 (2009).

[75] S. Wang and N. Mingo, Applied Physics Letters **94**, 203109 (2009).

[76] T. Damart, V. M. Giordano, and A. Tanguy, Physical Review B **92**, 094201 (2015).

[77] W. Kim and A. Majumdar, Journal of Applied Physics **99**, 084306 (2006).

[78] H. Zhang and A. Minnich, Scientific Reports **5**, 8995 (2015).

[79] H. Mizuno, S. Mossa, and J.-L. Barrat, Scientific Reports **5**, 14116 (2015), arXiv:1503.04080 .

[80] G. Pernot, M. Stoffel, I. Savic, F. Pezzoli, P. Chen, G. Savelli, A. Jacquot, J. Schumann, U. Denker, I. Mönch, C. Deneke, O. G. Schmidt, J. M. Rampnoux, S. Wang, M. Plissonnier, A. Rastelli, S. Dilhaire, and N. Mingo, Nature Materials **9**, 491 (2010).

[81] Z. Cheng, N. Tanen, C. Chang, J. Shi, J. McCandless, D. Muller, D. Jena, H. G. Xing, and S. Graham, Applied Physics Letters **115**, 092105 (2019).

[82] A. Giri, J. L. Braun, D. M. Shima, S. Addamane, G. Balakrishnan, and P. E. Hopkins, The Journal of Physical Chemistry C **122**, 29577 (2018).

[83] J. H. Kim, A. Feldman, and D. Novotny, Journal of Applied Physics **86**, 3959 (1999).

[84] R. Venkatasubramanian, Physical Review B **61**, 3091 (2000).

[85] T. Borca-Tasciuc, W. Liu, J. Liu, T. Zeng, D. W. Song, C. D. Moore, G. Chen, K. L. Wang, M. S. Goorsky, T. Radetic, R. Gronsky, T. Koga, and M. S. Dresselhaus, Superlattices and Microstructures **28**, 199 (2000).

[86] W. L. Liu, T. Borca-Tasciuc, G. Chen, J. L. Liu, and K. L. Wang, Journal of Nanoscience and Nanotechnology **1**, 39 (2001).

[87] S. T. Huxtable, A. R. Abramson, C.-L. Tien, A. Majumdar, C. LaBounty, X. Fan, G. Zeng, J. E. Bowers, A. Shakouri, and E. T. Croke, Applied Physics Letters **80**, 1737 (2002).

[88] J. L. Liu, A. Khitun, K. L. Wang, W. L. Liu, G. Chen, Q. H. Xie, and S. G. Thomas, Physical Review B **67**, 165333 (2003).

[89] J. Alvarez-Quintana, X. Alvarez, J. Rodriguez-Viejo, D. Jou, P. D. Lacharmoise, A. Bernardi, A. R. Goñi, and M. I. Alonso, Applied Physics Letters **93**, 013112 (2008).

[90] D. Li, Y. Wu, R. Fan, P. Yang, and A. Majumdar, Applied Physics Letters **83**, 3186 (2003).

[91] C. Dames and G. Chen, Journal of Applied Physics **95**, 682 (2004).

[92] T. Yao, Applied Physics Letters **51**, 1798 (1987).

[93] G. Savelli, S. Silveira Stein, G. Bernard-Granger, P. Faucherand, L. Montès, S. Dilhaire, and G. Pernot, Nanotechnology **26**, 275605 (2015).

[94] G. Savelli, S. Silveira Stein, G. Bernard-Granger, P. Faucherand, and L. Montès, Superlattices and Microstructures **97**, 341 (2016).

[95] B. Saha, Y. R. Koh, J. P. Feser, S. Sadasivam, T. S. Fisher, A. Shakouri, and T. D. Sands, Journal of Applied Physics **121**, 015109 (2017).

[96] W.-Y. Lee, J.-h. Lee, J.-y. Ahn, T.-h. Park, N.-W. Park, G.-S. Kim, J.-S. Park, and S.-K. Lee, Nanotechnology **28**, 105401 (2017).

[97] W. Ren, H. Li, L. Gao, Y. Li, Z. Zhang, C. Long, H. Ji, X. Niu, Y. Lin, and Z. Wang, Nano Research **10**, 247 (2017).

[98] Y. Zhou, K. Huang, L. Zhou, X. Cheng, M. Xu, H. Tong, and X. Miao, RSC Advances **9**, 9457 (2019).

[99] K. Termentzidis, P. Chantrenne, J.-Y. Duquesne, and A. Saci, Journal of Physics: Condensed Matter **22**, 475001 (2010).

[100] A. France-Lanord, S. Merabia, T. Albaret, D. Lacroix, and K. Termentzidis, Journal of Physics: Condensed Matter **26**, 355801 (2014).

[101] A. Giri, J. L. Braun, and P. E. Hopkins, Journal of Applied Physics **119**, 235305 (2016).

[102] D. G. Cahill, Review of Scientific Instruments **75**, 5119 (2004).

[103] P. L. Kapitza, Physical Review **60**, 354 (1941).

[104] E. T. Swartz and R. O. Pohl, Reviews of Modern Physics **61**, 605 (1989).

[105] C. Monachon, L. Weber, and C. Dames, Annual Review of Materials Research **46**, 433 (2016).

[106] W. A. Little, Canadian Journal of Physics **37**, 334 (1959).

[107] A. Giri and P. E. Hopkins, Advanced Functional Materials **1903857**, 1903857 (2019).

[108] B. C. Gundrum, D. G. Cahill, and R. S. Averback, Physical Review B - Condensed Matter and Materials Physics **72**, 245426 (2005).

[109] R. B. Wilson and D. G. Cahill, Physical Review Letters **108**, 255901 (2012).

[110] N. Snyder, Cryogenics **10**, 89 (1970).

[111] P. E. Hopkins, L. M. Phinney, J. R. Serrano, and T. E. Beechem, Physical Review B **82**, 085307 (2010).

[112] W.-P. Hsieh, A. S. Lyons, E. Pop, P. Keblinski, and D. G. Cahill, Physical Review B **84**, 184107 (2011).

[113] J. C. Duda, T. E. Beechem, J. L. Smoyer, P. M. Norris, and P. E. Hopkins, Journal of Applied Physics **108**, 073515 (2010).

[114] Y. Chalopin, K. Esfarjani, A. Henry, S. Volz, and G. Chen, Physical Review B **85**, 195302 (2012).

[115] R. Cheaito, J. T. Gaskins, M. E. Caplan, B. F. Donovan, B. M. Foley, A. Giri, J. C. Duda, C. J. Szwejkowski, C. Constantin, H. J. Brown-Shaklee, J. F. Ihlefeld, and P. E. Hopkins, Physical Review B **91**, 035432 (2015).

[116] Y. Chu, J. Shi, K. Miao, Y. Zhong, P. Sarangapani, T. S. Fisher, G. Klimeck, X. Ruan, and T. Kubis, Applied Physics Letters **115**, 231601 (2019), arXiv:1908.11578 .

[117] P. E. Hopkins, ISRN Mechanical Engineering **2013**, 1 (2013), 0207015 [cond-mat] .

[118] H. Malekpour and A. A. Balandin, Journal of Raman Spectroscopy **49**, 106 (2018).

[119] D. G. Cahill, Review of Scientific Instruments **61**, 802 (1990).

[120] N. O. Birge and S. R. Nagel, Review of Scientific Instruments **58**, 1464 (1987).

[121] S.-M. Lee, D. G. Cahill, and T. H. Allen, Physical Review B **52**, 253 (1995).

[122] D.-A. Borca-Tasciuc, L. Pietruszka, T. Borca-Tasciuc, R. Vajtai, and P. Ajayan, in *Semiconductor Thermal Measurement and Management IEEE Twenty First Annual IEEE Symposium, 2005.* (IEEE, 2005) pp. 247–252.

[123] T. Borca-Tasciuc, A. R. Kumar, and G. Chen, Review of Scientific Instruments **72**, 2139 (2001).

[124] L. Lu, W. Yi, and D. L. Zhang, Review of Scientific Instruments **72**, 2996 (2001).

[125] J. S. Heron, T. Fournier, N. Mingo, and O. Bourgeois, Nano Letters **9**, 1861 (2009).

[126] A. Jain and K. E. Goodson, Journal of Heat Transfer **130**, 1 (2008).

[127] H. Ftouni, D. Tainoff, J. Richard, K. Lulla, J. Guidi, E. Collin, and O. Bourgeois, Review of Scientific Instruments **84**, 094902 (2013).

[128] N. Bodenschatz, A. Liemert, S. Schnurr, U. Wiedwald, and P. Ziemann, Review of Scientific Instruments **84**, 104902 (2013).

[129] S. Kommandur and S. Yee, Review of Scientific Instruments **89**, 114905 (2018).

[130] S. Lefevre and S. Volz, Review of Scientific Instruments **76**, 10.1063/1.1857151 (2005).

[131] S. R. Choi, J. Kim, and D. Kim, Review of Scientific Instruments **78**, 084902 (2007).

[132] S. Gauthier, A. Giani, and P. Combette, Sensors and Actuators A: Physical **195**, 50 (2013).

[133] S. D. Lubner, J. Choi, G. Wehmeyer, B. Waag, V. Mishra, H. Natesan, J. C. Bischof, and C. Dames, Review of Scientific Instruments **86**, 014905 (2015).

[134] M. L. Bauer and P. M. Norris, Review of Scientific Instruments **85**, 064903 (2014).

[135] W. Hodges and C. Dames, Review of Scientific Instruments **90**, 094903 (2019).

[136] Y. Zhang, C. Wu, and T. Borca-Tasciuc, Journal of Applied Physics **127**, 185101 (2020).

[137] J. C. Jaeger and H. S. Carslaw, *Conduction of heat in solids* (Clarendon P, 1959).

[138] C. Dames and G. Chen, Review of Scientific Instruments **76**, 1 (2005).

[139] J. Kimling, S. Martens, and K. Nielsch, Review of Scientific Instruments **82**, 074903 (2011).

[140] Stanford Research Systems, About Lock-In Amplifiers, Application Note 3 (2004).

[141] J. Alvarez-Quintana and J. Rodríguez-Viejo, Sensors and Actuators A: Physical **142**, 232 (2008).

[142] Signal Recovery, *Lock-in SR7230 Instruction Manual*.

[143] M. R. Pinnel, Gold Bulletin **12**, 62 (1979).

[144] D. G. Cahill, M. Katiyar, and J. R. Abelson, Physical Review B **50**, 6077 (1994).

[145] J. H. Kim, A. Feldman, and D. Novotny, Journal of Applied Physics **86**, 3959 (1999).

[146] T. Tong and A. Majumdar, Review of Scientific Instruments **77**, 104902 (2006).

[147] S. P. Gurrum, W. P. King, and Y. K. Joshi, Journal of Applied Physics **103**, 10.1063/1.2937254 (2008).

[148] H. Wang and M. Sen, International Journal of Heat and Mass Transfer **52**, 2102 (2009).

[149] J.-Y. Duquesne, D. Fournier, and C. Frétigny, Journal of Applied Physics **108**, 086104 (2010).

[150] A. T. Ramu and J. E. Bowers, Journal of Applied Physics **112**, 043516 (2012).

[151] V. Mishra, C. L. Hardin, J. E. Garay, and C. Dames, Review of Scientific Instruments **86**, 054902 (2015).

[152] Z. Chen and C. Dames, *Applied Thermal Measurements at the Nanoscale*, Lessons from Nanoscience: A Lecture Notes Series, Vol. 7 (World Scientific, 2018).

[153] A. Degiovanni, Int. J. Heat Mass Transfer **31**, 553 (1988).

[154] D. Maillet, S. André, J. C. Batsale, A. Degiovanni, and C. Moyne, *Thermal Quadrupoles: Solving the Heat Equation through Integral Transforms* (2000).

[155] A. Feldman, High Temperatures-High Pressures **31**, 293 (1999).

[156] S.-M. Lee and D. G. Cahill, Journal of Applied Physics **81**, 2590 (1997).

[157] E.-K. Kim, S.-I. Kwun, S.-M. Lee, H. Seo, and J.-G. Yoon, Applied Physics Letters **76**, 3864 (2000).

[158] T. Yamane, N. Nagai, S. I. Katayama, and M. Todoki, Journal of Applied Physics **91**, 9772 (2002).

[159] A. Jacquot, F. Vollmer, B. Bayer, M. Jaegle, D. G. Ebling, and H. Böttner, Journal of Electronic Materials **39**, 1621 (2010).

[160] Z. X. Zong, Z. J. Qiu, S. L. Zhang, R. Streiter, and R. Liu, Journal of Applied Physics **109**, 10.1063/1.3559299 (2011).

[161] S. Rausch, D. Rauh, C. Deibel, S. Vidi, and H. P. Ebert, International Journal of Thermophysics **34**, 820 (2013).

[162] B. Shen, Z. Zeng, C. Lin, and Z. Hu, International Journal of Thermal Sciences **66**, 19 (2013).

[163] C. Zhou, G. Koblmüller, M. Bichler, G. Abstreiter, and M. Grayson, in *Quantum Sensing and Nanophotonic Devices X*, Vol. 8631, edited by M. Razeghi (2013) p. 863129.

[164] X. Li, W. Park, Y. P. Chen, and X. Ruan, Applied Physics Letters **111**, 10.1063/1.5006174 (2017).

[165] X. Li, Y. Yan, L. Dong, J. Guo, A. Aiyiti, X. Xu, and B. Li, Journal of Physics D: Applied Physics **50**, 104002 (2017).

[166] C. Dames, Annual Review of Heat Transfer **16**, 7 (2013).

[167] G. Wehmeyer, T. Yabuki, C. Monachon, J. Wu, and C. Dames, Applied Physics Reviews **4**, 041304 (2017).

[168] R. O. Pohl, X. Liu, and E. Thompson, Reviews of Modern Physics **74**, 991 (2002).

[169] S. Swaminathan, Y. Sun, P. Pianetta, and P. C. McIntyre, Journal of Applied Physics **110**, 094105 (2011).

[170] A. Jacquot, B. Lenoir, A. Dauscher, M. Stölzer, and J. Meusel, Journal of Applied Physics **91**, 4733 (2002).

[171] T. Ding, Y. Jannot, and A. Degiovanni, International Journal of Thermal Sciences **86**, 314 (2014).

[172] W. Jaber and P.-O. Chapuis, AIP Advances **8**, 045111 (2018).

[173] J.-L. Battaglia, C. Wiemer, and M. Fanciulli, Journal of Applied Physics **101**, 104510 (2007).

[174] B. W. Olson, S. Graham, and K. Chen, Review of Scientific Instruments **76**, 053901 (2005).

[175] Y. S. Ju and K. E. Goodson, Journal of Applied Physics **85**, 7130 (1999).

[176] D. Singhal, J. Paterson, D. Tainoff, J. Richard, M. Ben-Khedim, P. Gentile, L. Cagnon, D. Bourgault, D. Buttard, and O. Bourgeois, Review of Scientific Instruments **89**, 084902 (2018), arXiv:1811.08732 .

[177] X. Zhang, H. Xie, M. Fujii, H. Ago, K. Takahashi, T. Ikuta, H. Abe, and T. Shimizu, Applied Physics Letters **86**, 1 (2005).

[178] S. J. Mason, D. J. Wesenberg, A. Hojem, M. Manno, C. Leighton, and B. L. Zink, Physical Review Materials **4**, 065003 (2020).

[179] M. Handwerg, R. Mitdank, Z. Galazka, and S. F. Fischer, Semiconductor Science and Technology **31**, 125006 (2016), arXiv:1506.05294 .

[180] R. N. Bracewell, *The Fourier Transform and its applications* (New York : Mc-Graw-Hill, 1986).

[181] C. Kittel, Physical Review **75**, 972 (1949).

[182] W. Phillips, *Amorphous Solids*, edited by W. A. Phillips, Topics in Current Physics, Vol. 24 (Springer Berlin Heidelberg, Berlin, Heidelberg, 1981).

[183] G. Monaco and V. M. Giordano, Proceedings of the National Academy of Sciences **106**, 3659 (2009).

[184] Z. Hu, K. Nomoto, W. Li, N. Tanen, K. Sasaki, A. Kuramata, T. Nakamura, D. Jena, and H. G. Xing, IEEE Electron Device Letters **39**, 869 (2018).

[185] Y. Hsu, X. Fang, L. A. Wang, H.-W. Zan, H.-F. Meng, and S.-H. Yang, Organic Electronics **15**, 3609 (2014).

[186] M. J. Biercuk, D. J. Monsma, C. M. Marcus, J. S. Becker, and R. G. Gordon, Applied Physics Letters **83**, 2405 (2003).

[187] M. D. Groner, F. H. Fabreguette, J. W. Elam, and S. M. George, Chemistry of Materials **16**, 639 (2004).

[188] S. M. George, Chemical Reviews **110**, 111 (2010).

[189] A. Toriumi, T. Tabata, C. Hyun Lee, T. Nishimura, K. Kita, and K. Nagashio, Microelectronic Engineering **86**, 1571 (2009).

[190] R. Pillarisetty, Nature **479**, 324 (2011).

[191] K. El hajraoui, M. A. Luong, E. Robin, F. Brunbauer, C. Zeiner, A. Lugstein, P. Gentile, J.-L. Rouvière, and M. Den Hertog, Nano Letters **19**, 2897 (2019).

[192] D. Singhal, J. Paterson, M. Ben-Khedim, D. Tainoff, L. Cagnon, J. Richard, E. Chavez-Angel, J. J. Fernandez, C. M. Sotomayor-Torres, D. Lacroix, D. Bourgault, D. Buttard, and O. Bourgeois, Nanoscale **11**, 13423 (2019).

[193] S. D. Lubner, S. Kaur, Y. Fu, V. Battaglia, and R. S. Prasher, Journal of Applied Physics **127**, 105104 (2020).

[194] J. Paterson, D. Singhal, D. Tainoff, J. Richard, and O. Bourgeois, Journal of Applied Physics **127**, 245105 (2020).

[195] C. S. Gorham, J. T. Gaskins, G. N. Parsons, M. D. Losego, and P. E. Hopkins, Applied Physics Letters **104**, 253107 (2014).

[196] M. E. DeCoster, K. E. Meyer, B. D. Piercy, J. T. Gaskins, B. F. Donovan, A. Giri, N. A. Strnad, D. M. Potrepka, A. A. Wilson, M. D. Losego, and P. E. Hopkins, Thin Solid Films **650**, 71 (2018).

[197] P. A. Premkumar, A. Delabie, L. N. J. Rodriguez, A. Moussa, and C. Adelmann, Journal of Vacuum Science & Technology A: Vacuum, Surfaces, and Films **31**, 061501 (2013).

[198] E. A. Scott, J. T. Gaskins, S. W. King, and P. E. Hopkins, APL Materials **6**, 058302 (2018).

[199] S.-M. Lee, W. Choi, J. Kim, T. Kim, J. Lee, S. Y. Im, J. Y. Kwon, S. Seo, M. Shin, and S. E. Moon, International Journal of Thermophysics **38**, 176 (2017).

[200] D. G. Cahill, S. K. Watson, and R. O. Pohl, Physical Review B **46**, 6131 (1992).

[201] I. Stark, M. Stordeur, and F. Syrowatka, Thin Solid Films **226**, 185 (1993).

[202] A. Cappella, J.-L. Battaglia, V. Schick, A. Kusiak, A. Lamperti, C. Wiemer, and B. Hay, Advanced Engineering Materials **15**, 1046 (2013).

[203] C. Monachon and L. Weber, Advanced Engineering Materials **17**, 68 (2015).

[204] Z. Luo, H. Liu, B. T. Spann, Y. Feng, P. Ye, Y. P. Chen, and X. Xu, Nanoscale and Microscale Thermophysical Engineering **18**, 183 (2014).

[205] R. M. Costescu, A. J. Bullen, G. Matamis, K. E. O'Hara, and D. G. Cahill, Physical Review B **65**, 094205 (2002).

[206] T. Yamane, N. Nagai, S. I. Katayama, and M. Todoki, Journal of Applied Physics **91**, 9772 (2002).

[207] X. Li, W. Park, Y. Wang, Y. P. Chen, and X. Ruan, Journal of Applied Physics **125**, 045302 (2019).

[208] C. Monachon, M. Hojeij, and L. Weber, Applied Physics Letters **98**, 091905 (2011).

[209] M. Botzakaki, A. Kerasidou, L. Sygellou, V. Ioannou-Sougleridis, N. Xanthopoulos, S. Kennou, S. Ladas, N. Z. Vouroutzis, T. Speliotis, and D. Skarlatos, ECS Solid State Letters **1**, P32 (2012).

[210] S. Merabia and K. Termentzidis, Physical Review B **86**, 094303 (2012).

[211] P. E. Hopkins, R. N. Salaway, R. J. Stevens, and P. M. Norris, International Journal of Thermophysics **28**, 947 (2007).

[212] C. T. Lynch, *Practical Handbook of Materials Science*, 1st ed. (CRC Press, 1989).

[213] M. D. Tiwari and B. K. Agrawal, Physical Review B **4**, 3527 (1971).

[214] J. F. Shackelford, Y.-H. Han, S. Kim, and S.-H. Kwon, *CRC Materials Science and Engineering Handbook* (CRC Press, 2016).

[215] M. E. Suk and Y. Y. Kim, International Journal of Precision Engineering and Manufacturing **20**, 1435 (2019).

[216] M. Jeong, J. P. Freedman, H. J. Liang, C.-M. Chow, V. M. Sokalski, J. A. Bain, and J. A. Malen, Physical Review Applied **5**, 014009 (2016).

[217] M. Blank and L. Weber, Journal of Applied Physics **124**, 105304 (2018).

[218] F. L. Riley, Journal of the American Ceramic Society **83**, 245 (2004).

[219] H. Ftouni, C. Blanc, D. Tainoff, A. D. Fefferman, M. Defoort, K. J. Lulla, J. Richard, E. Collin, and O. Bourgeois, Physical Review B **92**, 125439 (2015).

[220] G. A. Slack, *CRC Handbook of Thermoelectrics*, edited by D. M. Rowe (CRC PRess, Boca Raton, FL, 1995).

[221] J. M. Zide, D. O. Klenov, S. Stemmer, A. C. Gossard, G. Zeng, J. E. Bowers, D. Vashaee, and A. Shakouri, Applied Physics Letters **87**, 112102 (2005).

[222] M. Jamet, A. Barski, T. Devillers, V. Poydenot, R. Dujardin, P. Bayle-Guillemaud, J. Rothman, E. Bellet-Amalric, A. Marty, J. Cibert, R. Mattana, and S. Tatarenko, Nature Materials **5**, 653 (2006).

[223] T. Devillers, *Etude des propriétés physiques des phases de Ge(1-x)Mn(x) ferromagnétiques pour l'électronique de spin*, Ph.D. thesis, Université Joseph Fourier (2008).

[224] A. Jain, M. Jamet, A. Barski, T. Devillers, I.-S. Yu, C. Porret, P. Bayle-Guillemaud, V. Favre-Nicolin, S. Gambarelli, V. Maurel, G. Desfonds, J. F. Jacquot, and S. Tardif, Journal of Applied Physics **109**, 013911 (2011).

[225] R. T. Lechner, V. Holý, S. Ahlers, D. Bougeard, J. Stangl, A. Trampert, A. Navarro-Quezada, and G. Bauer, Applied Physics Letters **95**, 023102 (2009).

[226] J. Alvarez-Quintana, J. Rodríguez-Viejo, F. Alvarez, and D. Jou, International Journal of Heat and Mass Transfer **54**, 1959 (2011).

[227] P. D. Desai, Journal of Physical and Chemical Reference Data **16**, 91 (1987).

[228] A. Minnich and G. Chen, Applied Physics Letters **91**, 073105 (2007).

[229] V. Jean, *Modélisation du transport de phonons dans les semi-conducteurs nanostructurés*, Ph.D. thesis, Université de Lorraine (2014).

[230] C.-W. Nan, R. Birringer, D. R. Clarke, and H. Gleiter, Journal of Applied Physics **81**, 6692 (1997).

[231] C. Mangold, S. Chen, G. Barbalinardo, J. Behler, P. Pochet, K. Termentzidis, Y. Han, L. Chaput, D. Lacroix, and D. Donadio, Journal of Applied Physics **127**, 244901 (2020), arXiv:2005.09591 .

[232] K. Ghosh, A. Kusiak, P. Noé, M.-C. Cyrille, and J.-L. Battaglia, Physical Review B **101**, 214305 (2020), arXiv:2006.02625 .

[233] Y. Liu, *Thermal engineering in an epitaxial nanostructured germanium semi-conductor*, Ph.D. thesis, Université Joseph Fourier (2015).

[234] V. Jean, S. Fumeron, K. Termentzidis, S. Tutashkonko, and D. Lacroix, Journal of Applied Physics **115**, 024304 (2014).

[235] P. Noé, C. Vallée, F. Hippert, F. Fillot, and J.-Y. Raty, Semiconductor Science and Technology **33**, 013002 (2018).

[236] P. Kowalczyk, F. Hippert, N. Bernier, C. Mocuta, C. Sabbione, W. Batista-Pessoa, and P. Noé, Small **14**, 1704514 (2018).

[237] J.-Y. Raty, P. Noé, G. Ghezzi, S. Maîtrejean, C. Bichara, and F. Hippert, Physical Review B **88**, 014203 (2013).

[238] M. Hong, J. Zou, and Z. Chen, Advanced Materials **31**, 1807071 (2019).

[239] K. S. Bayikadi, R. Sankar, C. T. Wu, C. Xia, Y. Chen, L.-C. Chen, K.-H. Chen, and F.-C. Chou, Journal of Materials Chemistry A **7**, 15181 (2019).

[240] E. M. Levin, M. F. Besser, and R. Hanus, Journal of Applied Physics **114**, 083713 (2013).

[241] R. Fallica, E. Varesi, L. Fumagalli, S. Spadoni, M. Longo, and C. Wiemer, physica status solidi (RRL) - Rapid Research Letters **7**, 1107 (2013).

[242] R. J. Warzoha, B. F. Donovan, N. T. Vu, J. G. Champlain, S. Mack, and L. B. Ruppalt, Applied Physics Letters **115**, 023104 (2019).

[243] A. Kusiak, J.-L. Battaglia, P. Noé, V. Sousa, and F. Fillot, Journal of Physics: Conference Series **745**, 032104 (2016).

[244] G. C. Sosso, D. Donadio, S. Caravati, J. Behler, and M. Bernasconi, Physical Review B **86**, 104301 (2012).

[245] R. Lan, R. Endo, M. Kuwahara, Y. Kobayashi, and M. Susa, Journal of Applied Physics **112**, 053712 (2012).

[246] D. Campi, L. Paulatto, G. Fugallo, F. Mauri, and M. Bernasconi, Physical Review B **95**, 024311 (2017).

[247] O. Bourgeois, E. André, C. Macovei, and J. Chaussy, Review of Scientific Instruments **77**, 126108 (2006).

[248] T. Nguyen, A. Tavakoli, S. Triqueneaux, R. Swami, A. Ruhtinas, J. Gradel, P. Garcia-Campos, K. Hasselbach, A. Frydman, B. Piot, M. Gibert, E. Collin, and O. Bourgeois, Journal of Low Temperature Physics **197**, 348 (2019).

[249] P. E. Hopkins, P. M. Norris, and R. J. Stevens, Journal of Heat Transfer **130**, 022401 (2008).

[250] D. M. Hamby, Environmental Monitoring and Assessment **32**, 135 (1994).

[251] A. Saltelli, M. Ratto, T. Andres, F. Campolongo, J. Cariboni, D. Gatelli, M. Saisana, and S. Tarantola, *Global Sensitivity Analysis. The Primer* (John Wiley and Sons, Ltd, Chichester, UK, 2008) pp. 1–292.

[252] J. S. Alper and R. I. Gelb, The Journal of Physical Chemistry **94**, 4747 (1990).

[253] G. Anderson, Geochimica et Cosmochimica Acta **40**, 1533 (1976).

[254] W. H. Press, S. A. Teukolsky, W. T. Vetterling, and B. P. Flannery, *Numerical Recipes: The Art of Scientific Computing*, 3rd ed. (Cambridge University Press, 2007).

[255] W. Clarkson, HOWTO estimate parameter-errors using Monte Carlo - an example with python (2014).

[256] J. Reddy, *An introduction to the finite element method* (New-York: McGraw-Hill, 2006).

[257] COMSOL, The Finite Element Method (FEM).

[258] Mathematica, Mathematica's Heat Transfer Tutorial.